Elasto-viscoplastic Numerical Analysis of Soil-Foundation Interaction in Soft Clay Ground

December 2005

Boonlert Siribumrungwong

Elasto-viscoplastic Numerical Analysis of Soil-Foundation Interaction in Soft Clay Ground

December 2005

Boonlert Siribumrungwong

Abstract

In these present times, the numerical method plays an important role in Geotechnical Engineering. It provides a solutions for analytically intractable problems with complex loading and boundary conditions. Therefore, the numerical method is commonly used in studies on the interaction between soil and foundations. In cases where a foundation is embedded in or laid on a soft clay ground, however, several complex issues will be encountered in the analysis. These issues involves large deformations of the ground, the rate sensitivity of clay, microstructural changes, strength degradation, and strain localization. It is still uncertain whether or not the numerical method should be applied to tackle these problems. The main propose of this dissertation is to study the soil-foundation interaction in soft clay grounds while taking the above-mentioned issues into consideration. The problems include the behavior of soil due to an excavation through a thick soft clay deposit and a case study of the large displacements of bulkhead piles caused by the construction of an embankment. In addition, the effects of microstructural changes, strength degradation, and strain localization on the bearing capacity of a shallow foundation on a clay stratum are examined. The dissertation ends with the introduction of an adaptive mesh refinement algorithm for the elasto-viscoplastic analysis method.

Numerical analyses using an elasto-viscoplastic constitutive model with a finite element formulation, based on the finite deformation theory, is adopted as a tool to study the soil-foundation interaction problem. Firstly, simulations are performed to examine the effects of various parameters on the lateral earth pressure of a vertical backface retaining wall which supportings horizontal backfill. The friction conditions between the wall and the soil, as well as the wall movement patterns, are found to have prominent effects on the deformation of the soils behind the wall and on the development of earth pressure.

Then, the soil-structure interaction problem of a braced excavation in a thick soft clay deposit is examined. Numerical simulations under idealized symmetric plane strain excavation geometry are carried out. The behavior of the excavation when sheet piles are not embedded in a firm stratum is studied. A comparison shows a reasonable agreement between the results of the numerical analysis and the data obtained from the case study, and thus, it is indicated that this study can quantitatively reproduce the behavior of the soil in the excavation works through thick soft clay deposits well. Moreover, it was found that the preloads cannot effectively limit the deformation of ground under the excavation level.

As another actual case study, the deformation of the ground and the displacement of bulkhead piles due to the construction of a large-scale embankment are analyzed. The construction site is located near the shores of the Aji River in the bay area of Osaka Prefecture. Laboratory tests are carried out to obtain the relevant soil parameters for an underlying thick alluvial clay layer in the construction field. Numerical analyses are then performed using these parameters. An elasto-viscoplastic constitutive model for clayey soils, considering structural changes, is employed to include the effects of microstructural changes and strength degradation in the analyses. The simulation method can well quantitatively reproduce the deformation of the ground and the displacement of the supporting structures in the field, and the structural changes and the strength degradation of the clay are found to play important roles in this achievement. Moreover, the results of the analyses show direct relations between the lateral pile displacement and the ground settlement and indicate that the lateral pile displacement and the ground settlement can be reduced by installing the piles into the firm stratum beneath the soft clay layer.

In order to study the effects of degradation on the bearing capacity problem, a series of analyses of footings on a clay deposit with different microstructural parameters is conducted. Numerical analyses under plane strain conditions and three-dimensional conditions are carried out to simulate the behavior of a clay ground subjected to loads from a strip footing and a square footing, respectively. The results of the analyses show that the strain localization develops only in the highly-structured clay ground due to the loading of the footings. These strain localization zones act as "slip lines" and affect the bearing behavior of the footings. The effects of footing roughness on the failure mechanism are also discussed.

Finally, an adaptive refinement method is introduced into the large strain finite element analysis using an elasto-viscoplastic model. The method is found to work well in reducing the errors estimated from the analyses and in giving better results for the cases in which strain localization is generated. The performance of the adaptive refinement method is also discussed, taking the computation time and costs into consideration.

Acknowledgement

My last year in Japan and my sixth year at the Laboratory of Geomechanics in the Department of Civil and Earth Resource Engineering at Kyoto University will almost pass with the finish of this dissertation. During this period, which I have been through the Master and Doctoral programs in the laboratory, it is unquestionable that I owe a dept of gratitude to all the people I met here.

I would like to express my profound gratitude to my supervisor, Professor Fusao Oka, for his invaluable guidance, and innumerable assistance in the process of writing this dissertation. His experience in the field and vast knowledge were great important to this thesis. Without his encouragement in both academic and personal concerns, this work could not have been completed. It has been a really great opportunity for me to be one of his students over the past six year.

Sincere appreciation is also extended to the member of Dissertation Committee, namely, Professor Takeshi Tamura and Professor Ohtsu Hiroyasu, for their valuable suggestions in the contents of the thesis.

I am also deeply indebted to Associate professor Takeshi Kodaka, for his invaluable suggestions and discussions on the research topics. My study would not be nearly as successful without any of his contribution. I also extremely grateful to Research Associate Sayuri Kimoto for her active discussions and kind assistance in the completion of this thesis. I would also wish to extend my gratitude to Dr. Shinichiro Nakashima, a former Research Associate, presently at the Public Works Research Institute, for his useful and generous advice.

Special thanks are especially due to Dr. Yosuke Higo, a former student who is now at the Geo-Research Institute, for his valuable and meaningful contribution to promote the analysis method and programming. Special thanks are also extended to Dr. Chih-Wei Lu, a former student who is now at the National Kaohsiung First University of Science and Technology, Dr. Young-Seok Kim, a former student who is now at the Korea Institute of Construction Technology for their friendship and generous advice in various ways. I also want to thank Ms. Chikato Itoh for her supports and assistance in my researches. Warm thanks go to all of my present and graduated colleagues in the Laboratory of Geomechanics, for their friendship, helping hands, and warm environments. They never

forget to be supportive and friendly to me and made my life in Japan easier. I will always remember these wonderful memories.

I also want to express my thanks to Mr. Shingo Furukawa and Mr. Nobuya Kawashima of the Office of Nishi-Osaka Chisui, Osaka Prefecture for the data of a case study.

I also very much indebted to the financial support provided by the Ministry of Education, Science and Culture, Government of Japan (MONBUSHO), which made this study possible. Sincerely gratitude is also due to my supervisor and instructors in Thailand, Associate Professor Boonsom Lerdhirunwong, Associate Professor Wanchai Teparaksa and Assistant Professor Boonchai Ukritchon for their kind recommendations for studying in Japan.

It is also appropriated to my friends, both in Thailand and Kyoto, for their care and assistance to me whenever I needed it.

Above all, my deepest gratitude goes to my family. My parents, Pisit and Prapaporn always give me moral support and tremendous love. My brothers, Boonying, Koopong, and Noppong always encourage me to carry on my works. Everything I achieved is the attribute from their love and encouragements.

Table of Contents

List of Figures

List of Tables

Chapter 1

Introduction

1.1 Background and Objectives

Nowadays, the numerical method is an effective tool for studying problems in Geotechnical Engineering. Analytically intractable problems with complex loading and boundary conditions, as well as load-deformation history prior to failure, can be studied through numerical analyses. Therefore, the numerical method is commonly chosen as a tool for studying the soil-structure interaction problems. When considering a foundation embedded in a soft clay ground, however, several important issues are encountered. These issues include large deformations of the ground, microstructural changes, strength degradation, and the strain localization of clay ground. In particular, the foundation system itself is at risk of having low-base stability. This results in large displacements of the lower supporting system and failure due to a large plastic deformation of the clay ground.

A case study of a large-scale braced excavation, performed through a thick soft clay deposit, was reported by Tanaka et al. (1989). The excavation was performed as part of the Tokyo International (Haneda) Airport extension project. The sheet piles in this case could not be successfully installed into the firm stratum lying below since the thickness of the soft clay in the area is over 50m. Large displacements of the sheet piles and a significant heave at the excavation surface were observed as the final stage of the excavation approached. Large displacements were reported even at the toes of the sheet piles, and the sheet piles continued to deform with time due to the effects of undrained creep.

There have also been several cases where an embankment was constructed in the shore area of a river near bulkhead piles that were not embedded into a firm soil stratum. This

situation brought about large long-termed lateral displacements of the pile heads and the pile tips, as well as cracks on the ground surface behind the pile heads, which were observed after the construction was completed. The large displacements of the pile tips indicated the low-base stability of the piles. The amount of ground settlement due to the construction of embankment became larger than the designed value as well . Countermeasure are now being plannned to cope with the dangers of the pile failure. This phenomenon shows the complexity of the mechanism of the soil-foundation interaction when foundation structures are constructed and embedded into thick soft clay deposits and indicates how important it is to adopt an analysis method that is capable of reproducing the characteristic behavior of clay, including rate dependency and dilatancy, the degradation of the soil strength from microstructural changes, and the mechanical instability of the soil in order to effectively simulate and study these problems.

The present study deals with the soil-foundation interaction of the foundation structures embedded into soft clay strata which are subjected to large long-term deformations and failure. A series of numerical analyses is firstly conducted to investigate the effects of several parameters on the lateral earth pressure between a vertical retaining wall and a clay ground. The constitutive model for normally consolidated clay used in these studies is based on the elasto-viscoplasticity theory proposed by Adachi, Oka, and Mimura (1987). The analysis is performed using the finite element formulation of a two-phase mixture based on the finite deformation theory in order to consider the transport of water in the ground and to cope with the large deformations and the strain localization. It is shown that this analysis method can simulate strain localization in lateral earth pressure problems and the effects of several parameters on the developed earth pressure, and can clarify the ground deformation.

Then, a case study of an excavation performed through a thick soft clay ground and a case study of a large embankment constructed near a the river shore are studied. The numerical simulations are carried out by using an elasto-viscoplastic constitutive model considering microstructural changes proposed by Kimoto (2002), Kimoto and Oka (2003), and Kimoto et al. (2004) to include the effects of the degradation of the soil strength from the microstructural changes in the analysis. The mechanism of the ground deformation and the effects of the degradation of the soil are discussed using the results of the numerical analyses. By comparing the numerical results and the measured data in the case studies, the ability of the analysis method is evaluated and possible countermeasures to the problems are studied.

The bearing capacity has always been one of the most highly interesting fundamental problems in Geotechnical Engineering. Analytical methods as well as the numerical method with several soil constitutive models have been used to address this problem. Up to now, however, the effects of the degradation of clay have not been included in the study of the bearing capacity problem. The degradation of the soil strength, due to the microstructural changes, can lead to the strain localization, which is generally considered to be a precursor of failure, and thus, the effects of microstructural changes should be included. The present study is concerned with the effects of structural changes and strain localization on the bearing capacity of a shallow foundation on a saturated clay stratum. For this purpose, an elasto-viscoplastic soil constitutive model considering the microstructure changes, which is mentioned previously, has been used. Through the results of the analyses, the effects of degradation, strain softening, and the footing frictional conditions on the bearing behavior of the surface strip footing are discussed.

When large deformation occurs in the analysis, the mesh-update process and the strain localization can lead to the ill-shape of the finite element meshes. The accuracy of the finite element mesh is affected and the adaptive finite element refinement is a popular choice for overcoming this problem. In this study, an adaptive finite element refinement is implemented for the finite element analysis using an elasto-viscoplastic model. The performance of the applied method is then discussed from the viewpoint of both the improvement of the numerical results and the computation time.

1.2 Scope and Organization

The present dissertation consists of seven chapters. An outline of each chapter is presented below.

In **Chapter 2**, the constitutive models for clay and sand adopted in this study are introduced with the finite element formulation for saturated soil used in the analysis. Firstly, an elasto-viscoplastic constitutive model for normally consolidated clay with the second material function Φ_2 proposed by Adachi, Oka, and Mimura (1987) is reviewed. Next, the constitutive model for clay considering structural changes, originally proposed by Kimoto (2002) Kimoto and Oka (2003), and Kimoto et al. (2004) is presented. A

structural collapse is introduced into the model in order to describe the strength degradation of structural clay. An elasto-plastic constitutive model for sand, based on the nonlinear kinematic hardening rule (Oka et al. (1999)), is reviewed. Finally, a finite element formulation for the analysis of water-saturated soil as a two-phase mixture, based on the finite deformation theory, is described. This formulation is used in the numerical analysis performed in this study.

The **Chapter 3** is divided into two parts. In the first part, the effects of various parameters on the lateral earth pressure are evaluated through numerical simulations under plane strain conditions. Computations are carried out separately for active and passive earth pressure problems of a vertical backface retaining wall which supports horizontal backfill. In the second part, the problem of the soil-structure interaction of a braced excavation in a thick soft clay deposit is examined. The typical behavior of an excavation when sheet piles are not embedded into a firm stratum is studied. The effects of the length of the sheet pile, the layouts of the struts and the preloads on the performance of the excavation are clarified. The countermeasure of the problem is proposed. The study is performed through numerical simulations under idealized symmetric plane strain excavation geometry.

In **Chapter 4**, the case study of an embankment constructed near a river is presented. Laboratory tests are carried out to obtain the material parameters of clay sampled at the construction site. Then, a numerical simulation is performed to study the problems of large long-term deformations of the ground and the displacement of the supporting structures caused by the construction of this embankment near bulkhead piles that were not embedded into a firm stratum. The mechanism of the ground deformation and the displacement of the supporting structures as well as the effects of the degradation of the soil are discussed using the analysis results and a validation of the efficiency of the applied analysis method. Finally, countermeasures to cope with the problems are proposed.

In **Chapter 5**, a finite element analysis of the bearing capacity of a shallow foundation on homogeneous and inhomogeneous saturated clay stratums was conducted by considering a strip footing and square footing. A series of analyses of the footings on clay deposit with different microstructural parameters was conducted. The effects of the microstructural changes, strength degradation, and the strain localization on the bearing behavior of the footings are studied.

In **Chapter 6**, a mesh refinement method based on an error estimator, using the SPR technique proposed by Zienkiewicz and Zhu (1992), is introduced into the finite element method using an elasto-viscoplastic constitutive model. Then, the efficiency of the mesh refinement is discussed by considering the performance of the analysis results and the computation time and costs.

In **Chapter 7**, the conclusions of this dissertation and the recommendations for future work are given.

Chapter 2

Constitutive Models for Clay and Sand and Finite Element Formulation for Water-Saturated Soil

2.1 Introduction

This study deals with the behavior of foundations on and under ground composing of clay and sand material. Behaviors of this kind of structure are closely related to the mechanical behavior of the soils that compose the ground. In order to study the behaviors of the foundations and the ground, the constitutive model for soil should be able to describe all characteristic behaviors of soil.

In this chapter, firstly, an elasto-viscoplastic constitutive model for normally consolidated clay with a second material function Φ_2 proposed by Adachi, Oka, and Mimura (1987) is reviewed. This model was found to be able to describe the acceleration creep failure behavior. This model will be used in the analysis of the earth pressure problem conducted in chapter 3.

In the model mentioned previously (Adachi et al. 1987), the large viscoplastic strain is generated with the increases of the stress ratio near the critical state line, therefore, the softening of soil can be reproduced by the shearing process. On the other hand, after we began the present work, a new constitutive soil model was developed by Kimoto (2002), Kimoto and Oka (2003), and Kimoto et al. (2004). This model is an elasto-viscoplastic constitutive model for both normally consolidated clay and overconsolidated

clay considering structural changes. The basic theory of viscoplasticity (Perzyna 1963) is the same as that of the elasto-viscoplastic model with the second material function Φ_2, but the degradation of soil strength, namely volumetric and shear strain softening due to the changes of microstructure can be reproduced in the model. Consequently, in this newly developed model, the microstructure changes and the strength degrades with respect to the accumulated viscoplastic strain ε_{ij}^{vp}. Therefore, the softening of soil can be simulated in both the shearing and the isotropic consolidation of soil. The model is explained in the next section, and will be used in the analyses conducted in chapter 3,4, 5 and 6.

Then, an elasto-plastic constitutive model for sand based on the nonlinear kinematic hardening rule (Oka et al. 1999) is presented. Later, we will refer to this model as elasto-plastic constitutive model for sand.

Finally, the finite element formulation for the analysis of water saturated soil which will be used in the analysis later in the present study is reviewed. The formulation is for two-phases mixtures based on the finite deformation theory.

2.2 Elasto-viscoplastic Constitutive Model for Normally Consolidated Clay with the Second Material Function

The elasto-viscoplastic constitutive model for normally consolidated clay will be presented in this section. Adachi and Oka (1982) had developed an overstress type elasto-viscoplastic constitutive model based on Cam-Clay Model (Roscoe et al. 1963) and a viscoplastic theory (Perzyna 1963). This model can express the rate dependent behavior of clay. It is assumed that clays never reach their static equilibrium state at the end of primary consolidation even for the case of isotropic consolidation. This means that natural ground is continuing to subside by its own weight with a very small strain rate. Thus, the static equilibrium state is defined as a state at which deviatoric strain rate and volumetric strain rate become zero. According to this definition, any deformation processes with definite strain rate are regared as dynamic state.

Perzyna (1963) indicated that the difference between behaviors of clay in static and dynamic state comes from the material strain rate sentivity and defined this behavior as viscoplastic. Then, he proposed the viscoplastic strain rate tensor $\dot{\varepsilon}_{ij}^{vp}$ which can describe

the rate dependent behavior based on the flow rule as follows:

$$\dot{\varepsilon}_{ij}^{vp} = \gamma \langle \Phi_1 (F) \rangle \frac{\partial f}{\partial \sigma'_{ij}} \tag{2.1}$$

$$F = \frac{f(\sigma_{ij}, \varepsilon_{ij}^{vp}) - \kappa_s}{\kappa_s} \tag{2.2}$$

$$\sigma'_{ij} = \sigma_{ij} - u_w \delta_{ij} \tag{2.3}$$

where, γ is a viscoplastic parameter, f is the dynamic yield function, κ_s is the work-hardening parameter, σ_{ij} is the total stress tensor, σ'_{ij} is Terzaghi's effective stress tensor, u_w is the pore water pressure, and δ_{ij} is Kronecker's delta.

$\langle \Phi_1 (F) \rangle$ is a function showing strain rate sensitivity, and should be determined by experiment results, and $\langle \rangle$ is MaCaulay's bracket as defined by the following relations.

$$\langle \Phi_1 (F) \rangle = \begin{cases} 0 & (F \leq 0) \\ \Phi_1 (F) & (F > 0) \end{cases} \tag{2.4}$$

In Equation (2.4), $F = 0$ represents the static yield function. From Equation (2.1) and (2.2), the following relations can be obtained.

$$f(\sigma_{ij}, \varepsilon_{ij}^{vp}) - \kappa_s = \kappa_s \Phi_1^{-1} (I_2^{vp} \left\{ \frac{\partial f}{\partial \sigma'_{kl}} \frac{\partial f}{\partial \sigma'_{kl}} \right\}^{-\frac{1}{2}}) \tag{2.5}$$

where $\Phi_1^{-1}(*)$ is an inverted function of $\Phi_1(*)$, $I_2^{vp} = \left(\dot{\varepsilon}_{ij}^{vp} \dot{\varepsilon}_{ij}^{vp} \right)^{\frac{1}{2}}$ is the second invariant of viscoplastic strain rate tensor.

Then, we define the dynamic yield function f as f_d. The material loses its rate sensitivity only when $F = 0$ (or $f = k_s$). At this state, f will be denoted by f_s. Furthermore, based on the critical state theory proposed by Roscoe et al. (1963), the static yield function f_s and the dynamic yield function f_d are assumed to be as follows:

$$f_s = \bar{\eta}^{*(s)} + M_f^* \ln \frac{\sigma_m^{\prime(s)}}{\sigma'_{m0}} = \kappa_s \tag{2.6}$$

$$f_d = \bar{\eta}^* + M_f^* \ln \frac{\sigma'_m}{\sigma'_{m0}} = \kappa_d \tag{2.7}$$

where the superscript (s) and (d) indicate the static state and the dynamic state, respectively, σ'_m is the mean effective stress, and σ'_{m0} is the unit mean effective stress. In Equations (2.7), (2.6), $\bar{\eta}^*$ is a relative stress ratio(Sekiguchi & Ohta 1977), which represents the stress ratio of anisotropic consolidated clay, namely,

$$\bar{\eta}^* = \left\{ \left(\eta_{ij}^* - \eta_{ij(0)}^* \right) \left(\eta_{ij}^* - \eta_{ij(0)}^* \right) \right\}^{\frac{1}{2}} \quad , \quad \eta_{ij}^* = \frac{S_{ij}}{\sigma'_m} \quad , \quad \eta_{ij(0)}^* = \frac{S_{ij(0)}}{\sigma'_{m(0)}} \tag{2.8}$$

in which, η_{ij}^* is the stress ratio tensor, M_f^* is the value of $\eta^* = \sqrt{\eta_{ij}^* \eta_{ij}^*}$ at failure. Subscript (0) denotes values of the parameters at the end of primary consolidation.

κ_s and κ_d are the strain hardening parameters and are defined as follows:

$$\kappa_s \equiv \ln \frac{\sigma_{my}^{\prime(s)}}{\sigma_{m0}^{\prime}} \tag{2.9}$$

$$\kappa_d \equiv \ln \frac{\sigma_{my}^{\prime(d)}}{\sigma_{m0}^{\prime}} \tag{2.10}$$

$\sigma_{my}^{\prime(s)}$、$\sigma_{my}^{\prime(d)}$ are the hardening parameters and hardening parameter $\sigma_{my}^{\prime(s)}$ is related to the incremental of inelastic volumetric strain dv^p through the following equation.

$$dv^p = \frac{\lambda - \kappa}{1+e} \cdot \frac{d\sigma_{my}^{\prime(s)}}{\sigma_{my}^{\prime(s)}} \tag{2.11}$$

where, λ is the compression index, κ is the extension index, and e is the void ratio.

As shown below, based on the experiment data (Adachi and Okano(1974), Oka(1979), the form of the material function Φ_1 has been determined as follows:

$$\gamma\Phi_1(F) = C_o M_f^* \sigma_m^{\prime} \exp\left\{ m^{\prime} \left(\ln \frac{\sigma_{my}^{\prime(d)}}{\sigma_{m0}^{\prime}} - \ln \frac{\sigma_{my}^{\prime(s)}}{\sigma_{m0}^{\prime}} \right) \right\} \tag{2.12}$$

where C_o and $m^{\prime}$ can be determined from laboratory results.

Substituting the dynamic yield function Equation (2.7) and the static yield function equation which is obtained by integrating Equation (2.11) into Equation (2.12) will yield,

$$\gamma\Phi_1(F) = C_o M_f^* \sigma_m^{\prime} \exp\left\{ m^{\prime} \left(\frac{\bar{\eta}^*}{M_f^*} + \ln \frac{\sigma_m^{\prime}}{\sigma_{myi}^{\prime(s)}} - \frac{1+e}{\lambda - \kappa} v^p \right) \right\} \tag{2.13}$$

When v^p is the incrementing of the plastic volumetric strain and $\sigma_{myi}^{\prime(s)}$ indicates the initial value of $\sigma_{my}^{\prime(s)}$. Then, Equation (2.13) is transformed as follows;

$$\begin{aligned}
\gamma\Phi_1(F) &= C_o M_f^* \sigma_m^{\prime} \exp\left\{ m^{\prime} \left(\frac{\bar{\eta}^*}{M_f^*} + \ln \frac{\sigma_m^{\prime}}{\sigma_{me}^{\prime}} - \ln \frac{\sigma_{myi}^{\prime(s)}}{\sigma_{me}^{\prime}} - \frac{1+e}{\lambda - \kappa} v^p \right) \right\} \\
&= C_o M_f^* \sigma_m^{\prime} \exp\left\{ -m^{\prime} \ln \frac{\sigma_{myi}^{\prime(s)}}{\sigma_{me}^{\prime}} \right\} \exp\left\{ m^{\prime} \left(\frac{\bar{\eta}^*}{M_f^*} + \ln \frac{\sigma_m^{\prime}}{\sigma_{me}^{\prime}} - \frac{1+e}{\lambda - \kappa} v^p \right) \right\} \\
&= C M_f^* \sigma_m^{\prime} \exp\left\{ m^{\prime} \left(\frac{\bar{\eta}^*}{M_f^*} + \ln \frac{\sigma_m^{\prime}}{\sigma_{me}^{\prime}} - \frac{1+e}{\lambda - \kappa} v^p \right) \right\}
\end{aligned} \tag{2.14}$$

$$C = C_o \exp\left\{ -m^{\prime} \ln \frac{\sigma_{myi}^{\prime(s)}}{\sigma_{me}^{\prime}} \right\} \tag{2.15}$$

where σ'_{me} is initial consolidation stress.

By defining a parameter C as shown in Equation (2.15), this parameter C can be determined from the laboratory tests, and it is not necessary to acquire the initial value of hardening parameter $\sigma'^{(s)}_{myi}$. The flow rule of the viscoplastic strain rate tensor with second material function, Φ_2, can be given by;

$$\dot{\varepsilon}^{vp}_{ij} = \gamma \langle \Phi_1 (F) \rangle \Phi_2(\xi) \frac{\partial f}{\partial \sigma'_{ij}} \tag{2.16}$$

ξ is an internal state variable which controls the failure of material structure, and the second material function was introduced as to describe the the failure state. It is known that the failure condition of soil does not depend on the strain rate. The second material function was defined in consideration of such a point. The second material function is assumed to satisfy the following two conditions as:

1. When ξ become infinity, Φ_2 will also become infinity
2. ξ is positive

Similar to Equation (2.5), the dynamic yield function is defined as follows.

$$f(\sigma_{ij}, \varepsilon^{vp}_{ij}) - \kappa_s = \kappa_s \Phi_1^{-1} \left(\frac{I_2^{vp}}{\gamma \Phi_2(\xi)} \left\{ \frac{\partial f}{\partial \sigma'_{kl}} \frac{\partial f}{\partial \sigma'_{kl}} \right\}^{-\frac{1}{2}} \right) \tag{2.17}$$

If Φ_2 become infinity, Equation (2.17) will become,

$$f(\sigma_{ij}, \varepsilon^{vp}_{ij}) = \kappa_s \tag{2.18}$$

Namely, the term of I_2^{vp} will disappear, and the rate dependency of the yield function will vanish.

To express the accelerate creep behavior, the internal variable and the second material function are assumed to follow an evolutional equation. For the isotropically consolidated clay, Φ_2 is given by

$$\dot{\xi} = \frac{M_f^{*2}}{G_2^*(M_f^* - \eta^*)} \dot{\eta}^* \quad , \quad \eta^* = \frac{\sqrt{2J_2}}{\sigma'_m} \tag{2.19}$$

in which, $t = 0$, $\xi(0) = 0$, $\eta^*(0) = 0$, at the initial state, G_2^* is a softening parameter.

$$\Phi_2(\xi) = 1 + \xi \tag{2.20}$$

The second material function will prominently increase as the critical state is approached. Therefore, before the states near failure, the material behavior is mainly controlled by $\Phi_1(F)$ which was already described.

Under the anisotropic consolidation conditions, by employing $\bar{\eta}^*$, where $\bar{\eta}^*$ is the relative stress ratio given by Equation (2.19), the integrated form of evolutional equation of the internal state variable ξ is extended as:

$$\xi = \frac{M_f^* \bar{\eta}^*}{G_2^* \left\{ M_f^* - \frac{\eta_{mn}^* (\eta_{mn}^* - \eta_{mn(0)}^*)}{\bar{\eta}^*} \right\}} \tag{2.21}$$

Next, Terzaghi's effective stress concept is used for water-saturated soil as

$$\sigma_{ij} = \sigma'_{ij} + u_w \delta_{ij} \tag{2.22}$$

where σ_{ij} is the total stress tensor, σ'_{ij} is the effective stress tensor, u_w is the pore water pressure, and δ_{ij} is Kronecker's delta.

Furthermore, it is assumed that the total strain rate tensor consists of the elastic strain rate tensor and the viscoplastic strain rate tensor, so that

$$\dot{\varepsilon}_{ij} = \dot{\varepsilon}_{ij}^e + \dot{\varepsilon}_{ij}^{vp} \tag{2.23}$$

The elastic strain rate tensor $\dot{\varepsilon}_{ij}^e$ is given by a non-linear Hooke type of law, i.e.

$$\dot{\varepsilon}_{ij}^e = \frac{1}{2G} \dot{S}_{ij} + \frac{\kappa}{3(1+e)\sigma'_m} \dot{\sigma}'_m \delta_{ij} \tag{2.24}$$

where $\dot{S}_{ij}$ is the deviatoric stress rate tensor, G is the elastic shear modulus. The elastic shear modulus G is assumed to be proportional to $\sqrt{\sigma'_m}$ as:

$$G = G_0 \sqrt{\frac{\sigma'_m}{\sigma'_{m0}}} \tag{2.25}$$

where G_0 is the initial value of G at σ'_{m0}.

Since $\frac{\partial f}{\partial \sigma'_{ij}}$ is calculated as

$$\frac{\partial f}{\partial \sigma'_{ij}} = \frac{1}{M_f^* \sigma'_m} \left[\frac{\eta_{ij}^* - \eta_{ij(0)}^*}{\bar{\eta}^*} + \left\{ M_f^* - \frac{\eta_{kl}^* \left(\eta_{kl}^* - \eta_{kl(0)}^* \right)}{\bar{\eta}^*} \right\} \frac{1}{3} \delta_{ij} \right], \tag{2.26}$$

The derived constitutive model can express both the strain rate dependency and the accelerate creep types behavior. The total strain rate tensor can be expressed as follows;

$$\begin{aligned} \dot{\varepsilon}_{ij} &= \frac{1}{2G} \dot{S}_{ij} + \frac{\kappa}{3(1+e)} \dot{\sigma}'_m \delta_{ij} \\ &+ \gamma \langle \Phi_1(F) \rangle \Phi_2(\xi) \frac{1}{M_f^* \sigma'_m} \left[\frac{\eta_{ij}^* - \eta_{ij(0)}^*}{\bar{\eta}^*} + \left\{ M_f^* - \frac{\eta_{kl}^* \left(\eta_{kl}^* - \eta_{kl(0)}^* \right)}{\bar{\eta}^*} \right\} \frac{1}{3} \delta_{ij} \right] \end{aligned} \tag{2.27}$$

2.3 Elasto-viscoplastic Constitutive Model for Clay Considering Structural Changes

In the constitutive equation for clay, an elasto-viscoplastic constitutive model considering structural changes, proposed by Kimoto (2002), Kimoto and Oka (2003), and Kimoto et al. (2004) was used. This model is extended from the elasto-viscoplastic model for water-saturated clay proposed by Adachi & Oka (1982) in order to consider the degradation of soil structures. Similar to the model reviewed previously, this model is based on the Cam clay model and a Perzyna type of viscoplastic theory. On the other hand, a characterization of the material instability and strain softening is proposed considering microstructural changes in the geomaterials. The structural changes are described as the shrinking of both the overconsolidation boundary surface and the static yield surface with the evolution of the viscoplastic strain.

2.3.1 Overconsolidation Boundary Surface

In the model presented here, it is assumed that an overconsolidation (OC) boundary surface exists which delineates the OC region ($f_b < 0$) from the normal consolidated (NC) region ($f_b \geq 0$). A similar OC boundary surface was used in an elasto-plastic model for sands, which will be shown later in this chapter. The OC boundary surface was introduced to control the shape of the plastic potential function and the yield function.

$$f_b = \bar{\eta}^*_{(0)} + M^*_m \ln\left(\sigma'_m/\sigma'_{mb}\right) = 0 \tag{2.28}$$

where M^*_m is the value of $\sqrt{\eta^*_{ij}\eta^*_{ij}}$ at the maximum compression, σ'_m is the mean effective stress, and $\bar{\eta}^*_{(0)}$ is a relative stress ratio which represents the stress ratio of anisotropic consolidated clay, given by Equation (2.29), namely,

$$\bar{\eta}^*_{(0)} = \left\{\left(\eta^*_{ij} - \eta^*_{ij(0)}\right)\left(\eta^*_{ij} - \eta^*_{ij(0)}\right)\right\}^{1/2} \tag{2.29}$$

where (0) denotes the state at the end of consolidation, in other words, the initial state before deformation occurs.

σ'_{mb} controls the size of the surface, which is defined as the isotropic consolidation yield stress. The hardening rule for the OC boundary surface was defined in respect to the viscoplastic volumetric strain as

$$\sigma'_{mb} = \sigma'_{mbi} \exp\left(\frac{1+e_0}{\lambda-\kappa}\varepsilon^{vp}_v\right) \tag{2.30}$$

where λ is the compression index, e_0 is the initial void ratio, ε^{vp}_v is the viscoplastic volumetric strain, and σ'_{mbi} is the initial value of σ'_{mb}.

Herein, strain softening is introduced into the model as an additional hardening parameter with the viscoplastic strain in order to describe the degradation of the material caused by the structural changes. This degradation parameter is given by the following equation.

$$\sigma'_{ma} = \sigma'_{maf} + (\sigma'_{mai} - \sigma'_{maf}) \exp(-\beta z^{\alpha}) \tag{2.31}$$

in which σ'_{mai} and σ'_{maf} are the initial and the final values of σ'_{ma}, and z is an accumulation of the second invariant of the viscoplastic strain rate. z can be determined as

$$z = \int_0^t \dot{z} dt \tag{2.32}$$

$$\dot{z} = \left(\dot{\varepsilon}^{vp}_{ij} \dot{\varepsilon}^{vp}_{ij}\right)^{\frac{1}{2}} \tag{2.33}$$

Upon substitution of σ'_{ma} into Equation (2.30), σ'_{mb} is given by the hardening rule with respect to the viscoplastic volumetric strain and by the softening parameter with respect to the structural changes as

$$\sigma'_{mb} = \sigma'_{ma} \exp\left(\frac{1+e_0}{\lambda - \kappa} \varepsilon^{vp}_v\right) \tag{2.34}$$

α and β are the parameters which denote the degradation rate of σ'_{ma}. Since z is equal to 0 at the initial state, we can obtain the relation of $\sigma'_{ma} = \sigma'_{mai} = \sigma'_{mbi}$. Hence, three independent parameters, namely, α, β and σ'_{maf} are introduced to describe the soil structures. The ratio of σ'_{maf} to σ'_{mai}, namely,

$$n = \sigma'_{maf} / \sigma'_{mai} \tag{2.35}$$

represents the degree for a possible collapse of the initial structure. The soil loses its structure perfectly when n reaches 1. It can be seen from Equation (2.31) and (2.34) that when the viscoplastic strain are zero, $z = 0$, σ'_{ma} is equal to σ'_{mai}. When the value of z becomes larger, however, σ'_{ma} will decrease and softening occurs due to the degradation of the structure.

2.3.2 Static Yield Function

To describe the mechanical behavior of clay at its static equilibrium state, Adachi and Oka (1982) adopted a Cam-clay type of static yield function as

$$f_y = \bar{\eta}^*_{(0)} + \tilde{M}^* \ln \frac{\sigma'_m}{\sigma'^{(s)}_{my}} = 0 \tag{2.36}$$

where $\acute{\sigma}^{(s)}_{my}$ is the static-hardening parameter and $f_y = 0$ represents the static state which may be reached after an infinite period of time. At this state, no viscoplastic deformation occurs.

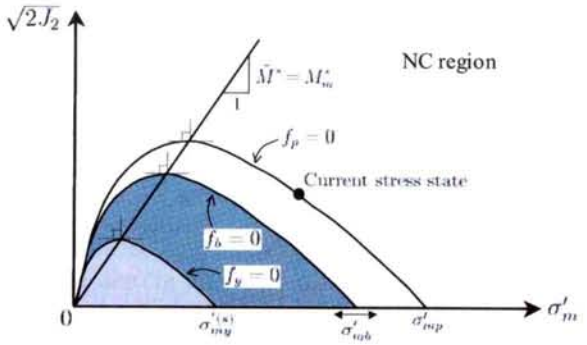

Figure 2.1 OC boundary surface, static yield function, and potential function in the NC region (Kimoto et al. 2004)

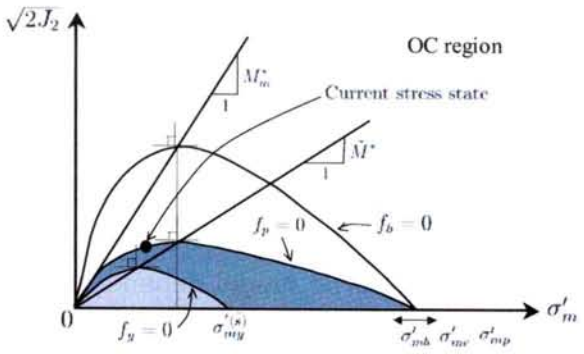

Figure 2.2 OC boundary surface, static yield function, and potential function in the OC region (Kimoto et al. 2004)

Considering volumetric strain hardening, the hardening rule $\acute{\sigma}^{(s)}_{my}$ is given as follows

$$\sigma'^{(s)}_{my} = \sigma'^{(s)}_{myi} \exp\left(\frac{1+e_0}{\lambda-\kappa}\varepsilon^{vp}_v\right) \tag{2.37}$$

in which $\acute{\sigma}^{(s)}_{myi}$ is the initial value of $\acute{\sigma}^{(s)}_{my}$. In a similar way for overconsolidation boundary surface f_b, strain softening by structural degradation is incorporated in order to express the effect of a structural collapse through changes in $\acute{\sigma}^{(s)}_{my}$ with the viscoplastic strain.

$$\sigma'^{(s)}_{my} = \{n + (1-n)\exp(-\beta z)\}\, \sigma'^{(s)}_{myi} \exp\left(\frac{1+e_0}{\lambda-\kappa}\varepsilon^{vp}_v\right) \tag{2.38}$$

The static yield function shrinks according to the structural collapse with the decrease in $\sigma'^{(s)}_{my}$ defined by Equation (2.38).

2.3.3 Viscoplastic Potential Function

Viscoplastic potential function f_p is given as follows:

$$f_p = \bar{\eta}^*_{(0)} + \tilde{M}^* \ln\frac{\sigma'_m}{\sigma'_{mp}} = 0 \tag{2.39}$$

where $\tilde{M}^*$ is assumed to be constant in the NC region, while the value of $\tilde{M}^*$ varies with the current stress and σ'_{mc} in the OC region as

$$\tilde{M}^* = \begin{cases} M^*_m & : \ f_b \geq 0 \\ -\dfrac{\sqrt{\eta^*_{ij}\eta^*_{ij}}}{\ln(\sigma'_m/\sigma'_{mc})} & : \ f_b < 0 \end{cases} \tag{2.40}$$

where σ'_{mc} denotes the mean effective stress at the intersection of the OC boundary surface and the σ'_m axis as

$$\sigma'_{mc} = \sigma'_{mb} \exp\frac{\sqrt{\eta^*_{ij(0)}\eta^*_{ij(0)}}}{M^*_m} \tag{2.41}$$

σ'_{mc} equals σ'_{mb} in the case of isotropic consolidation.

Overconsolidation boundary surface f_b, static yield function f_y, and viscoplastic potential function f_p at $\eta^*_{ij(0)} = 0$ for the NC and OC regions are demonstrated in the $\sigma'_m - \sqrt{S_{ij}S_{ij}}$ space in Figures 2.1 and the 2.2, respectively. σ'_{mb} and $\acute{\sigma}^{(s)}_{my}$ decrease as the accumulation of viscoplastic strain increases. The increments in viscoplastic strain for the overstress type model depend on the difference between the current stress state and the static stress state, therefore, the shrinkage of the static yield surface due to the soil structure degradation yields increases in the viscoplastic strain increments. The static yield function and the potential surface are transformed smoothly between the OC and the NC regions. Consequently, the calculations can be conducted continuously without discontinuity.

2.3.4 Viscoplastic Flow Rule

Based on an the overstress type of viscoplasticity theory (Perzyna 1963), viscoplastic strain rate tensor $\dot{\varepsilon}^{vp}_{ij}$ is given as

$$\dot{\varepsilon}^{vp}_{ij} = \gamma \langle \Phi_1 (f_y) \rangle \frac{\partial f_p}{\partial \sigma'_{ij}} \tag{2.42}$$

$$< \Phi_1(f_y) >= \begin{cases} \Phi_1(f_y) & ; \quad f_y > 0 \\ 0 & ; \quad f_y \leq 0 \end{cases} \tag{2.43}$$

in which Φ_1 is a function showing strain rate sensitivity and is determined by the experiment results. Material function Φ_1 is given as follows:

$$\begin{aligned} \gamma\Phi_1(f_y) &= C'\sigma'_m \exp\left\{ m' \left(\bar{\eta}^*_{(0)} + \tilde{M}^* \ln \frac{\sigma'_m}{\sigma'^{(s)}_{my}} \right) \right\} \\ &= C_0\sigma'_m \exp\left\{ m' \left(\bar{\eta}^*_{(0)} + \tilde{M}^* \ln \frac{\sigma'_m}{\sigma'_{mb}} \right) \right\} \end{aligned} \tag{2.44}$$

$$C_0 = C' \exp\left(m'\tilde{M}^* \ln \frac{\sigma'_{mai}}{\sigma'^{(s)}_{myi}} \right) \tag{2.45}$$

Herein, Equations (2.34), (2.35) and (2.38) are used. m' and C are viscoplastic parameters. Finally, by substituting Equation(2.44) into Equation(2.42), the viscoplastic deviatoric strain rate and the viscoplastic volumetric strain rate are obtained as follows:

$$\dot{e}^{vp}_{ij} = C_0\sigma'_m \exp\left\{ m' \left(\bar{\eta}^*_{(0)} + \tilde{M}^* \ln \frac{\sigma'_m}{\sigma'_{mb}} \right) \right\} \frac{\eta^*_{ij} - \eta^*_{ij(0)}}{\bar{\eta}^*_{(0)}} \tag{2.46}$$

$$\dot{\varepsilon}^{vp}_{v} = C_0\sigma'_m \exp\left\{ m' \left(\bar{\eta}^*_{(0)} + \tilde{M}^* \ln \frac{\sigma'_m}{\sigma'_{mb}} \right) \right\} \left(\tilde{M}^* - \frac{\eta^*_{ij}(\eta^*_{ij} - \eta^*_{ij(0)})}{\bar{\eta}^*_{(0)}} \right) \tag{2.47}$$

2.3.5 Determination of the Material Parameters

The constitutive model introduced in the previous section required eleven material parameters. They are the compression index λ, the swelling index κ, initial void ratio e_0, the elastic shear modulus G_0, compression yield stress σ'_{mbi}, the stress ratio at maximum compression M^*_m, viscoplastic parameter m, C_0, and structural parameters σ'_{maf}, β, and α. All of these parameters can be determined by the isotropic consolidation tests and more than two undrained triaxial compression tests with different strain rates.

Initial void ratio e_0 can be obtained from tests for physical properties. Compression index λ and swelling index κ are given by the slope of the isotropic consolidation and the swelling tests, respectively. Compression yield stress σ'_{mbi} is assumed to be the pre-consolidation stress and can be determined from the yield point of the isotropic consolidation tests.

Elastic shear modulus G_0 is determined by the initial slope of the undrained triaxial compression tests, namely, $G_0 = \Delta q/(3\Delta\varepsilon_{11})$, in which Δq is the increment in deviator stress and $\Delta\varepsilon_{11}$ is the increment in axial strain. The stress ratio at maximum compression M^*_m is defined as the stress ratio whereby the maximum compression occurs in the drained compression tests. For clay, however, it has been assumed to equal the stress ratio at the critical state. Herein, M^*_m is determined from the stress ratio at the residual state in the undrained triaxial compression tests.

Viscoplastic parameters m' and C_0 can be determined from undrained triaxial tests with different strain rates. From Equation(2.46), viscoplastic deviatoric strain rate $\dot{e}^{(1)}_{11}$ in the triaxial stress state can be obtained as

$$\dot{e}^{vp}_{11} = \sqrt{\frac{2}{3}} C_0 \exp\left\{ m' \left(\sqrt{\frac{2}{3}} \frac{q}{\sigma'_m} + \tilde{M}^* \ln \frac{\sigma'_m}{\sigma'_{mb}} \right) \right\} \tag{2.48}$$

Considering the undrained conditions, and by assuming that the elastic strain rate is negligible, we obtain $\dot{e}^{vp}_{11} = \dot{\varepsilon}_{11}$. From the undrained triaxial tests with different strain rates, the following equations are obtained at the point where the mean effective stress takes the same value in the stress path.

$$\frac{\dot{\varepsilon}^{(1)}_{11}}{\dot{\varepsilon}^{(2)}_{11}} = \exp\left\{ m' \sqrt{\frac{2}{3}} \left(\left(\frac{q}{\sigma'_m} \right)^{(1)} - \left(\frac{q}{\sigma'_m} \right)^{(2)} \right) \right\} \tag{2.49}$$

$$m' = \sqrt{\frac{3}{2}} \frac{\ln \dot{\varepsilon}^{(1)}_{11} - \ln \dot{\varepsilon}^{(2)}_{11}}{(\frac{q}{\sigma'_m})^{(1)} - (\frac{q}{\sigma'_m})^{(2)}} \tag{2.50}$$

where (1) and (2) denote the stress state from the tests with different strain rates and the same mean effective stresses rates. After determining m', we can now calculate C_0 from Equation (2.48)

Structual parameter σ'_{maf} can be obtained by the deviator stress at the residual stress state. Structural parameters β and α, which control the decreasing rate of deviator stress at large strain, are determined by the curve fitting.

2.4 Elasto-plastic Constitutive Model for sand based on the Nonlinear Kinematic Hardening Rule

In the constitutive equation for sand, an elasto-plastic constitutive model based on the nonlinear kinematic hardening rule, proposed by Oka et al. (1999) is adopted. The constitutive model is reviewed in this section.

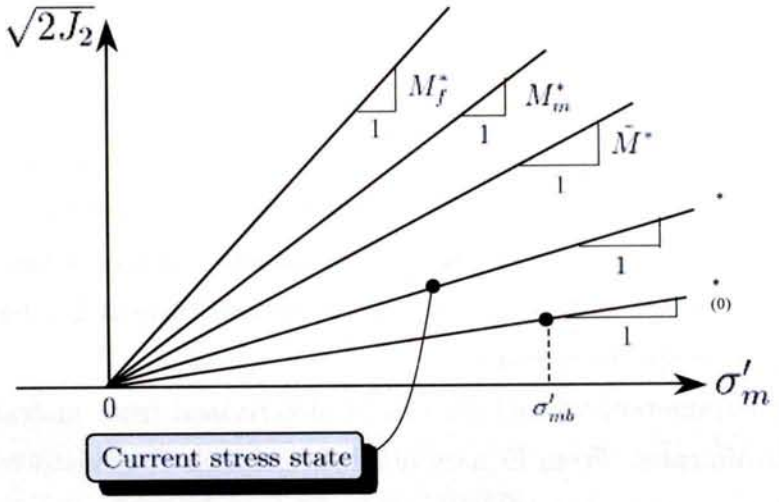

Figure 2.3 Various parameters for the stress ratio

2.4.1 Overconsolidation Boundary Surface

Overconsolidation boundary surface f_b, used for the model presented in this section, is similar to that used in the previous section, that is

$$f_b = \bar{\eta}^*_{(0)} + M^*_m \ln\left(\sigma'_m/\sigma'_{mb}\right) = 0 \tag{2.51}$$

$$\sigma'_{mb} = \sigma'_{mbi} \exp\left(\frac{1+e_0}{\lambda-\kappa}\varepsilon^{vp}_v\right) \tag{2.52}$$

where η^*_{ij} is the stress ratio, σ'_m is the mean effective stress, M^*_m is the value of the stress ratio expressed by $(\eta^*_{ij}\eta^*_{ij})^{\frac{1}{2}}$ at the phase transformation ratio, σ'_{mb} is the parameter that controls the size of the surface, λ is the compression index, κ is the swelling index, e is the void ratio, and ε^{vp}_v is the plastic volumetric strain. Futhermore, σ'_{mc}, is the mean effective

stress at the intersection of the overconsolidation boundary surface and the σ'_m axis and it is defined as

$$\sigma'_{mc} = \sigma'_{mb} \exp\left(\frac{\eta^*_{(0)}}{M^*_m}\right) \tag{2.53}$$

in which $\eta^*_{(0)} = \sqrt{\eta^*_{ij(0)}\eta^*_{ij(0)}}$. $\eta^*_{ij(0)}$ and σ'_{mb} are the values of η^*_{ij} and σ'_m at the end of anisotropic consolidation respectively.

Figure 2.3 shows various parameters for the stress ratio and for the values of M^*_f and M^*_m obtained through the drained triaxial tests, in which M^*_f is related to the angle of failure state ϕ_f and M^*_m is related to the angle of phase transformation ϕ_m

$$M^*_f = \sqrt{\frac{2}{3}}\,\frac{6\sin\phi_f}{3-\sin\phi_f}, \qquad M^*_m = \sqrt{\frac{2}{3}}\,\frac{6\sin\phi_m}{3-\sin\phi_m} \tag{2.54}$$

and $\tilde{M}^*$, which will be used later in the plastic potential function, can be determined by the current stress and σ'_{mc}

2.4.2 Yield Function

The yield function for changes in the stress ratio is denoted as

$$f = \left\{\left(\eta^*_{ij} - \chi^*_{ij}\right)\left(\eta^*_{ij} - \chi^*_{ij}\right)\right\}^{\frac{1}{2}} - k = 0 \tag{2.55}$$

in which k is a parameter that controls the size of the elastic region and χ^*_{ij} is the nonlinear kinematic hardening parameter. χ^*_{ij} is called the back stress parameter and has the same dimensions as stress ratio η^*_{ij}. The evolution of the hardening parameter is defined in the following equation.

$$d\chi^*_{ij} = B^*\left(A^* de^P_{ij} - \chi^*_{ij} d\gamma^{P*}\right) \tag{2.56}$$

$$d\gamma^{P*} = \left(de^P_{kl} de^P_{kl}\right)^{1/2} \tag{2.57}$$

A^* and B^* are the material parameters, de^p_{ij} is the plastic deviatoric strain increment tensor, and $d\gamma^p$ is the second invariant of de^p_{ij}. A^* and B^* are related to the stress ratio at failure M^*_f and the initial plastic shear modulus normalized to the mean effective stress G^P as follows:

$$A^* = M^*_f \tag{2.58}$$

$$B^* = G^P / M^*_f \tag{2.59}$$

Parameter B^* is assumed to follow an evolution equation as

$$dB^* = C^*_f(B^*_1 - B^*)d\gamma^{P*} \tag{2.60}$$

in which C^*_f and B^*_1 are material parameters.

2.4.3 Plastic Potential Function

The plastic potential function is given as

$$g = \left\{\left(\eta_{ij}^{*} - \chi_{ij}^{*}\right)\left(\eta_{ij}^{*} - \chi_{ij}^{*}\right)\right\}^{1/2} + \tilde{M}^{*} \ln\left(\frac{\sigma_{m}^{'}}{\sigma_{ma}^{'}}\right) = 0 \tag{2.61}$$

$$\tilde{M}^{*} = \begin{cases} -\frac{\eta^{*}}{\ln(\sigma_{m}^{'}/\sigma_{mc}^{'})} & : \text{(OC region, } f_b < 0) \\ M_{m}^{*} & : \text{(NC region, } f_b \geq 0) \end{cases} \tag{2.62}$$

where

$$\sigma_{mc}^{'} = \sigma_{mb}^{'} \exp\left(\frac{\eta_{(0)}^{*}}{M_{m}^{*}}\right) \tag{2.63}$$

It is assumed that $\tilde{M}^{*}$ becomes equal to M_{m}^{*} once $\tilde{M}^{*}$ has reached M_{m}^{*}. The plastic strain is obtained from the flow rule as

$$d\varepsilon_{ij}^{P} = \Lambda \frac{\partial g}{\partial \sigma_{ij}^{'}} \tag{2.64}$$

By applying the chain rule

$$\frac{\partial g}{\partial \sigma_{ij}^{'}} = \frac{\partial g}{\partial \sigma_{m}^{'}} \frac{\partial \sigma_{m}^{'}}{\partial \sigma_{ij}^{'}} + \frac{\partial g}{\partial s_{kl}} \frac{\partial s_{kl}}{\partial \sigma_{ij}^{'}} \tag{2.65}$$

Substituting Equation (2.61) into Equation (2.65), the following equation is obtained as

$$\frac{\partial g}{\partial \sigma_{ij}^{'}} = \frac{\delta_{ij}}{3\sigma_{m}^{'}} \left\{\tilde{M}^{*} - \frac{\eta_{st}^{*}(\eta_{st}^{*} - \chi_{st}^{*})}{\bar{\eta}_{\chi}^{*}}\right\} + \frac{1}{\sigma_{m}^{'}} \frac{\eta_{ij}^{*} - \chi_{ij}^{*}}{\bar{\eta}_{\chi}^{*}} \tag{2.66}$$

in which

$$\bar{\eta}_{\chi}^{*} = \left\{\left(\eta_{st}^{*} - \chi_{st}^{*}\right)\left(\eta_{st}^{*} - \chi_{st}^{*}\right)\right\}^{1/2} \tag{2.67}$$

From Equation(2.66), $\partial g / \partial \sigma_{kk}^{'}$ is given as

$$\frac{\partial g}{\partial \sigma_{kk}^{'}} = \frac{1}{\sigma_{m}^{'}} \left\{\tilde{M}^{*} - \frac{\eta_{mn}^{*}(\eta_{mn}^{*} - \chi_{mn}^{*})}{\bar{\eta}_{\chi}^{*}}\right\} \tag{2.68}$$

Differentiating plastic potential g with respect to s_{ij}, we obtain

$$\frac{\partial g}{\partial s_{ij}} = \frac{1}{\sigma_{m}^{'}} \frac{\eta_{ij}^{*} - \chi_{ij}^{*}}{\bar{\eta}_{\chi}^{*}} \tag{2.69}$$

From Equations (2.64) and (2.66), incremental plastic volumetric strain $d\varepsilon_{kk}^{p}$ is obtained as

$$d\varepsilon_{kk}^{P} = dv^{P} = \frac{\Lambda}{\sigma_{m}^{'}} \left\{\tilde{M}^{*} - \frac{\eta_{mn}^{*}(\eta_{mn}^{*} - \chi_{mn}^{*})}{\bar{\eta}_{\chi}^{*}}\right\} \tag{2.70}$$

In the same way, the plastic deviator strain is obtained from Equations (2.64) and (2.66),

$$de_{ij}^{P} = \frac{\Lambda}{\sigma_{m}^{'}} \frac{\eta_{ij}^{*} - \chi_{ij}^{*}}{\bar{\eta}_{\chi}^{*}} \tag{2.71}$$

Moreover, the second invariant of de_{ij}^{P} is obtained as

$$d\gamma^{P*} = \left(de_{ij}^{P} de_{ij}^{P}\right)^{1/2} = \frac{\Lambda}{\sigma_m^{'}} \tag{2.72}$$

Finally, the stress-dilatancy relation can be derived as follows:

$$\frac{dv^{P}}{d\gamma^{P*}} = \tilde{M}^{*} - \frac{\eta_{mn}^{*}(\eta_{mn}^{*} - \chi_{mn}^{*})}{\{(\eta_{st}^{*} - \chi_{st}^{*})(\eta_{st}^{*} - \chi_{st}^{*})\}^{1/2}} \tag{2.73}$$

2.4.4 Plastic Flow Rule

In the elasto-plastic theory, the effective stress increment tensor is given by

$$d\sigma_{ij}^{'} = D_{ijkl}^{EP} d\varepsilon_{kl} = D_{ijkl}^{E} d\varepsilon_{kl}^{E} = D_{ijkl}^{E}\left(d\varepsilon_{kl} - d\varepsilon_{kl}^{P}\right) \tag{2.74}$$

where D_{ijkl}^{E} is a fourth order elastic stiffness tensor. By substituting Equations (2.56), (2.72), and (2.74) into the consistency condition, which is given as

$$df = \frac{\partial f}{\partial \sigma_{ij}^{'}} d\sigma_{ij}^{'} + \frac{\partial f}{\partial \chi_{ij}^{*}} d\chi_{ij}^{*} = 0 \tag{2.75}$$

The following equation can be obtained;

$$df = \frac{\partial f}{\partial \sigma_{ij}^{'}} D_{ijkl}^{E}\left(d\varepsilon_{kl} - d\varepsilon_{kl}^{P}\right) + \frac{\partial f}{\partial \chi_{ij}^{*}} B^{*}\left\{A^{*} de_{ij}^{P} - \chi_{ij}^{*}\left(de_{pq}^{P} \cdot de_{pq}^{P}\right)^{1/2}\right\} = 0 \tag{2.76}$$

Then, substuting Equations (2.64) and (2.71) into Equation (2.76), we have

$$\frac{\partial f}{\partial \sigma_{ij}^{'}} D_{ijkl}^{E}\left(d\varepsilon_{kl} - \Lambda \frac{\partial g}{\partial \sigma_{kl}^{'}}\right) + \frac{\partial f}{\partial \chi_{ij}^{*}} B^{*}\left\{A^{*}\Lambda \frac{\partial g}{\partial s_{ij}} - \chi_{ij}^{*}\Lambda\left(\frac{\partial g}{\partial s_{pq}} \cdot \frac{\partial g}{\partial s_{pq}}\right)^{1/2}\right\} = 0 \tag{2.77}$$

in which Λ is derived as follows:

$$\begin{aligned} \Lambda &= \frac{\frac{\partial f}{\partial \sigma_{ij}^{'}} \cdot D_{ijkl}^{E} \cdot d\varepsilon_{kl}}{\frac{\partial f}{\partial \sigma_{ij}^{'}} D_{ijkl}^{E} \frac{\partial g}{\partial \sigma_{kl}^{'}} - B^{*} \frac{\partial f}{\partial \chi_{ij}^{*}}\left\{A^{*} \frac{\partial g}{\partial s_{ij}} - \chi_{ij}^{*}\left(\frac{\partial g}{\partial s_{pq}} \cdot \frac{\partial g}{\partial s_{pq}}\right)^{1/2}\right\}} \\ &= \frac{\frac{\partial f}{\partial \sigma_{ij}^{'}} \cdot D_{ijkl}^{E} \cdot d\varepsilon_{kl}}{h} \end{aligned} \tag{2.78}$$

when

$$h = \frac{\partial f}{\partial \sigma_{ij}^{'}} D_{ijkl}^{E} \frac{\partial g}{\partial \sigma_{kl}^{'}} - B^{*} \frac{\partial f}{\partial \chi_{ij}^{*}}\left\{A^{*} \frac{\partial g}{\partial s_{ij}} - \chi_{ij}^{*}\left(\frac{\partial g}{\partial s_{pq}} \cdot \frac{\partial g}{\partial s_{pq}}\right)^{1/2}\right\} \tag{2.79}$$

Substituting Equations (2.64), (2.71), and (2.78) into Equation (2.74), we finally obtain

$$\begin{aligned} d\sigma_{ij}^{'} &= D_{ijkl}^{E}\left(d\varepsilon_{kl} - d\varepsilon_{kl}^{P}\right) \\ &= D_{ijkl}^{E} d\varepsilon_{kl} - D_{ijkl}^{E} \Lambda \frac{\partial g}{\partial \sigma_{kl}^{'}} \\ &= D_{ijkl}^{E} d\varepsilon_{kl} - D_{ijmn}^{E} \frac{\partial g}{\partial \sigma_{mn}^{'}} \cdot \frac{1}{h} \frac{\partial f}{\partial \sigma_{pq}^{'}} \cdot D_{pqkl}^{E} \cdot d\varepsilon_{kl} \\ &= \left\{D_{ijkl}^{E} - \frac{1}{h} D_{ijmn}^{E} \frac{\partial g}{\partial \sigma_{mn}^{'}} \cdot \frac{\partial f}{\partial \sigma_{pq}^{'}} \cdot D_{pqkl}^{E}\right\} d\varepsilon_{kl} \end{aligned} \tag{2.80}$$

2.5 Finite Element Formulation for the Analysis of Water Saturated Soil

A finite element formulation for a two-phases mixtures, based on the finite deformation theory, is presented in this section. Biot's (1962) two-phase mixture theory is adopted to give the governing equations of the soil-water coupling problem. For simplified and practical formulations, both the grain particles and the fluid are assumed to be incompressible.

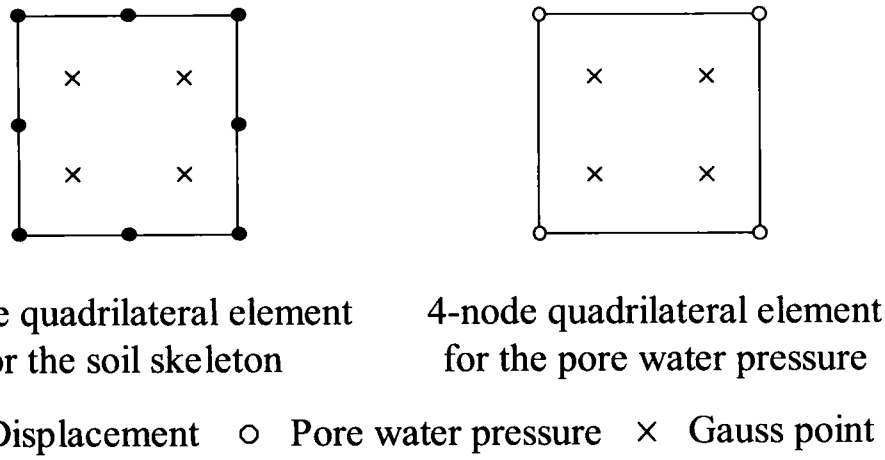

Figure 2.4 Finite elements and the Gauss integration points

An updated Lagrangian method with the objective Jaumann rate of Cauchy stress is used for the weak form of the equilibrium equation in the formulations. As for the element type, an eight-node quadrilateral isoparametric element with a reduced Gaussian four-points integration is used for the displacement in order to eliminate shear locking as well as to reduce the appearance of a spurious hourglass mode. The pore water pressure is defined by a four-node quadrilateral isoparametric element (see Figure 2.4).

2.5.1 Equilibrium Equation

Based on Terzaghi's concept of effective stress, the total stress tensor and the time rate of stresses are given as

$$T_{ij} = T'_{ij} + u_w \delta_{ij} \tag{2.81}$$

$$\dot{T}_{ij} = \dot{T}'_{ij} + \dot{u}_w \delta_{ij} \tag{2.82}$$

in which T_{ij} denotes the total Cauchy stress tensor, T'_{ij} denotes the effective Cauchy stress tensor, u_w denotes the pore water pressure, and δ_{ij} denotes Kronecker's delta, and the superimposed dot indicates the time differentiation.

Nominal stress rate tensor $\dot{S}_{ij}$ and the effective nominal stress tensor are given by the following equations:

$$\dot{S}_{ij} = \dot{T}_{ij} + L_{kk}T_{ij} - T_{ik}L_{jk} \tag{2.83}$$

$$\dot{S}'_{ij} = \dot{T}'_{ij} + L_{kk}T'_{ij} - T'_{ik}L_{jk} \tag{2.84}$$

where L_{ij} is the velocity gradient tensor. To obtain the relation between $\dot{S}_{ij}$ and $\dot{S}'_{ij}$, substituting Equations (2.81) and (2.82) into Equation(2.83) gives

$$\dot{S}_{ij} = \dot{S'}_{ij} + \dot{u}_w\delta_{ij} + B_{ij} \tag{2.85}$$

while $B_{ij} = L_{kk}u_w\delta_{ij} - u_w\delta_{ik}L_{jk}$. Similarly, the last term on the right-hand side of Equation (2.84) is written as

$$-T'_{ik}L_{jk} = A_{ij} \tag{2.86}$$

Then, Equation (2.84) will become the following equation:

$$\dot{S}'_{ij} = \dot{T}'_{ij} + A_{ij} + T'_{ij}trL \tag{2.87}$$

The weak form of the equilibrium equation for the whole fluid-solid mixture is

$$\int_V \dot{S}_{ij,j}\delta v_i dV = 0 \tag{2.88}$$

in which δv_i denotes the virtual velocity vector components, and by substituting relation

$$\left(\dot{S}_{ij}\delta v_i\right)_{,j} = \dot{S}_{ij,j}\delta v_i + \dot{S}_{ij}\delta v_{i,j} \tag{2.89}$$

into Equation(2.88), yields

$$\int_V \left(\dot{S}_{ij}\delta v_i\right)_{,j} dV - \int_V \dot{S}_{ij}\delta v_{i,j}dV = 0 \tag{2.90}$$

By taking the Gauss principle, the first term on the left-hand side of Equation(2.90) can be written as

$$\int_V \left(\dot{S}_{ij}\delta v_i\right)_{,j} dV = \int_\Gamma \left(\dot{S}_{ij}\delta v_i\right) n_j d\Gamma \tag{2.91}$$

By considering the second term in Equation(2.90), $L_{ij} = v_{i,j}$ (L_{ij} is the velocity gradient tensor), Equation(2.90) yields

$$\int_V \dot{S}_{ij}\delta v_{i,j}dV = \int_V \dot{S}_{ij}\delta L_{ij}dV \tag{2.92}$$

Substituting Equations(2.91) and (2.92) into Equation(2.90) gives

$$\int_\Gamma \left(\dot{S}_{ij}\delta v_i\right) n_j d\Gamma - \int_V \dot{S}_{ij}\delta L_{ij}dV = 0 \tag{2.93}$$

Upon the substitution of Equation(2.85) into the second term in Equation(2.93), we obtain

$$\hat{S}_{ti} = \dot{S}_{ij} n_j$$

where

$$\int_V \dot{S}'_{ij} \delta L_{ij} dV + \int_V \dot{u}_w \delta D_{kk} dV + \int_V B_{ij} \delta L_{ij} dV = \int_\Gamma \hat{S}_{ti} \delta v_i d\Gamma \tag{2.94}$$

in which D_{ij} is the stretching tensor. By substituting the effective nominal stress rate in Equation(2.87) into the Equation (2.94), the following relation is obtained:

$$\int_V \dot{T}'_{ij} \delta L_{ij} dV + \int_V A_{ij} \delta L_{ij} dV + \int_V T'_{ij} tr L \delta L_{ij} dV + \int_V \dot{u}_w \delta D_{kk} dV + \int_V B_{ij} \delta L_{ij} dV = \int_\Gamma \hat{S}_{ti} \delta v_i d\Gamma \tag{2.95}$$

From the symmetry of the effective Cauchy stress tensor,

$$\dot{T}'_{ij} L_{ij} = \frac{1}{2} \dot{T}'_{ij} (L_{ij} + L_{ji}) = \dot{T}'_{ij} D_{ij} \tag{2.96}$$

is obtained.

Finally, by substituting Equation (2.96) into Equation(2.95), a weak form of the equilibrium equation can be obtained as

$$\int_V \dot{T}'_{ij} \delta D_{ij} dV + \int_V A_{ij} \delta L_{ij} dV + \int_V L_{kk} T'_{ij} \delta L_{ij} dV + \int_V \dot{u}_w \delta D_{kk} dV + \int_V B_{ij} \delta L_{ij} dV = \int_\Gamma \hat{S}_{ti} \delta v_i d\Gamma \tag{2.97}$$

For the discretization of the weak form of the equilibrium equation, the following matrix relations are used:

$$\{D\} = [B] \{v^*\} \tag{2.98}$$

$$\{v\} = [N] \{v^*\} \tag{2.99}$$

$$\{L\} = [B_M] \{v^*\} \tag{2.100}$$

$$trD = \{B_v\}^T \{v^*\} \tag{2.101}$$

$$\dot{u}_w = \{N_h\} \{\dot{u}^*_w\} \tag{2.102}$$

where $[B]$ is the matrix which transforms the nodal velocity vector to the stretching vector, and $\{v^*\}$ is the nodal velocity vector, $\{v\}$ is the velocity vector in an element, $[N]$ is a shape function of the eight-node quadrilateral element, $[B_M]$ is the matrix which transforms the nodal velocity vector into the velocity gradient vector, $\{B_v\}$ is the vector which transforms the nodal velocity into the trace of D, $\dot{u}_w$ represents pore pressure rate,

$\{\dot{u}_w^*\}$ represents the nodal pore pressure rate vector, and $\{N_h\}$ represents the four-node qualidrilateral element shape function.

In the formulation, the finite deformation theory with Jaumann rate of Cauchy stress tensor $\hat{T}'_{ij}$ is adopted. Jaumann rate of Cauchy stress tensor $\hat{T}'_{ij}$ is an objective tensor and is defined as

$$\hat{T}'_{ij} = \dot{T}'_{ij} - W_{ik}T'_{kj} + T'_{ik}W_{kj} \tag{2.103}$$

where W_{ij} is the spin tensor.

Total stretching tensor D_{ij} is assumed to be a composition of elastic stretching tensor D^e_{ij} and viscoplastic stretching tensor D^{vp}_{ij}.

$$D_{ij} = D^e_{ij} + D^{vp}_{ij} \tag{2.104}$$

The relation between the elastic stretching tensor D^e_{ij} and Jaumann rate of Cauchy stress tensor $\hat{T}'_{ij}$ can be obtained as

$$\hat{T}'_{ij} = C^e_{ijkl}D^e_{kl} \tag{2.105}$$

which leads to the relation

$$\hat{T}'_{ij} = C^e_{ijkl}(D_{kl} - D^{vp}_{kl}) \tag{2.106}$$

Viscoplastic stretching tensor D^{vp}_{ij} can be obtained by the flow rule as

$$D^{vp}_{ij} = \gamma \langle \Phi_1 (f_y) \rangle \frac{\partial f_p}{\partial T'_{ij}} \tag{2.107}$$

For clay material, the tangent modulus method (Peirce et al. 1984) is adopted hereing to evaluate the viscoplastic stretching tensor D^{vp}_{ij}. The relation between the rate of effective stress and the stretching tensor can be written in the matrix form as follows:

$$\left\{\hat{T}'\right\} = [C]\{D\} - \{Q\} \tag{2.108}$$

Substituting Equation(2.103) into Equation(2.108) yields

$$\left\{\dot{T}'\right\} = [C]\{D\} - \{Q\} + \{W^*\} \tag{2.109}$$

where $[C]$ is the tangential stiffness matrix, $\{Q\}$ is the relaxation stress vector, and $\{W^*\} = \{WT - TW\}$ is the vector of the spin tensor. By all the matrices and vector relations obtained previously and considering the arbitrariness of the unconstrained virtual nodal velocities $\{\delta v^*\}^T$, we have

$$[K]\{v^*\} - \int_V [B]^T \{Q\}\, dV + \int_V [B]^T \{W^*\}\, dV + [K_L]\{v^*\} + [K_v]\{\dot{u}_w^*\} = \left\{\dot{F}\right\} \tag{2.110}$$

in which

$$[K] = \int_V [B]^T [C][B] dV \tag{2.111}$$

$$[K_L] = \int_V [B_M]^T [D'_s][B_M] dV + \int_V [B_M]^T [U][B_M] dV + \int_V [B_M]^T \{T'\} \{B_v\}^T dV \tag{2.112}$$

$$[K_v] = \int_V \{B_v\} \{N_h\}^T dV \tag{2.113}$$

$$\left\{\dot{F}\right\} = \int_\Gamma [N]^T \left\{\hat{S}_t\right\} d\Gamma \tag{2.114}$$

In the above equations, the matrix forms of A_{ij} and B_{ij}, $[A]$ and $[B]$ are defined as

$$[A] = [D'_s][B_M] \{v^*\} \tag{2.115}$$

$$[B] = [U][B_M] \{v^*\} \tag{2.116}$$

The relation between the nodal velocity vector and the nodal displacement vector can be obtained by using Euler's approximation as

$$\{v^*\} = \frac{\{\Delta u^*\}}{\Delta t} \qquad \{\Delta u^*\} \text{ : Nodal displacement vector} \tag{2.117}$$

Similarly, the pore water pressure can be obtained as

$$\{\dot{u}^*_w\} = \frac{\{u^*_w\}_{t+\Delta t} - \{u^*_w\}_t}{\Delta t} \tag{2.118}$$

Substituting Equations (2.117) and (2.118) into Equation (2.110) yields

$$[K]\frac{\{\Delta u^*\}}{\Delta t} + [K_L]\frac{\{\Delta u^*\}}{\Delta t} + [K_v]\frac{\{u^*_w\}_{t+\Delta t} - \{u^*_w\}_t}{\Delta t} - \int_V [B]^T \{Q\} dV + \int_V [B]^T \{W^*\} dV = \left\{\dot{F}\right\} \tag{2.119}$$

Finally, by transforming the above equation, the weak form of the equilibrium equation is obtained as:

$$\begin{aligned} \left[[K] + [K_L]\right] \{\Delta u^*\} + [K_v] \{u^*_w\}_{t+\Delta t} &= \Delta t \left\{\dot{F}\right\} + [K_v] \{u^*_w\}_t \\ &+ \Delta t \int_V [B]^T \{Q\} dV - \Delta t \int_V [B]^T \{W^*\} dV \end{aligned} \tag{2.120}$$

2.5.2 Continuity Equation

Boundary surface Γ of a closed domain V can be decomposed into two components, namely,

$$\Gamma = \Gamma_p + \Gamma_v \tag{2.121}$$

where Γ_p is the boundary where the pore pressure is specified and Γ_v is the boundary when the flow of water is specified. On the boundary Γ_p,

$$u_w = \bar{u}_w \tag{2.122}$$

On the boundary Γ_v,

$$\frac{k}{\gamma_w}\nabla u_w = \bar{v} \tag{2.123}$$

Letting k be the coefficient of permeability, and γ_w be the pore water density, the equilibrium equation of the fluid phase can be written as

$$\frac{k}{\gamma_w}u_{w,ii} + D_{ii} = 0 \tag{2.124}$$

Considering the test function of $\hat{u}_w$, the weak form of the continuity equation can be obtained as

$$\int_V \left(\frac{k}{\gamma_w}u_{w,ii} + D_{ii}\right)\hat{u}_w dV = \frac{k}{\gamma_w}\int_V u_{w,ii}\hat{u}_w dV + \int_V D_{ii}\hat{u}_w dV = 0 \tag{2.125}$$

From the relation

$$u_{w,ii}\hat{u}_w = (u_{w,i}\hat{u}_w)_{,i} - u_{w,i}\hat{u}_{w,i} \tag{2.126}$$

Equation (2.125) can be rewritten as

$$\frac{k}{\gamma_w}\int_V (\hat{u}_w u_{w,i})_{,i}\, dV - \frac{k}{\gamma_w}\int_V \hat{u}_{w,i}u_{w,i}dV + \int_V \hat{u}_w D_{ii}dV = 0 \tag{2.127}$$

By applying Gauss's theory to the previous equation, the following equation can be obtained:

$$\int_{\Gamma_v} \bar{v}\cdot n d\Gamma - \frac{k}{\gamma_w}\int_V \hat{u}_{w,i}u_{w,i}dV + \int_V \hat{u}_w D_{ii}dV = 0 \tag{2.128}$$

in which n is the unit normal vector of the body. Herein, the following matrix is defined as

$$u_w = \{N_h\}\{u_w^*\} \tag{2.129}$$

$$\{u_{w,i}\} = [N_{h,i}]\{u_w^*\} = [B_h]\{u_w^*\} \tag{2.130}$$

$$[N_{h,i}] = \nabla\{N_h\} \tag{2.131}$$

$$D_{ii} = trD = \{B_v\}^T\{v^*\} \tag{2.132}$$

Using these equations, Equation(2.128) is discretized as

$$\int_{\Gamma_v} \{\hat{u}_w^*\}^T \{N_h\}^T \{\bar{v}\}^T \{n\}\, d\Gamma - \frac{k}{\gamma_w}\int_V \{\hat{u}_w^*\}^T [B_h]^T [B_h] \{u_w^*\}\, dV + \int_V \{\hat{u}_w^*\}^T \{N_h\}^T \{B_v\} \{v^*\}\, dV = 0 \tag{2.133}$$

By taking the arbitration of the test function, dividing the previous equation by $\{\hat{u}_w^*\}^T$ gives

$$\frac{k}{\gamma_w}\int_\Gamma \{N_h\} \{n\}^T [B_h] d\Gamma \{u_w^*\} - \frac{k}{\gamma_w}\int_V [B_h]^T [B_h] dV \{u_w^*\} + \int_V \{N_h\} \{B_v\}^T dV \{v^*\} = 0 \tag{2.134}$$

where

$$[K_h] = \frac{k}{\gamma_w}\int_V [B_h]^T [B_h] dV \tag{2.135}$$

$$[K_v]^T = \int_V [N_h]^T [B_v] dV \tag{2.136}$$

$$[V] = -\int_{\Gamma_v} [N_h]^T \{\bar{v}\}^T \{n\}\, d\Gamma \tag{2.137}$$

Using Euler's approximation, the discretization of the continuity equation is obtained as follows:

$$[K_v]^T \{\Delta u^*\} - \Delta t\, ([K_h] + [V])\, \{u_w^*\}_{t+\Delta t} = 0 \tag{2.138}$$

Combining Equations (2.120) and (2.138) gives the governing equation for the finite element formulation as

$$\begin{bmatrix} [K] + [K_L] & [K_v] \\ [K_v]^T & -\Delta t\, ([K_h] + [V]) \end{bmatrix} \begin{Bmatrix} \Delta u^* \\ u^*_{w,t+\Delta t} \end{Bmatrix}$$

$$= \begin{Bmatrix} \Delta t \left\{\dot{F}\right\} + [K_v] \{u_w^*\}_t + \Delta t \int_V [B]^T \{Q\}\, dV - \Delta t \int_V [B]^T \{W^*\}\, dV \\ 0 \end{Bmatrix} \tag{2.139}$$

Chapter 3

Large Deformation Analysis of Lateral Earth Pressure and an Excavation through a Thick Soft Clay Deposit

3.1 Introduction

When an excavation is to be performed through a thick soft clay deposit, it may be difficult to install the retaining structures into a firm soil stratum, and this will lead to difficulties in controlling the ground movements. Large deformations due to undrained creep and the plastic flow of soil may occur within a short period of time. This not only shows the complexity of the mechanism of soil-pile interaction below the excavation level when the excavation is performed through a thick soft clay deposit, but also points out the important effects of the nonlinear behavior, as well as the rate sensitivity, of clay. A numerical analysis using an elasto-viscoplastic soil model has been conducted to study on the soil-structure interaction between retaining structures and a clay deposit.

This chapter is divided into two parts. In the first part, the effects of various factors on the lateral earth pressure, including both of the active and passive earth pressure, will be evaluated. In the design and construction of almost every kind of retaining structures and ground excavation, the lateral forces acting between the retaining structures and the soil masses being retained are due to lateral earth pressure. It is important, therefore, to understand the lateral earth pressure. This first part is devoted to the study of the lateral earth pressure.

In the second part, the behavior of a braced excavation performed through a thick soft clay deposit will be studied. It is found that an excavation performed through a thick soft clay deposit results in the concentration of large deformations under the excavation level. The deformations will continue even after the stop of the excavation. The effects of various parameters on the performance of the supporting system are also studied.

3.2 Numerical Simulation of the Lateral Earth Pressure of Normally Consolidated Soft Clay

Retaining structures such as retaining walls, basement walls, and bulk-heads are commonly used in the Foundation Engineering to support almost all vertical slopes of earth masses. The proper design and construction of these structures require a thorough knowledge of the lateral forces acting between the retaining structures and the soil masses being retained. These lateral forces acting on the retaining structures are brought about by lateral earth pressure, which is usually determined by a classical theory of soil mechanics such as Rankine's theory or Coulomb's theory. Classical theories consider only the conditions that would correspond to a collapse condition. However, there are situations for which the movements of earth-retaining structures must be seriously considered, and for some cases, the consideration of only the stability is inadequate for a proper design. The deformation of the soil bodies close to the wall and the distribution of earth pressure on the wall are complex due to the pattern of strain localization zones and other several factors, such as the type of wall movements, friction conditions between the soil and the wall, and soil properties such as soil permeability. Realistic earth pressures levels can be simulated using constitutive models that can reproduce the formations of shear zones.

In this section, the finite element analysis for earth retaining structures on the normally-consolidated homogeneous soft clay is conducted using an elasto-viscoplastic constitutive model with material function Φ_2 proposed by Adachi, Oka, and Mimura (1987) and the finite element formulation proposed in Chapters 2. The earth pressures on the wall as well as the ground deformation behind the wall will be studied by taking into account the effects of the friction conditions between the soil and the wall as well as the patterns of the wall movement. The results of the simulations will be shown and their effects on the problem will be discussed. $\sigma'_v = (\gamma_s - \gamma_w) \times z + \sigma'_{h0}$

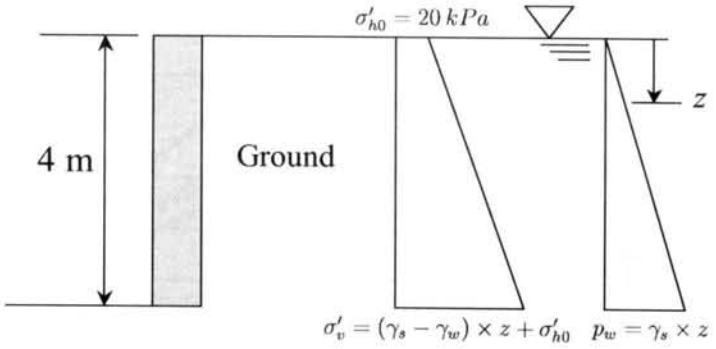

Figure 3.1 Initial conditions of the ground

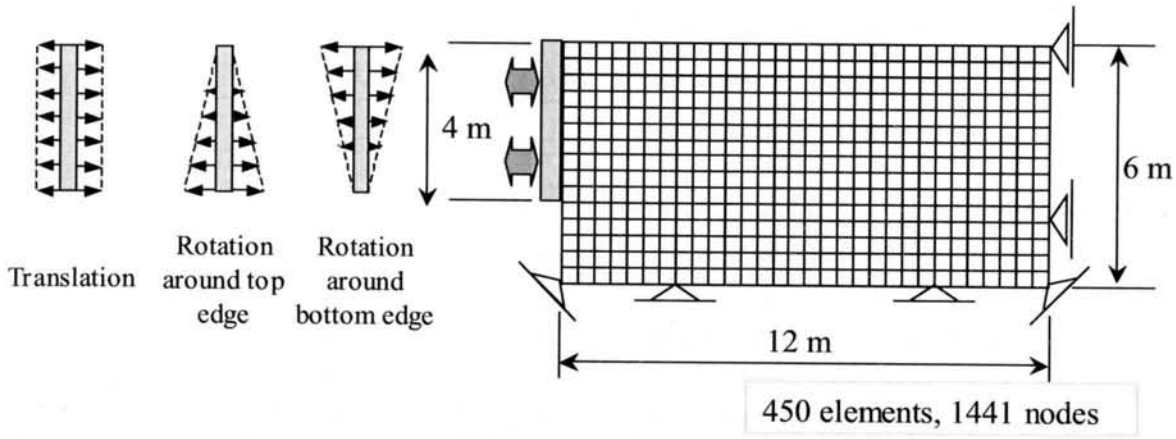

Figure 3.2 Finite element mesh used in the analysis

3.2.1 Numerical Simulations

We will restrict the simulations to the case of a retaining wall with a vertical backface which supports a horizontal backfill. Computations have been carried out separately for active and passive earth pressure problems. A rigid wall, 4m in height, is pulled and pushed into an uniform regular soil mass to simulate the active and the passive earth pressure types respectively. The rate of the wall movement used is $4.0 \times 10^{-3} m/min$.. The initial stress state has been determined by the unit weight of the saturated soil, $\gamma_{sat} = 20kN/m^3$, with the water level assumed to be at the ground surface, and by a coefficient of earth pressure at rest, $K_0 = 1.0$ (see Figure 3.1). The FE mesh is shown in Figure 3.2. The geometry of the clay ground is 12m in width and 6m in height, and consists of 450 square elements. Plane strain conditions are assumed. All the boundaries of the ground are set to be impermeable. The boundary conditions include a fixed base and rollers which allow only vertical movement along the right-hand side boundary, the other two boundaries are free. The material parameters used in the analysis are listed in Table 3.1.

Table 3.1 Soil parameters used in the analysis of the active and passive earth pressures

Coefficient of permeability k_0 (m/s)	1.54×10^{-8}
Elastic shear modulus G (kPa)	$G_0(\sigma'_m/\sigma'_{m0})^{1/2}$
Compression index λ	0.172
Swelling index κ	0.054
Initial void ratio e_0	0.72
Coefficient of earth pressure K_0	1.0
Stress ratio at failure M_f^*	1.05
Viscoplastic parameter m'	21.5
Viscoplastic parameter C (1/s)	4.5×10^{-8}
Viscoplastic parameter G_2^*	100.0

Note: γ_s=20 kN/m^3, γ_w=9.81 kN/m^3, G_0 varies with depth and is calculated by the relation: $G = G_0(\sigma_m/\sigma_{m0})^{1/2}$, G_0=5,500 kPa when σ'_m=392.0 kPa.

Table 3.2 Friction conditions and the wall movement patterns used in the analyses

	Friction conditions of the wall	Wall movement patterns
Effects of the friction conditions between the soil and the wall	Very rough	Translation
	Coefficient of friction, μ=0.8	Translation
	Coefficient of friction, μ=0.5	Translation
	Smooth	Translation
Effects of the wall movement patterns	Very rough	Translation
	Very rough	Rotation around top edge
	Very rough	Rotation around bottom edge

All the conditions used in the analysis are shown in Table 3.2. μ is the coefficient of friction between the soil and the wall and "Very rough" indicates the "no-slip" condition between the soil and the wall. The numerical results will be discussed in the following section.

3.2.2 Results of Analyses

3.2.2.1 Effects of the friction of the wall on the earth pressure

The friction between the wall and the soil mass has been varied to evaluate its effect on the earth pressure. The numerical analysis has been divided into four cases for simulations

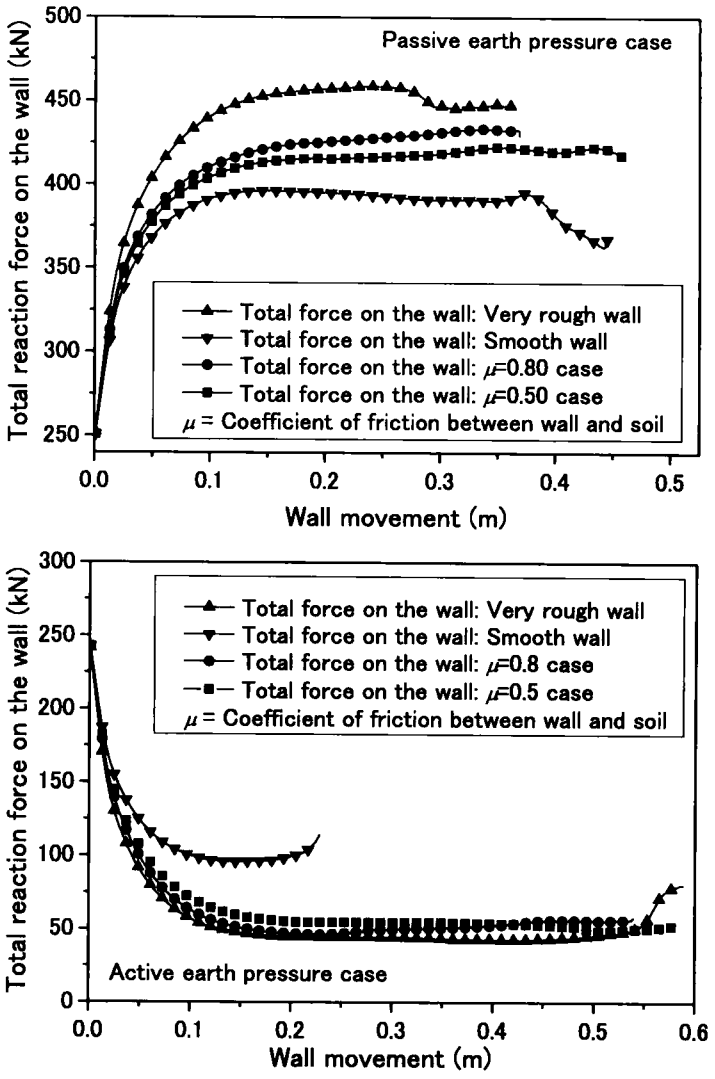

Figure 3.3 Total earth pressure on the wall under different friction conditions

of active and passive wall movements. These four cases include two extreme conditions of wall friction, a very rough wall, by assuming "no-slip" conditions between the soil and the smooth wall, namely, a frictionless wall, and other two other cases of wall friction with coefficients of friction of μ=0.5 and 0.8, respectively. In the following, the very rough wall, the wall with coefficients of friction, μ=0.8 and 0.5, and the smooth wall will be referred to as Cases 1,2,3,and 4, respectively. Starting from the passive case, we will now compare the results of the total earth pressures acting on the wall from all cases, which are shown in Figure 3.3. The earth pressure on the wall was calculated as the sum of the nodal forces in the horizontal direction along the wall surface.

Simulations show that the wall under no-slip conditions yields the largest peak passive pressure on wall, followed by the wall with coefficients of friction μ=0.8 and 0.5, and

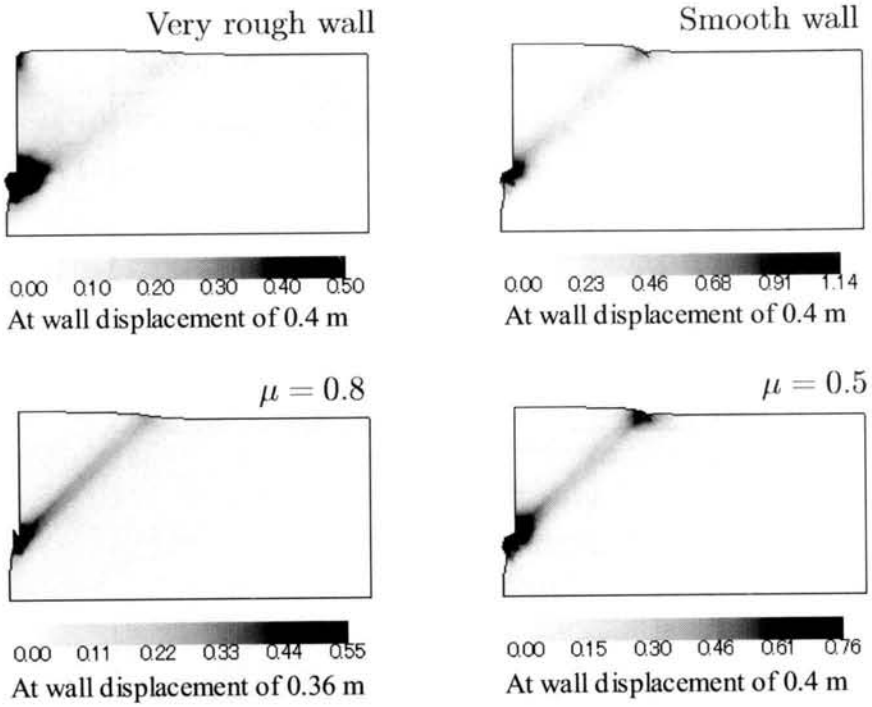

Figure 3.4 Comparison of the accumulated viscoplastic shear strain from soil under different friction conditions between the soil and the wall in the passive earth pressure case

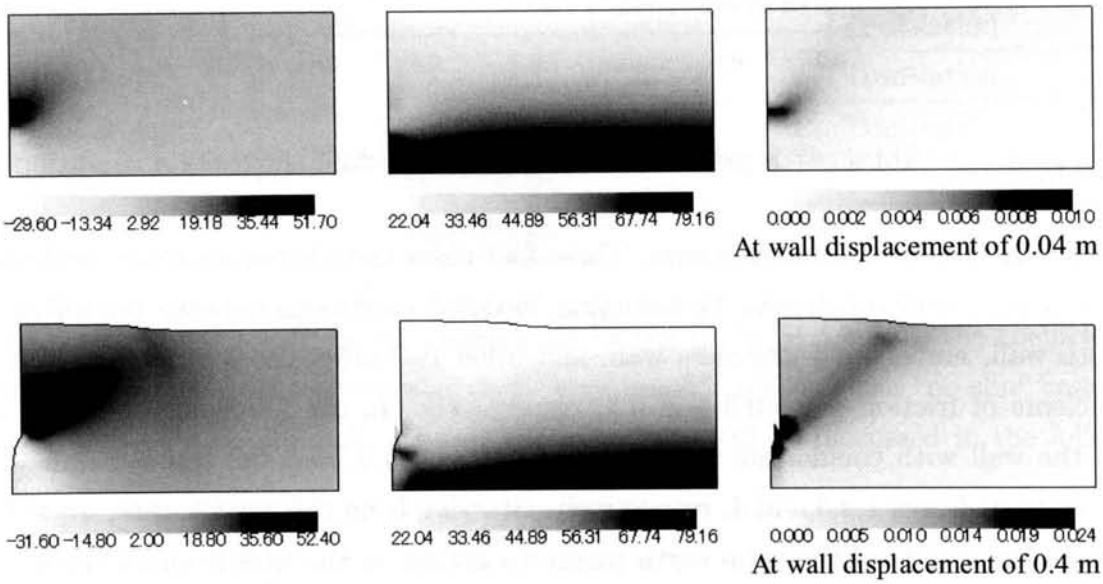

Figure 3.5 From left to right: the distribution of excess pore water pressure, mean effective stress, and viscoplastic volumetric strain for the smooth wall in the passive earth pressure case

then the smooth wall, respectively. The features of the results agree with the results by Coulomb's theory of earth pressure.

Figure 3.4 shows a comparison of the distribution of the accumulated viscoplastic shear strain $\gamma^p \equiv \int \sqrt{de_{ij}^{vp} de_{ij}^{vp}}$, for all cases. In all cases, the localization started from the lower edge of the wall, and proceeded through the ground surface. In Case 1, three shear bands appear. The first shear band starts from the lower edges of the wall and appears to curve and bend upward. It then connects to the second shear band, which extends farther through the ground surface. The angle of the second shear band is around 45°. This value agrees with the angle of shear zones obtained from Rankine's theory in the case of a clay ground with an angle of internal friction of zero ($\phi = 0$). The next shear zone appears at the soil adjacent to the wall. This zone is caused by the no-slip conditions between the soil and the wall which prevents the soil adjacent to the wall from moving upward when it is subjected to the wall movement. As for the Case 4, only one shear zone can be observed. The band starts from the lower edge of the wall and spreads to the ground surface with an angle around 45°. There is no shear band in the soil adjacent to the wall, because the soil was not subjected to a vertical movement restraint as in the Case 1.

Only one shear zone appears in Cases 2 and 3. The angle of each shear bands is around 45°, and it bends a slightly in a curved pattern near the lower edge of the wall in both cases. There is no shear zone observed in the soil adjacent to the wall which is similar to Case 4. The behavior of Cases 2 and 3 can be thought of as the intermediate states of Cases 1 and 4.

Let us now consider the distribution of the pore water pressure, the mean effective stress, and the viscoplastic volumetric strain. Case 4, namely, the case of the wall with no friction, is chosen to be the representative case. The distribution of the pore water pressure, the mean effective stress, and the viscoplastic volumetric strain obtained from this case for a wall displacement of 0.4m are shown in Figure 3.5. The figure clearly shows a decreasing of mean effective stress along with an increasing of the pore water pressure and the viscoplastic volumetric strain in the soil around the localization zone. This behavior is caused by the effects of the negative dilatancy of normally consolidated clay, namely, a reduction in the volume of clay during the shearing process. It was found that this type of clay behavior can be simulated well by the soil model.

Now, we consider the active earth pressure case. Figure 3.3 shows the total earth pressure on the wall for all cases. Similar to the case of passive earth pressure, the simulated results with the smallest value of active earth pressure in Case 1, the earth pressure decreases extensively from the initial values. The earth pressure in Cases 2 and

3 yields larger active earth pressure values, and the Case 4 produces the largest value of active earth pressure.

In Cases 1 and 4, the total active earth pressure decreases from that under the initial conditions by the values of 200.0 kN and 146.9 kN respectively. These values can be compared to those obtained from Cases 1 and 4 of the passive earth pressure case, in which the earth pressure values increase by 206.6 kN and 144.1 kN, respectively. This trend shows the effects of friction between the wall and the soil in the extreme cases. However, it is seen that the friction between the wall and the soil tends to have stronger effects on the earth pressure in the case of active earth pressure than in the case of passive earth pressure.

Figure 3.6 shows the distributions of the accumulated viscoplastic shear strain of the analysis results for the case of the active earth pressure. Similar to the results for the case of passive earth pressure, the localization started from the lower edge of the wall and then spread toward the ground surface. The patterns of the shear bands from the active case are identical to those from the passive case, that is, three shear bands in Case 1 and one shear band in Case 4. In addition, it should be noted that for Cases 2 and 3, the localization is observed in the soil adjacent to the wall during the late stages of deformation. This pattern cannot be observed in either Cases 2 or Case 3 for the case of passive earth pressure, and thus, larger effects of friction between the wall and the soil in the case of the active earth pressure are seen than in the case of the passive earth pressure.

Let us now take a look at the distributions of the pore water pressure, the mean effective stress, and viscoplastic volumetric strain. Similarly to the case of the passive earth pressure case, Case 4 is chosen as the representative case and the obtained results are shown in Figure 3.7. The figures show a reduction in the mean effective stress and the viscoplastic volumetric strain. The decrease in the pore water pressure in the soil mass behind the wall can also be seen in the figure as a result of the wall movements. It is clear that the decrease in pore water pressure in the case of the active earth pressure case is small in contrast to the increase in pore water pressure in the case of the passive earth pressure case (see Figure 3.5). This can be explained as the effects of the negative dilaltancy of normally consolidated clay, in which the increase in pore water pressure caused by a reduction in the volume of soil during the shearing process will compensate for the reduction in the pore water pressure results from the active wall movements.

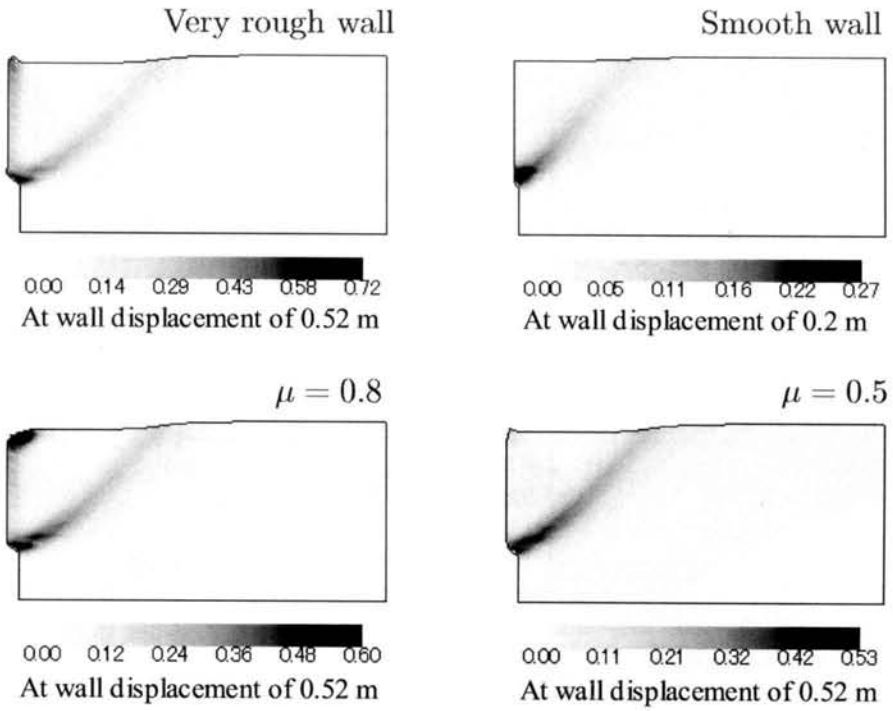

Figure 3.6 Comparison of the accumulated viscoplastic shear strain from soil under different friction conditions between the soil and the wall in the active earth pressure case

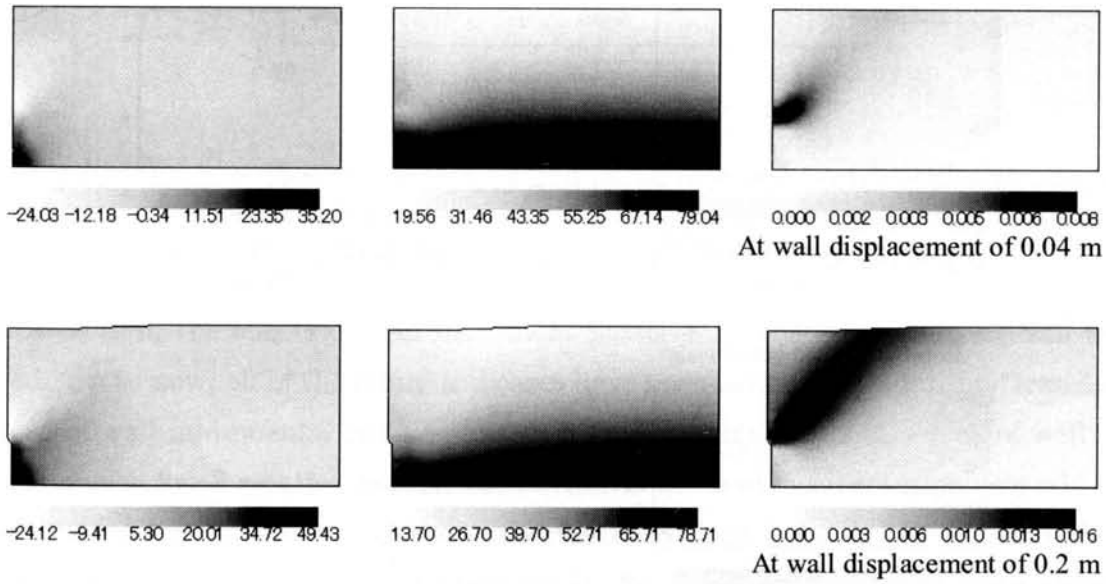

Figure 3.7 From left to right: the distribution of excess pore water pressure, mean effective stress, and viscoplastic volumetric strain for the smooth wall in the active earth pressure case

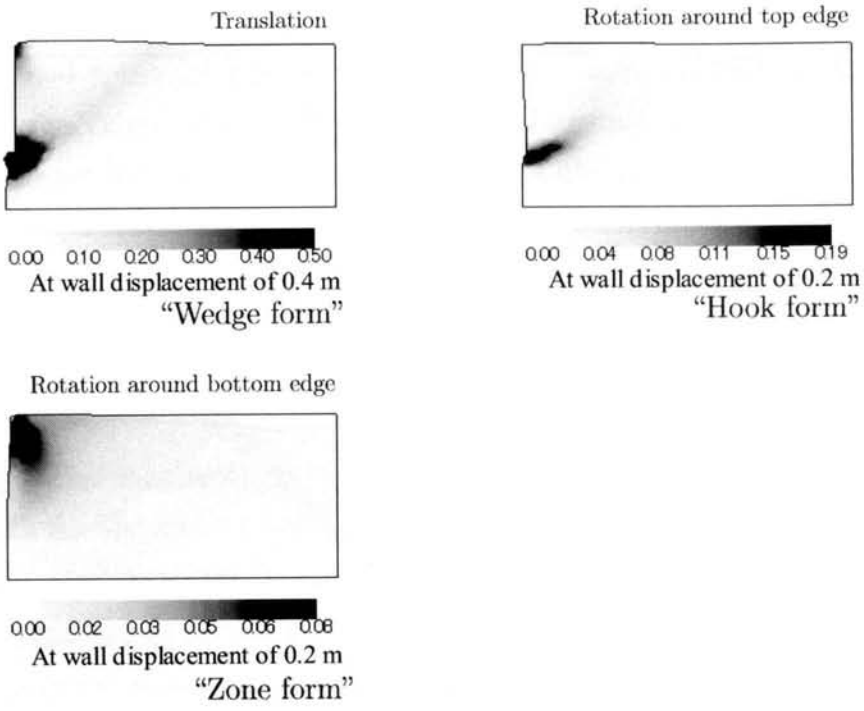

Figure 3.8 Comparison of the accumulated viscoplastic shear strain from soil under different patterns of wall movements in the passive earth pressure case

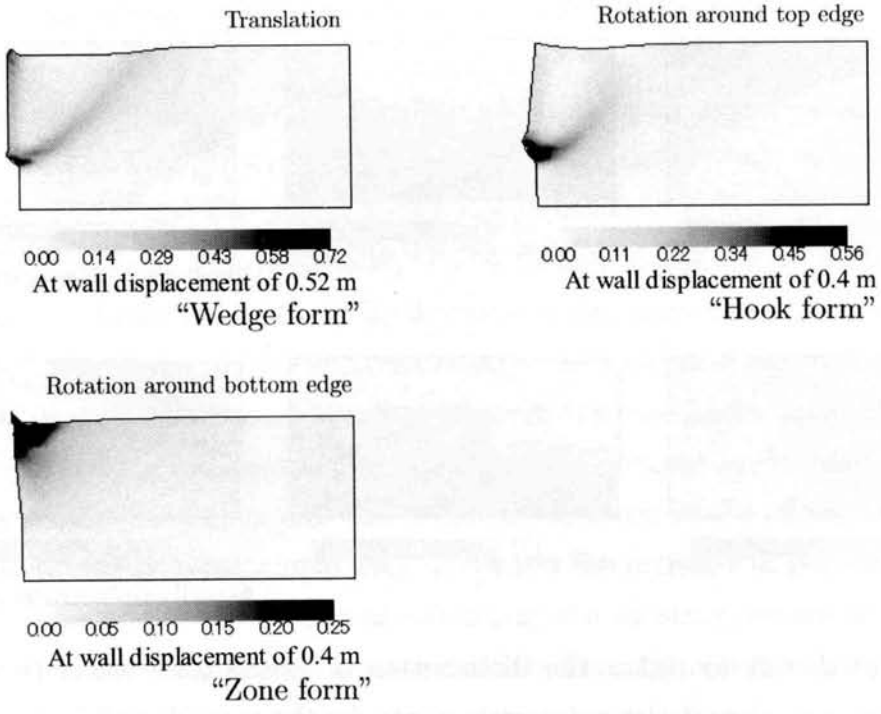

Figure 3.9 Comparison of the accumulated viscoplastic shear strain for soil under different patterns of wall movements in the active earth pressure case

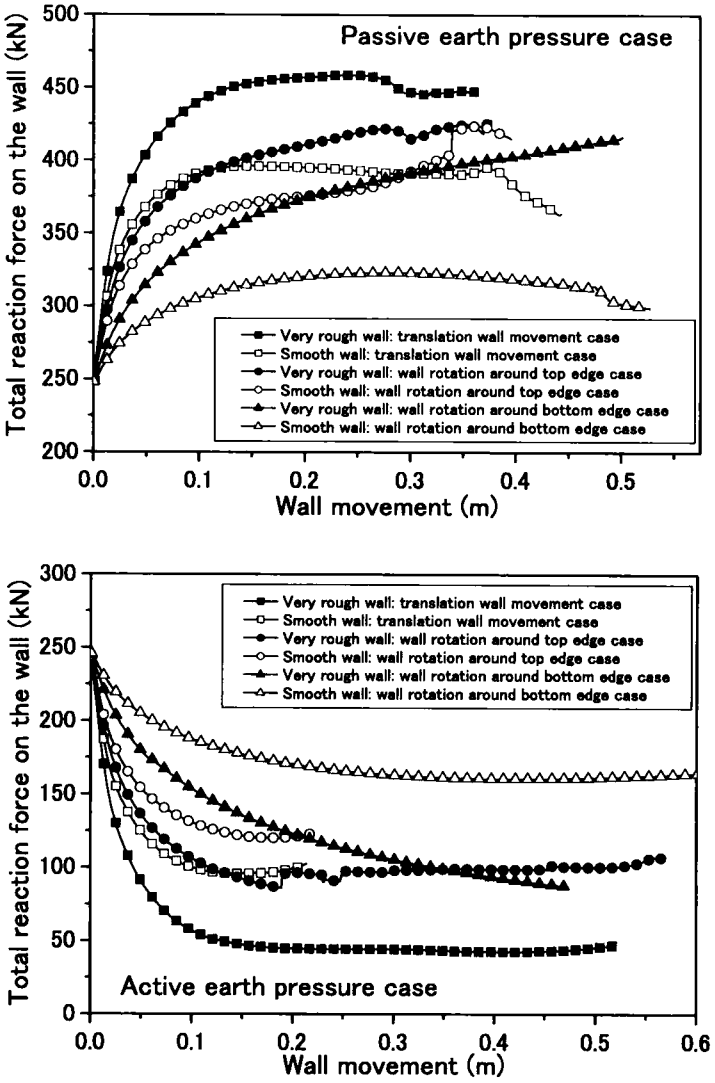

Figure 3.10 Total earth pressure on the wall under different patterns of wall movements

3.2.2.2 Effects of wall movement patterns on the earth pressure

In this section, the effects of wall movement patterns on the earth pressure will be discussed. Up to now, all of the numerical cases have been simulated under the "translation" pattern of wall movements. In this section, however, two additional modes of wall movement, namely, "wall rotation around the bottom edge" and "wall rotation around the top edge" are analyzed. The two extreme friction conditions between the soil and the wall are adopted in the analysis. From now on in this section, the case of translation wall movement, wall rotation around the top edge, and wall rotation around the bottom edge will be referred to as Cases 1, 2, and 3, respectively.

Figures 3.8 and 3.9 show the comparisons of the accumulated viscoplastic shear strain for all cases. It can be seen that the difference in wall movement patterns results in

totally different shearing behavior of the soil behind the wall. In Case 2, for both the passive and the active earth pressure analyses, the localization starts from the lower edge of the wall and then progresses through the surface of the soil in the same way as that obtained from the case of the translation wall movement. However, the shape of the shear bands appears in a curved form, and the shear bands start with a low angle against the horizontal plane and then bend upward with an increase in the angle to around 90° near the ground surface. It should be noted that, for both the active and the passive earth pressure cases, the shear bands do not reach the ground surface as has been observed in the translation case. Under the very rough wall conditions in the case of the active earth pressure case, localization can also be observed in the soil adjacent to the wall; this is not observed in the case of the passive earth pressure. This indicates the strong effect of friction between the wall and the soil in the case of active earth pressure.

Let us now consider Case 3. From the deformed mesh and the distributions of the accumulated viscoplastic shear strain, the formation of a "shear band" cannot be clearly observed. The soil behind the wall tends to deform in a larger zone, which extends from the lower edge of the wall to the ground surface behind the wall at a distance approximately equal to the wall length. This indicates that all of the soil in this zone approaches the failure state. Figure 3.10 shows the reaction force on the wall for all cases. The same trend can be seen for both the passive and the active earth pressure cases. The very rough wall case still results in a higher value of earth pressure than that of the smooth wall case. Case 1 yields the highest earth pressure, followed by Case 2, and then Case 3. The developments of earth pressures in Cases 2 and 3 is different from that in Case 1. In Case 1, the earth pressure tends to increase and then rapidly decrease in the early stages, approaching its peak value after 15-20 cm of wall movements. Cases 2 and 3 result in a slower development of earth pressure on the wall, particularly for Case 3 in which the pressure continues to grow larger even until their late stages of wall movement. This can be understood by looking at a comparison of the distribution of pressure at the wall shown in Figure 3.11.

For Case 1, the soil behind the wall at every depth is subjected to the movement of the wall by the same amount and at the same time from the start of the wall movement. This makes the earth pressure on the entire wall increases and/or decreases uniformly and it approaches its peak value from the early stages of wall movement. As for Case 2, the soil behind the wall near the ground surface will be subjected to smaller movements than the soil in deeper positions. This causes the development of the soil pressure of soil near the ground surface to be slower than that of the soil in deeper positions. The initial

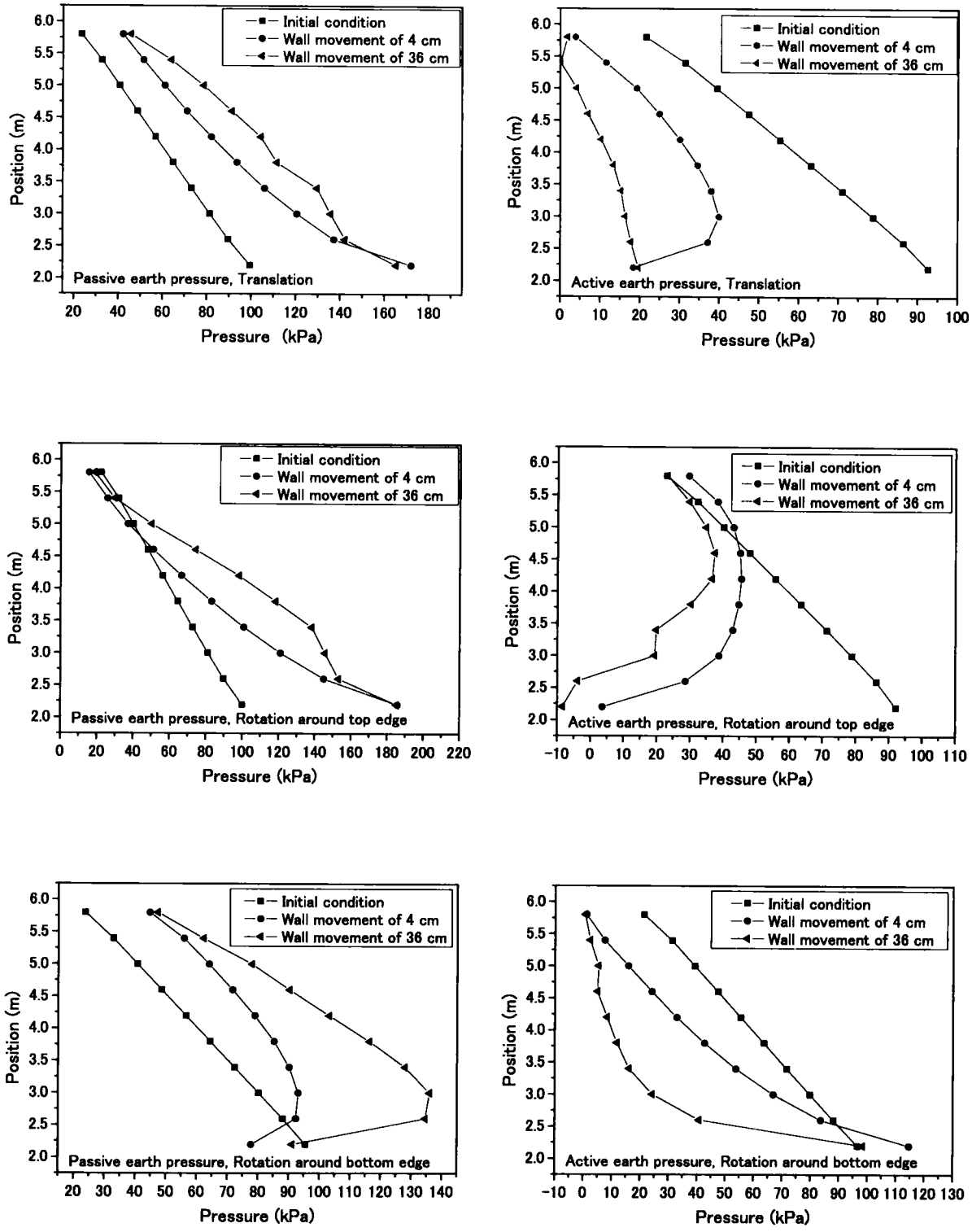

Figure 3.11 Comparison of the distribution of total earth pressure on the wall from soil under different patterns of wall movements in both the passive and the active earth pressure cases

mean effective stress of soil at the deeper positions is larger than that of the soil near the ground, and thus, the soil in deeper positions has a larger peak strength than the soil near the ground. Therefore, a larger part of the total earth pressure on the wall can be developed during the early stages of wall movement from the soil near the lower edge of the wall and results in the fast development of earth pressure, although at a slower rate than in Case 1. In Case 3, the soil behind the wall near the ground surface will be subjected to the larger movements than that of the soil in the deeper positions, and thus, the soil pressure near the ground surface develops faster than that of the soil in deeper positions. Since the soil near the ground surface has a smaller peak strength than that of the soil in deeper positions, only a small part of the total earth pressure behind the wall can be developed during the early stages of wall movement. This makes the development of earth pressure on the wall in this case slower than that in Case 2. As can be seen in the figures, however, when the wall movements become larger, the pressure of the soil in deeper positions is also growing larger. As a results, it can be seen in Figure 3.10 that when the wall is subjected to large movements, more than around 0.4m (see the line of black triangles in the figure, the increasing (passive case) and the decreasing (active case) of the total earth pressure behind the wall approach and/or even start to exceed the value obtained from the case of wall rotation around the top edge.

3.2.3 Summary: Numerical simulation of the lateral earth pressure of normally consolidated soft clay

The effects of various factors on the active and the passive earth pressures are discussed in this section. Numerical simulations of soil under undrained boundary conditions were conducted under plane strain conditions with displacement control. The conclusions obtained from the numerical study are as follows:

The friction between the wall and the soil affects the active and the passive earth pressures in a similar way, that is, a larger friction between the wall and the soil will bring about a larger decrease and/or increase in pressures on the wall from the initial values. In the case of a smooth wall, the shear band behind the wall will appears in a straight line with an angle of around 45° to the horizontal plane. In the case of friction and a very rough wall, the shear band will tends to bend slightly at the starting position on the lower edge of the wall, then it will connect with a straight band which will extend to the ground surface. The negative dilatancy of normally consolidated clay has an effect on the changes in pore water pressure and the strain of the soil behind the wall. The

friction more strongly influences the changes of earth pressure in the case of active earth pressure than in the case of passive earth pressure.

Wall movement patterns have a great effects on the deformations of the soil behind the wall and on the development of earth pressure. The pattern of the wall rotates around the top edge results in a shear zone shaped like a "hook". The pressure of the soil around the deeper parts of the wall will develop first, followed by the pressure from the soil near the ground surface. In the case of wall rotation around the bottom edge, the soil tends to deform in "zone" rather than in the shear bands. The pressure from the soil near the ground surface will develop before the pressure from soil in the deeper positions. The rate of development of earth pressure on the wall in the translation movement pattern case is the fastest, followed by that from the rotation around the top edge case, and then the rotation around the bottom edge case, respectively.

3.3 Large Deformation Analysis of an Excavation through a Thick Soft Clay Deposit

Modern techniques of excavation combined with an abundance of measured data and construction experience provide effective methods for minimizing deformations in the surrounding soil. However, it is difficult to fully control the ground movements brought about by excavations in which the toe of the wall is embedded in soft clay. This situation can occur when the site is covered with very thick soft clays and it is difficult to practically install the retaining structures into a firm soil stratum. Tanaka et al. (1989) reported a case study of a large-scale brace excavation performed through a thick soft clay deposit. The depth of the excavation was about 11 m, which is not all that large in terms of construction techniques in these moderns times. However, the thickness of the soft clay in the area is over 50 m, and thus, the sheet piles were supported by a soft clay stratum. As the excavation approached the final stage, large displacements of the sheet piles and a significant heave at the excavation surface were observed. Large displacements even at the toes of the sheet piles were reported and the sheet piles continued to deform with time due to the undrained creep of the soil. This led to the complexity of the mechanism of the soil-pile interaction under the excavation level when the excavation was performed through the thick soft clay deposit. In addition, it was pointed out how important it is to consider the rate sensitivity of clay in the analysis of this problem.

In this section, the mechanism of the soil-structure interaction of the braced excavation system performed through thick soft clay deposit will be studied by a numerical simulation. The elasto-viscoplastic constitutive soil model with structural changes, mentioned in the previous chapter, is used with the finite element formulation introduced in Chapter 2. First, the case study is reviewed, and then an outline of the analysis is shown. Next, the numerically simulated results of excavation cases are presented in order to discuss the mechanism of the soil-structure interaction during the excavation.

3.3.1 Review of a Case Study

3.3.1.1 Geometry of the excavation

A case study of a large-scale braced excavation performed through a thick soft clay deposit was been reported by Tanaka et al. (1989). As a part of the construction of the Tokyo International (Haneda) Airport Extension Project (Phase I), a large-scale braced excavation (35 m in width, 11 m in depth, and 560 m in length) was carried out to construct

an access road. The soil conditions at the construction site are shown in Figure 3.12, in which;

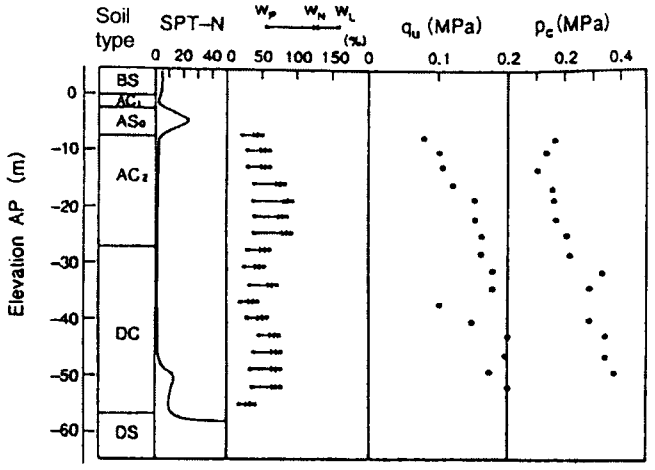

Figure 3.12 Soil conditions at the construction site (Tanaka et al. 1989)

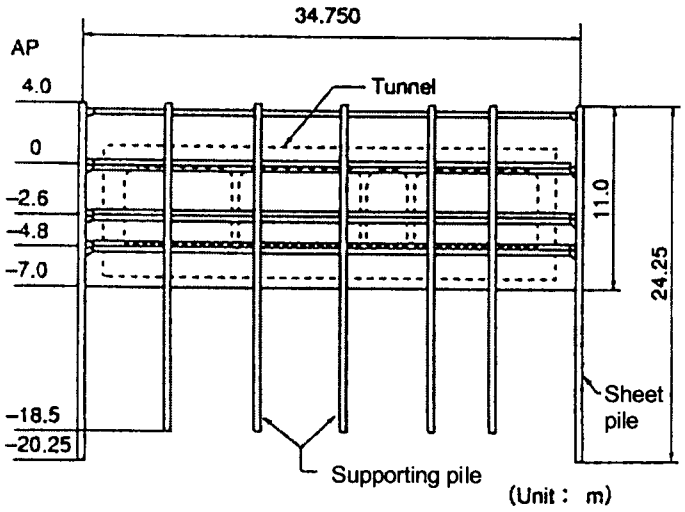

Figure 3.13 Typical cross section showing the bracing method (Tanaka et al. 1989)

- BS: stratum composed of reclaimed construction waste soils
- AC_1: stratum composed of reclaimed waste water slag
- AS: alluvial sand stratum
- AC_2: alluvial soft clay stratum
- DC: diluvial soft clay stratum
- DS: diluvial firm stratum

A bracing layout was designed based on the conventional design method. A typical cross section is shown in Figure 3.13. The sheet piles were driven to a depth of approximately 25 m. However, the site is covered by thick soft clay down to a depth of 50 m and the sheet piles did not reach a firm stratum. Four sets of braces were installed at a pitch of 5 m along the length of the road.

3.3.1.2 Observed behavior

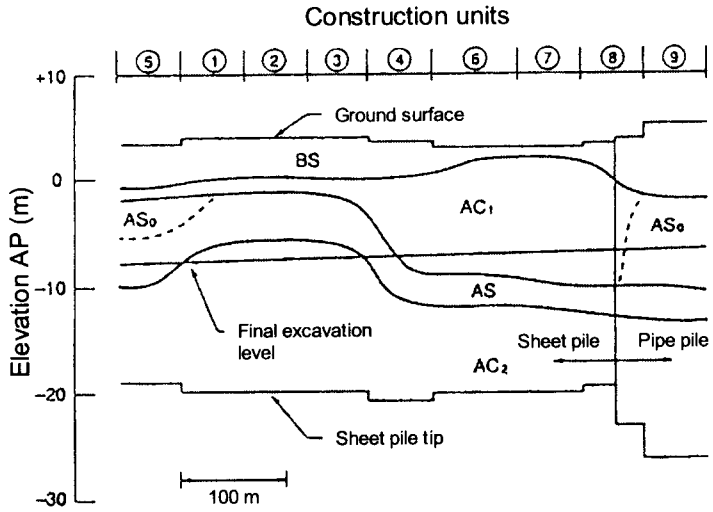

Figure 3.14 Soil profiles in the longitudinal section and layout of the construction section (Tanaka et al. 1989)

As shown in Figure 3.14, the project was divided into nine construction sections or units, the length of each unit being 60m. The alluvial sand (AS) stratum was removed during the 4^{th} stage of the excavation during the construction of Units 1 to 3.

In the construction of Units 1 to 3, large lateral displacements of the retaining walls and a significant heave of the supporting piles were observed. The progress of the lateral displacement of the sheet pile wall measured during the construction of Unit 3 is shown in Figure 3.15. The shaded portion of Figure 3.15 approximately corresponds to the undrained creep displacement. The maximum horizontal displacement was 300mm, and a considerable amount of the displacements was measured even at the bottom tips of the sheet piles. Figure 3.16 shows the heave of the supporting piles measured at the pile heads in the construction of Unit 1. This shows out the complexity of the mechanism of the soil-pile interactions under the excavation level and also points out the importance of using the elasto-viscoplastic soil model to simulate the nonlinear and the rate-sensitive behavior of clay. It should be noted that, with the large ground deformations described above, the excavation was stopped and the remedial measures were taken, and the deformations of the sheet pile walls ceased.

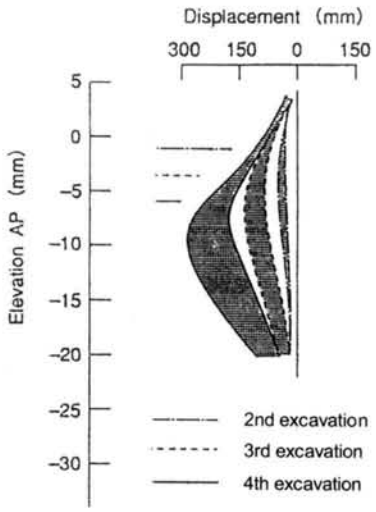

Figure 3.15 Measured horizontal displacement of the sheet pile wall for Unit 3 (Tanaka et al. 1989)

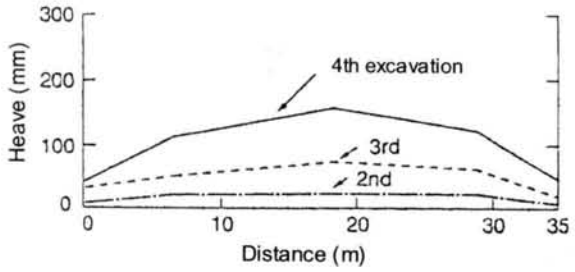

Figure 3.16 Measured heave of the supporting piles (Tanaka et al. 1989)

3.3.2 Outline of the Numerical Analysis

3.3.2.1 Initial ground conditions and the soil parameters

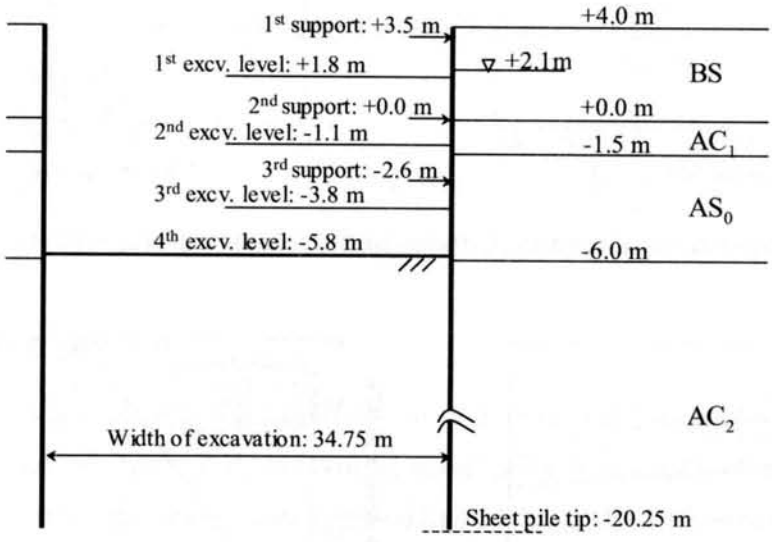

Figure 3.17 Cross section of construction Units 1 to 3

The soil conditions and the geometry of the excavation site for Units 1 to 3, where large displacements of the sheet pile wall were observed, are shown in Figure 3.17. The engineering properties of the soil at the site are listed in Table 3.3 (Sekiguchi and Oka 1997).

Table 3.3 Material properties of the soils

Soil	SPT-N	γ_t (kN/m^3)	υ	$q_u/2$ (kPa)	ϕ'(degree)	K_0
BS	2-10	18	0.375	-	30.0	0.50
AC_1	-	16	0.475	2.0-5.0	0.0	0.90
AS	5-20	19	0.375	-	40.0	0.75
AC_2	0-4	16	0.475	40-80	0.0	0.90
DC	2-4	16	0.475	50-100	0.0	0.90
DS	>50	20	0.375	-	45.0	0.80

Note: υ represents Poisson's ratio and ϕ' represents the angle of internal friction

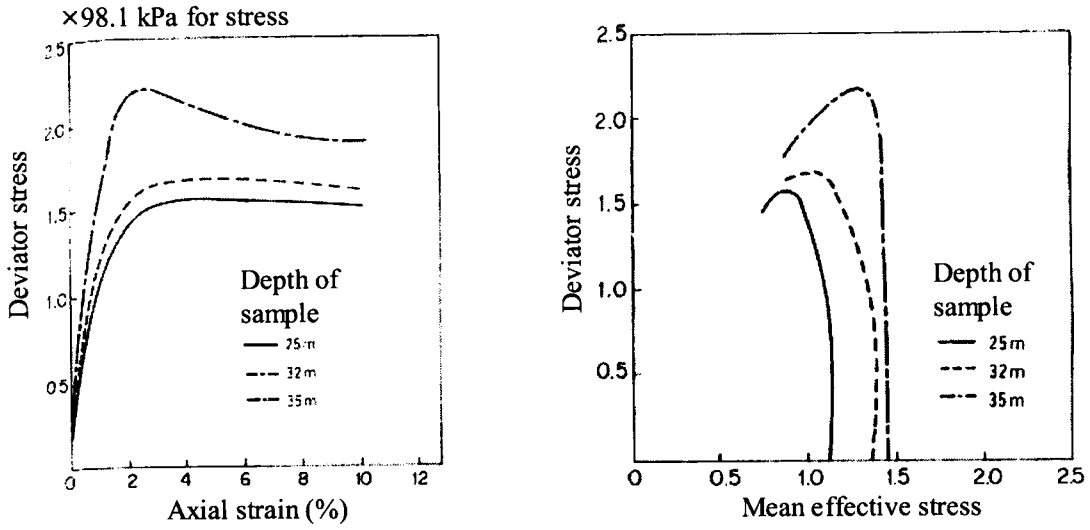

Figure 3.18 Experimental results of undrained triaxial compression tests (Tsuchida 1990)

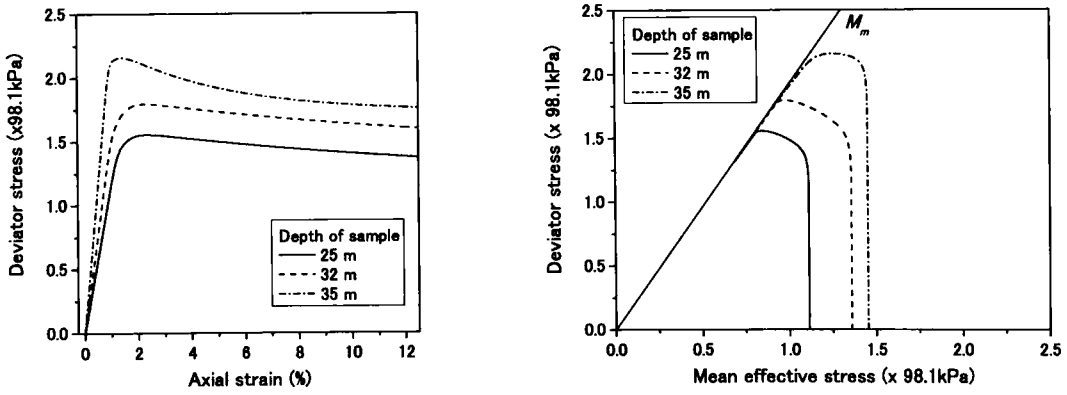

Figure 3.19 Simulation results of undrained triaxial compression tests

Tsuchida (1990) carried out the undrained triaxial tests on soil samples taken from the AC_2 layer at the construction site of the same construction project. The test results are shown in Figure 3.18. Since the consolidation tests have not been performed on the samples from the site, the material parameters λ and κ are calculated from the consolidation test results of the soil samples from the Yokohama Bay area (Tsuchida 1990) instead. Viscoplastic parameter m' was determined from the one-dimensional long-term consolidation test results presented in the same paper. Note that in the paper, the secondary compression index C_α is reported to be 0.033. The calculated value of m' is 20.45, which falls in the range of values for organic clays and silts recommended by Leroueil and Hight (2003) and Mesri et al. (1995). Then, the viscoplastic parameter C_0, structural parameter σ'_{maf}, α, and β are determined by the curve fitting. A comparison between the simulation results and the experiment results is shown in Figures 3.18 and 3.19. The comparison indicates that the constitutive model adopted in this study can effectively reproduce the behavior of the soil during shearing.

As for the soil in stratums AC_1, BS, and AS stratum, there is no experiment data available. Therefore, the typical parameters for soft clay and loose sand are adopted for these materials. The following empirical relationships are used with the c_u and the N values presented in Table 3.3 to estimate the Young's modulus of the soils in these stratums. Equation (3.1) (Takenaka 1962) is used for the clay material and Equation (3.2) (Uto 1967) is used for the sand material. The soil parameters used in the calculations are summarized in Table 3.4.

$$E = 210c_u \tag{3.1}$$

$$E = 2800N(kPa) \tag{3.2}$$

3.3.2.2 Bracing method

The bracing methods was designed based on the conventional design method. The retaining wall was formed by driving V_L-type steel sheet piles to a depth of approximately 25 m, therefore, the tips of the sheet piles were embedded into the AC_2 stratum. Four sets of braces were installed at a pitch of 5m along the length of the excavation. Supporting piles were installed transversely to prevent the braces from buckling. The material properties of the structural elements, including the sheet piles and braces, are summarized in Table 3.5. The joint efficiency factor of the sheet piles is assumed to be 40%, based on Tanaka et al. (1989), while the efficiency factor of the braces was set at 0.1.

Table 3.4 Soil parameters

Parameters for the elasto-viscoplastic model for clay materials

Parameters	AC_1	AC_2
Coefficient of permeability k_0 (m/s)	1.54×10^{-8}	1.54×10^{-8}
Compression index λ	0.172	0.3257
Swelling index κ	0.054	0.03257
Initial void ratio e_0	2.50	1.994
Coefficient of earth pressure K_0	0.90	0.90
OCR	1.0	1.25
Stress ratio at maximum compression M_m^*	1.05	1.5567
Viscoplastic parameter m'	20.0	20.45
Viscoplastic parameter C_0 (1/s)	9.3×10^{-10}	9.3×10^{-10}
Structural parameter σ'_{maf} (kPa)	$1.0 \times \sigma'_{mi}$	$0.8 \times \sigma'_{mi}$
Structural parameter β	0.0	15.0

Note: σ'_{mi} represents initial mean effective stress

Parameters for the elasto-plastic model for granular materials

Parameters	BS	AS
Coefficient of permeability k_0 (m/s)	8.0×10^{-7}	8.0×10^{-7}
Compression index λ	0.03	0.03
Swelling index κ	0.002	0.002
Initial void ratio e_0	0.90	0.90
Coefficient of earth pressure K_0	0.50	0.75
Stress ratio at maximum compression M_m^*	0.909	0.909
Stress ratio at of failure state M_f^*	1.336	1.336
Control parameter of anisotropy C_d	2000	2000
Hardening parameter B_0^*	2000	2000
Hardening parameter B_1^*	400	400
Parameter of dilatancy D_0	1.0	1.0
Parameter of dilatancy n	2.0	2.0

Table 3.5 Material properties of the supporting structures

Supporting structures	Nominal name	Axial Stiffness EA ($\times 10^5$ kN/m)	Bending Stiffness EI ($\times 10^5$ kNm^2/m)
Sheet pile	V_L Type	56.2	1.32
1^{st} Brace	1-H350×350	7.30	0.00
2^{nd} Brace	1-H350×350	14.60	0.00
3^{rd} Brace	1-H400×400	18.36	0.00
4^{th} Brace	1-H400×400	18.36	0.00

3.3.2.3 Simulation of the excavation

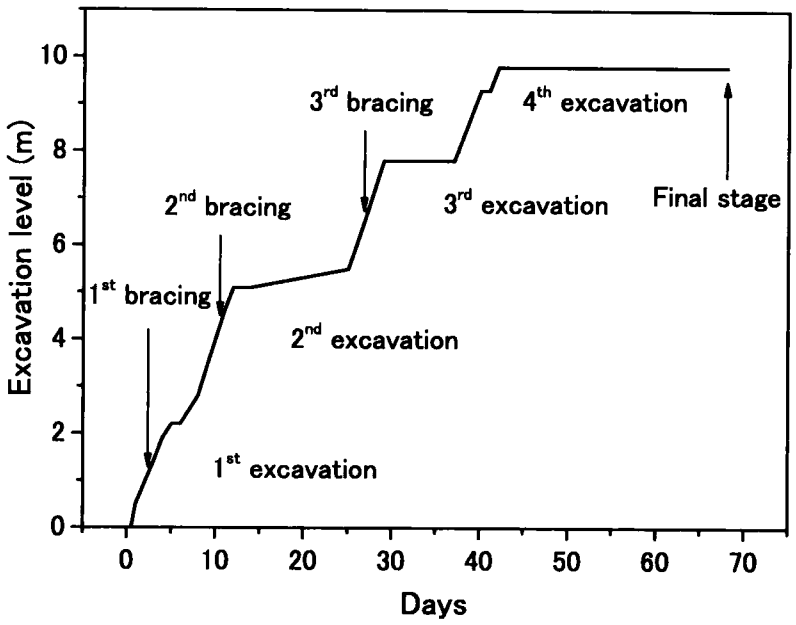

Figure 3.20 Progress of the excavation used in the analysis

The excavation sequence is shown in Figure 3.20. The braces are installed and the preloads are performed after the excavation is performed to the determined level. The preloads were originally designed as 80, 160, and 240 kN/m for the 1^{st}, 2^{nd}, and 3^{rd} bracings respectively, and these preloads are also employed in the present study. After the 4^{th} level of excavation is finished, the simulations are then performed for 26 days. The time point is referred to as the final stage of the simulations in the followings.

3.3.3 Results of the Analyses

3.3.3.1 Ground deformations and the displacements of the wall

Figure 3.21 shows the computed horizontal displacements of the sheet pile wall with the progress of the excavation. Figure 3.22 shows the development of the maximum wall lateral deflection with time.

It can be seen that, the analysis gives a minus lateral displacement of the sheet piles near the ground surface. This kind of behavior is not obtained in the measurement results and is caused by the preload being applied to the supporting struts. The effects of the preload on the deformation of the ground and the displacement of the wall will be discussed later in this chapter. The positions of the maximum lateral wall displacements are found to be located beneath the excavation level. The figure also shows the large displacements of the toe of the wall with the progress of the excavation. The position of the maximum lateral displacement is located below the excavation surface. After the 4^{th} stage of the excavation, the displacement of the wall, in particular beneath the lowest supporting struts to the toe of the wall, still continues to grow larger with time, while the further movement of the wall above the lowest supporting level is relatively small. The rate of the wall displacement after the end of the excavation remains almost constant at 2.7 mm/day (7.13 cm/26 days). This result is comparable to the measured results (2.8-4.0 mm/day) from the construction of Unit 3 which was reported in the literature (Tanaka et al. 1989). This indicates that the analysis method and the constitutive model used in this study can effectively simulate the rate-dependent behavior of the clay ground in the problem, which can not be studied with a typical elasto-plastic soil constitutive model (Sekiguchi and Oka 1997).

During the final stage of the excavation, the calculated maximum lateral displacement of the sheet piles is 24.5 cm with a maximum heaving of 35.0 cm. The calculated maximum backfill settlement is 11.8 cm located at a distance around 19 m behind the wall. The heaving at the end of the 4^{th} stage of the calculated excavation (26 cm) is considerably larger than that in the measured results (17 cm).

Compared to the lateral displacement of the sheet pile wall measured in the construction of Unit 3, which is shown in Figure 3.15, it is seen that the predicted maximum lateral deflection of the sheet pile wall (24.5 cm) at the final stage is lower than the measured value (30 cm). The predicted position of the maximum lateral displacement is lower than that of the measured results while the lateral displacement of the sheet pile tips is higher. However, it may be seen that generally, the agreements between the calculated and the measured results are generally fair to good. Moreover, the analysis can well simulate the

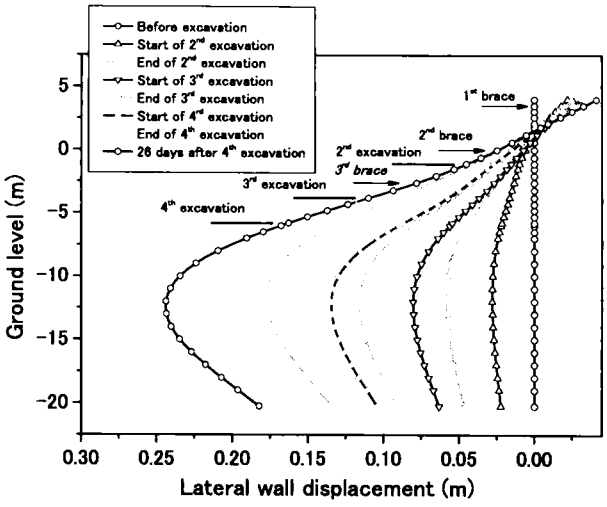

Figure 3.21 Development of lateral wall displacements with the progress of the excavation

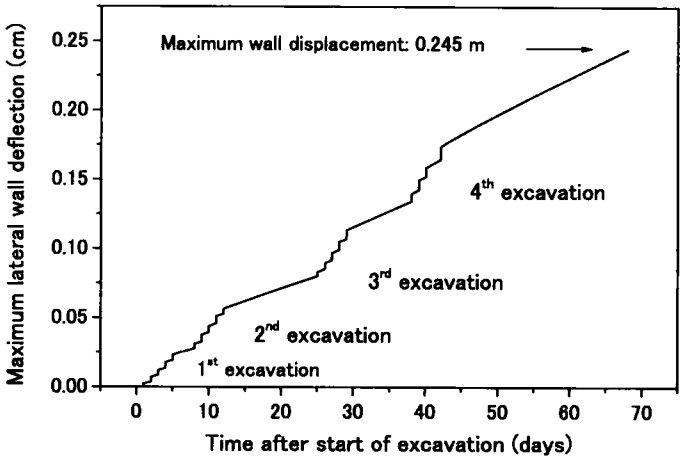

Figure 3.22 Development of the maximum lateral wall deflection with time

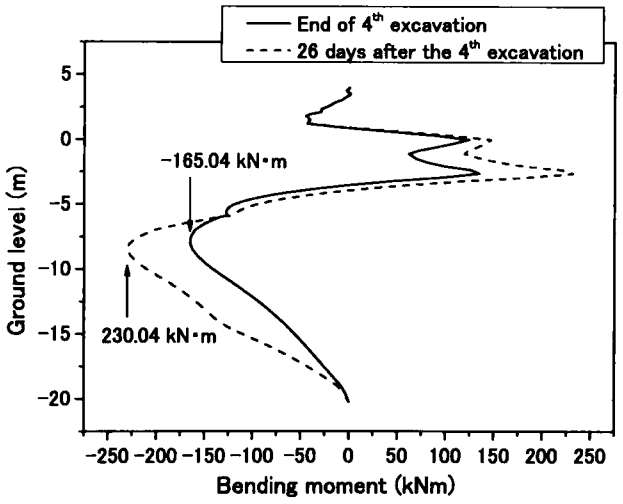

Figure 3.23 Bending moments of the sheet piles

displacement of the sheet piles due to the viscoplastic property of the soil after the 4^{th} stage of the excavation, as described previously.

Figure 3.23 shows the calculated bending moments of the sheet piles. From the maximum bending moment at the final stage of the simulation (230.04 kNm), the maximum stress in the section is calculated to be 162 MN/m^2. Note that the section modulus used in the calculation of the maximum stress is the value of the 420×175×22 U-type sheet pile, which has lower moment of inertia (I_0=55,200 cm^4) than that of the section used in the case study (I_0=66,000 cm^4). Hence, the results are given on the safe side. The obtained maximum stress is only a little lower than the allowable stress of the ASTM A328 steel (170 MN/m^2). This agrees with the fact that there was no report of a failure of the sheet piles in the case study. However, the measurement gives a higher wall deflection than the analysis results, and therefore, the sheet piles are considered to be at risk of yielding due to the deformation.

3.3.3.2 Earth pressure on the sheet pile walls

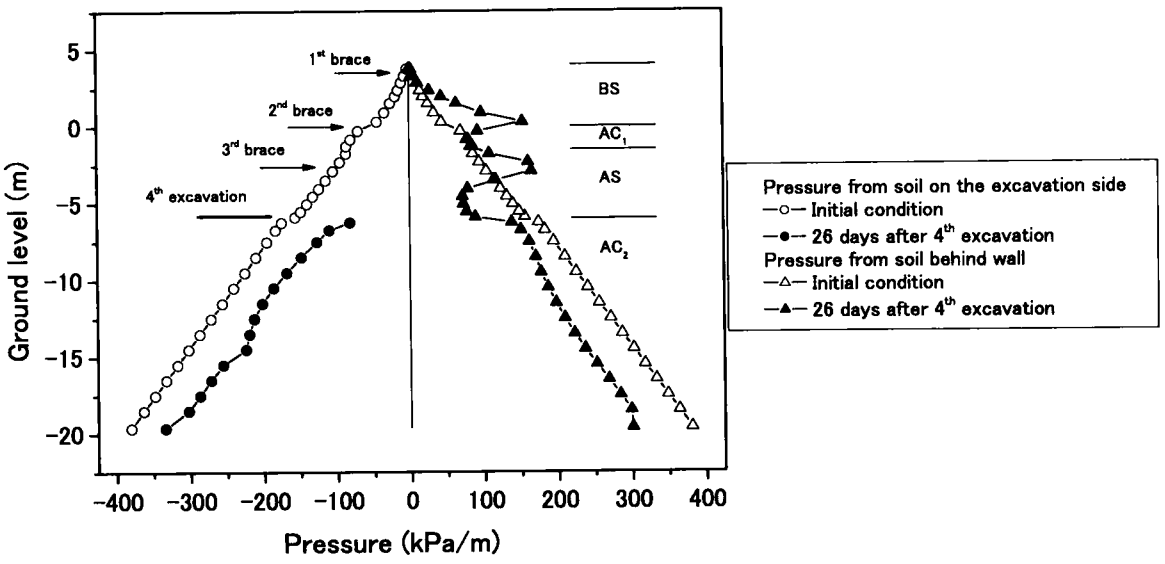

Figure 3.24 Development of the total lateral earth pressure on the sheet pile wall with the progress of the excavation

Figure 3.24 shows the distribution of earth pressures on the sheet pile wall with the progress of the excavation. The earth pressures of the soil behind the wall above the excavation level becomes larger than the initial value at the final stage. The increasing of earth pressure is caused by the reaction forces acting on the wall from the supporting struts and the preload applied when the wall tends to deform further to the excavation side. Let us now consider the earth pressures on both sides of the wall below the excavation level. The simulation results show that the earth pressure values on both sides of the wall

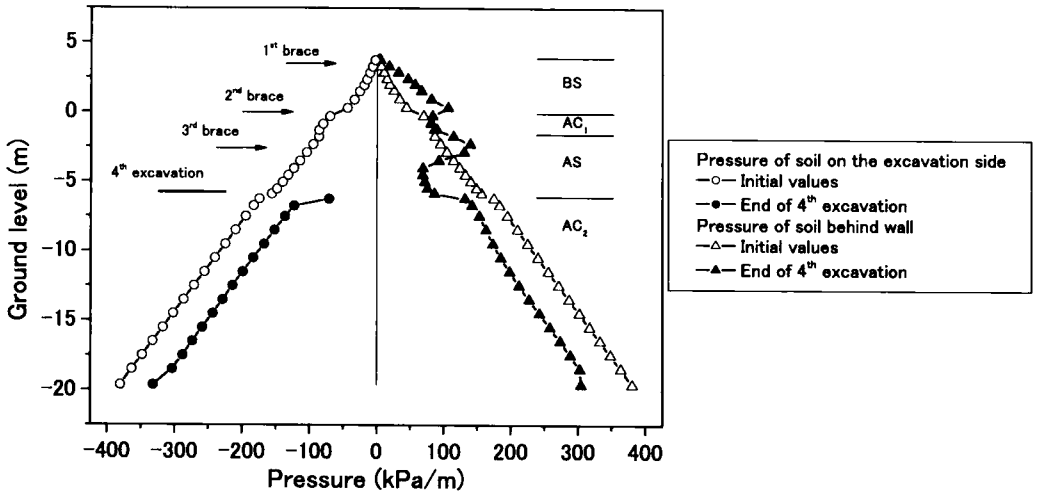

Figure 3.25 Calculated lateral earth pressure values on the wall after the 4th excavation

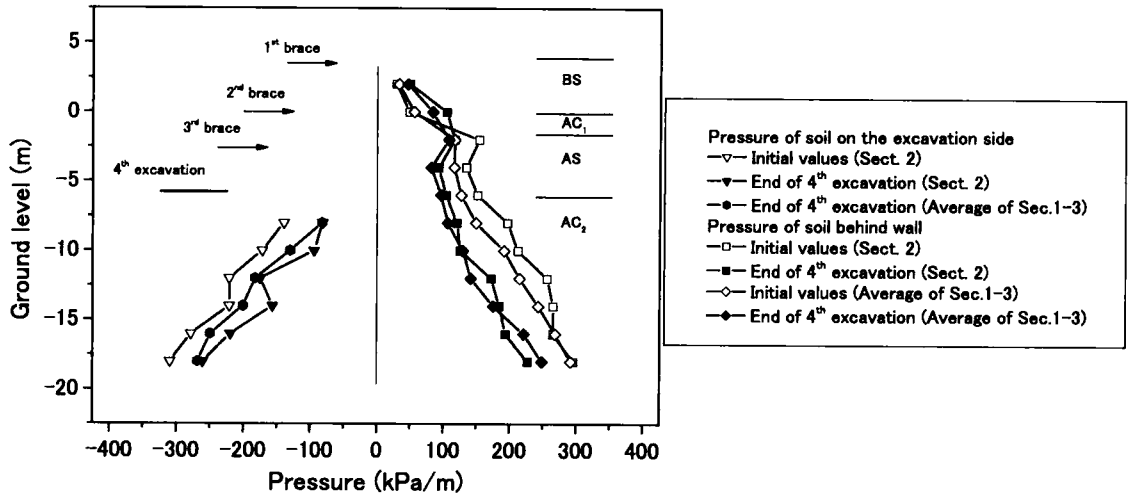

Figure 3.26 Measured lateral earth pressure values on the wall after the 4th excavation

have decreased from the initial value. In order to compare the analysis results to the measurement values, the calculated earth pressures values before the excavation and after the 4^{th} stage of the excavation are plotted in Figure 3.25. The earth pressures measured during the construction of Unit 2 and the average values from Units 1 to 3 (Tanaka et al. 1989), before the excavation and after the 4^{th} stage of the excavation, are plotted in Figure 3.26. The comparison shows an agreement between the decreasing calculated earth pressures and the measured earth pressure on the excavation side. However, the analysis tends to show a smaller decrease in earth pressure behind the wall than the measured values. The decreasing earth pressures values on the excavation side can be understood by considering the components of earth pressures separately as the effective stress of soil and the pore water pressures.

Figures 3.27 and 3.28 show the evolution of the pore water pressure values and the effective stresse levels on the wall, respectively. It can be seen that the pore water pressure of the soil on the excavation side under the excavated level decreases from the initial conditions by a considerable amount, while the pore water pressure of the soil behind the wall changes only in small values. This is due to the loss of stress acting on the excavation surface. Let us consider the effective stress on the wall. It can be seen that on the soil behind the wall, the effective stresses levels of the soil decreases from the initial values, following the active movements of the wall. Consequently, the effective stress levels of soil on the passive side (soil on the excavation side) increase due to the passive wall movement. On the passive side, since the decrease in pore water pressures is larger than the increase in effective stress, the total earth pressures become smaller with the progress of the excavation.

3.3.3.3 Stress and strain in soil

Let us consider the stress state of the soil below the excavation level of the ground on both sides of the wall. Figures 3.29 and 3.30 show the changes in the effective stress levels in x (horizontal) and y (vertical) directions. The positions of the soil elements in the finite element mesh are also indicated in the figure. Horizontal effective stress (σ'_{xx}), of the soil immediately behind the wall, decreases with the progress of the excavation. The stress path of the Element 1407 exhibits a similar pattern, but with less of a change in the effective stress. This is because the elements are farther away from the sheet pile wall, and therefore, are subjected to fewer effects of the excavation. As for the stress levels of the soil in front of the wall, due to the excavation, the vertical effective stress levels of the soil at all the positions decrease due to a reduction in the stress of the excavated soil. However, the soil adjacent to the wall shows fewer reductions in vertical effective stress (σ'_{yy}) due to the effects of friction between the wall and the soil. For the horizontal effective stress, the soil adjacent to the wall is subjected to the compression by the passive wall movement, and thus, results in the increase in the horizontal stress levels in the soil. The soil at the more distant positions from the wall shows no sign of an increasing of horizontal effective stress. This indicates that the influence of the passive wall movement is to be concentrated on the small volume of soil adjacent to the wall. Nevertheless, the increase in the horizontal effective stress of the soil on the excavation side is small compared to the decrease in vertical effective stress. This fact points out that the soil on the excavation side is sheared and deformed mainly by the decrease in load brought about by the excavation rather than by the pressure from the passive wall movement.

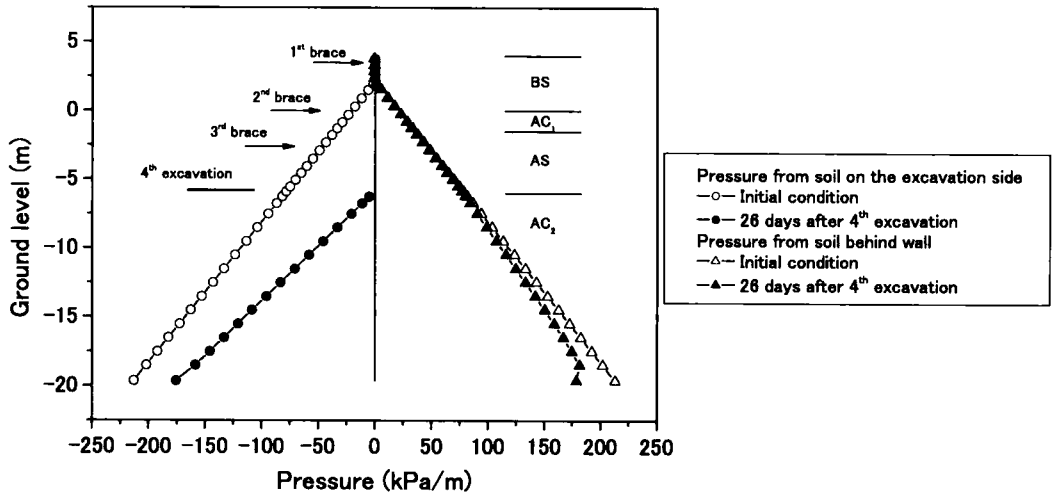

Figure 3.27 Development of the pore water pressure values on the wall with the progress of the excavation

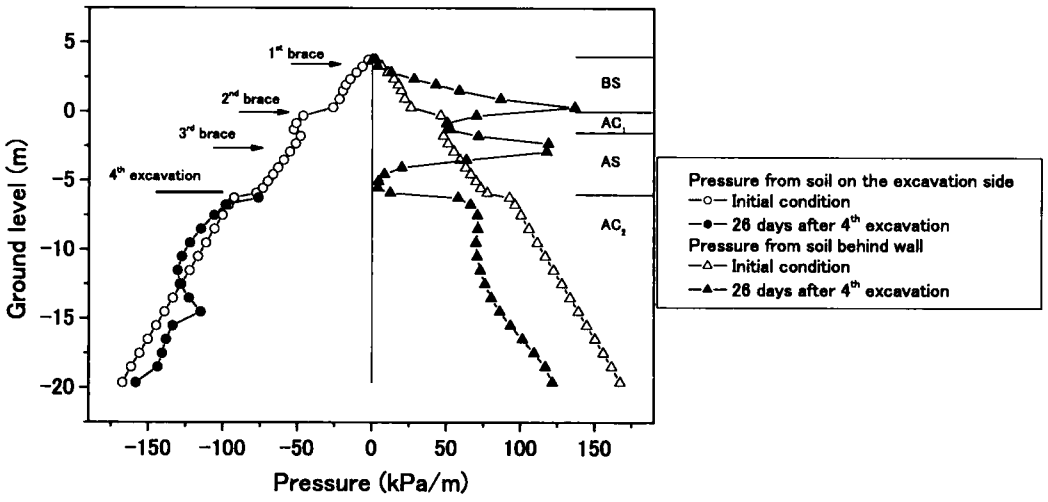

Figure 3.28 Development of the effective lateral earth pressure levels on the wall with the progress of the excavation

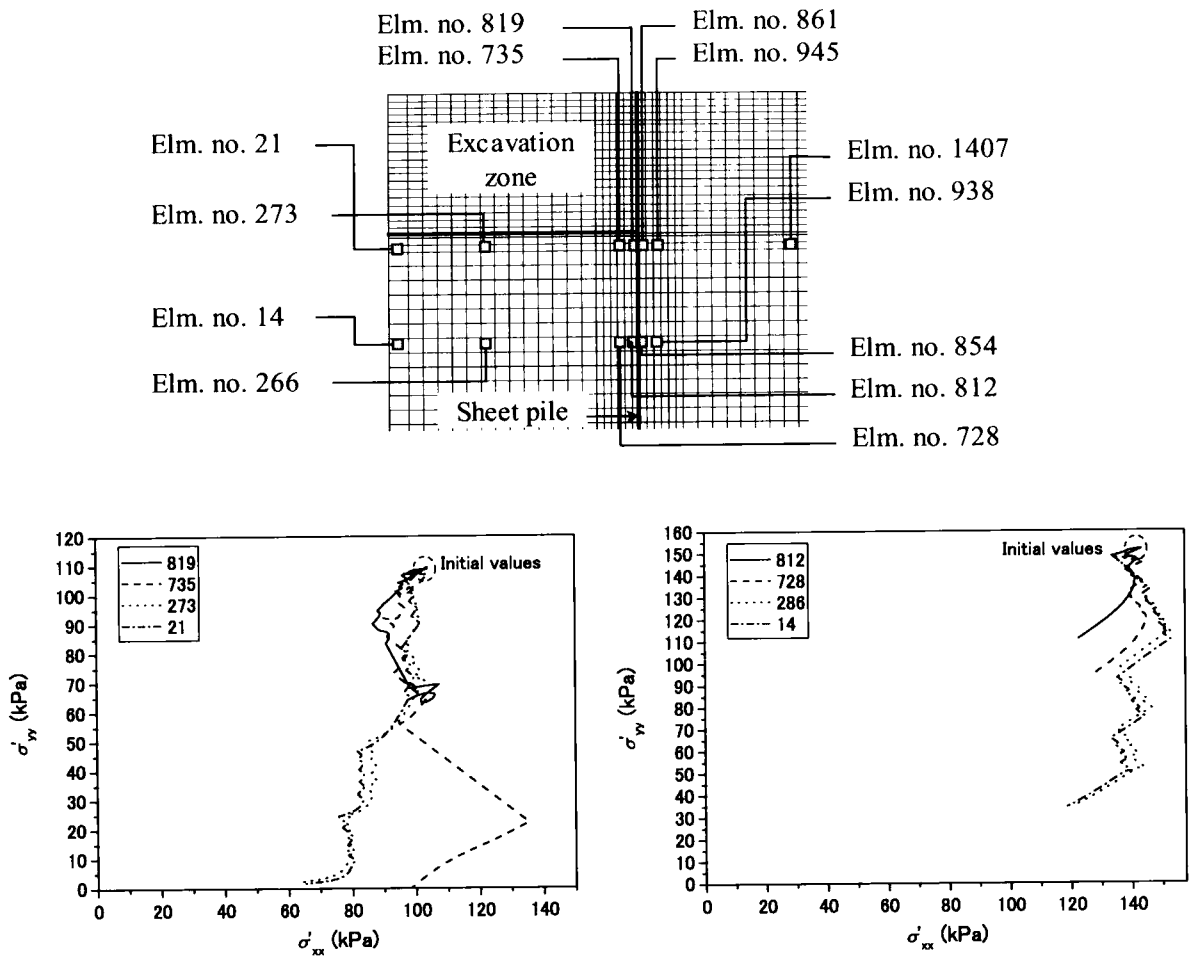

Figure 3.29 Changes in the vertical and the horizontal effective stress levels of the soil in front of the wall

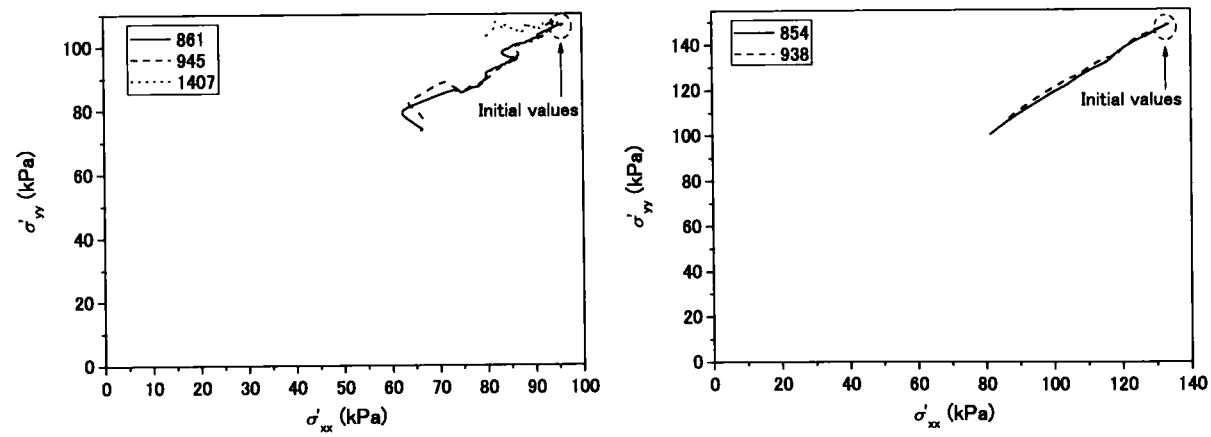

Figure 3.30 Changes in the vertical and the horizontal effective stress levels of the soil behind the wall

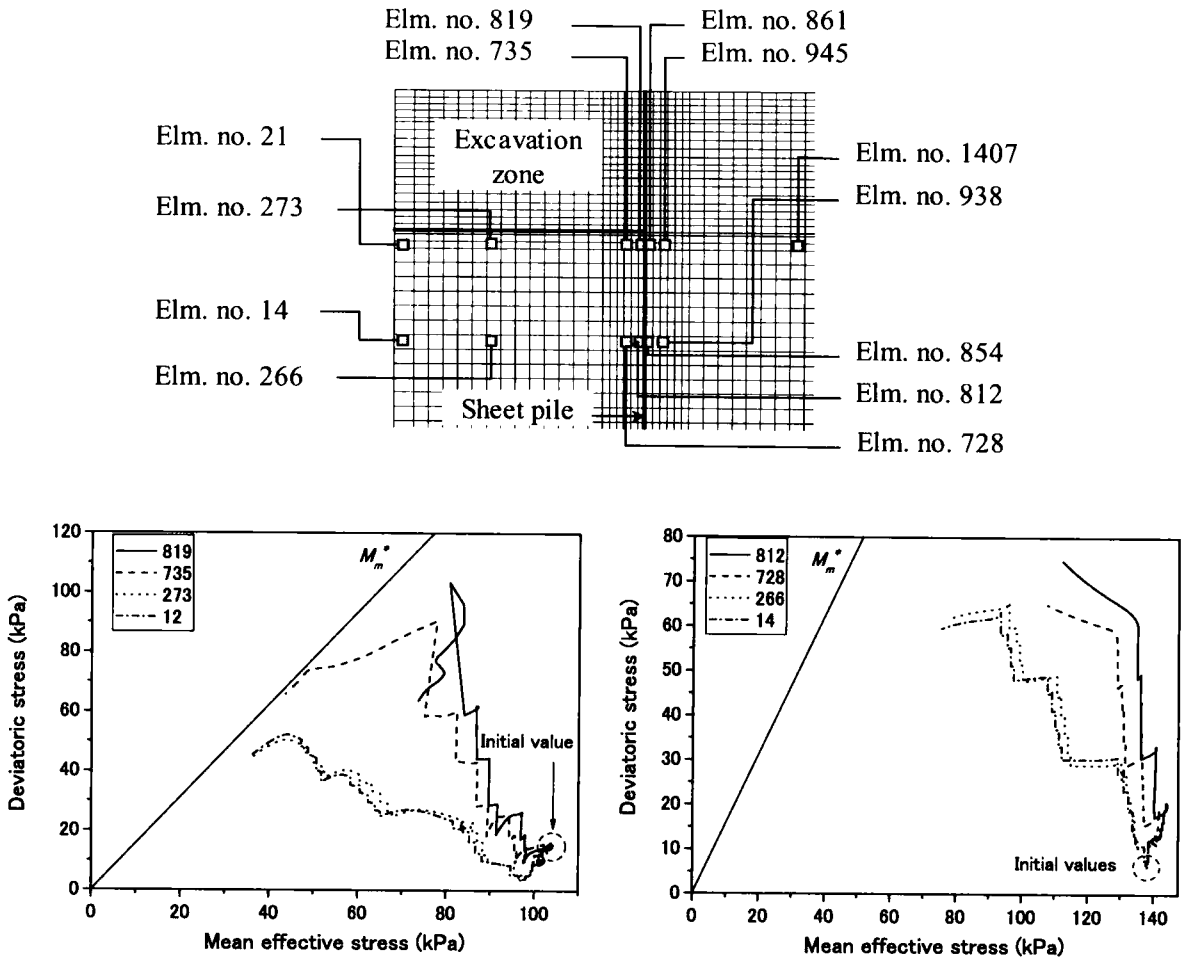

Figure 3.31 Stress paths of the soil in front of the wall

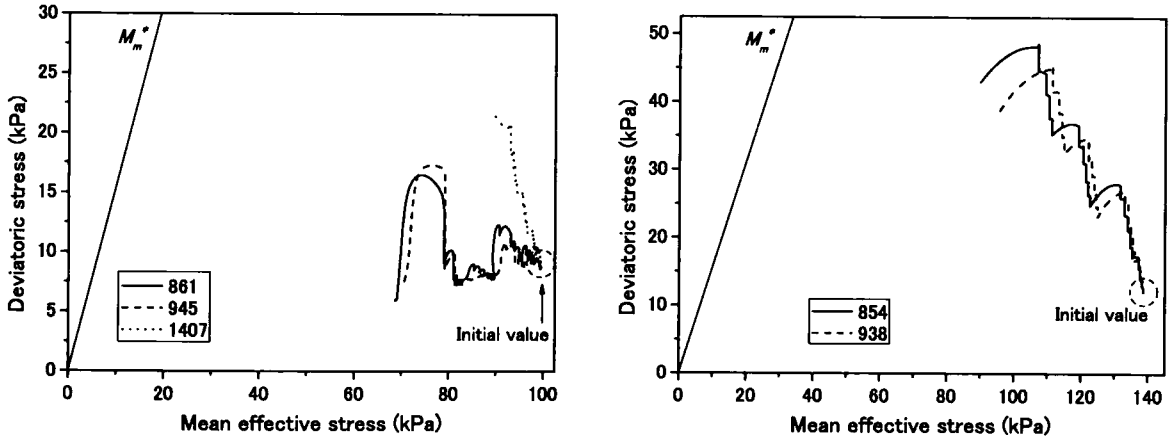

Figure 3.32 Stress paths of the soil behind the wall

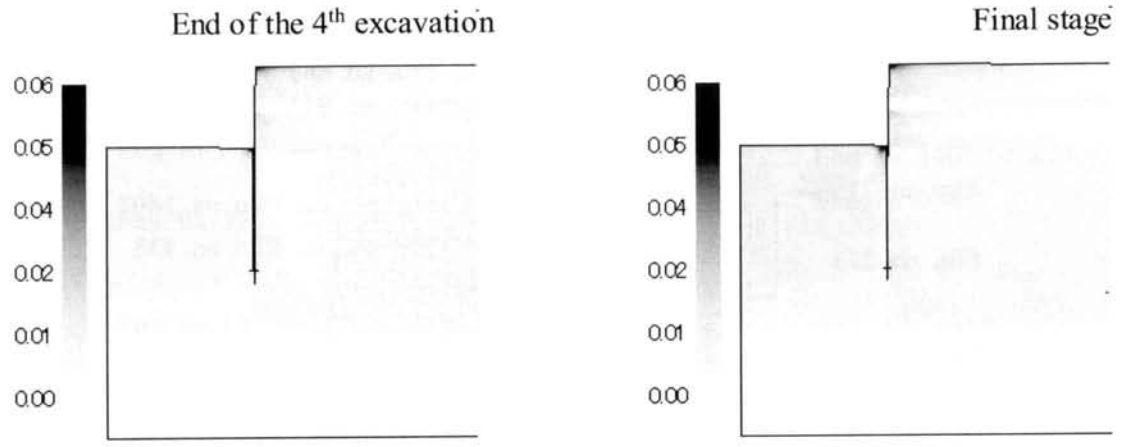

Figure 3.33 Contours of the accumulated viscoplastic shear strain

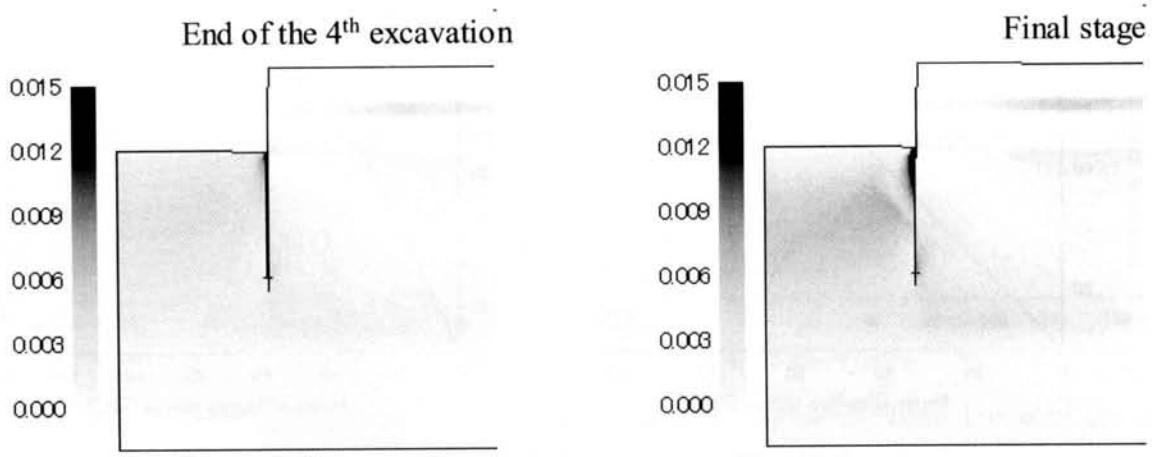

Figure 3.34 Contours of the viscoplastic volumetric strain

Figures 3.31 and 3.32 present the stress paths of the soil in the $\sigma'_m - \sqrt{S_{ij}S_{ij}}$ space. It can be seen that, the stress states of the soil on the excavation side approach the critical state line, especially for the soil that is located near the excavation surface. The stress paths of the Elements 21 and 14 show small changes in stresses since they are located far from the wall. Hence, they are subjected to small changes in horizontal stress from the wall movement.

The stress states of the soil behind the wall show rather small changes in the stress ratio compared to the soil on the excavation side. Accordingly, the displacement of the wall is thought to be mainly caused by the deformation and the heaving of the soil on the excavation side.

Figures 3.33 and 3.34 present the accumulated viscoplastic shear strain $\gamma^p \equiv \int \sqrt{de_{ij}^{vp} de_{ij}^{vp}}$ and the viscoplastic volumetric strain of the soil at the end of the 4^{th} stage of the excava-

tion and at the final stage. It can be seen that a large increase in the viscoplastic strain extends from the excavation surface to the level near the toe of the wall on the excavation side. A large value for the viscoplastic strain can also be observed in the soil behind the wall near the toe of the wall, which is brought about by the large movement of the toe of the wall. The comparison also shows the increments in viscoplastic strain after the end of the 4^{th} stage of the excavation until the final stage. This indicates that the viscoplstic flow can be considered as one of the source that causes the further displacements of the wall after the end of the excavation.

3.3.4 Effects of the Preload and the Positions of the Supporting Struts

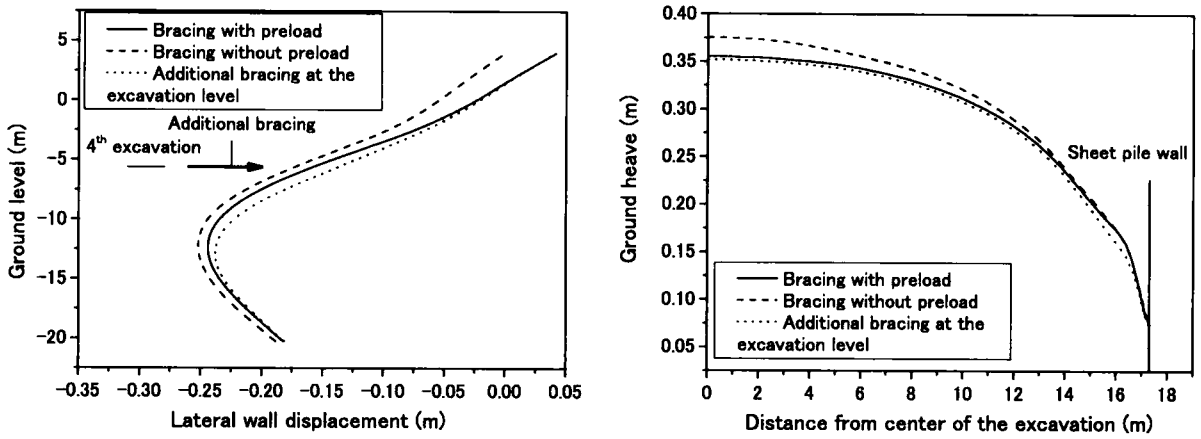

Figure 3.35 Lateral wall displacements and the base heaves of various struts and the preload arrangement at the final stage

In this section, the effects of the positions of the supporting struts, as well as the preload, on the performance of the excavation systems are studied. Two additional analysis cases have been performed. In the first case, the positions of the supporting struts are similar to those in the original case, but no preload is applied. In the second case, the positions of the supporting struts and the preloads applied are similar to those in the original case, but a strut is added at the excavation level which may not be applicable in the real construction projects. The preload applied to this additional strut is 100kN/m.

Figure 3.35 shows the simulation results of the lateral wall displacements and the base heave at the final stage of the simulation. It can be seen that, when the preload is not applied, the wall near the ground surface bends out from the initial position and agrees more with the measurement results. This points out that the actually preload forces

working in the bracings may be less than the design values. The results also indicate that the preload can effectively reduce the displacement of the wall above the excavation level. However, it does not seems to be effectively reducing the heaving and the displacement of the wall under the excavation level. As for the second case, it is shown that adding a strut at the excavation level can further reduces the wall displacement, but has a very small effect on the base heave. These results emphasize the fact that when the excavation is performed through the ground with low-base stability and large heaving, the preload and the arrangement of the strut positions can only help to reduce the ground deformation and the wall displacement above the excavation level. However, other measures must be taken to reduce the ground deformation below the excavation level.

3.3.5 Remedial Measures

As mentioned before, the 4^{th} stage of the excavation had been halted after the large ground deformation was observed. The following remedial measures were taken as:

1. Remove the soils from the behind of the sheet pile wall.
2. Lower the ground water level by the deep well method.

As a result, the deformation of the ground and the displacement of the wall ceased, and the excavation was continued. Therefore, these methods are proven to be effective measures for the large displacement of the sheet piles in the problem being addressed.

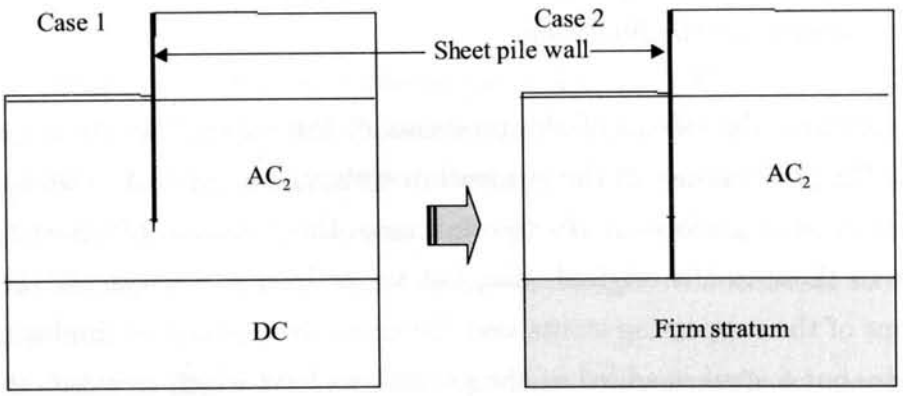

Figure 3.36 Geometry of the extended wall and the firm stratum

Three additional analyses have been performed to study the other possibility of preventing the problem from occurring. In the previous section, the sheet pile wall was installed approximately 25m deep into the ground, and the tips of the sheet piles are

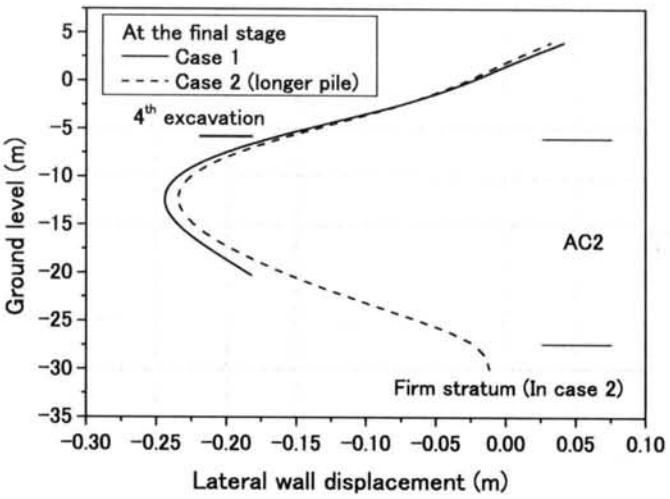

Figure 3.37 Comparison of the sheet pile wall displacements in Cases 1 and 2

embedded in the AC_2 stratum. This analysis will be referred to as "Case 1". The first additional analysis performed in this section assumes that the length of the sheet piles is therefore extended from 25m in Case 1 to 34m and that they are embedded into a firm stratum located at a depth of 31.4m under the ground surface. This change is illustrated in Figure 3.36. This analysis will be referred to as "Case 2".

The comparison between the lateral displacements at the final stages of Case 1 and Case 2 are shown in Figure 3.37. From this figure, no significant difference is observed between the displacements of the sheet piles in these cases. These results indicate that it does not help to only install the sheet piles into the firm stratum lying below the soft clay stratum to reduce the ground deformation if the corresponding firm stratum is located too deep into the ground.

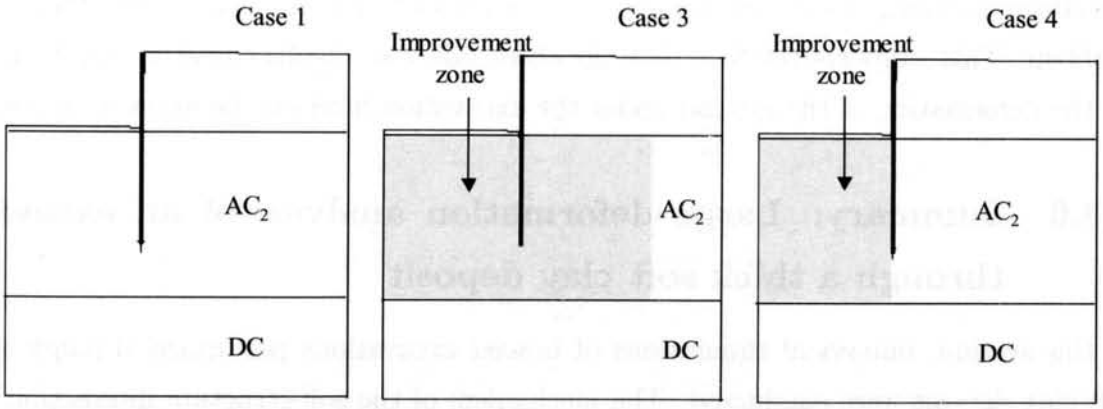

Figure 3.38 Ground improvements in Cases 3 and 4

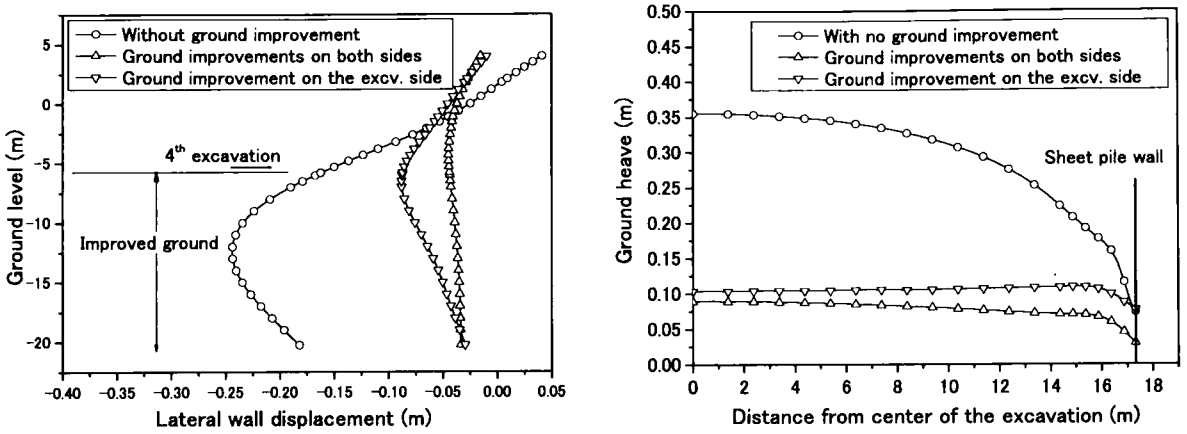

Figure 3.39 Comparison of the sheet pile wall displacements and the heave of the excavation surfaces in Cases 1, 3, and 4

In the second and third additional analyses, which will be referred to as "Case 3" and "Case 4", instead of extending the length of the sheet piles, it is assumed that a soil improvement is performed. In Case 3, the ground under the excavation level on both sides of the wall is improved, while only the ground under the excavation level on the excavation side is improved in Case 4. The ground improvements in these cases are illustrated in Figure 3.38. The elastic shear modulus of the improved ground is assumed to be 2×10^4 kPa, which is approximately 5 times of the original value. Viscoplastic parameter C_0 of the improved ground is assumed to be 1.3×10^{-13} (1/s).

The analysis results are shown with in Figure 3.39 along with the results of Case 1 (the original case). It can be seen that the sheet pile displacements and the base heave are reduced substantially by the soil improvements in both of the cases. The wall displacement in Case 4 is less than 10 cm and the base heave is almost equal to that of Case 3. It is recommended, therefore, that the ground improvements only on the excavation side are effective enough to reduce the ground deformation and the wall displacement in the problem. This supports the fact that the sheet pile wall displacement is mainly induced by the deformation of the ground under the excavation level on the excavation side.

3.3.6 Summary: Large deformation analysis of an excavation through a thick soft clay deposit

In this section, numerical simulations of braced excavations performed through a thick soft clay deposit were conducted. The mechanism of the soil-structure interaction of the excavation was studied. From the results of the study, the following conclusions may be

drawn.

It was found that, the wall tends to deflect with the position of the maximum lateral deflection located beneath the excavation level. The simulations also indicate large displacements of the toe of the wall and a large amount of heaving. This shows the low-base stability of the excavation system. The lateral deflections of the wall continue to grow largely with time even after the stop of the excavation. The continuing of wall deflection was found to be the results of both the consolidation process and the viscoplastic flow of the soil masses. A comparison shows the agreement of the wall and the ground deformation patterns from the numerical results and the data from the case study, and thus, indicates that the numerical method can quantitatively reproduce the behavior observed in the case study. Moreover, we found that the analysis method and the constitutive model used in this study can effectively simulate the rate-dependent behavior of the clay ground in the problem, which can not be studied by using a typical elasto-plastic soil constitutive model.

In the excavation performed through thick soft clay deposits, a good support may help to improve the performance of the excavation above the excavation level. However, since the deformation is concentrated in the soil under the excavation level, the low bending-stiffness of the sheet pile wall may not effectively constraints the deformation of the soil under the excavation level. Therefore, it is better to choose ground improvements to increase the strength of the soil in order to prevent the large deformation of the ground and the supporting system when the excavation is to be performed through a thick soft clay deposit.

Chapter 4

Case Study of the Ground Deformation and the Settlement of an Embankment Constructed near a River

4.1 Introduction

Any river mouth with a low ground level is at risk for seasonal flooding. Therefore, it is necessary to construct an embankment in this kind of area in order to prevent flood damage that may be caused by the passing of a typhoon. If the ground is comprisesd of thick soft clay layers, a large amount of ground settlement as well as ground deformation can be expected as a results of the embankment construction. This deformation could in turn lead to the damage of nearby structures, especially if the structures are also embedded in a soft clay layer.

There have been cases where an embankment was constructed near the bulkhead piles that were not embedded into a firm soil stratum. The area surrounding the construction site in the present study was subjected to an earthquake before the construction was started. After the construction was completed, large long-term lateral displacement of the pile heads and pile tips was observed by means of the measuring instruments installed in the field with cracks appearing on the ground surface behind the heads of the bulkhead sheet piles. The large displacement of the pile tips indicate the low base stability of the piles. Furthermore, the amount of ground settlement under the constructed embankment became larger than the designed value. Both the earthquake and the construction of the

embankment are believed to be responsible for the large deformation of the ground and the supporting structures. At the present, a countermeasure is being planned to cope with the danger of the progressive failure of the piles.

This chapter addresses the problem of large deformations in the ground and the large displacement of a foundation structure. Only the influence from the construction of the embankment is considered. The numerical simulation is carried out using the elasto-viscoplastic constitutive model considering structural changes for clay, the elasto-plastic constitutive model for sand, and the finite element formulation, which are all reviewed in Chapter 2. The existing data from observations and measurements will be shown in the next section. Then, a model of the problem, the soil parameters, and the sequence of the analysis are presented. Finally, the mechanism of the ground deformation and the effects of the degradation of the soil from the obtained analysis results are discussed.

4.2 Review of the Existing Data

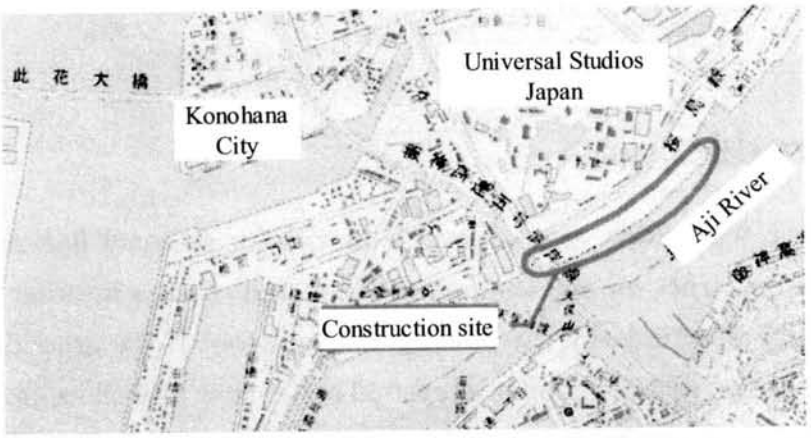

Figure 4.1 Location of the embankment construction site

A large-scale embankment has been constructed on the shore of the Aji River located in the bay area of Osaka, Japan. This embankment is a part of a super embankment project that will increase the efficiency of the flood prevention system in the area. The data of this case study was obtained from the materials for the technical committee on the reinforcement method for the bank revetment of the Aji River (2005). The history of this project is as shown below.

- 1993-1994: The bulkhead sheet piles (ϕ=1200 mm, L=26.5 m) were installed in front of the existing sheet piles.
- January 17,1995: The 1995 Hyogo-ken Nambu Earthquake occurred in the southern

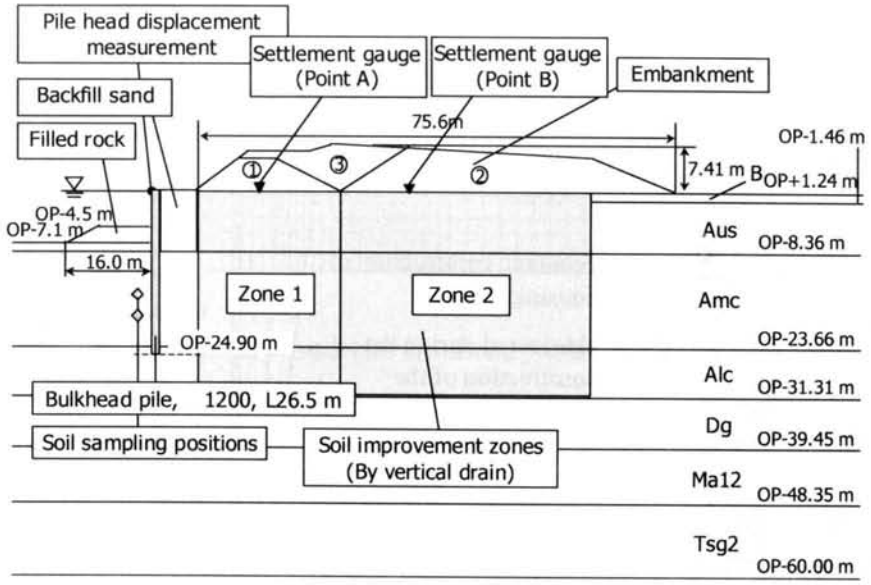

Figure 4.2 Geometry of the embankment's cross section, the locations of the measuring instruments, the soil sampling positions, and the soil layers

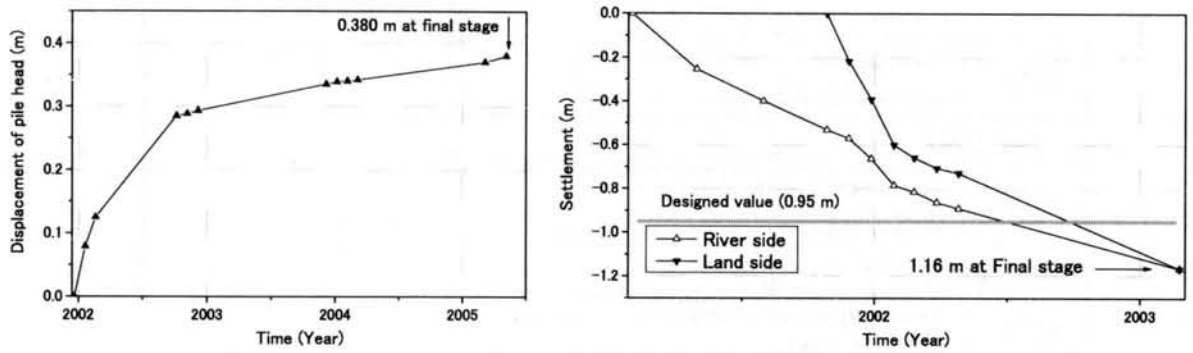

Figure 4.3 Measured lateral displacement of the pile head and the measured ground settlements

part of Hyogo Prefecture, Japan. The earthquake caused the settlement of the backfill soil as well as cracks in the overlay concrete.

- 1997-2002: An embankment with a height of 6.26m was constructed on the river shore. Vertical drain methods, including paper drain and sand drain, were performed to accelerate the consolidation of the soil underlying the embankment.

- December 2001: The displacements of the bulkhead piles were realized during the construction, and the measurements of the pile head displacement were started.

- March 2005-the Present: The continuation of the displacement of the pile heads has been observed. An investigation to find the cause of this behavior has been

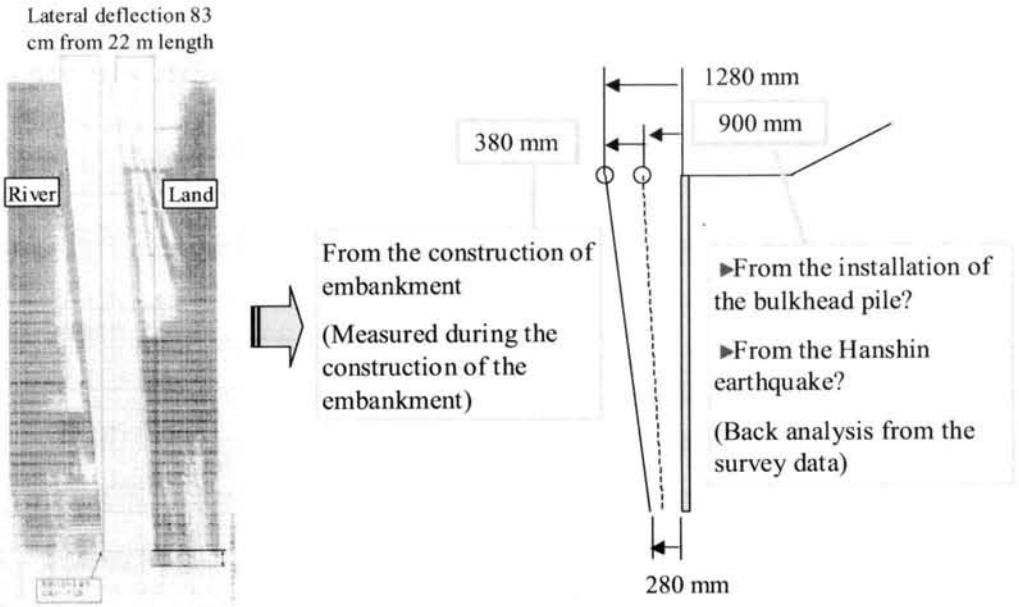

Figure 4.4 Ultrasound test results and the displacement of the bulkhead pile

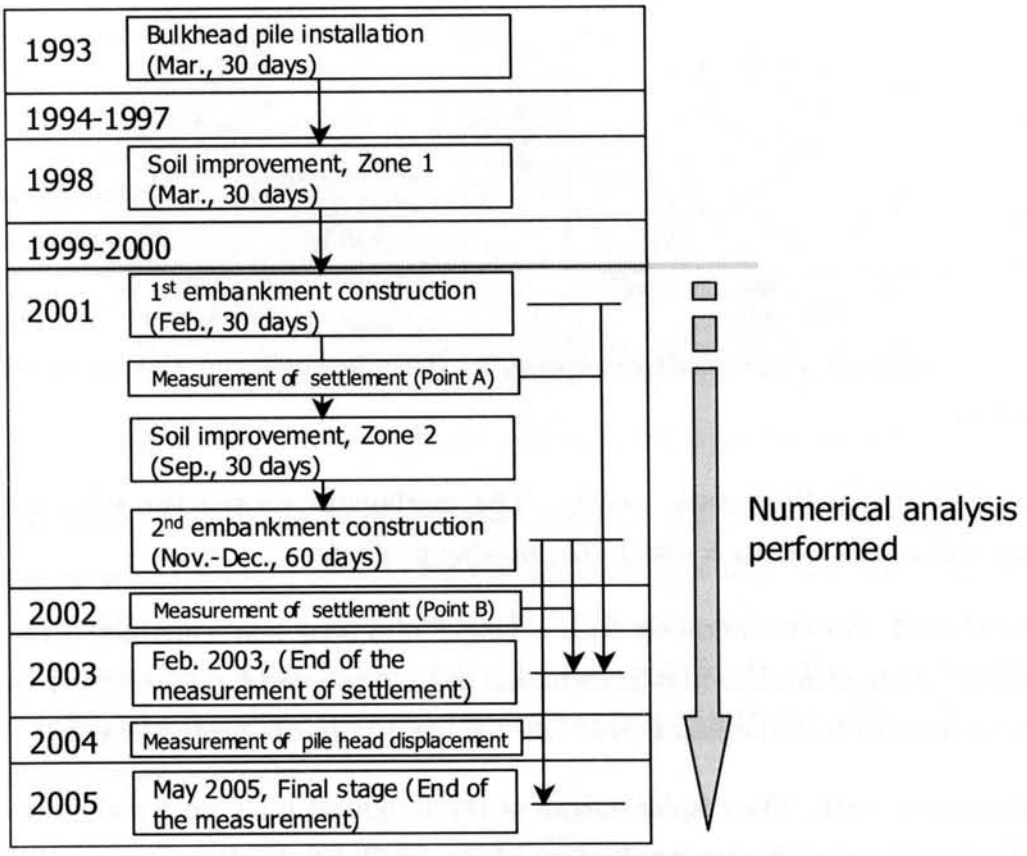

Figure 4.5 Construction sequence and the measurement schedule

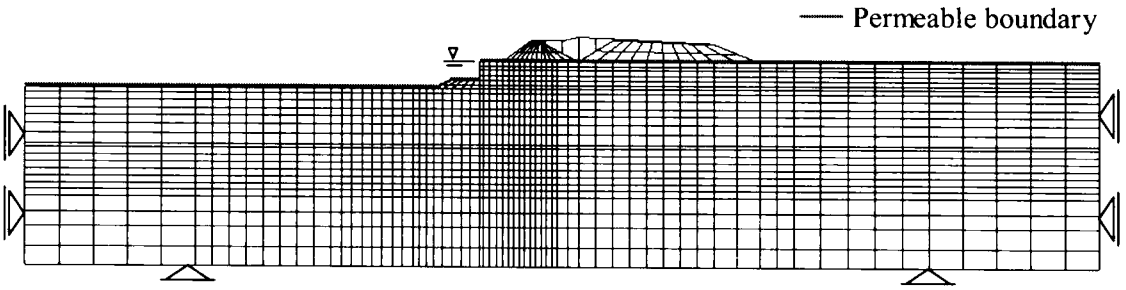

Figure 4.6 Geometry and the boundary conditions of the problem

performed.

Figure 4.1 indicates the location of the embankment construction site on the map. Figure 4.2 illustrates the geometry of the embankment's cross section and the location of the instruments installed to measure the ground settlement and the pile head displacement. The soil conditions at the construction site are also shown in this figure where 'B' indicates the stratum composed of embankment materials, 'Aus' indicates the upper stratum of alluvial sandy soil, 'Amc' and 'Alc' indicate the middle and the lower stratums composed of alluvial clay, respectively. 'Dg' indicates the stratum composed of diluvial sandy soil and 'Ma12' indicates the stratum composed of diluvial clay. Since the largest horizontal displacement of the pile heads was observed in Section No.4, this section is therefore chosen to be the object of study in this chapter. At two points of the ground surface, the settlements have been measured. The locations of the two points are shown in Figure 4.2 and the results of the settlement are shown in Figure 4.3. An additional investigation by means of ultrasound tests was carried out during June of 2005. The profile of the lateral displacement of the piles was obtained, as shown in Figure 4.4. Figure 4.5 includes the construction sequence and all of the measured results for Section No.4.

4.3 Numerical Simulation

4.3.1 Geometry, Boundary Conditions, and Soil Conditions

The geometry and the FEM mesh of the model ground used in the analyses are presented in Figure 4.6. The boundary conditions of the displacement and the pore water pressure are also shown in the figure. The ground water level is assumed to be at the ground level of the land-side as shown in the figure.

The material parameters and the constitutive model used in the analysis for each soil layer and the foundation structure are listed in Table 4.1. The soil samples were taken at

Table 4.1 Material parameters

Parameters for the elasto-plastic model for granular materials

Parameters	Filled rock	Backfill sand
Coefficient of permeability k_0 (m/s)	8.0×10^{-7}	8.0×10^{-7}
Compression index λ	0.03	0.03
Swelling index κ	0.002	0.002
Elastic shear modulus (kPa)	$4878.5 \times \sigma'_{m0}$	$1336.6 \times \sigma'_{m0}$
Initial void ratio e_0	0.80	0.80
Stress ratio at maximum compression M^*_m	1.150	1.150
Stress ratio at failure state M^*_f	1.4183	1.4183
Control parameter of anisotropy C_d	2000	2000
Hardening parameter B^*_0	2500	2500
Hardening parameter B^*_1	200	200
Parameter of dilatancy D_0	2.0	2.0
Parameter of dilatancy n	2.0	2.0

Parameters for the elasto-viscoplastic model for clay materials

Parameters	Amc	Alc	Ma12
Coefficient of permeability k_0 (m/s)	1.60×10^{-9}	1.60×10^{-9}	5.30×10^{-10}
Compression index λ	0.3201	0.326	0.217
Swelling index κ	0.0482	0.0326	0.0217
Initial void ratio e_0	1.70	1.30	1.20
Coefficient of earth pressure K_0	0.566	0.528	0.466
OCR	1.15	1.20	1.90
Stress ratio at maximum compression M^*_m	1.14	1.12	1.30
Viscoplastic parameter m'	20.59	20.00	20.00
Viscoplastic parameter C_0 (1/s)	1.5×10^{-11}	3.0×10^{-12}	1.16×10^{-11}
Structural parameter σ'_{maf} (kPa)	$0.70 \times \sigma'_{mi}$	$0.70 \times \sigma'_{mi}$	$0.70 \times \sigma'_{mi}$
Structural parameter β	0.0,10.0	0.0,10.0	0.0

Note: σ'_{mi} represents the initial mean effective stress

Table 4.1 Material parameters (Continued)

Parameters for the elastic materials

Material model	N value	γ (kN/m^3)	E (kPa)	υ
B	13	19.0	36,400	0.30
Aus	2	18.0	5,600	0.30
Dg	60	19.0	168,000	0.30
Tsg2	60	18.5	168,000	0.30
Embankment	10	18.0	28,000	0.30

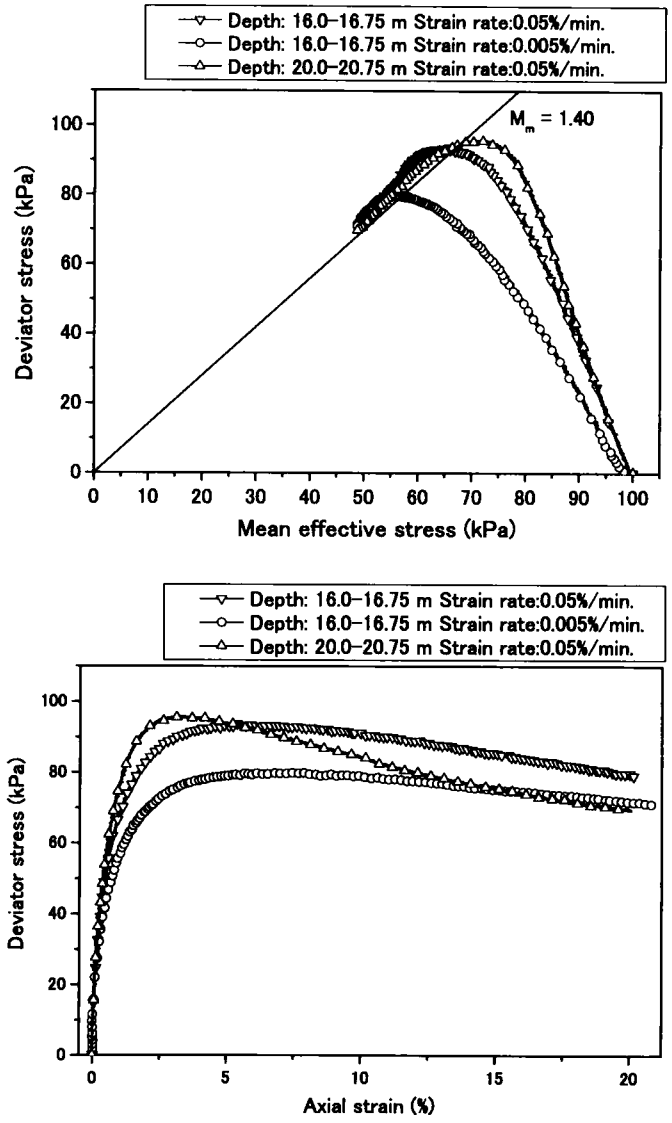

Figure 4.7 Results from the undrained triaxial compression tests

the borehole located in front of the bulkhead piles under water. The depths of the samples taken for the undrained compression triaxial tests are 16.0-16.75 m and 20.0-20.75 m. The depths are measured from the ground surface of the land side, and therefore, all of the samples were taken from the Amc layer. Consolidation tests and undrained triaxial tests on these soil samples were carried out and the results of the tests are shown in Figure 4.7. It can be seen from the undrained triaxial compression test results that the clayey soil of the Amc layer is a structural clay in which the microstructural changes may cause the strong degradation of the soil strength. Material parameters λ and κ were obtained from the one-dimensional consolidation tests. Viscoplastic parameter m' was determined from one-dimensional long-term consolidation tests. M_m^*, G_0, and σ'_{maf} were calculated from the undrained triaxial compression tests. After m' was fixed, viscoplastic parameter C_0 was determined by the peak stress. Structural parameter σ'_{maf} was obtained by the deviator stress at the residual stress stage, while α and β, which dominate the decreasing rate of the deviator stress, were determined by the curve fitting.

Figures 4.8 shows a comparison between the simulation results and the experiment results of the undrained triaxial compression tests. It should be noted that these simulation results are obtained by integrating the constitutive equation under the triaxial stress state, using the Runge-Kutta method. The comparison shows that the initial part of the stress path is different between the test results and the simulations. However, the peak and the residual stress levels in the stress-strain relations, the strain rate sensitivity, and the dilatancy characteristics of the clay samples are well reproduced.

For the Alc and the Ma12 layers, only the data on the slope of the compression curve obtained from standard consolidation tests C_c, and the angle of friction ϕ', determined from CU tests are available. λ and M_m^* were assumed from these data. For the remaining parameters, typical values for organics clay were used. All of the parameters are listed in Table 4.1.

All the granular materials except for the backfill sand and the debris, are assumed to be elastic. The parameters used are also shown in Table 4.1. Young's modulus E is determined from the relation $E = 2800N$ (kN/m^2) (Uto 1967), in which N is the SPT blow count and Poisson's ratio is assumed to be 0.30. The elasto-plastic soil model mentioned previously in Chapter 2 is used to simulate the debris and the backfill sand behind the bulkhead sheet pile. The soil parameters used are shown in Table 4.1. Note that in order to study the effects of the structural changes in the clay on the results of the analyses, another numerical analysis has been performed without structural changes, namely, the structural parameter β is set to be zero as shown in Table 4.1.

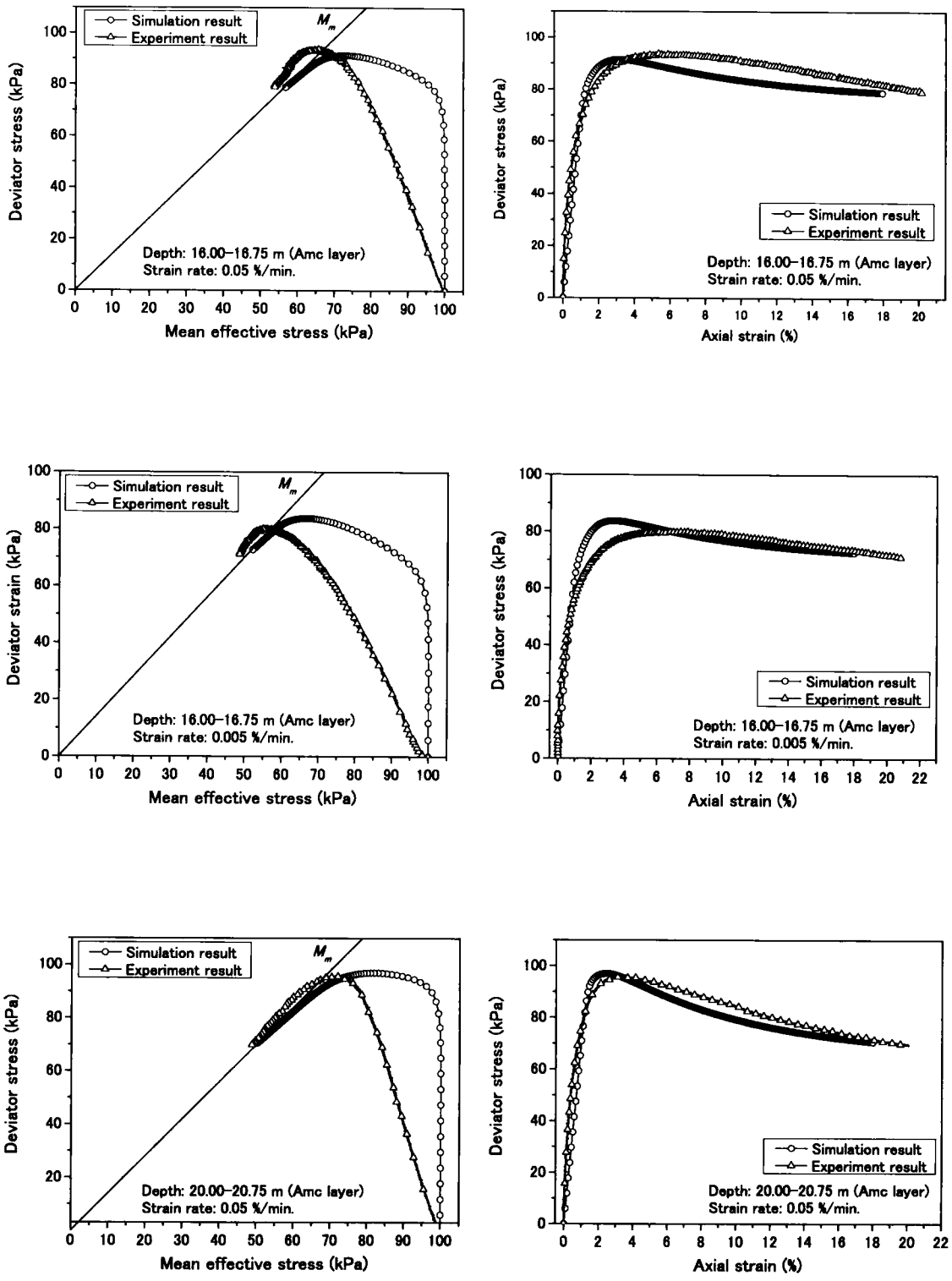

Figure 4.8 Comparison between the simulation results and the experiment results of the undrained triaxial compression tests

4.3.2 Sequence of the Analysis

In this study, only the influence from the construction of the embankments on the deformation of the ground and the displacement of the supporting structures is considered. Consequently, as shown in Figure 4.5, the numerical simulation begins in Stage 5, namely, the beginning of the construction of the first part of the embankment, which was started in February of 2001. This stage took one month (28 days) to complete. Measurements of the river side settlement under this first embankment section were started at the same point in time (February of 2001). Then, the construction site was left as is for six months (184 days). Before constructing the second part of the embankment, the underlying ground was improved by the vertical drained method. This process took one month (30 days) and is referred to as Stage 7. The construction site was then left again as is for one month (31 days). Finally, the remaining third part of the embankment was constructed during this stage, which took two months (61 days) to complete. The measurements of the settlement of the land side as well as the displacement of the pile head were begun during this stage of construction. The numerical simulation was then continued for another 1220 days and was terminated at the end of May 2005.

4.4 Results of the Analyses

4.4.1 Mechanism of the Ground Deformation and the Effects of the Degradation of the Soil Strength

Figures 4.9 and 4.10 show the distributions of accumulated viscoplastic deviatoric strain $\gamma^p \equiv \int \sqrt{de_{ij}^{vp} de_{ij}^{vp}}$ and the distributions of viscoplastic volumetric strain calculated after each stage of the construction. It can be seen that a large amount of viscoplastic strain is generated in the clay layer under the embankment. This large strain extends to the deep parts of the layer. Since the pile tips are embedded in the Alc layer, just around one meter under the Amc layer, a large pile tip displacement can then be expected from the deformation of this deep part of the soil. Figures 4.11 and 4.12 show the vector of the accumulated nodal displacement from the beginning to the end of the analysis for the structural soil case and the nonstructural soil case, respectively. We confirm that the large amount of the soil deformation and the lateral displacement of the piles extended through the bottom of the clay layer.

Let us now consider the effects of structural degradation along with the deformation pattern of the ground and the supporting structures. Figures 4.13 and 4.14 show the

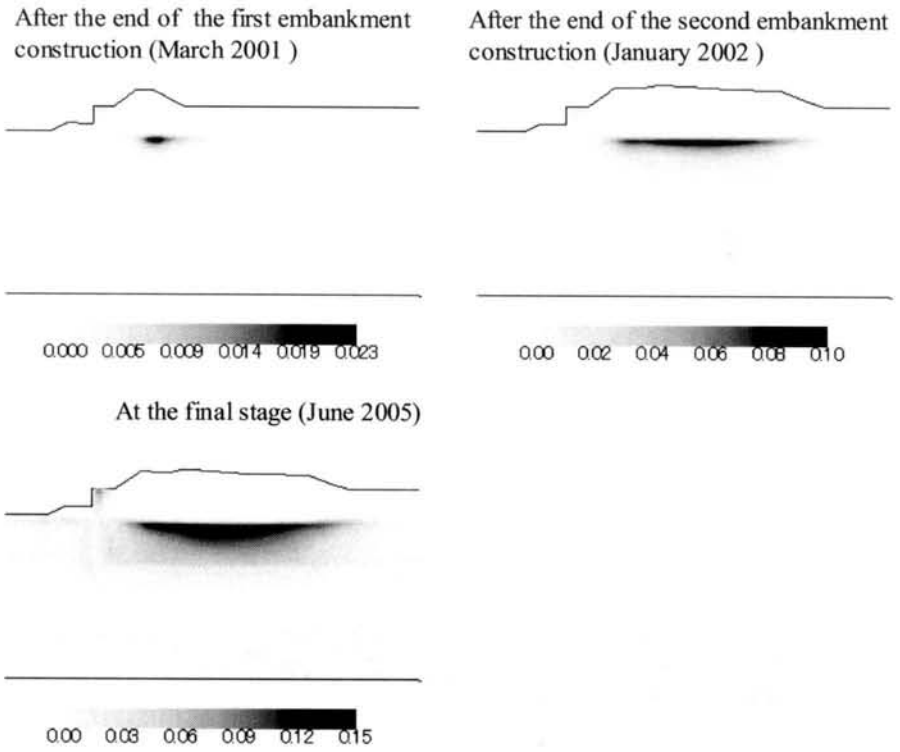

Figure 4.9 Distributions of the accumulated viscoplastic deviatoric strain after each stage of construction for the structural soil case

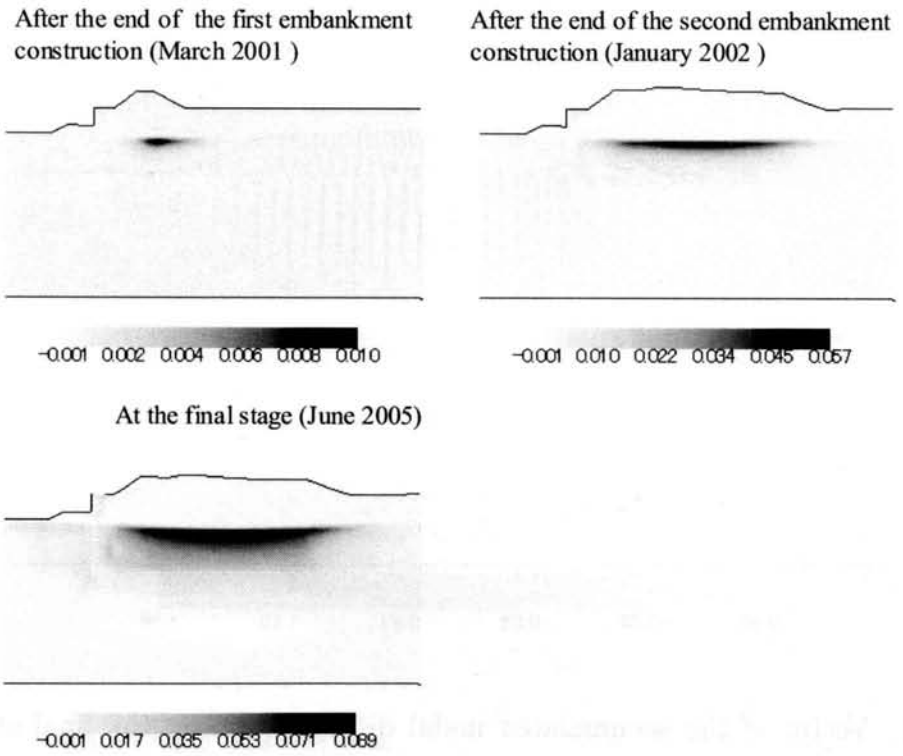

Figure 4.10 Distributions of the viscoplastic volumetric strain after each stage of construction for the structural soil case

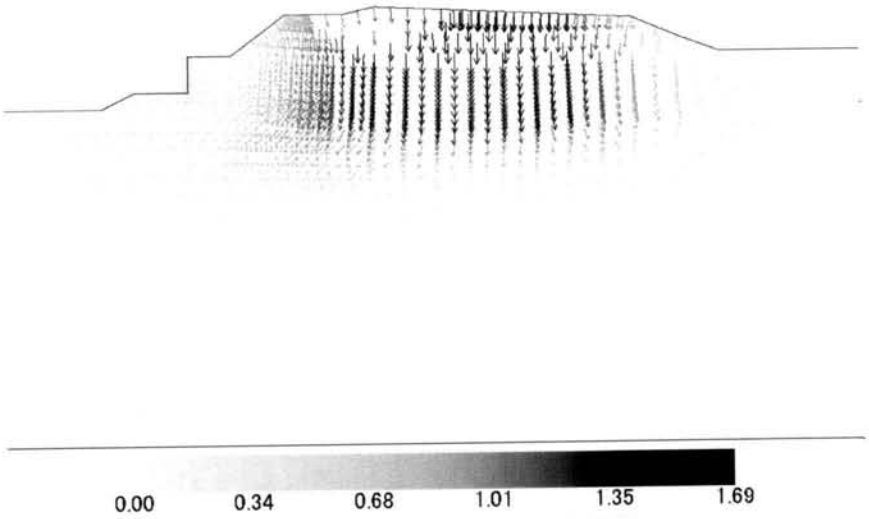

Figure 4.11 Vector of the accumulated nodal displacements in the final stage for the structural soil case

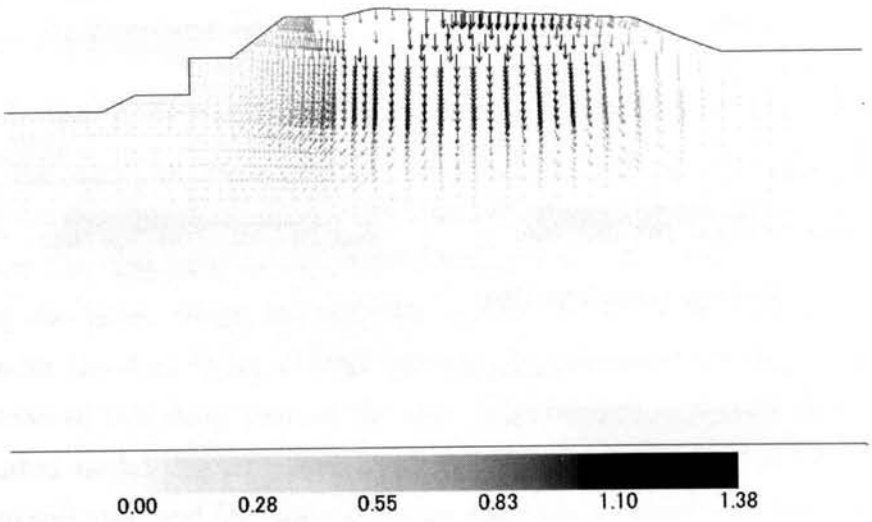

Figure 4.12 Vector of the accumulated nodal displacements in the final stage for the nonstructural soil case

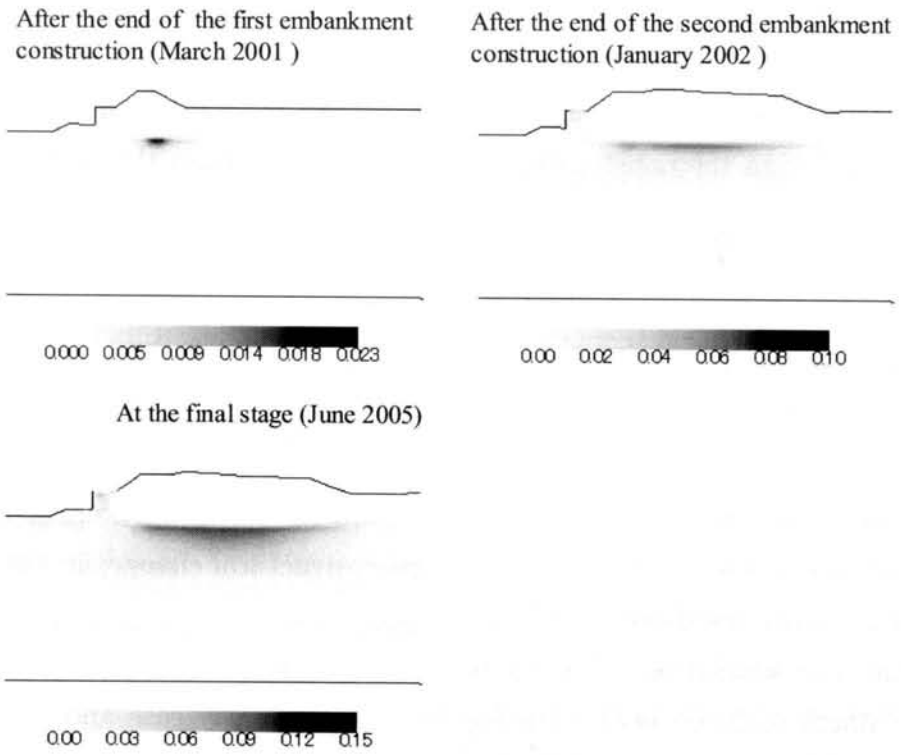

Figure 4.13 Distributions of the accumulated viscoplastic deviatoric strain after each stage of construction for the nonstructural soil case

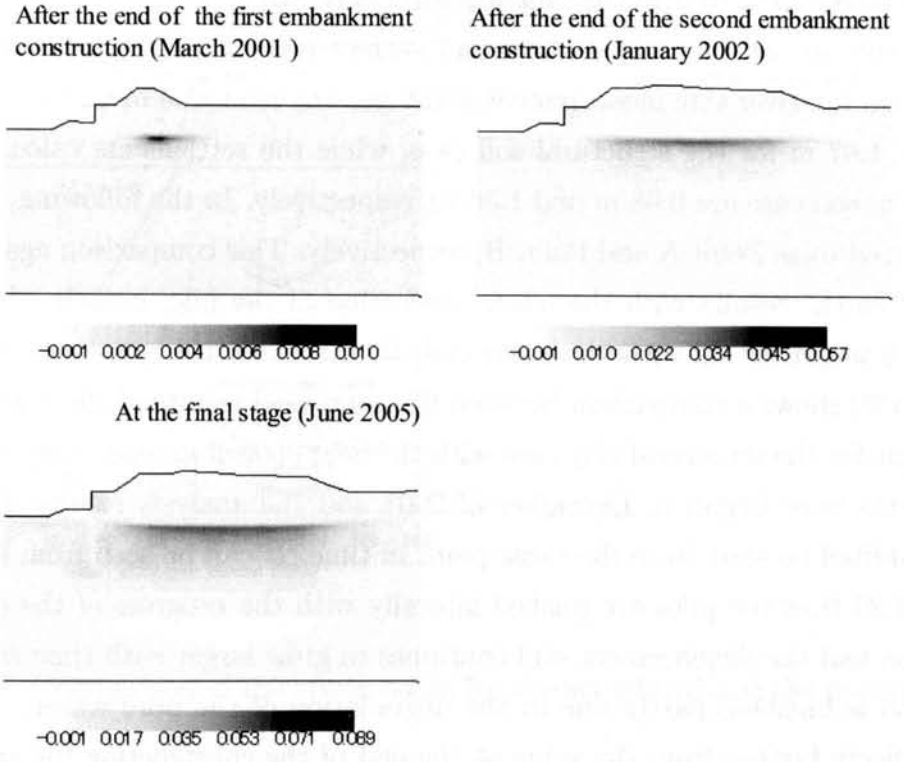

Figure 4.14 Distributions of the viscoplastic volumetric strain after each stage of construction for the nonstructural soil case

distributions of the accumulated viscoplastic deviatoric strain and the distributions of viscoplastic volumetric strain for nonstructural clay case, respectively. A comparison shows that the accumulated viscoplastic deviatoric and the volumetric strain in the clay stratum obtained from the nonstructural clay case is lower than that obtained from the structural clay case. Figures 4.15 and 4.16 show the stress paths and the generation of pore water pressure with the elapse of time obtained from both cases. The positions of the soil elements in the finite element mesh are also shown in Figures 4.15 and 4.16. It can be seen from the stress paths that for the structural clay case, the increase in mean effective stress during consolidation tends to be lower than that obtained for the nonstructural clay case. Consequently, a larger excess pore water pressure is generated by the construction load in the case of structural clay, as shown in Figure 4.16. This phenomenon is the result of the degradation of soil strength due to the microstructural changes in the clay.

Figure 4.17 shows the development, with time, of the pile head lateral displacement obtained from the simulation. The total lateral displacement of the pile head at the final stage (March of 2005) is 41.1 cm for the structural clay case and 34.4 cm for the nonstructural clay case. Figure 4.18 shows the computed horizontal deflection of the bulkhead pile with the progress of the embankment construction. The comparisons in these figures indicate that the lateral deflection of the bulkhead sheet pile in the structural clay case is larger than that in the nonstructural clay case.

Figure 4.19 shows the computed ground surface settlements. The total settlement obtained from the river side measurement point and the land side measurement point are 0.84 m and 1.67 m for the structural soil case, while the settlements calculated for the nonstructural soil case are 0.68 m and 1.36 m, respectively. In the following, these points will be referred to as Point A and Point B, respectively. This comparison again shows the same trend as the results with the lateral deflection of the pile, namely, the calculated settlement is larger for the structural clay case than that for the nonstructural clay case.

Figure 4.20 shows a comparison between the computed results of the pile head lateral displacement for the structural clay case with the field measurements. Note that the field measurements were begun in December of 2001 and the analysis results shown in this figure are shifted to start from the same point in time. It can be seen from Figures 4.17, 4.18, and 4.20 that the piles are pushed laterally with the progress of the embankment construction and the displacement still continues to grow larger with time even after the construction is finished, partly due to the degradation of the pore water. The head of the pile deflects further from the value at the end of the construction for around 29 cm during 1240 days. It is seen that the measured value of the pile heads lateral deflection

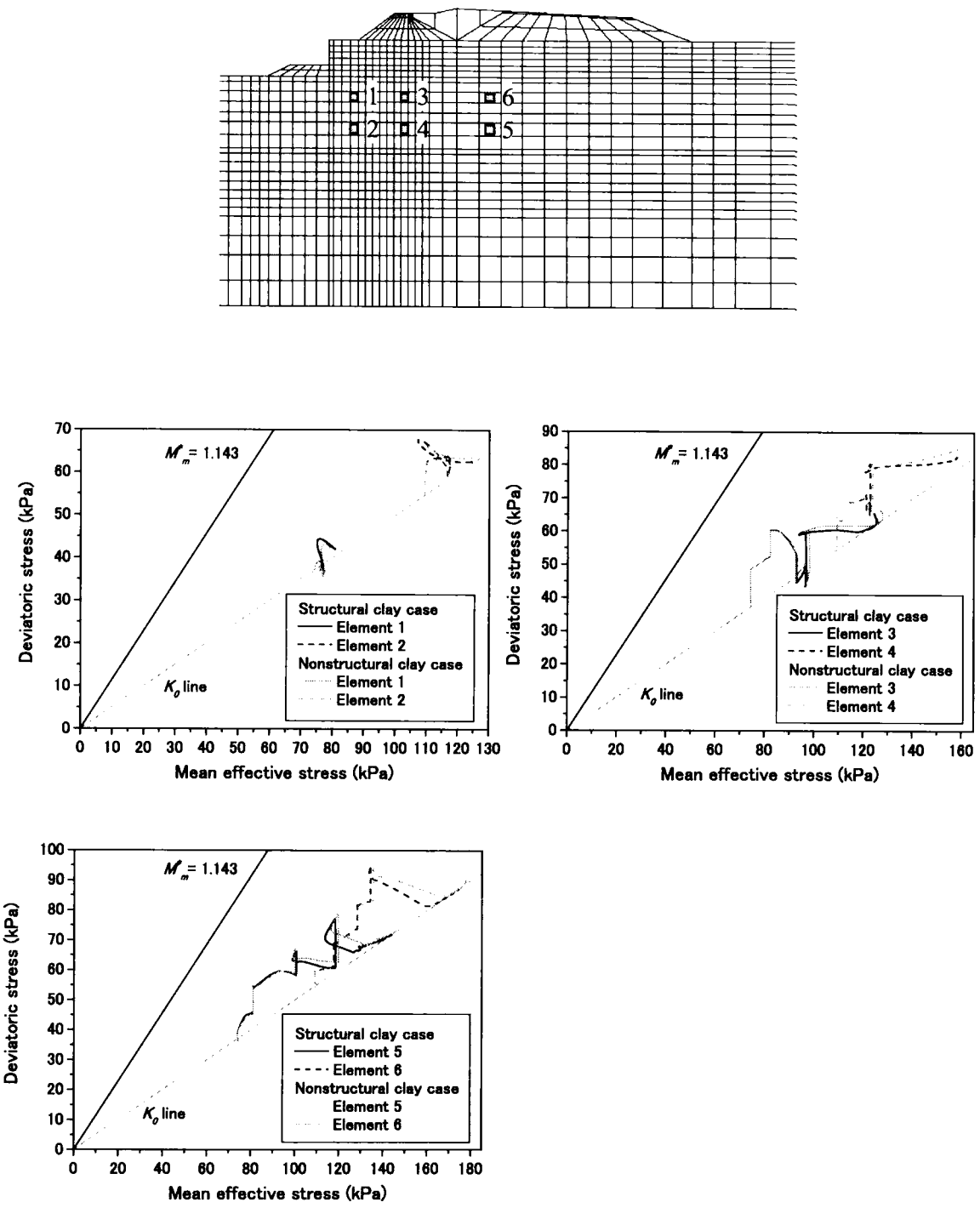

Figure 4.15 Comparison of the stress paths for the structural and the nonstructural soil cases

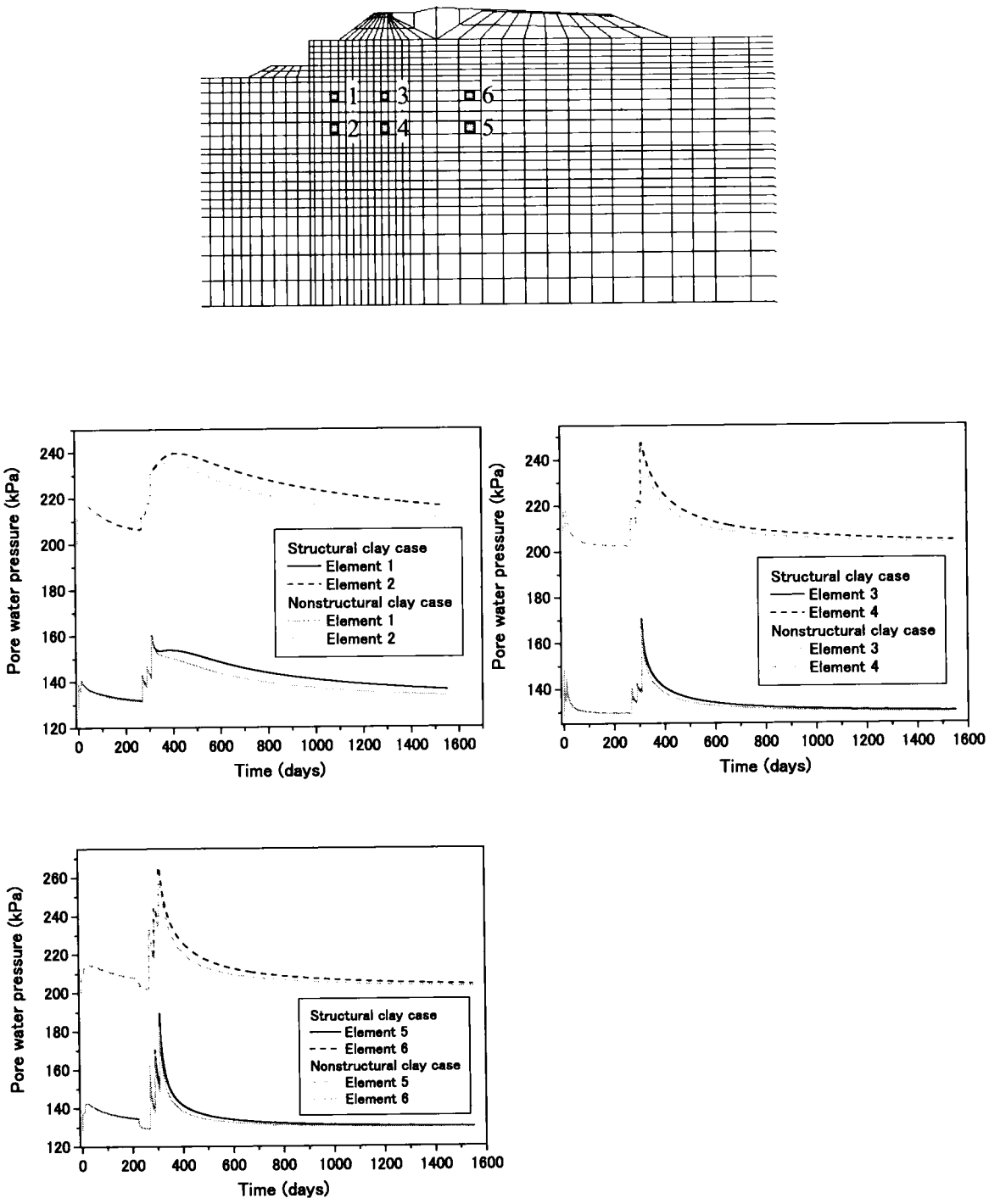

Figure 4.16 Comparison of the generation of pore water pressure for the structural and the nonstructural soil cases

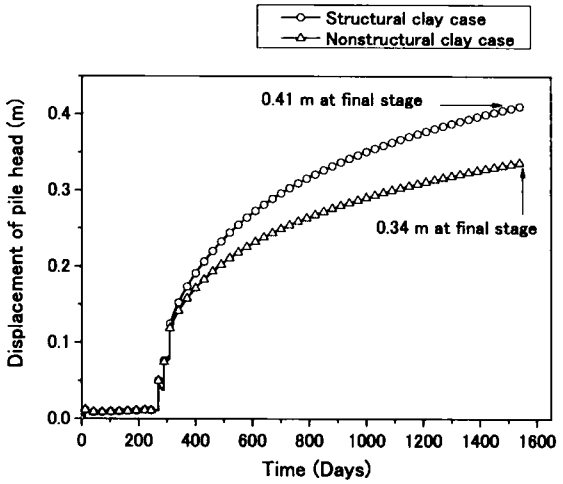

Figure 4.17 Pile head lateral displacements from the start of the analysis

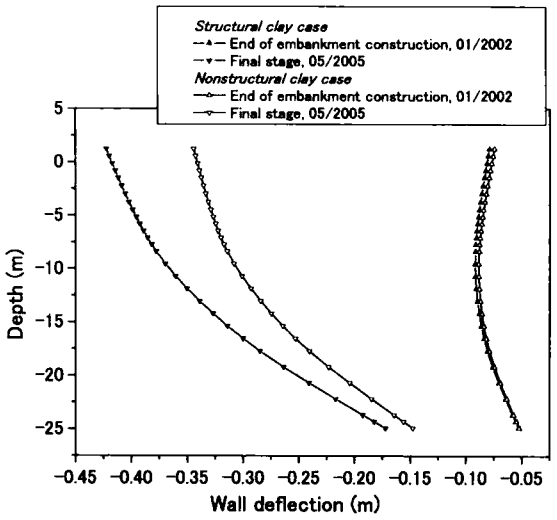

Figure 4.18 Development of the lateral pile deflection with the progress of the embankment construction

at the final stage (38.0 cm) is larger than that in the simulation results (32.8cm). For the profile of the pile lateral deflection, we cannot make a quantitative comparison between the simulation results and the measured results since there is no measured value for the displacement of the pile tips. However, the results obtained from the ultrasound tests shows that the piles deformed in a cantilever pattern with large pile tip lateral deflection. This agrees well with the simulation results, in which the lateral deflection of the pile tip is 17 cm and the pile deflects in the cantilever mode.

A comparison between the simulation results for the structural soil case and the field measurement results of the ground surface settlements is shown in Figure 4.21. Similar to the pile deflection, the starting point of the settlement is shifted to match with the field measurements for both Points A and B. For Point B, the computed settlement at the end of the field measurements is 1.26 m, which is a little bit higher than the measured value (1.17 m). However, by considering the comparison of the development of settlement with time, it can be seen that the simulation results agree well with the observed values. Now consider the settlement at Point A. The computed settlement and the measured one from the field are also shown in Figure 4.21. The analysis gives only a settlement of 0.66 m at the end of the field measurement time. This value is merely 56% of the value measured from the field. Figure 4.22 illustrates the profile of the surface settlement obtained from the analysis at the final stage. It can be seen that the ground surface around Point B, which is located near the center of the embankment, gives a larger settlement than that of the surface near the edge of the embankment, which is located at Point A. On the other hand, the field measurement values of the settlement at Point A are almost

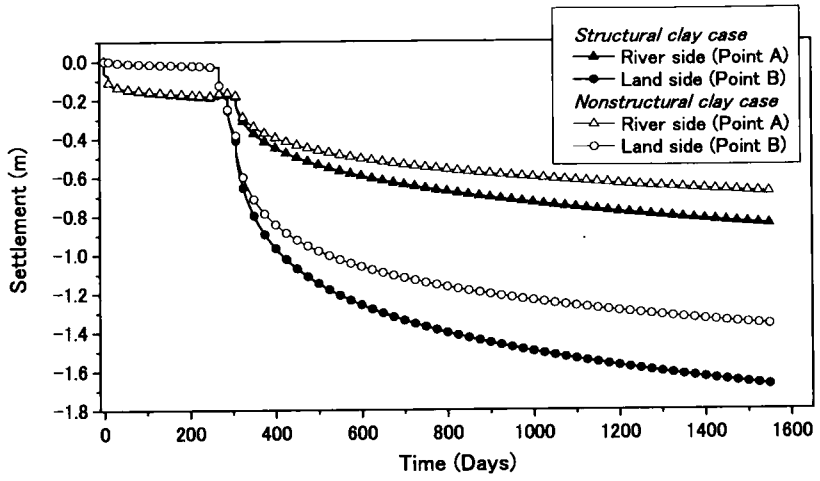

Figure 4.19 Ground settlements from the start of the analysis

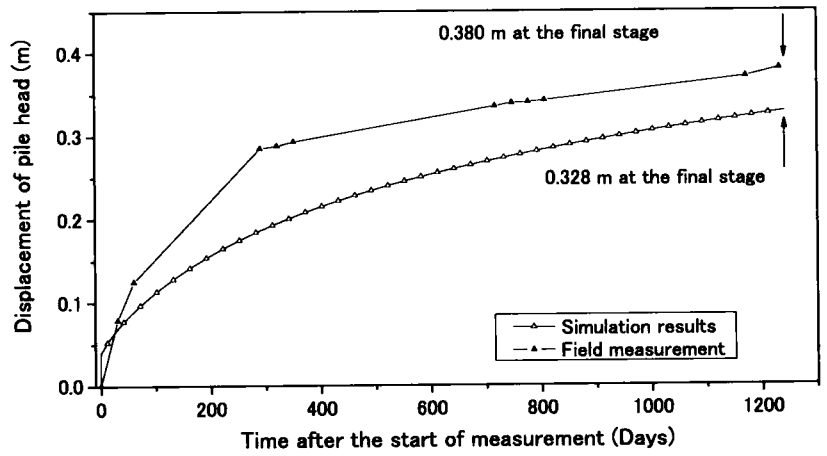

Figure 4.20 Pile head lateral displacements from the start of the field measurements

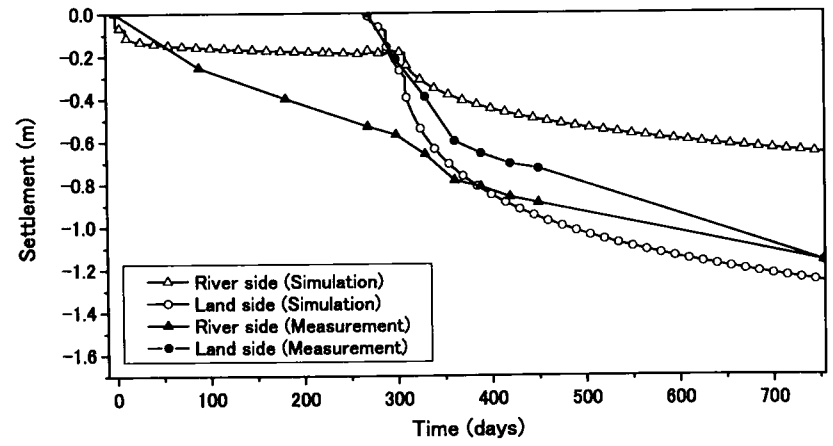

Figure 4.21 Ground settlements from the start of the field measurements

similar to those of Point B. This may be because the ground under Point A, which has been improved, settled in a "block form". Hence, the settlement at Point A is not much different from that at Point B.

Figure 4.23 shows the comparisons between the ground surface settlements and the settlements of the Amc layer and the Alc layer. It is seen that the settlement of the Amc layer is large compared to the settlement of the Alc layer, and that about 80% of the ground settlement under the embankment takes place in the Amc layer. This again emphasizes the essentiality of using a soil model that can well reproduce the important behavior of clay materials well in order to study this problem.

4.4.2 Effects of Pile Stiffness and Pile the Tip Positions on the Deformation of the Ground

From the results of the analysis mentioned in the previous chapter, we recognize that the construction of large embankments brings about large ground deformations which will extend through the bottom of the clay layer. Consequently, the bulkhead pile tips, which are embedded in this clay layer, lead to a large displacement. Furthermore, from the profile of the bulkhead sheet pile lateral deflection, it is clear that that the profile shows a very small curvature. Hence, the sheet piles are subjected to a very small bending moment. All of this indicates that the sheet piles themselves "flow" horizontally as a whole with the deformation of the soil in the clay layer and the piles are not able to resist the deformation of the soil located at deep levels. Therefore, increasing only the sheet pile stiffness should not help reduce the deformation of the ground or the displacement of the supporting structures. To examine this perception, a numerical analysis has been carried out in which the level of the stiffness of the bulkhead pile is increased to two times. The profile of the lateral displacement of the bulkhead pile and the ground settlements are demonstrated in Figure 4.24. For comparison purposes, the results of the analysis obtained from the previous section are also shown in the figure. It is seen that the curvature of the bulkhead sheet pile deflection obtained is smaller compared to the results obtained from the previous section, since the stiffness of the bulkhead pile is higher. However, the calculated lateral displacement of the bulkhead pile and the calculated ground settlements are almost equal to the amounts obtained in the previous section. This confirms that merely increasing the stiffness of the bulkhead pile is not enough to increase the stability of the supporting system.

In this case study, the bulkhead piles are embedded in the clay layer and the large deformation, which extends through the bottom of the clay layer, causes the whole of

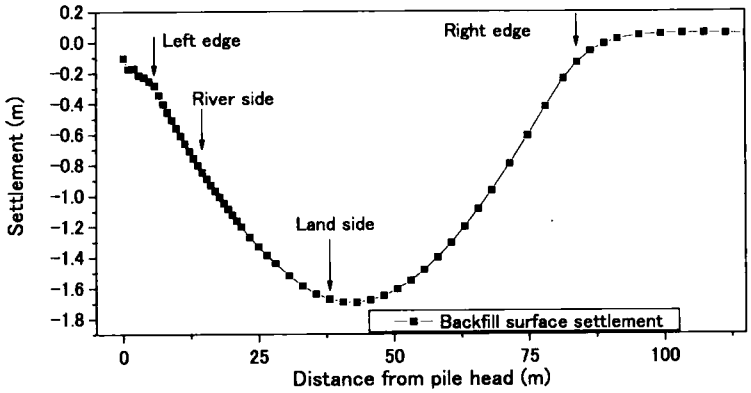

Figure 4.22 Profile of the backfill settlement in the final stage

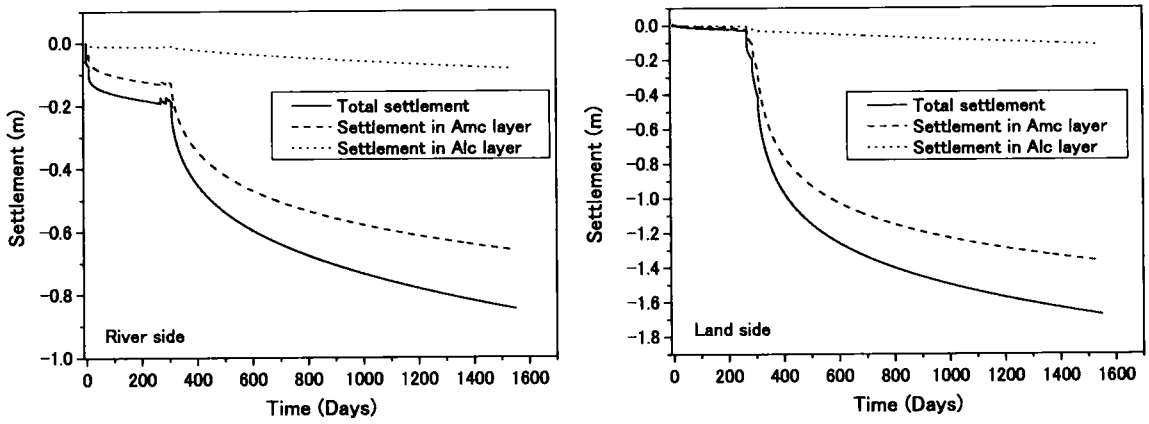

Figure 4.23 Ground settlements from the start of the field measurements for each clay layer

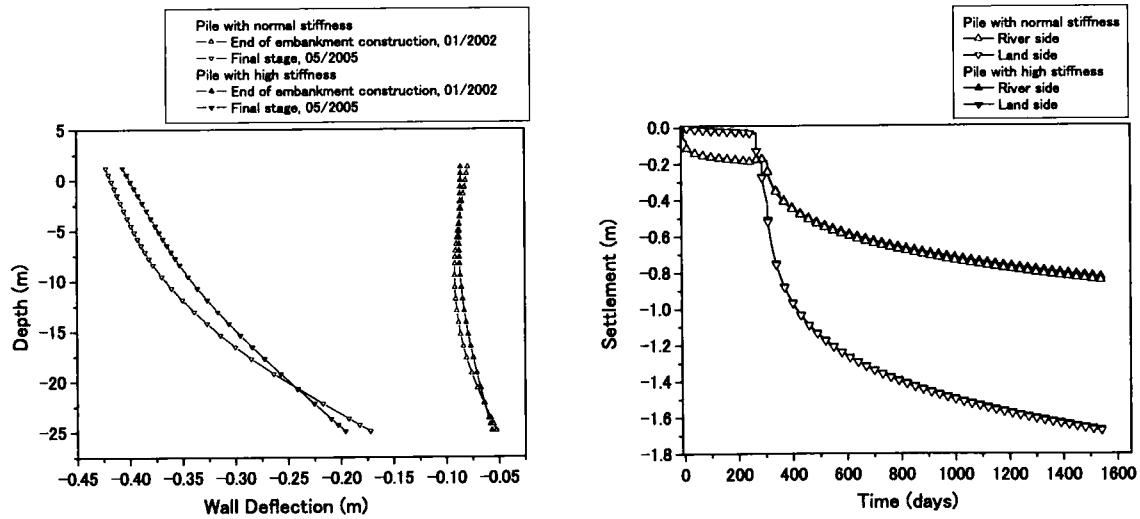

Figure 4.24 Lateral pile deflections and the ground settlements for the case of a highly stiff pile

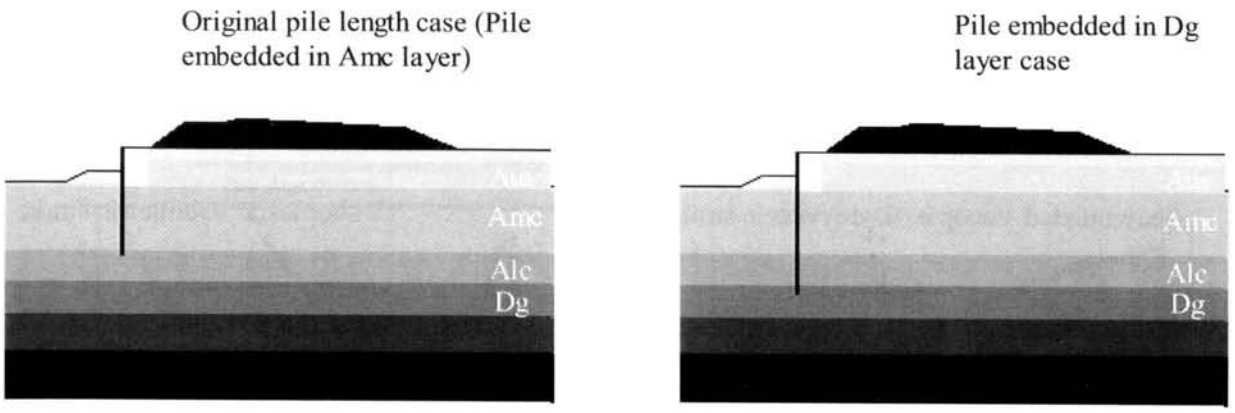

Figure 4.25 Schematic diagram of the pile embedded into a firm stratum

the piles to flow laterally. To prevent this kind of behavior, the bulkhead piles must be installed in a lower firm stratum. Another analysis case has been performed in which level of stiffness of the bulkhead pile is increased to two times. The pile length is extended to 34.6m. With this length, the pile tip is embedded into the Dg layer underlying the Alc layer, as shown in Figure 4.25. The distribution of accumulated viscoplastic deviatoric strain and the distribution of viscoplastic volumetric strain obtained after the final stage are demonstrated in Figure 4.26. Figure 4.27 shows the vector of accumulated nodal displacement from the start to the end of the analysis. By comparing these results with the results from the analysis in the previous section, we can see that the viscoplastic strain which developed in this case is smaller. Furthermore, the vector of the accumulated nodal displacement shows that the deformation of the soil in the deep level of the clay layer is smaller when the bulkhead pile is embedded in a lower firm layer.

Profiles of the lateral displacement of the bulkhead pile and the ground settlements are shown in Figures 4.28 and 4.29, respectively. The results of the analysis obtained from the previous section are also included in the figures for comparison. The displacement at the head of the bulkhead pile during the final stage is 0.28 m, which is considerably lower than the value in the previous section, namely, 0.41 m. Similar to the displacement of the pile head, the displacement of the tip of the pile is smaller when the pile is embedded in a lower firm stratum. The settlement obtained is smaller as well.

The results of the analysis point out that in this case study, the ground settlement is directly related to the lateral displacement of the bulkhead pile. This is because the pile and the ground are allowed to move and spread horizontally due to the surcharge of the embankment. This causes the settlement in the case study to be larger than the design value, which is calculated by assuming 1D consolidation conditions. Furthermore, the slice method was used to calculate the safety factor of the problem in the designing

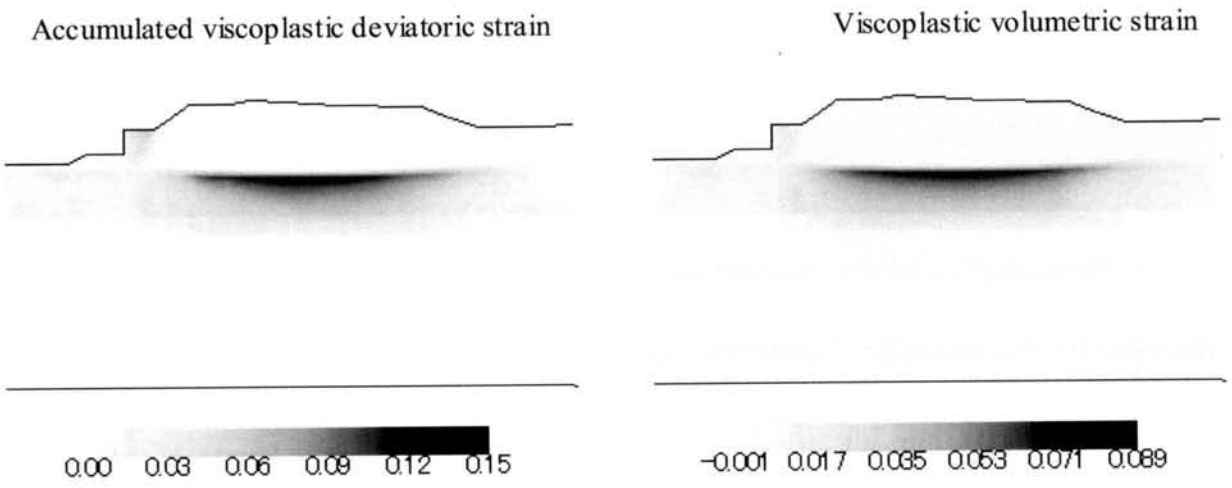

Figure 4.26 Distributions of the accumulated viscoplastic deviatoric strain and the viscoplastic volumetric strain in the final stage for the case of a pile embedded into a firm stratum

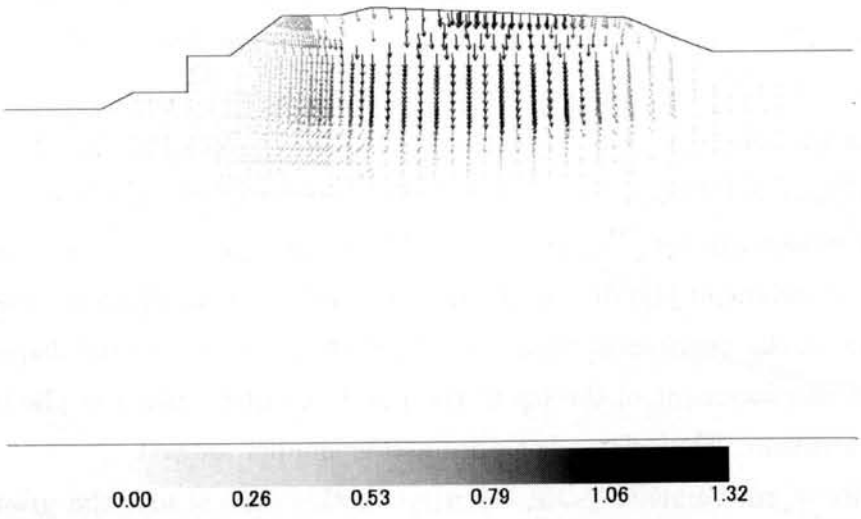

Figure 4.27 Vector of the accumulated nodal displacements in the final stage for the case of a pile embedded into a firm stratum

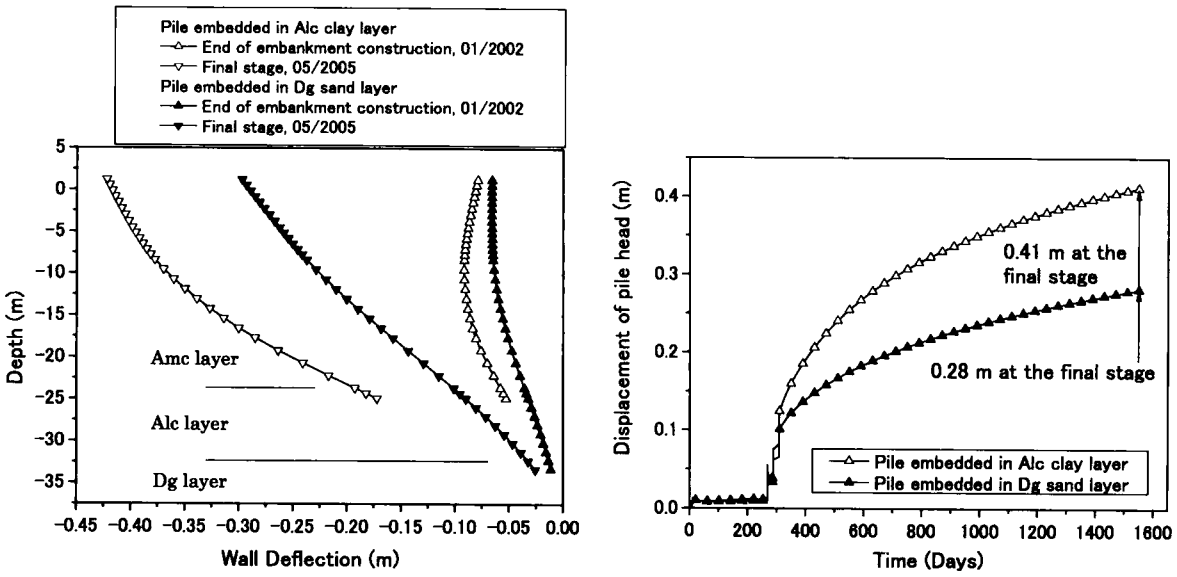

Figure 4.28 Development of the lateral pile deflection with the progress of the embankment construction for the case of a pile embedded into a firm stratum

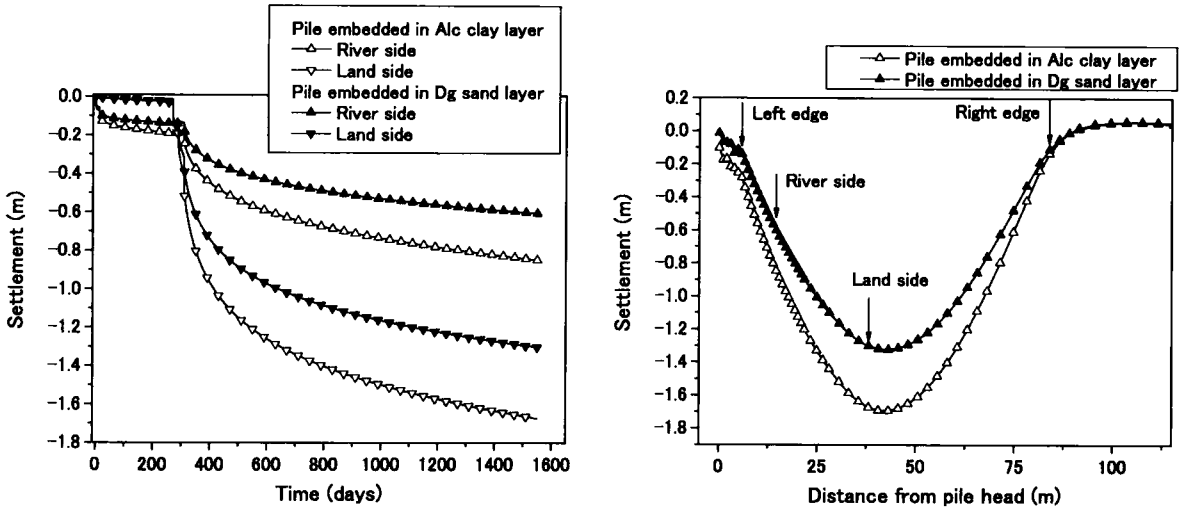

Figure 4.29 Ground settlements from the start of the analysis for the case of a pile embedded into a firm stratum

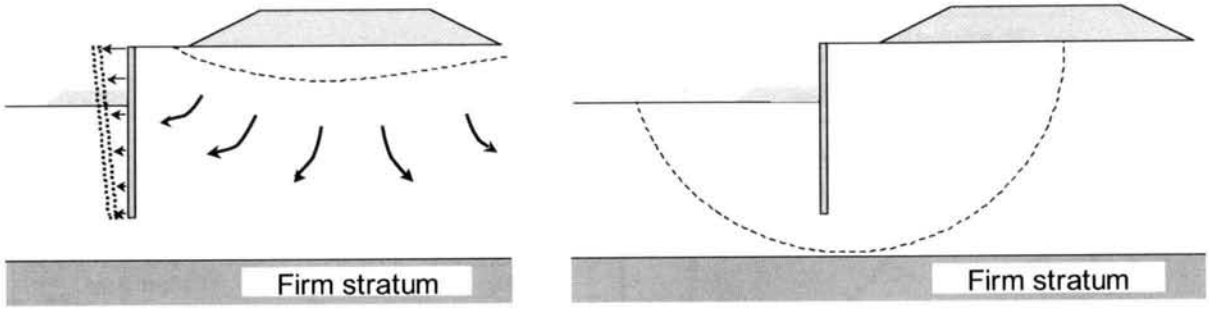

Figure 4.30 Comparison between the mechanism of the ground deformation in the case study and the failure surface of the slice method used in the design

of the piles and the supporting systems. However, the results of the study show that the ground and the wall deformation mechanism are different, as illustrated in Figure 4.30. This must be taken into account when the same kinds of problems are faced in the future.

From the above discussions, we can confirm in this case study that the ground deformation and the displacement of the supporting structures caused by the construction of the embankment can be reduced by installing the bulkhead piles into a firm stratum before beginning the construction. This is because the base stability of the bulkhead piles is increased and the deformation of the soil in the deep sections of the clay layer is then resisted by the bulkhead piles. Since the construction is finished in the present stage, however, countermeasured that suit to this problem would be the improvement of the strength of the soil in front of and behind the bulkhead piles and the reinstallment of a longer pile into a firm stratum.

4.5 Summary

In this chapter, numerical simulations of a case study of an embankment constructed near the shore of a river were conducted using the soil parameters obtained from the laboratory tests. The pattern of deformations of the ground and the displacement of the supporting structures were studied. The effects of the microstructural changes of the clay, and the stiffness and the length of the bulkhead pile were evaluated. It was found that large deformations of the soil is extended to deep sections of the clay layer due to the construction of the large embankment. This ground deformation could lead to the damages of the nearby structures if the structures are embedded in a soft stratum. A comparison between the simulation results and the field measurement values yields a good

agreement and indicates that the calculation method adopted here can be used effectively to study the problem, including a large deformation of the geomaterials. The results obtained from the analyses also emphasizes the importance of including the structural changes and the strength degradation of the clay into the numerical analysis to effectively simulate the geotechnical problems of grounds that are composed of structured clay.

The results of the analysis show that when a bulkhead piles are embedded in a soft layer, the piles and the ground can move horizontally due to the surcharge of the embankment. Hence, the settlement may exceed the design values, which assumes 1D conditions in the calculation. Moreover, the deformation mechanism of the ground is different from the slice method used in the design stage and this must be taken into account when the same kinds of problem are faced in the future.

Since the bulkhead piles moved as a whole, the stability of the supporting system could not be improved by merely increasing the stiffness of the supporting structure. It was necessary to install the piles into an underlying firm stratum. This course of action can prevent the ground flow at deep levels and will result not only in a lower lateral displacement of the pile, but also in a smaller settlement of the ground.

Chapter 5

Elasto-viscoplastic Finite Element Study of the Effect of Degradation on the Bearing Capacity of Clay

5.1 Introduction

The bearing capacity has always been one of the most highly interesting and fundamental problems in Geotechnical Engineering. Near-surface foundations on both clay and sand are usually designed with the well-established classical bearing capacity formulas of Terzaghi (1943), Hansen (1970), Meyerhof (1950), Davis and Booker (1973), and others. These formulas take into account the foundation shape, the size and depth, and the assumption that the soil strength parameters are either constant or vary with depth in some simple manner. The design of foundations is therefore relatively straightforward. However, the above formulas assume that there are no prefailure deformations of the soil, i.e., the soil is a rigid plastic.

In the recent years, the finite element method has been used to analyze the bearing capacity problem. The advantages of this method includes nonlinearity and path-dependency. This means that analytically intractable problems with complex loading and boundary conditions can be studied. Moreover, the method can furnish information on the collapse load of earth structures as well as on the load-deformation history prior to failure. Several soil constitutive models for soil, such as the Mohr-Coulomb failure criterion (Griffiths 1982; Sloan and Randolph 1982) and the modified Cam clay model (Zdravkovic et al. 2003) have been used with FEM to study the bearing capacity of footings and also its behavior prior to failure. Several researchers (Sloan 1988; Sloan and

Kleeman 1995; Ukritchon et al. 1998, Merifield et al. 1998) have used the numerical method with a limit analysis, which yields upper and lower boundary solutions for the true failure load, to study the bearing capacity problem. Up until now, the effects of the structural changes of clay, have not been included in the studies on the bearing capacity problem. The microstructure leads to the softening of the soil strength and also affects the strain localization. Since the strain localization is generally considered to be important as a precursor of failure, the effect of microstructural changes should not be neglected.

This chapter is concerned with the effects of structural changes and strain localization on the bearing capacity of a shallow foundation on a saturated clay stratum. For this purpose, an elasto-viscoplastic soil constitutive model that can considering structural changes is used. This model and the finite element formulation are reviewed in Chapter 2. The plan of this chapter is as follows. In the next section, a numerical simulation of a surface strip footing on a saturated clay stratum is presented. Both the homogeneous and the inhomogeneous clay stratums with strength increasing with depth are considered. Furthermore, the smooth, the rough, and the frictional footing-soil interface conditions are also included in the analysis. With the results of the analyses of the footing on the homogeneous clay deposit, the effects of degradation and the strain softening on the bearing behavior of the surface strip footing are then discussed. Then, the numerical results of the footing on the inhomogeneous clay deposit are discussed, which highlighting the effects of structural changes and the frictional conditions of the footing on the predicted failure pattern. Finally, a three-dimensional numerical analysis of the square footing on a homogeneous clay ground is conducted and the the results obtained are compared to those of the strip footing case.

5.2 Numerical Simulation of a Strip Footing

5.2.1 Geometry and Boundary Conditions

Numerical simulations are performed for a 2 m wide strip surface footing, 2 m width. The geometry and the FEM mesh used are presented in Figure 5.1. Only half of the geometry is considered because the problem is symmetric. The displacement boundary conditions and the pore water pressure boundary conditions are also shown in Figure 5.1. The soil at the ground surface nearby the footing may bulges up due to the loading of the footing, and generates negative pore water pressure in the soil in the area. In this analysis, therefore, impermeable boundaries are set at all of the boundary surfaces in order to prevent the pore water from flowing into the ground by this negative pore water

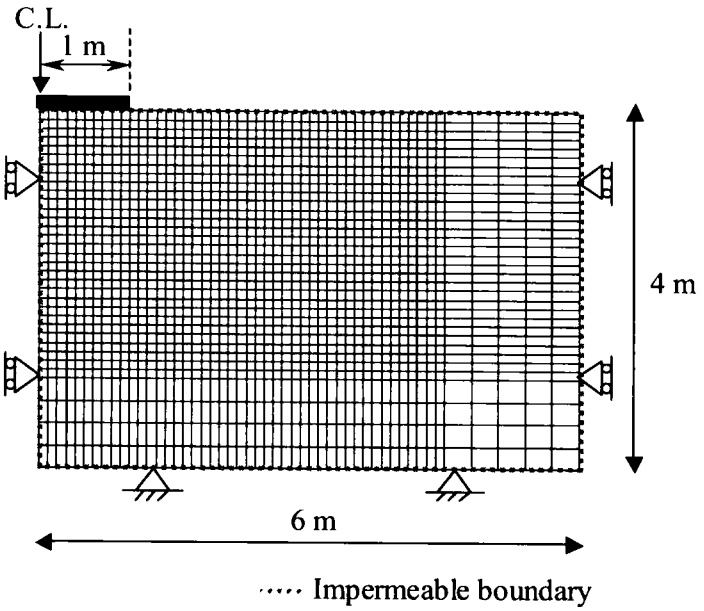

Figure 5.1 Geometry and the finite element mesh used in the analyses

pressure. The boundary conditions underneath the footing are chosen to represent the rough, the smooth, and the frictional footing-soil interfaces. In the case of the rough interface, the horizontal displacements at the boundary nodes underneath the footing are set at be zero, while the horizontal force at the nodes is set to at zero in the case of the smooth interface. For the frictional interface, a horizontal force equal to the nodal vertical reaction force, multiplied by the coefficient of friction, is applied as the friction force to the node at the friction surface. The loading process is simulated by applying increments of uniform vertical displacements to nodes at the boundary underneath the footing. The resulting reaction forces represent the equivalent loads. The rate of footing movement used in the analysis is 2×10^{-4} m/min with a time increment of 30 s per step.

5.2.2 Soil Conditions

The analyses are performed for both the homogeneous and inhomogeneous soil cases. The analysis of the footing on the homogeneous soil is performed in order to study the general bearing behavior and the failure pattern obtained from the method used. The analysis results will be compared to the results from the plasticity solution. The soil parameters employed in the analysis are shown in Table 6.1. A series of analyses using different values for the microstructural parameters β and n is carried out in order to study the effects of microstructural changes on the bearing behavior of the footing. β denotes the rate of the microstructure and the strength degradation of clay, while n provides the degree of a possible collapse of the structure at the initial state. Both the rough and smooth footing

Table 5.1 Soil parameters

Coefficient of permeability k_0 (m/s)	0.8×10^{-9}
Elastic shear modulus G_0 (kPa)	10250
Compression index λ	0.508
Swelling index κ	0.0261
Initial void ratio e_0	1.70
Coefficient of earth pressure K_0	1.0
Compression yield stress σ'_{mbi} (kPa)	61.0
Stress ratio at maximum compression M^*_m	1.09
Viscoplastic parameter m'	18.5
Viscoplastic parameter C_0 (1/s)	1.3×10^{-13}
Structural parameter σ'_{maf} (kPa)	31.5
Structural parameter β	0,1,5,20
Footing roughness (Note: μ is the coefficient of friction)	Rough,μ=0.1,μ=0.2, and smooth

interfaces are also used in the analyses.

For the inhomogeneous soil case, the analyses are performed using the same geometry and boundary conditions as those been used in the homogeneous soil study. However, the mean effective stress of the soil used in the analysis is linearly increases with depth, and it is assumed that the water table is located at the ground surface. The soil profile, the initial stress, and structural parameter σ'_{maf} are shown in Figure 5.15. The relation of the initial stress with depth is $\sigma'_{v0} = 40.0 + 10.2z$ (σ'_{v0}:kPa) when z is the depth from the ground surface (z:m). Table 6.1 also shows the parameters employed in the analysis for the NC clay. Different conditions of footing roughness conditions and β values are used in order to study their effects on the deformation pattern and the bearing capacity.

5.2.3 Results of the Analyses: Bearing Capacity of a Homogeneous Clay Stratum

Firstly, let us consider the effects of microstructural changes and soil strength degradation on the bearing behavior of the foundation. The microstructure parameter n is fixed at 0.52, while the microstructure β=20 is used to represent highly structured soil. For low-structured soil, β=0 is adopted and there will be no changes in the soil structure or the

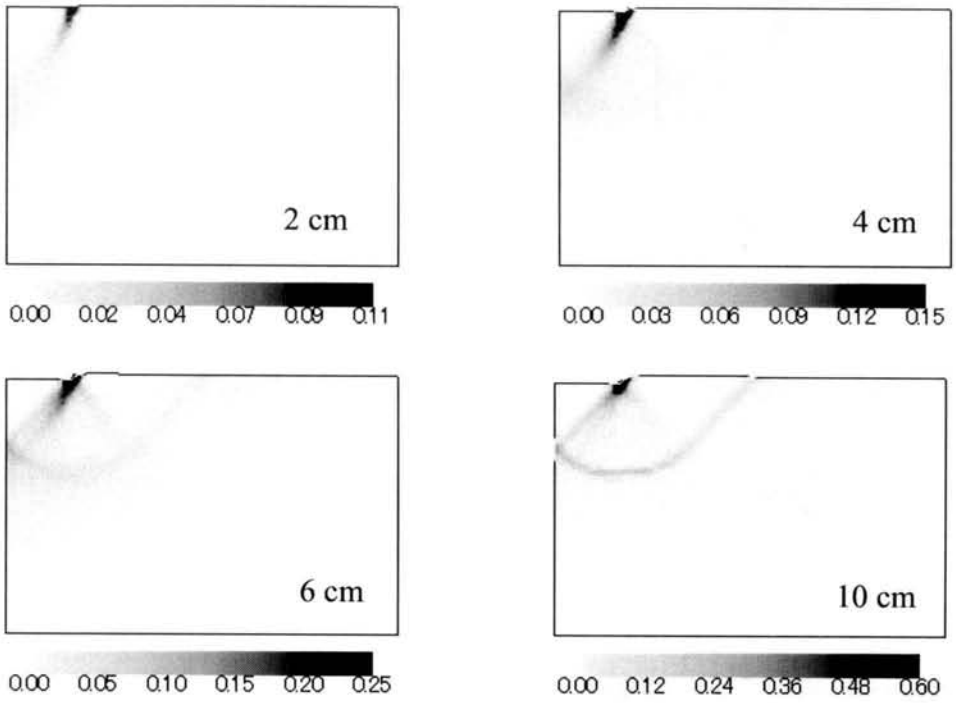

Figure 5.2 Distributions of the accumulated viscoplastic deviatoric strain at 2, 4, 6, and 10 cm of footing displacement for the homogeneous soil case in which β=20

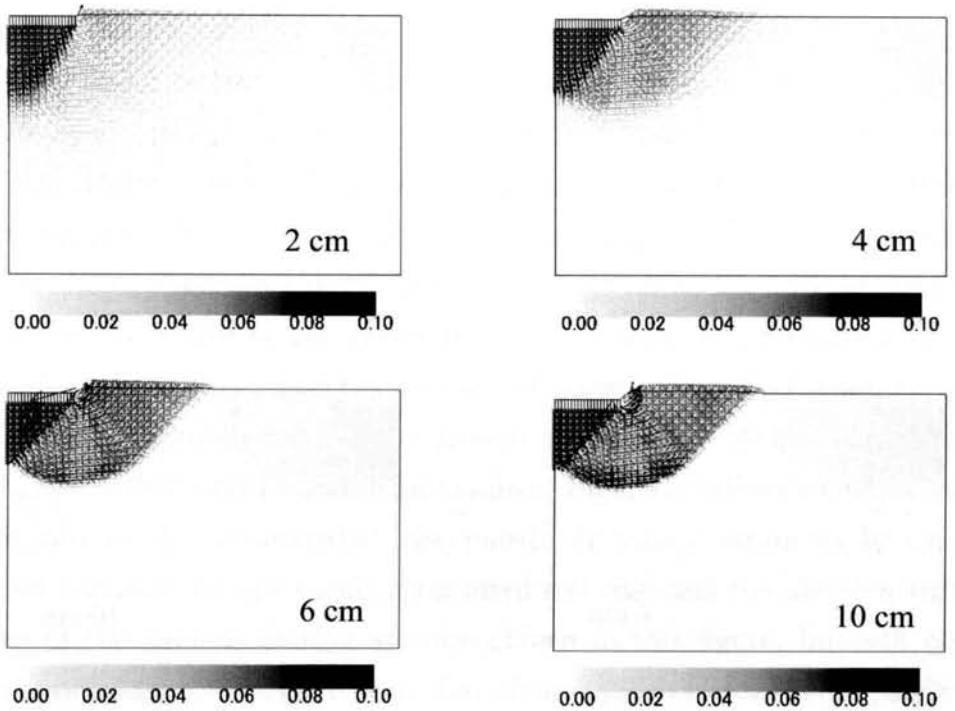

Figure 5.3 Vectors of the incremental nodal displacement at 2, 4, 6, and 10 cm of footing displacement for the homogeneous soil case in which β=20

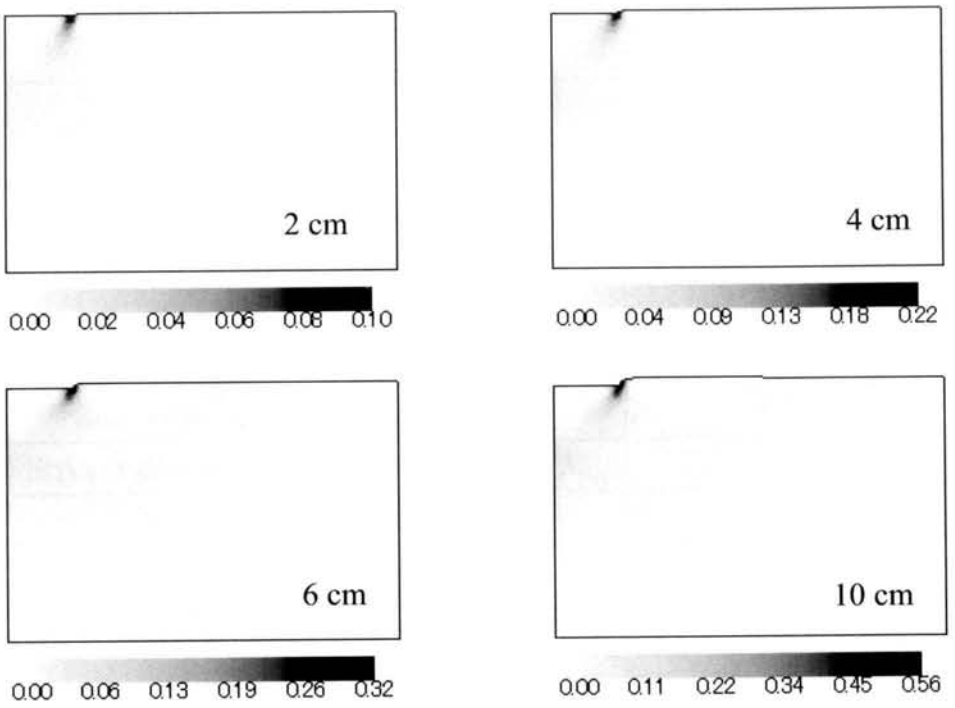

Figure 5.4 Distributions of the accumulated viscoplastic deviatoric strain at 2, 4, 6, and 10 cm of footing displacement for the homogeneous soil case in which β=0

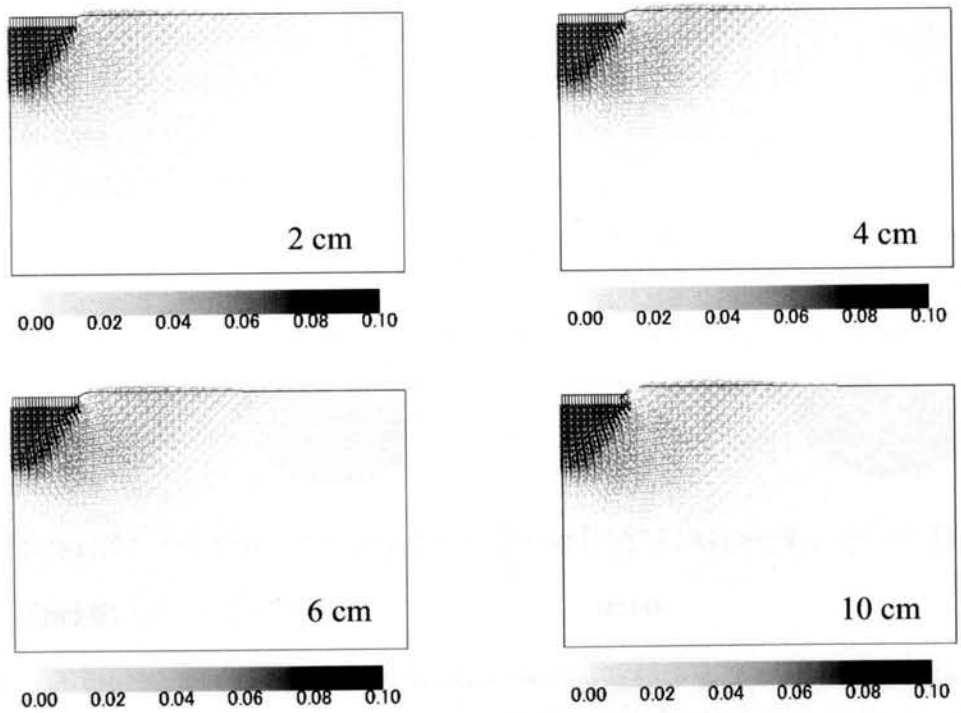

Figure 5.5 Vectors of the incremental nodal displacement at 2, 4, 6, and 10 cm of footing displacement for the homogeneous soil case in which β=0

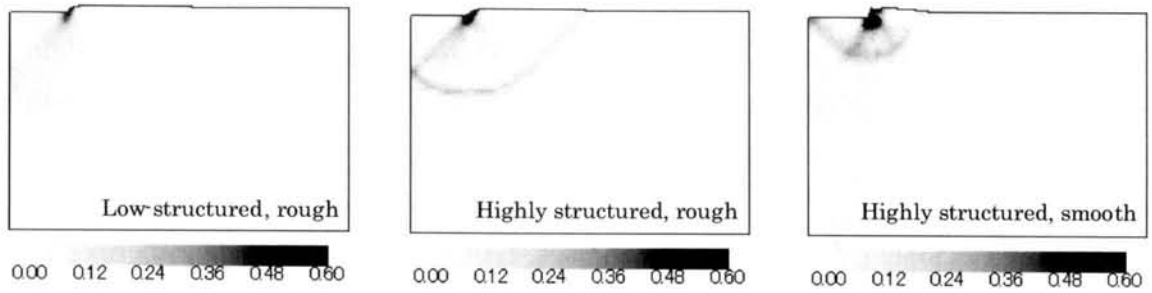

Figure 5.6 Distributions of the accumulated viscoplastic deviatoric strain at 10 cm of footing displacement for the homogeneous soil case with different values for β

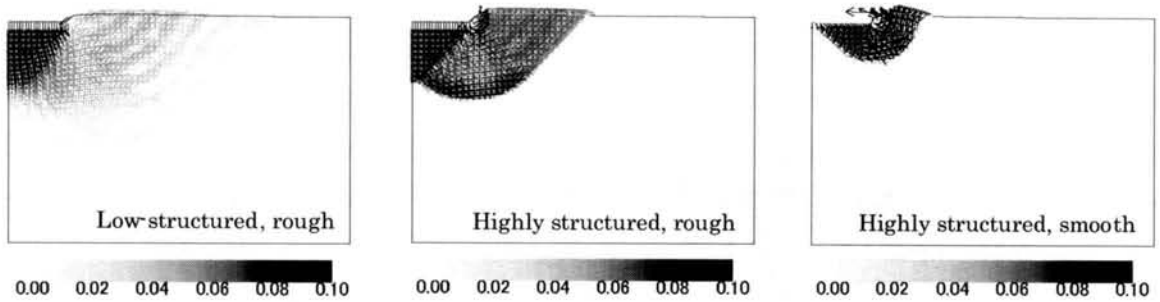

Figure 5.7 Vectors of the incremental nodal displacement at 10 cm of footing displacement for the homogeneous soil case with different values of β

degradation of the soil strength.

Figures 5.2 and 5.3 show the accumulated viscoplastic shear strain, $\gamma^p \equiv \int \sqrt{de_{ij}^{vp} de_{ij}^{vp}}$, and the increment nodal displacement vector obtained from the highly structured soil case, (β=20), when the footing is pushed into the ground for 2, 4, 6 and 10 cm respectively. The results obtained from the low-structured soil case, (β=0), are shown in Figures 5.4 and 5.5. It can be seen from Figure 5.2 that a shear zone starts from the edge of the footing, and then progresses downward to the symmetric axis. A second shear zone is then develops and progresses as a curve connected to the last shear zone, which extends farther as a straight line and eventually reaches the ground surface. The strain deformation pattern obtained agrees with Prandtl's failure mechanism. Figure 5.6 shows a comparison between the distribution of the accumulated viscoplastic deviatoric strain at 10 cm of footing displacement obtained for the highly structured soil case and the low-structure soil case. The results of the smooth footing are also shown in this figure, but will be discussed later. From this figure, it can be seen that clear strain localization is predicted in the case of soil with highly structured soil, namely, (β=20). The contour of the accumulated viscoplastic shear strain from the low-structured soil, (β=0), is also shown for comparison in Figure 5.6. No clear shear localization can be observed. However, the increment nodal

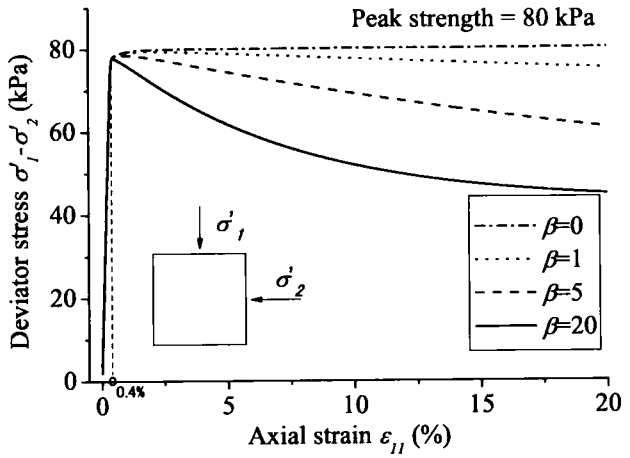

Figure 5.8 Results of the one element simulation with different values for β

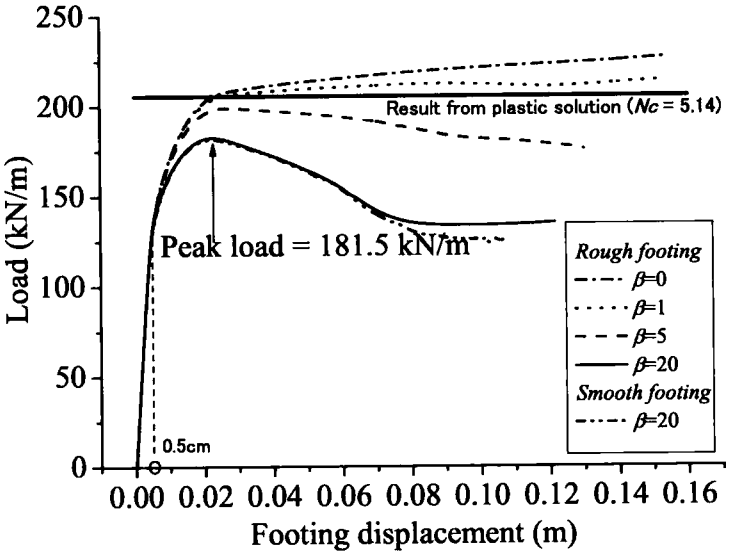

Figure 5.9 Load-displacement curves for the strip footing for the homogeneous soil case with different values for β

displacement vectors presented in Figure 5.7 shows that the mechanism of the ground deformation is the same as that for the highly structured soil, namely, the Prandtl's mechanism. Strain localization does not occur because of the lack of strain softening in the soil.

Figure 5.8 shows the results of a one element simulation of the shearing of soil with different microstructural parameters for β under plane strain conditions. Figure 5.9 shows the development of load at the footing surface obtained from the analysis. Ths strength of the highly structured soil degrades significantly with strain. Consequently, the bearing capacity obtained from this soil is lower than that obtained from the low-structured soil. All of the cases result in the same amount of loads at a footing displacement of 0.5 cm.

During this time, the total load increases almost linearly from zero. This is because the soil under low shear strain acts elastically, and the highly structured soil does not undergo the process of degradation. With the further displacement of the footing, the load from the case of highly structured soil, (β=20), reaches a peak value and then drops gradually to the residual value. As for the case of low-structured soil, (β=0), the increasing rate of the load drops rapidly after around 2 cm of footing displacement. Then, the load continues to increase monotonically with further displacement of the footing, and neither peak nor residual value is observed.

For the highly structured soil, a shear zone clearly develops. This shear zone acts like a "slip line". Only the soil located inside this "slip line" deforms further with the displacement of the footing. In the case of low-structured soil, there is no development of such a shear zone. Hence, by pushing the footing deeper into the soil, the soil that is located at deeper positions will be sheared and this results in a gradually increase in the load. It should be noted that the soil that is squeezed laterally and vertically from under the footing also results in the changes in the geometry of the problem and affects the results of the analysis.

Let us now compare the bearing capacity factors N_c calculated from the obtained load with the conventional solution for the bearing capacity. The value of bearing capacity factor N_c for homogeneous cohesive soil from the rigid plasticity solution (Hill 1950) is 5.14 (i.e., N_c=2+π). It should be noted that this value is the result of an analytical solution under perfectly undrained conditions and assumes no prefailure deformations of the soil. In contrast to the analytical solution, the soil constitutive model used in this study is rate-dependent with the finite strain analysis, and the loading has not been conducted under undrained conditions. For these reasons, it can be expected in advance that the bearing capacity factor obtained from the numerical analysis will be different from the factor obtained from the plasticity solution. However, a comparison between the obtained N_c and the theoretical value should facilitate our understanding of the effect of the degradation of the structure, i.e., the effect of the strain softening of the soil on the bearing capacity.

The peak shear strength obtained from the one element simulation, shown in Figure 5.8 (peak strength = 80 kPa), and the peak load from the highly structured soil (β=20), shown in Figure 5.9 (peak load = 181.5 kN/m), have been used to calculate the bearing capacity factor N_c. The calculation yields a N_c of 4.56, which is considerably lower than the value from the plasticity solution, namely, N_c = 5.14. This can be explained by considering the stress paths and the increase in deviator stress with the footing displacement of the

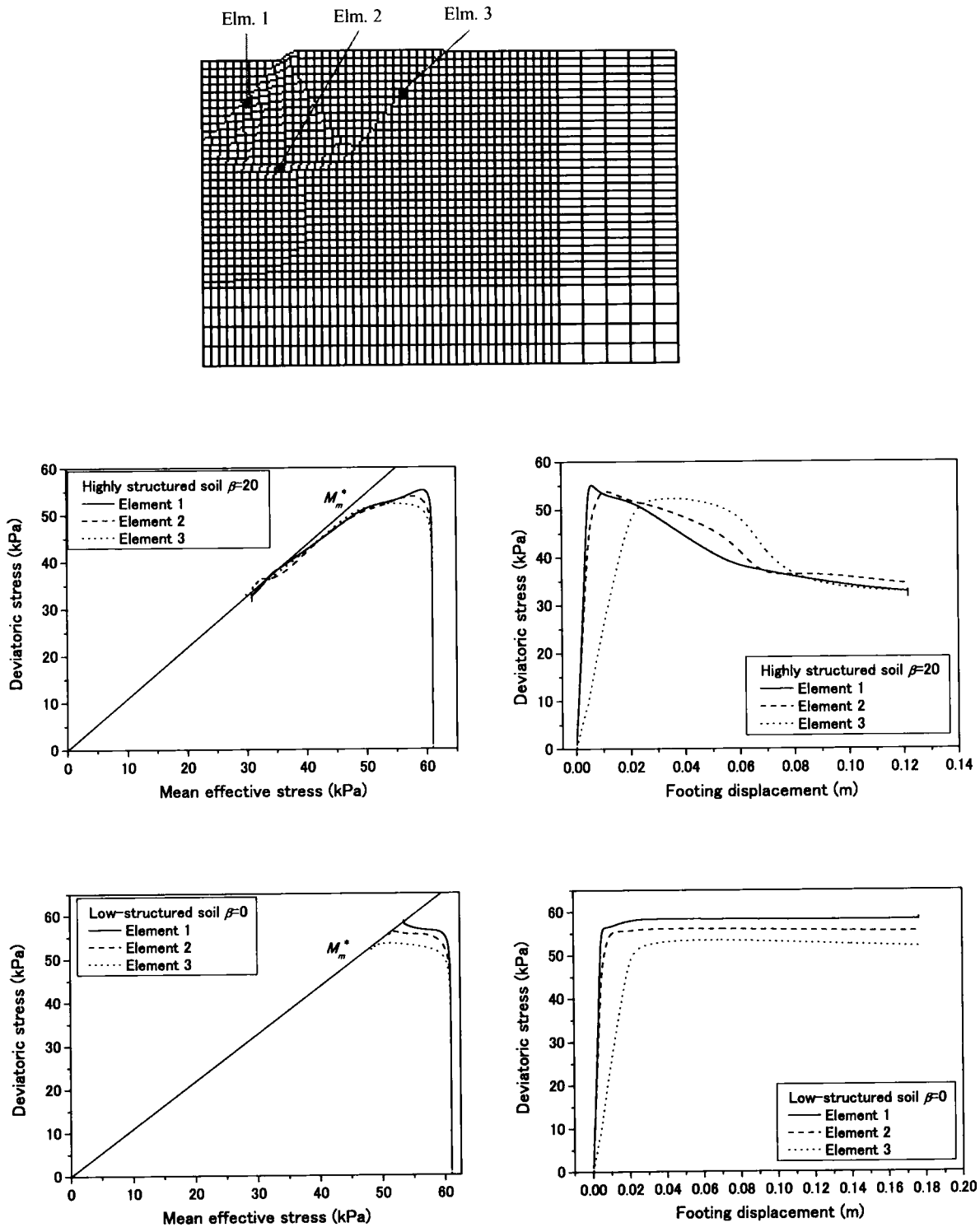

Figure 5.10 Stress paths and the development of deviator stress with the footing displacement for the homogeneous soil case with different values for β

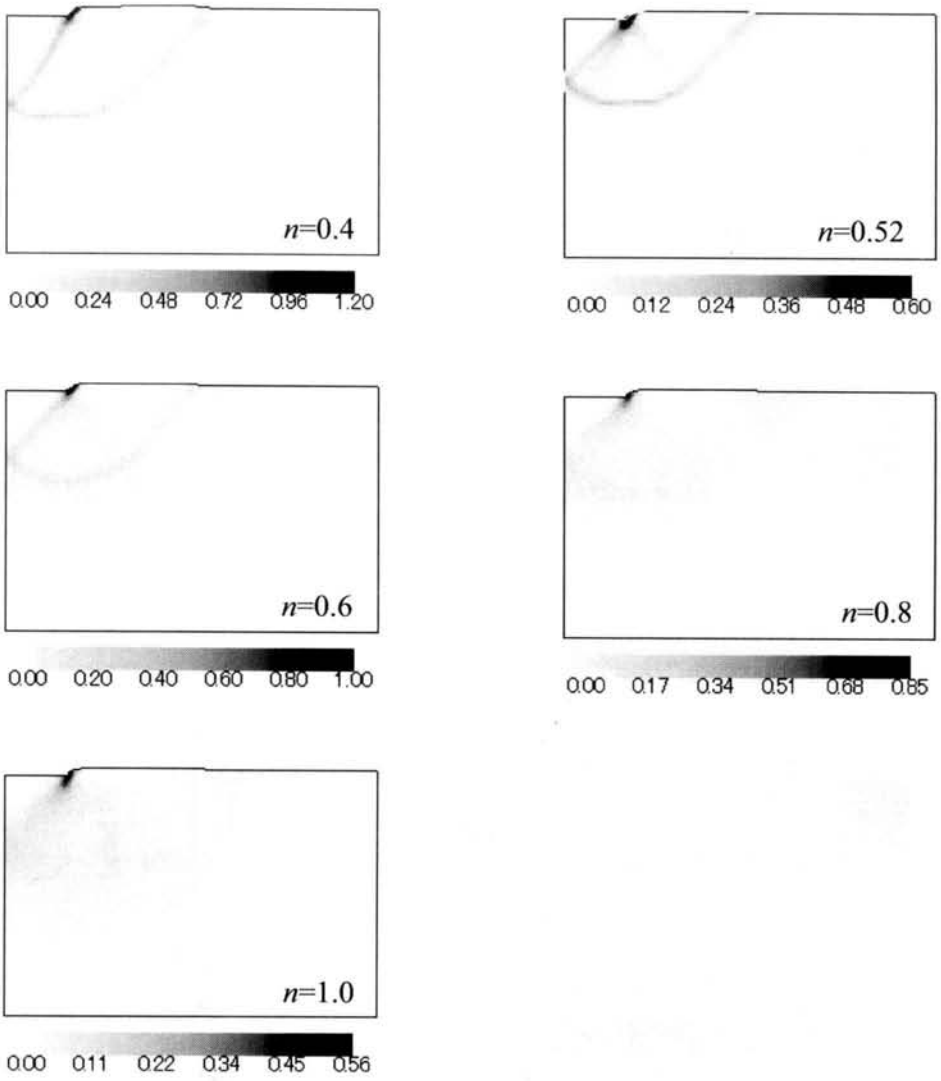

Figure 5.11 Distributions of the accumulated viscoplastic deviatoric strain at 10 cm of footing displacement for the homogeneous soil case with different values for n

elements in the shear zones shown in Figure 5.10. It can be seen that, as the shear zones develop in a manner of progression along with the loading of the footing. The soil along the shear zone is, therefore, neither sheared to its peak strength nor degraded to its residual strength at the same time. This results in a lower bearing capacity factor N_c for the highly structured soil.

Let us now consider the effects of friction between the surface of the footing and the soil. For the smooth strip footing on clay soil with constant undrained shear strength, both Hill and Prandtl's failure mechanisms are theoretically possible. For a rough footing, however, only the Prandtl's mechanism is valid while Hill's mechanism is not appropriate since it implies horizontal soil movements at the soil-footing interface. It can be seen

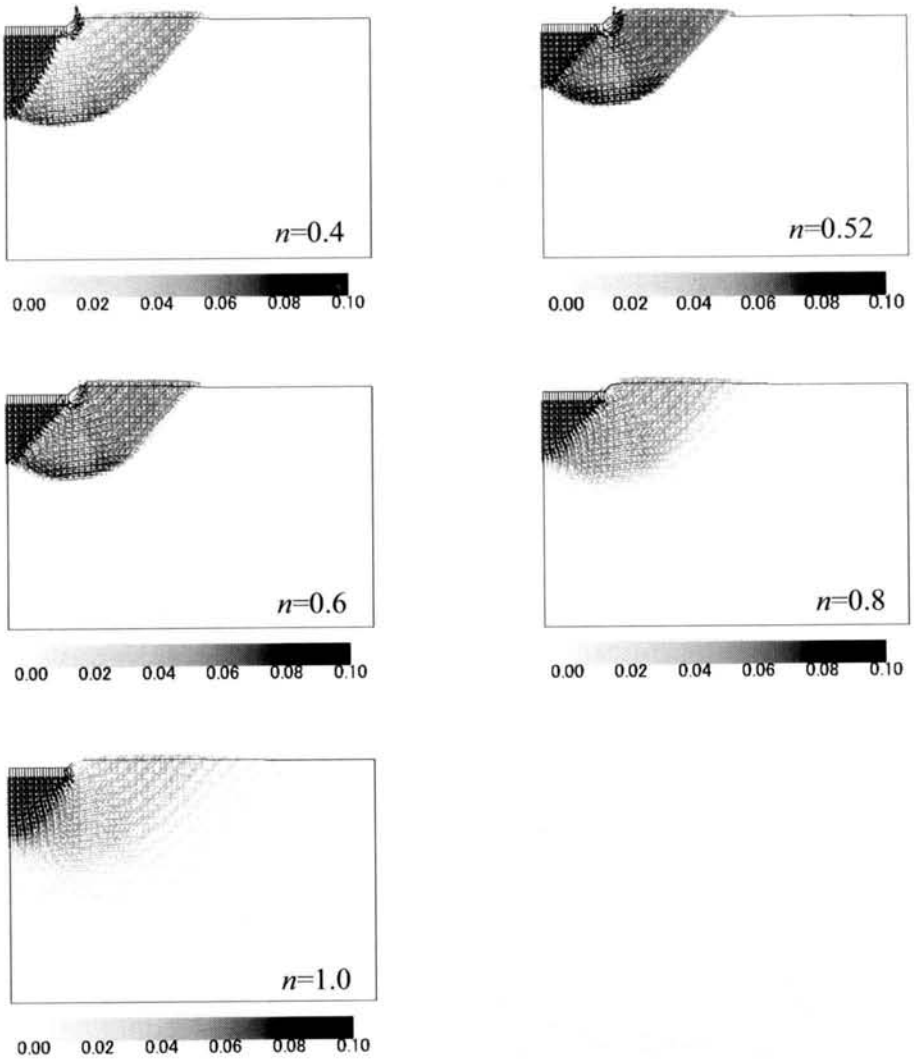

Figure 5.12 Vectors of the incremental nodal displacement at 10 cm of footing displacement for the homogeneous soil case with different values for n

in Figures 5.6 and 5.7 that by the method used here, Hill's mechanism is predicted for the smooth footing and Prandtl's mechanism is predicted for the rough footing. The classical plasticity solutions with two different mechanisms give the same value of $N_c = 5.14$ (Hill 1950). However, the comparison in Figure 5.9 shows that with a large footing displacement, the load predicted for the smooth footing is lower than predicted for the rough footing, which is different from that of the plasticity solution.

Next, in order to study the effects of microstructural parameter $n = \sigma'_{maf}/\sigma'_{mai}$, an analysis has been carried out with the microstructural parameter β fixed at 20, while microstructure parameter n was varied from 0.40 to 1.00. Microstructural parameter n provides a degree for the possible collapse of the structure at the initial stage and

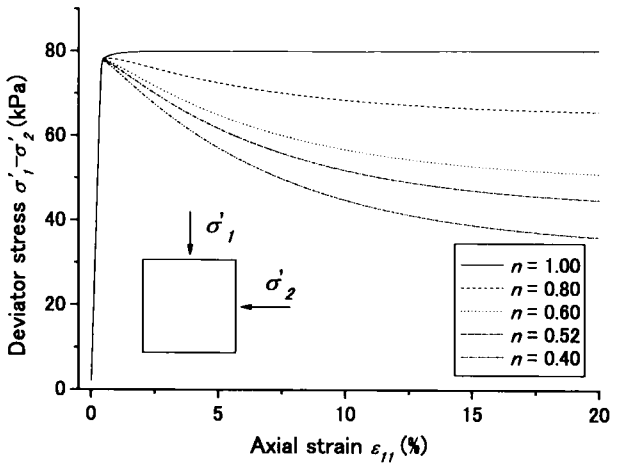

Figure 5.13 Results of the one element simulation with different values for n

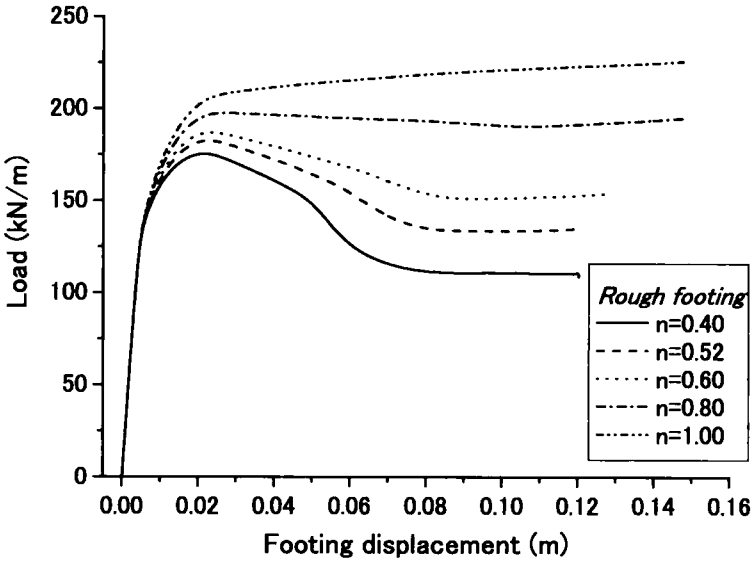

Figure 5.14 Load-displacement curves of the strip footing for the homogeneous soil case with different values for n

the results of the one element simulation of the shearing of the soil with different n under plane strain conditions are shown in Figure 5.13. Figures 5.11 and 5.12 show the comparisons of the accumulated viscoplastic deviatoric strain and the vectors of the incremental displacement, respectively, obtained from the soil with varied values for n when the footing is pushed 10 cm deep in to the ground. It is seen that when n approaches one, the degree of possible degradation of the soil strength is low, and no clear strain localization is obtained. On the other hand, when n is small, the strength of the soil can degrade more and a clear strain localization can be observed. Hence, we can conclude that the effects of the microstructural parameter n on the deformation behavior the of soil resemble the effects of β.

Figure 5.14 shows the development of load at the footing surface obtained from the analysis. Since β=20 is used, it can be seen that when n is not equal to zero, the load at the footing surface will rise to its peak value and then drop to its residual value afterward. These residual values for the load are controlled by n. When the value of n used is small enough, a clear strain localization can be developed and acts as the slip line, as mentioned in the previous section. As a result, the load obtained from these cases (n=0.4 and n=0.52) remains almost constant after it reaches the residual value. On the other hand, for cases in which the value of n used is rather large (n=0.6 and n=0.8), the strain localization which develops is not clear and cannot act perfectly as a slip line. Thus, the load increases again after it drops to the residual value.

5.2.4 Results of the Analyses: Bearing Capacity on a Clay Stratum with Strength which Increases with Depth

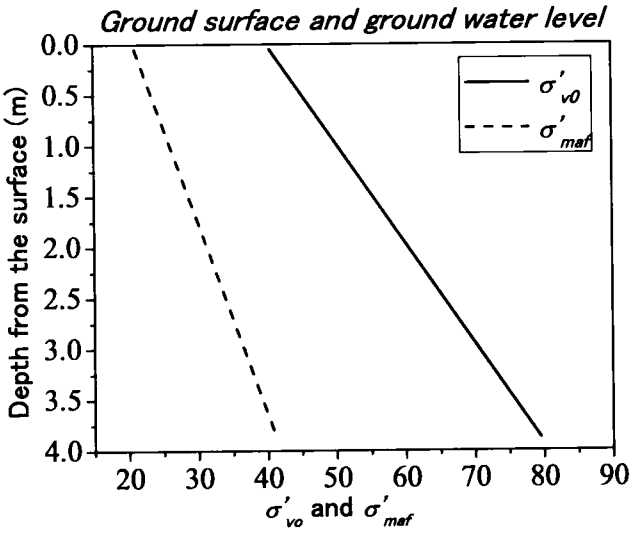

Figure 5.15 Profile of the initial stress of the soil and structural parameter σ'_{maf}

Figures 5.16 and 5.17 show the accumulated viscoplastic shear strain and the nodal displacement vectors obtained from the analyses, respectively. The failure mechanism from the rough footing appears to be Prandtl's mechanism. However, the distribution of the soil deformation is shallower than that for the homogeneous soil case. This is because the strength and the stiffness of the soil are increases with depth, and consequently, preventing the deformation zone from beings forced into the deeper soil. For the smooth footing case, Hill's mechanism is predicted. Figure 5.18 shows a comparison between the loads at the footing surface. The bearing capacity for the smooth footing is smaller than

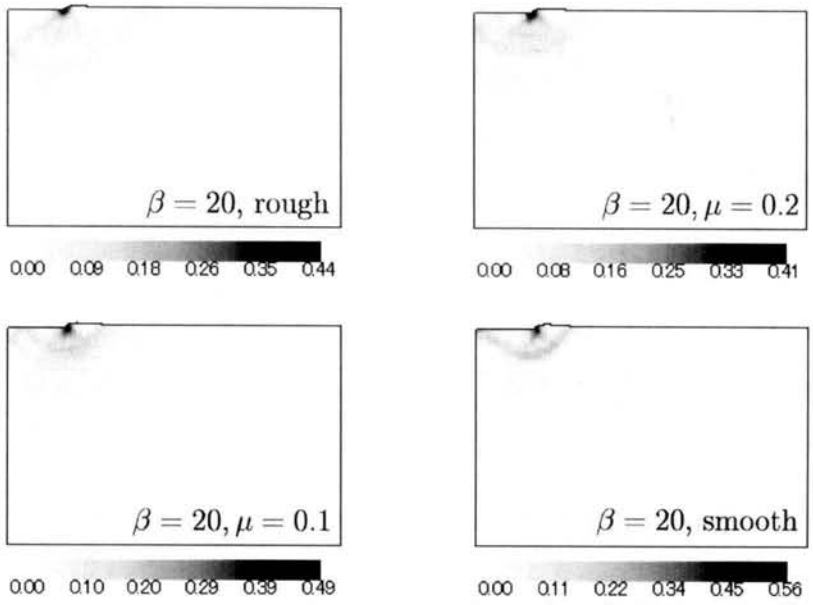

Figure 5.16 Distributions of the accumulated viscoplastic deviatoric strain at 6 cm of footing displacement for the inhomogeneous soil case

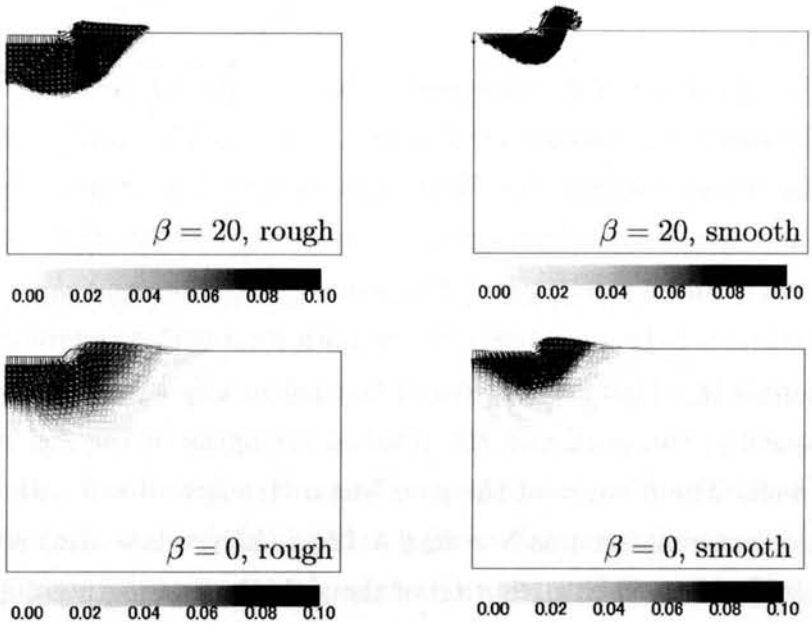

Figure 5.17 Vectors of the incremental nodal displacement at 6 cm of footing displacement for the inhomogeneous soil case

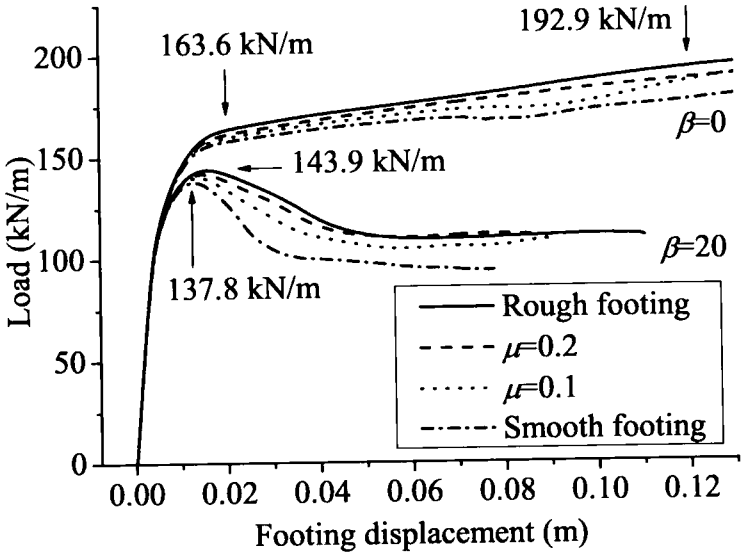

Figure 5.18 Load-displacement curves of the strip footing for the inhomogeneous soil case

that for the rough footing. This is because the horizontal restraint imposed at the soil-footing interface causes the deformation mechanism to penetrate deeper into the soil in the rough footing case. As the undrained shear strength increases with depth, as shown in Figure 5.15, the bearing capacity obtained is larger for the rough footing than that for the smooth footing.

Distributions of accumulated viscoplastic shear strain for the case of footing with coefficients of friction μ=0.1 and 0.2 are also shown in the Figure 5.16. The failure pattern obtained from these cases can be thought of as the intermediate strain localization pattern for the rough and the smooth footings and therefore, it shows the transition between Prandtl's and Hill's failure mechanisms. Consequently, the bearing capacity obtained for the frictional footing is between those of the smooth footing and the rough footing as can be seen in Figure 5.18. The initial stress of the soil in this case increases linearly with depth. Consequently, the peak and the residual strengths of the soil increase linearly with depth as well. The relation of the peak shear strength of soil with depth obtained from the one element simulation is $S = 52.8 + 12.5z$ (kPa) while z(m) is the depth from the ground surface. Since the distribution of the soil shear strength is linear with depth, it is possible to obtain an estimate of the bearing capacity using the results from the plasticity solutions proposed by Davis and Booker (1973) and Nakase (1981). The peak shear strength obtained from the one element simulation mentioned before and the peak loads from the highly structured soil, β=20, shown in Figure 5.18, 143.9 kN/m for the

rough footing and 137.9 kN/m for the smooth footing, have been used to calculate the bearing capacity factor N_c. The calculation yields N_c values of 5.22 and 5.45 for the smooth and the rough footings, respectively. The obtained valued from the numerical simulation is considerably lower than that from the plasticity solution, which yields N_c values of 5.48 and 5.85 for the soil profile used in this study. For the low-structured soil, the total load at the footing gradually increases with the displacement of the footing due to the lack of strain localization and strength degradation. The trend of the results obtained is similar to that for the homogeneous soil case.

It is worth noting that, since the strength and the stiffness of soil increase with depth, the increasing rate of the load in the low-structured soil is considerably high compared to that for the homogeneous soil case. As shown in Figure 5.18, the load for the rough footing on low-structured soil obtained at footing displacement of 12 cm is almost 20% higher than the load obtained at a footing displacement of 2 cm.

5.3 Numerical Simulation of a Square Footing

5.3.1 Finite Element Formulation, Geometry, and Soil Conditions

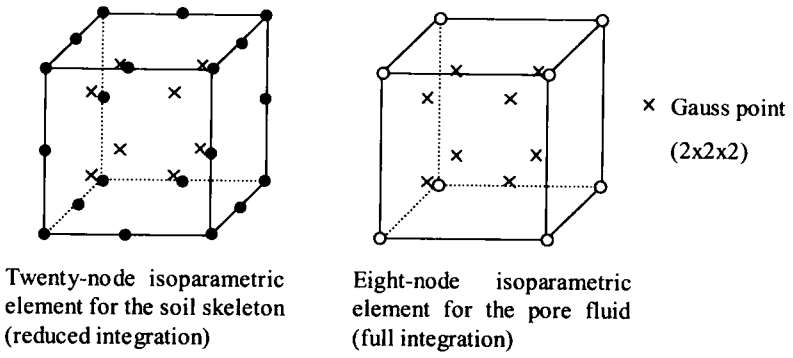

Figure 5.19 Isoparametric elements used in the three-dimensional finite element method

The finite formulation used in this section is the same as that presented in Chapter 2, but the finite element code is formulated in a three-dimensional setting. The element type used is a twenty-node isoparametric element with a reduced Gaussian (2×2×2) integration for the soil skeleton and an eight-node isoparametric element with full (2×2×2) integration for the pore fluid, as illustrated in Figure 5.19.

Simulations of the square rigid footing on a clay ground are conducted under three-dimensional conditions. The size of the square footing is 2 m×2 m. The finite element

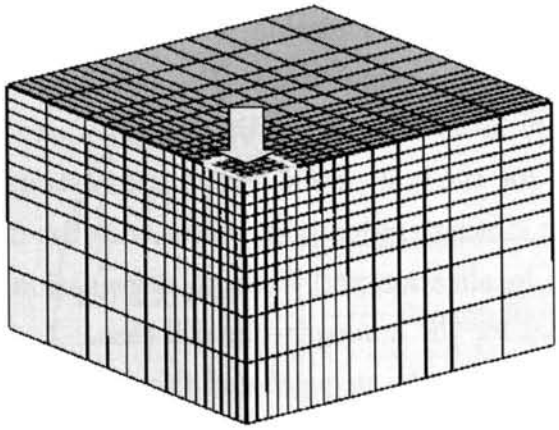

Figure 5.20 Finite element mesh used in the 3D analysis of the square footing

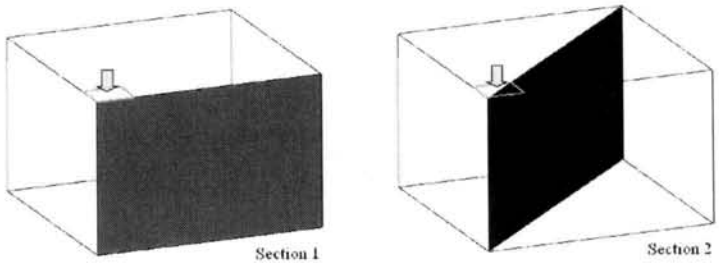

Figure 5.21 Sections used to demonstrate the accumulated viscoplastic deviatoric strain

mesh of the model footing with width and depth (6.0 m×6.0 m×4.0 m), respectively, is composed of (15×15×11) elements. Note that the size of one side of the mesh is the same as the size of the mesh used in the analysis of the strip footing, but a coarser mesh is used due to computation time and cost limitations of the computing systems available. A quarter of the footing with (5×5) elements and (0.2 m×0.2 m) width spans is simulated in the upper corner of the mesh, as shown in Figure 5.19. The boundary conditions underneath the footing are chosen to represent rough and smooth footing-soil interfaces. The rate of footing movements used in the analysis is 2×10^{-4} m/min, which is equal to that used in the strip footing case. The time increment employed is 60 s per one step.

In the analysis of the square footing case, only the homogeneous soil condition is considered. The soil parameters used in the strip footing case are used again here. Two values for the microstructural parameter, β=0 and β=20, are employed to represent the low-structured soil and the highly structured soil, respectively.

5.3.2 Results of the Analyses

Figures 5.22-5.25 show the accumulated viscoplastic shear strain and the increment nodal displacement vectors of the highly structured soil case, β=20, when the footing is pushed into the ground for 2, 4, 6 and 10 cm, respectively. The distribution of the accumulated viscoplastic shear strain is shown in two sections, namely, a section on one side of the mesh and a section across the mesh. These sections are illustrated in Figure 5.21. The results of the low-structured soil case, β=0, are shown in Figures 5.26-5.29. From the obtained results, it can be seen that the deformation pattern of the soil is similar to Prandtl's failure mechanism. Compared to the results from the strip footing case, however, it is clear that the distribution of the soil deformation beneath the footing is shallower in the square footing case. Moreover, the zone of soil that is pressed sideways and upward by the footing displacement is smaller as well. The slip surface does not extend through the soil surface, but ends somewhere inside the soil. Therefore, unlike the strip footing case, the obtained deformation pattern agrees with the "local shear failure".

Let us now consider the difference between the results of a highly structured soil case and a low-structured soil case. The viscoplastic strain produced is larger, and a clearer strain localization is predicted for the highly structured soil case. However, the comparison shows that the strain localization given in the square footing case is not as clear as that in the strip footing case. This difference is partly due to the mesh finenesses and partly due to the fact that there is a lower constraint of the soil under the three-dimensional conditions than under the plane strain conditions.

Figure 5.31 shows a comparison between the development of the load at the footing surface obtained from the square footing case and that obtained from the strip footing case. Note that the sizes of the footing in the two cases are equal to each other, and therefore, the amounts of the calculated load can be directly compared. The same trend is obtained from the square footing case, that is the load increases to the peak value and then drops to the residual value for the highly structured soil case, while the load continues to increase with the displacement of the footing for the low-structured soil case. It can be seen from the increment nodal displacement vectors, that the slip line predicted in the highly structured soil in the strip footing case is also observed in the highly structured soil in the square footing case, and hence, the same trend is seen in the results.

During the early part of loading, in which the loads increase almost linearly with the footing displacement, the increasing gradient is higher in the case of the square footing. This is due to the resistance of the soil behind the square footing. Consequently, for the low-structured soil case, the load and the gradient of the load increment from the

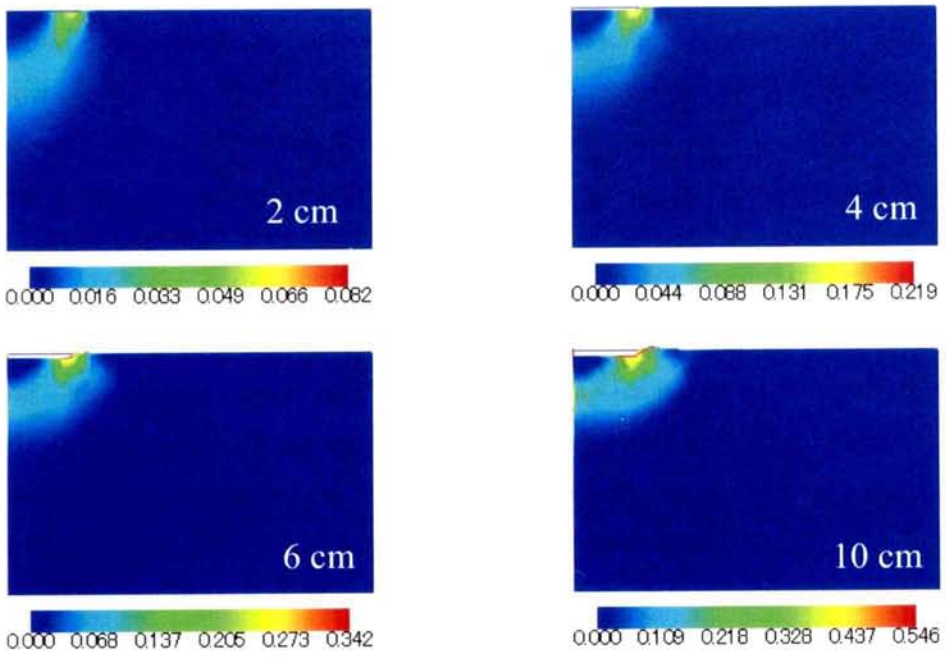

Figure 5.22 Distributions of the accumulated viscoplastic deviatoric strain at 2, 4, 6 and, 10 cm of footing displacement for the square rough footing case in which β=20 in Section 1

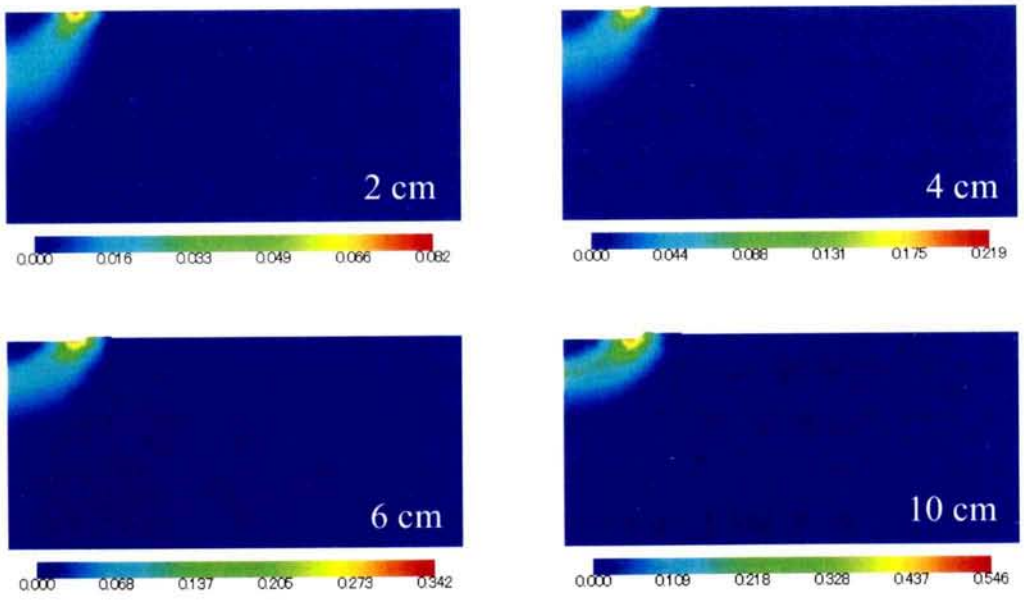

Figure 5.23 Distributions of the accumulated viscoplastic deviatoric strain at 2, 4, 6, and 10 cm of footing displacement for the square rough footing case in which β=20 in Section 2

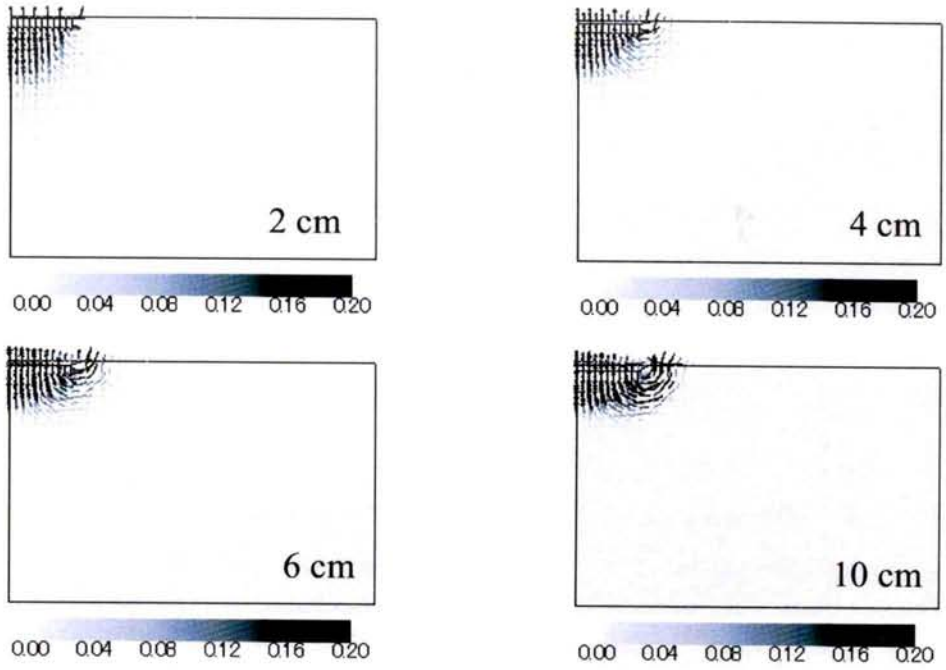

Figure 5.24 Vectors of the incremental nodal displacement at 2, 4, 6, and 10 cm of footing displacement for the square rough footing case in which β=20 in Section 1

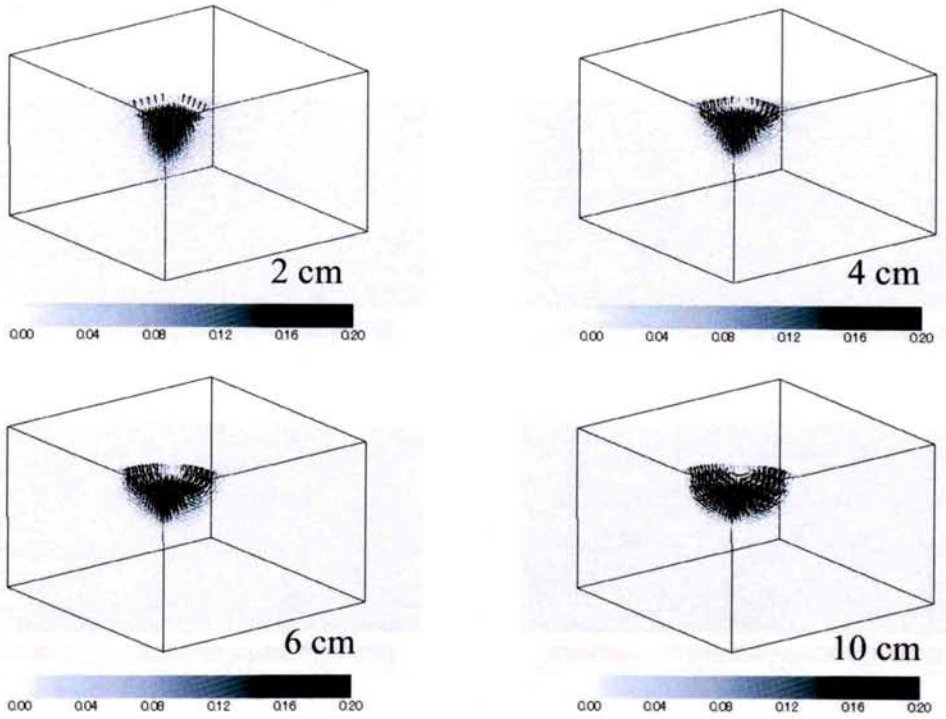

Figure 5.25 Vectors of the incremental nodal displacement at 2, 4, 6, and 10 cm of footing displacement for the square rough footing case in which β=20

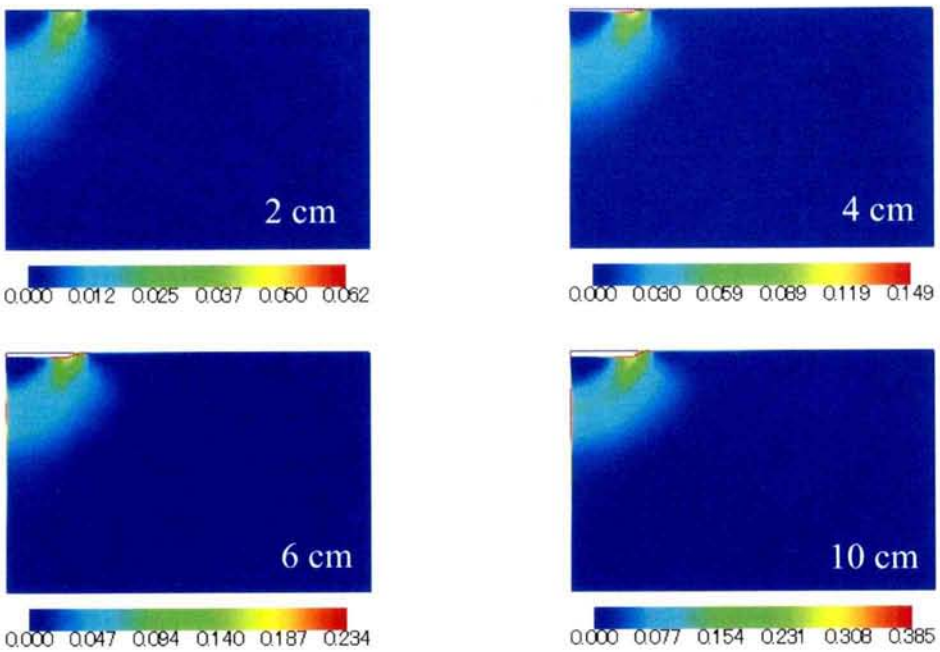

Figure 5.26 Distributions of the accumulated viscoplastic deviatoric strain at 2, 4, 6, and 10 cm of footing displacement for the square rough footing case in which β=0 in Section 1

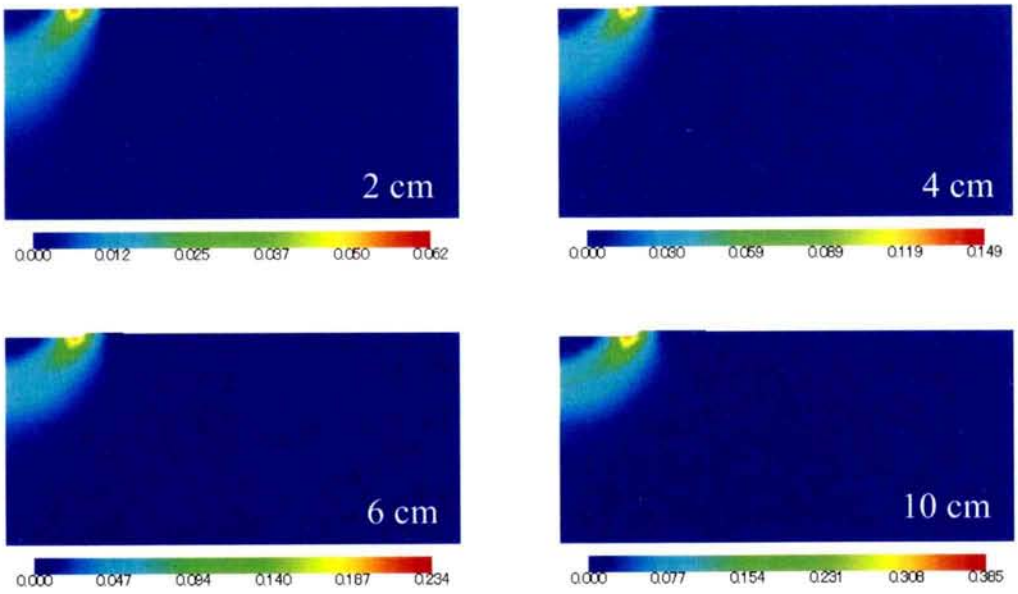

Figure 5.27 Distributions of the accumulated viscoplastic deviatoric strain at 2, 4, 6, and 10 cm of footing displacement for the square rough footing case in which β=0 in Section 2

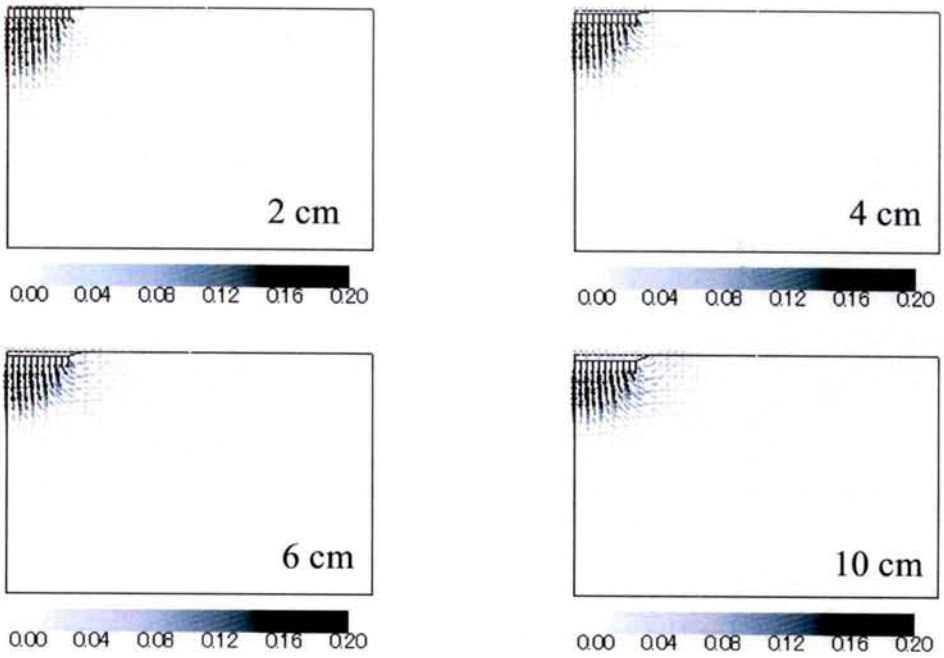

Figure 5.28 Vectors of the incremental nodal displacement at 2, 4, 6, and 10 cm of footing displacement for the square rough footing case in which β=0 in Section 1

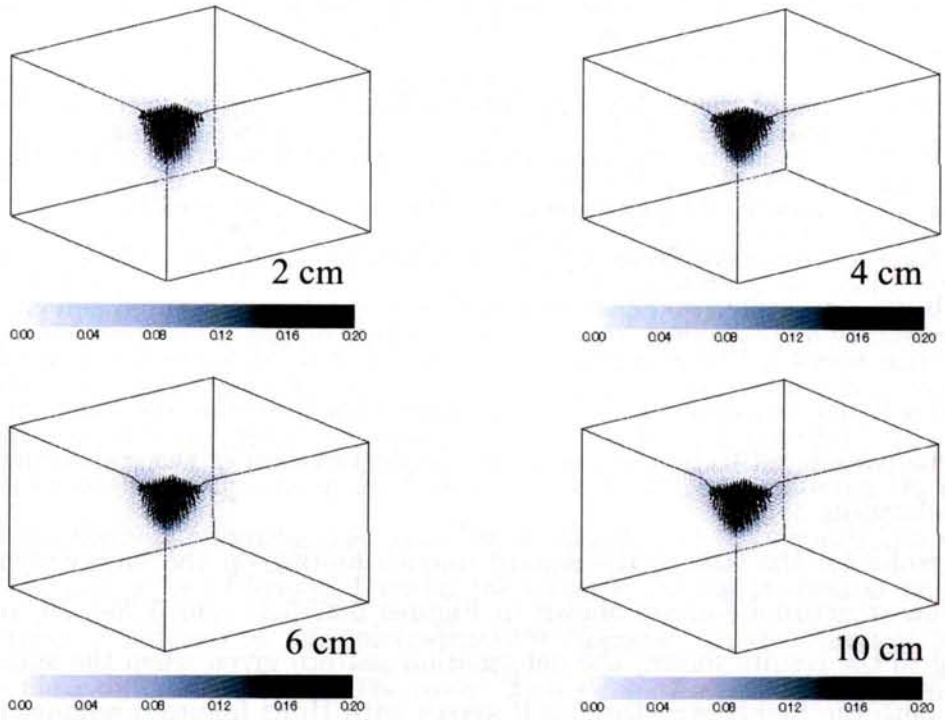

Figure 5.29 Vectors of the incremental nodal displacement at 2, 4, 6, and 10 cm of footing displacement for the square rough footing case in which β=0

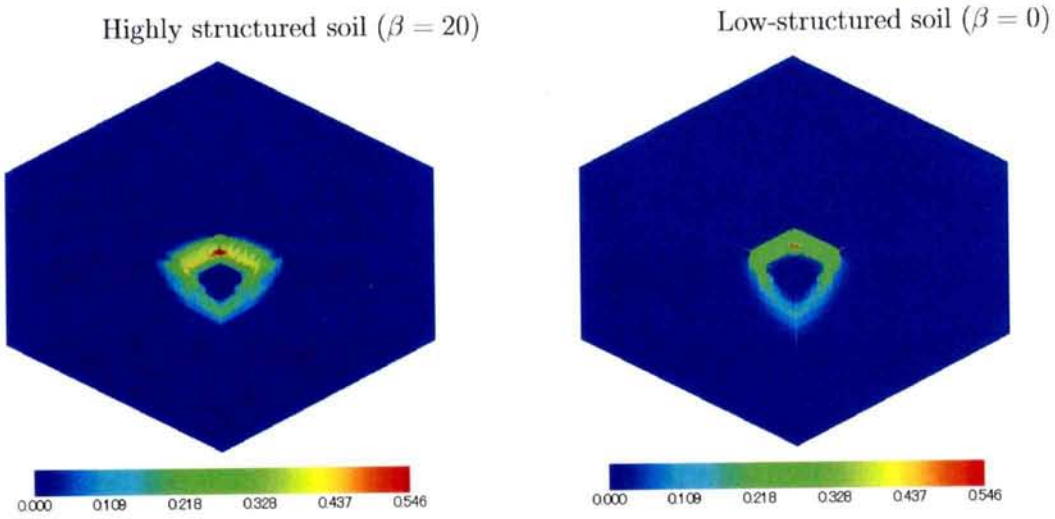

Figure 5.30 Distributions of the accumulated viscoplastic deviatoric strain at 10 cm of footing displacement for the square rough footing case on highly structured soil and low-structured soil

square footing are considerably higher than those from the strip footing. The same trend was obtained from the results of studies proposed by Siddiquee et al. (2001) and Ahadi (2003), in which the rectangular and strip footings with the same width-to-length ratio on a sandy ground were compared.

As for the results of the highly structured soil case, it can be seen that the peak load obtained from the square footing case is almost equal to that from the strip footing case, despite the above mentioned soil resistance. This can be explained by considering Figure 5.30, in which a comparison between the accumulated viscoplastic shear strain obtained from the highly structured soil case and that from the low-structured soil case when the footing displacement is 10 cm, is shown. It is seen that the deformation zone of the highly structured soil case is smaller and shallower than that from the low-structured soil case. This can be considered to be the results of the degradation of the soil strength and the strain localization.

The results for the case of the square smooth footing on the highly structured soil and the low-structured soil are shown in Figures 5.32-5.35 and 5.36-5.39, respectively. According to the results shown, the deformation pattern given when the smooth footing is loaded onto the highly structured soil agrees with Hill's failure mechanism, while the deformation given in the low-structured soil case agrees with Prandtl's failure mechanism. The footing loads of the rough and the smooth square footing cases are plotted against the footing displacement in Figure 5.41. Since the friction condition at the footing does not

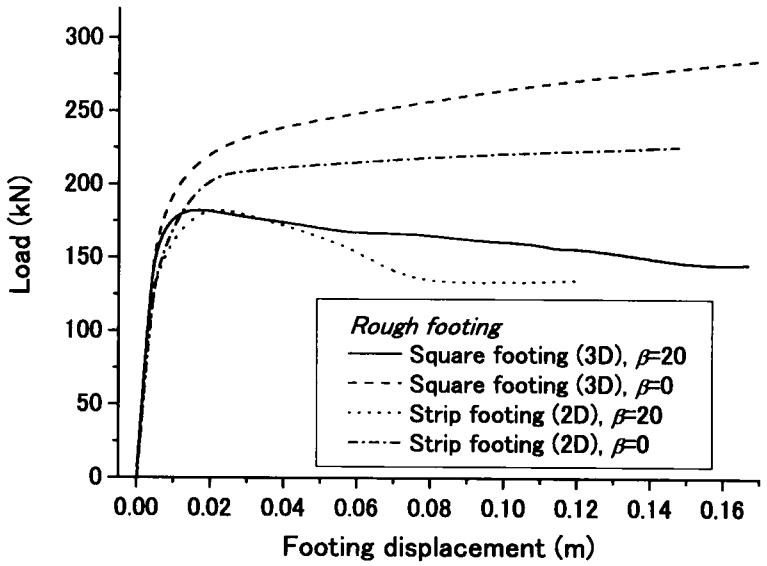

Figure 5.31 Comparison between the load-displacement curves of the strip footings and the square footings

affect much of the soil deformation mechanism in the low-structured soil case, it can be seen that the load obtained from the smooth footing is almost equal to that of the rough footing. On the other hand, the loads of the smooth footing on the highly structured soil are quite a bit than those of the rough footing on highly structured soil. This result is due to the difference in the deformation patterns.

Moreover, it can be seen from Figures 5.32 and 5.33 that the soil at the footing surface is sheared horizontally due to the lack of the friction from the footing when loaded by the smooth footing. As a result, the microstructure of the soil at the footing surface is destroyed, and hence, the strength degradation of the soil. This phenomenon is confirmed by the a comparison between the stress paths obtained from the soil elements under the center of the footing in both the rough and the smooth footing cases. The positions of the soil elements and the corresponding stress paths are shown in Figure 5.42. In the Element 1, which is located directly under the footing, a clear difference between the stress path obtained from the rough footing case and that obtained from the smooth footing case can be seen. The soil in the Element 1 under the smooth footing is sheared and the mean effective stress is reduced as the microstructure changes. In the Element 2, however, there is no clear difference between the cases. This strength degradation of the soil under the footing and the difference in the deformation mechanism lead to a smaller bearing capacity of the smooth footing on highly structured soil.

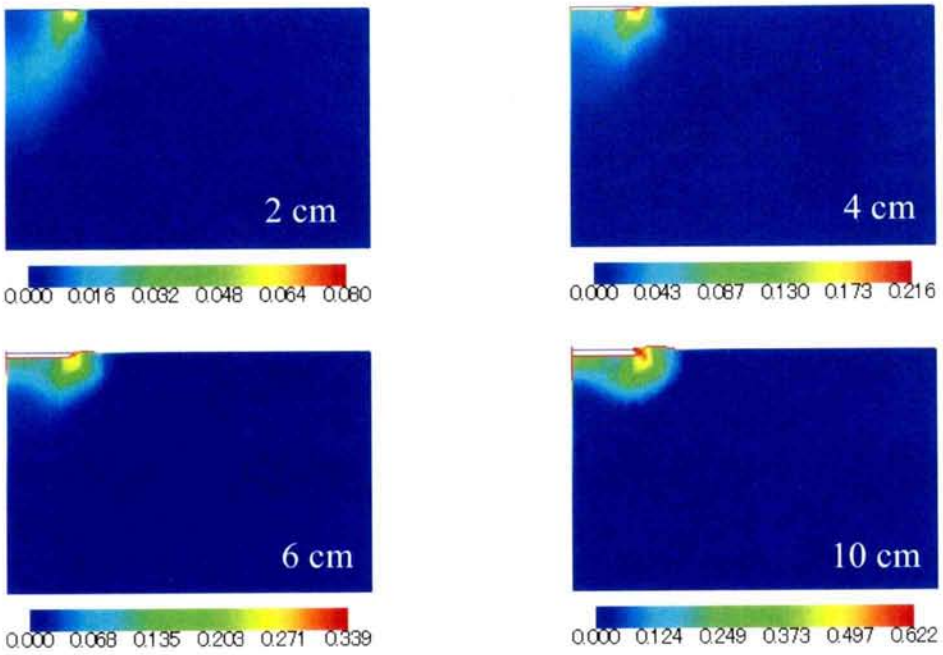

Figure 5.32 Distributions of the accumulated viscoplastic deviatoric strain at 2, 4, 6, and 10 cm of footing displacement for the square smooth footing case in which β=20 in Section 1

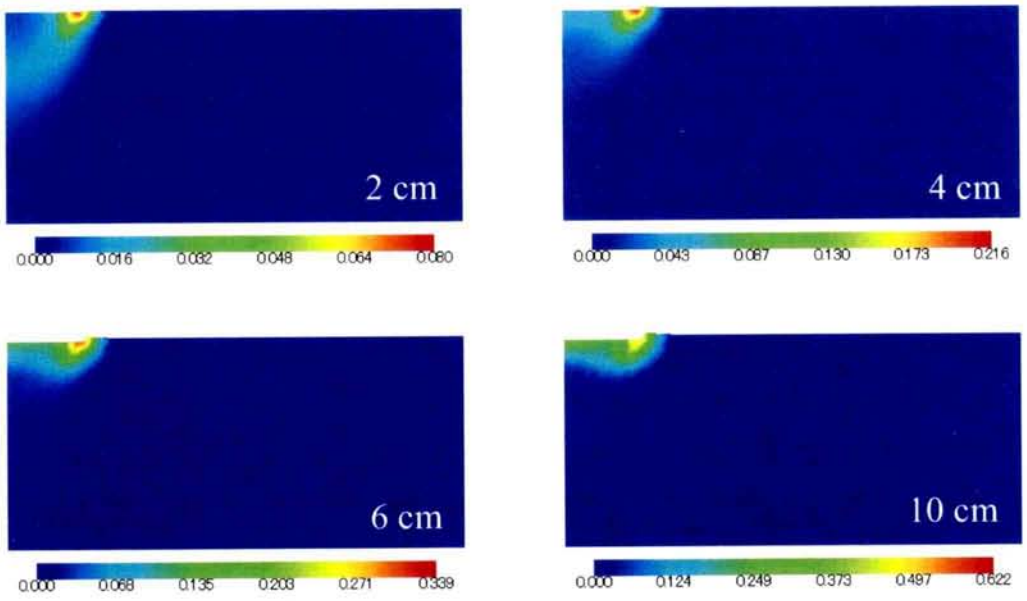

Figure 5.33 Distributions of the accumulated viscoplastic deviatoric strain at 2, 4, 6, and 10 cm of footing displacement for the square smooth footing case in which β=20 in Section 2

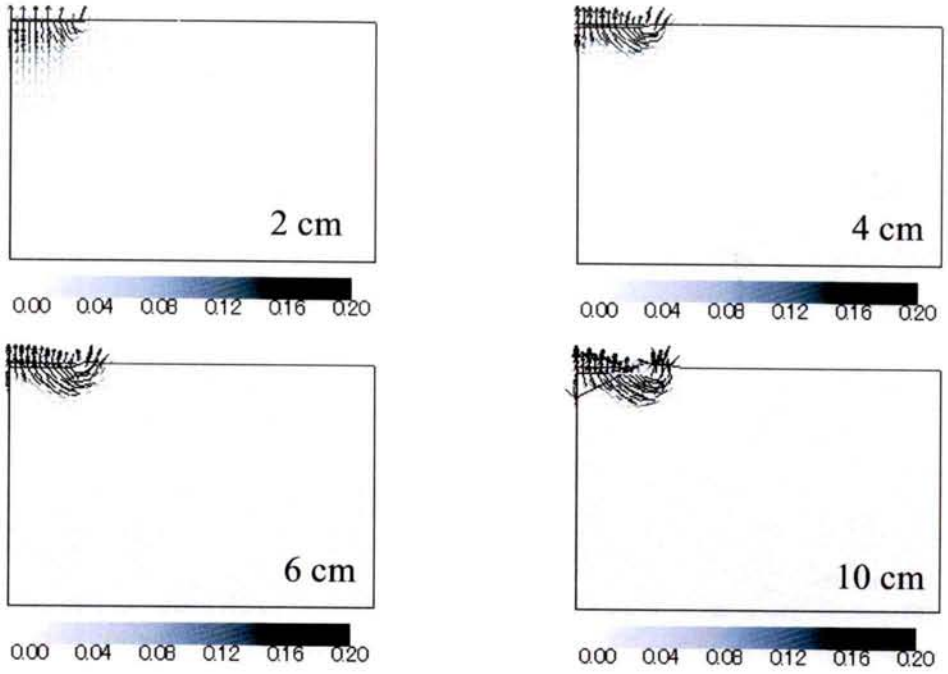

Figure 5.34 Vectors of the incremental nodal displacement at 2, 4, 6, and 10 cm of footing displacement for the square smooth footing case in which β=20 in Section 1

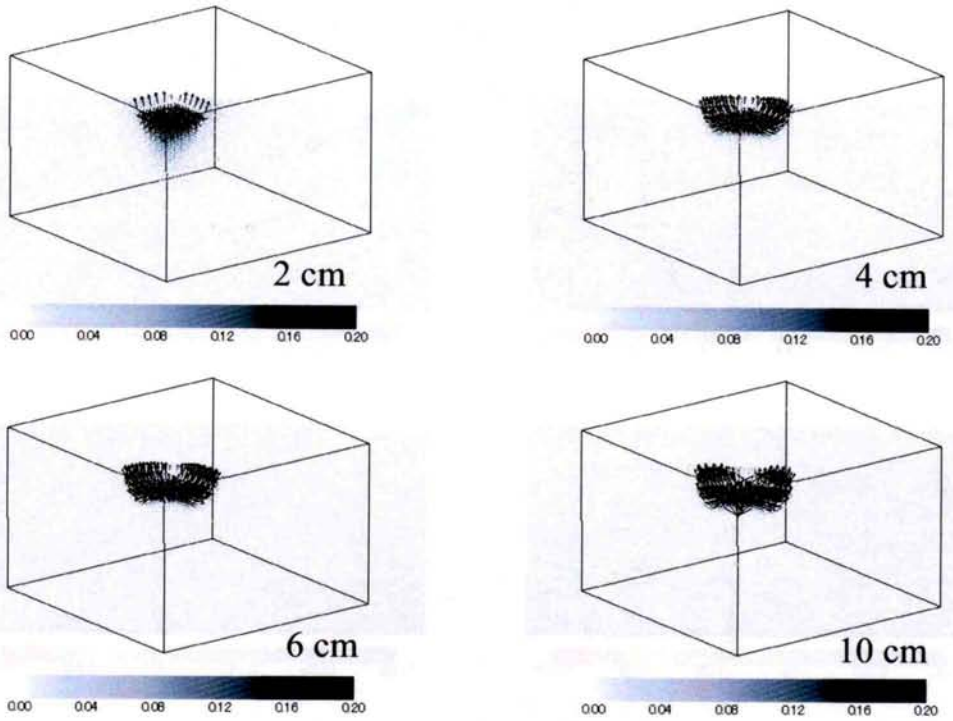

Figure 5.35 Vectors of the incremental nodal displacement at 2, 4, 6, and 10 cm of footing displacement for the square smooth footing case in which β=20

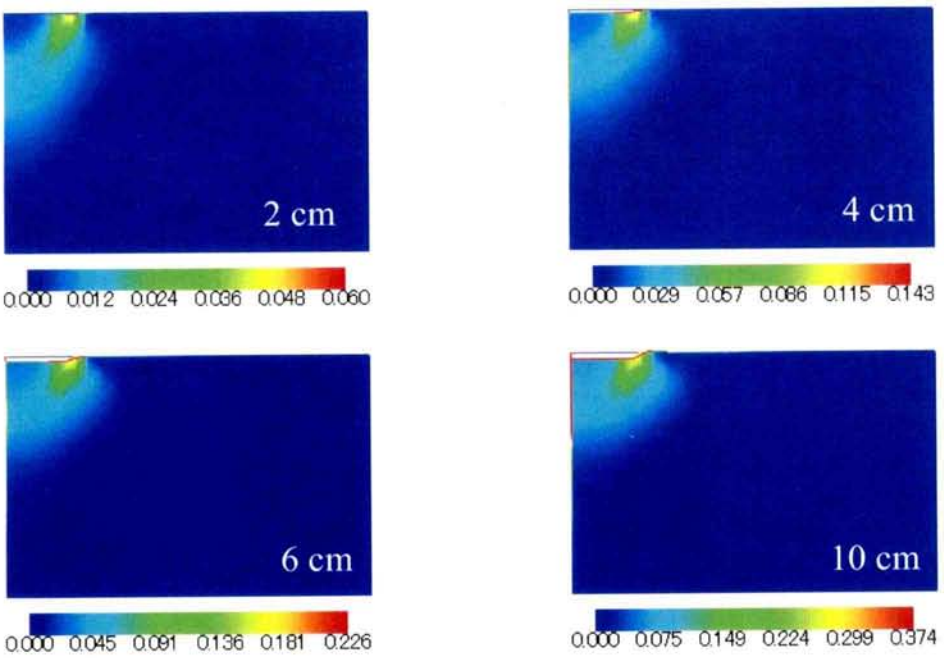

Figure 5.36 Distributions of the accumulated viscoplastic deviatoric strain at 2, 4, 6, and 10 cm of footing displacement for the square smooth footing case in which β=0 in Section 1

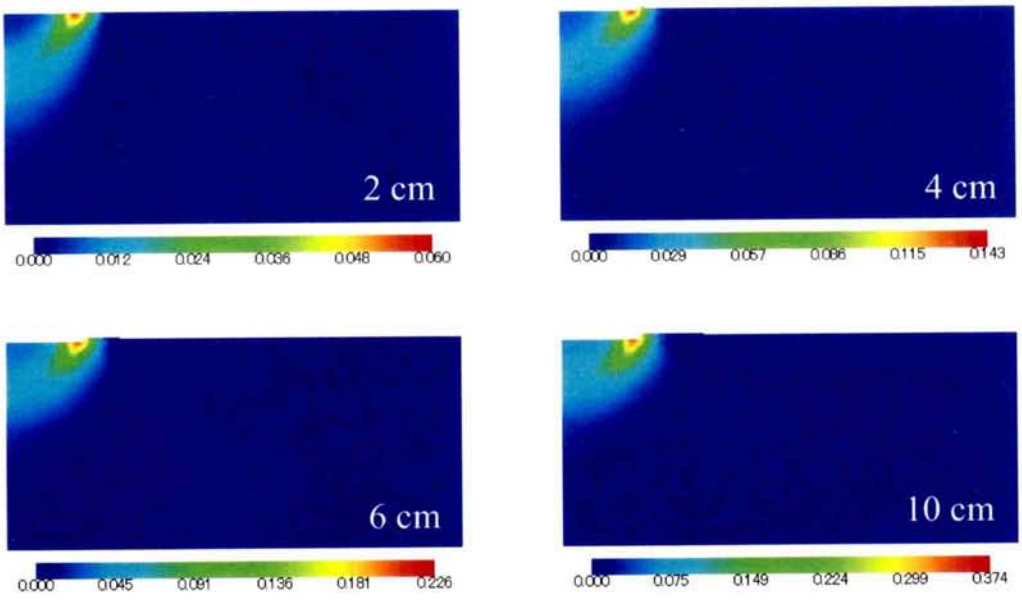

Figure 5.37 Distributions of the accumulated viscoplastic deviatoric strain at 2, 4, 6, and 10 cm of footing displacement for the square smooth footing case in which β=0 in Section 2

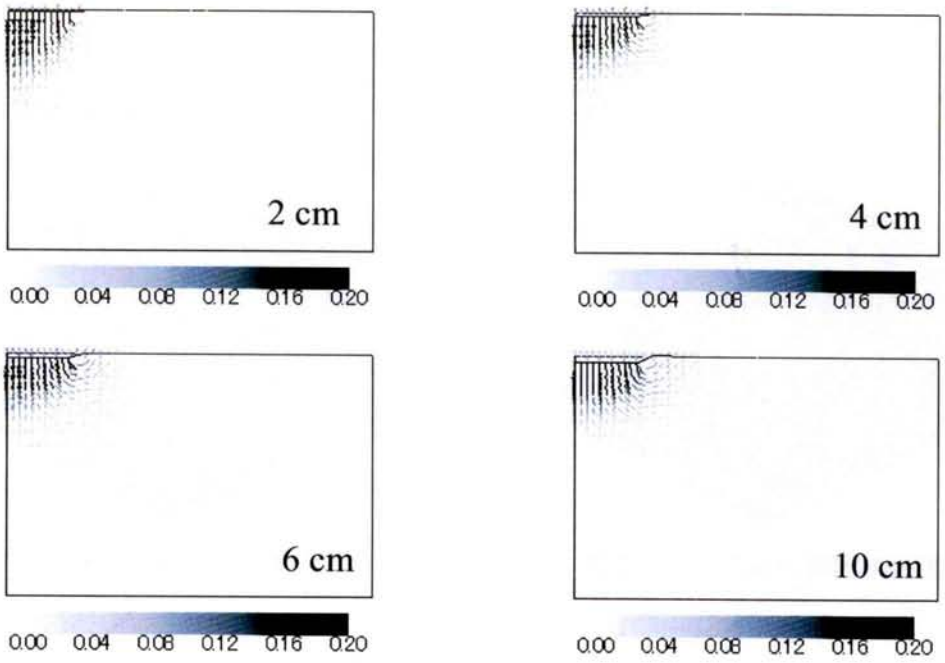

Figure 5.38 Vectors of the incremental nodal displacement at 2, 4, 6, and 10 cm of footing displacement for the square smooth footing case in which β=0 in Section 1

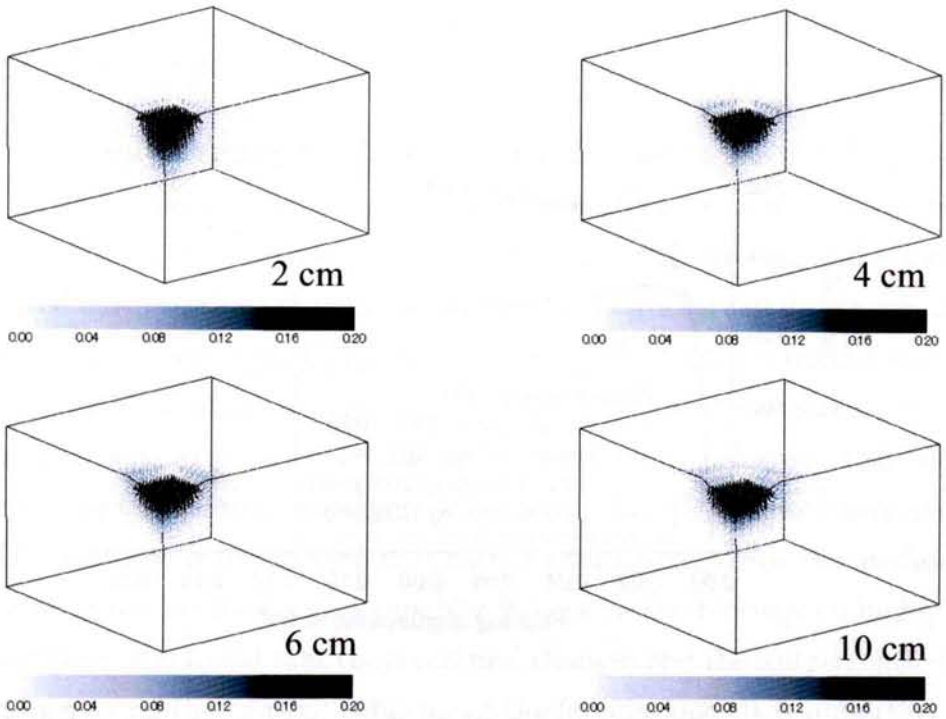

Figure 5.39 Vectors of the incremental nodal displacement at 2, 4, 6 and 10 cm of footing displacement for the square smooth footing case in which β=0

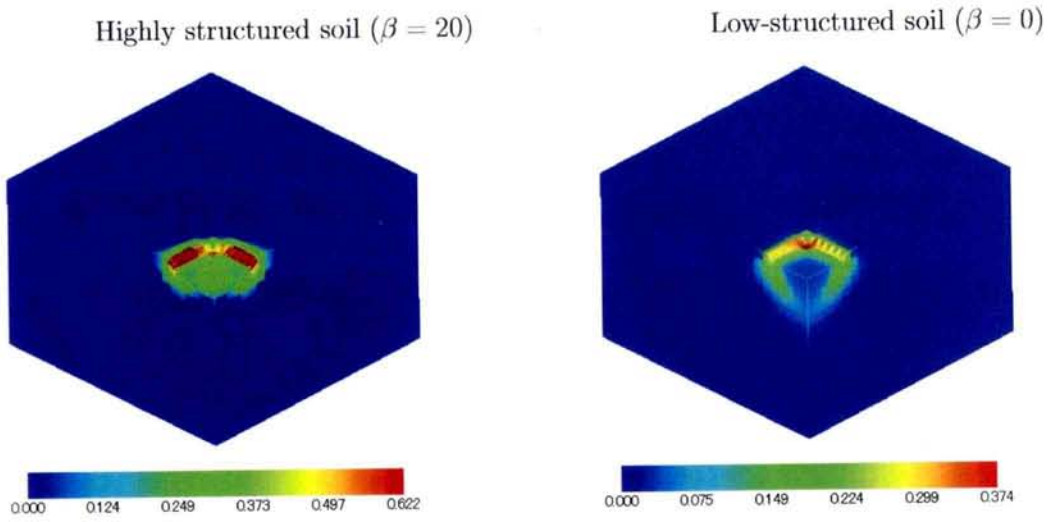

Figure 5.40 Distributions of the accumulated viscoplastic deviatoric strain at 10 cm of footing displacement for the square smooth footing case on highly structured soil and low-structured soil

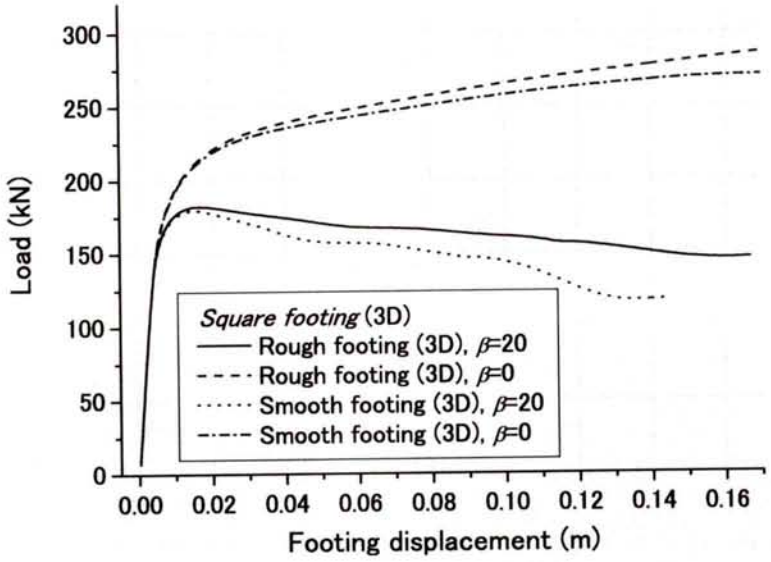

Figure 5.41 Comparison between the load-displacement curves for rough and smooth square footings

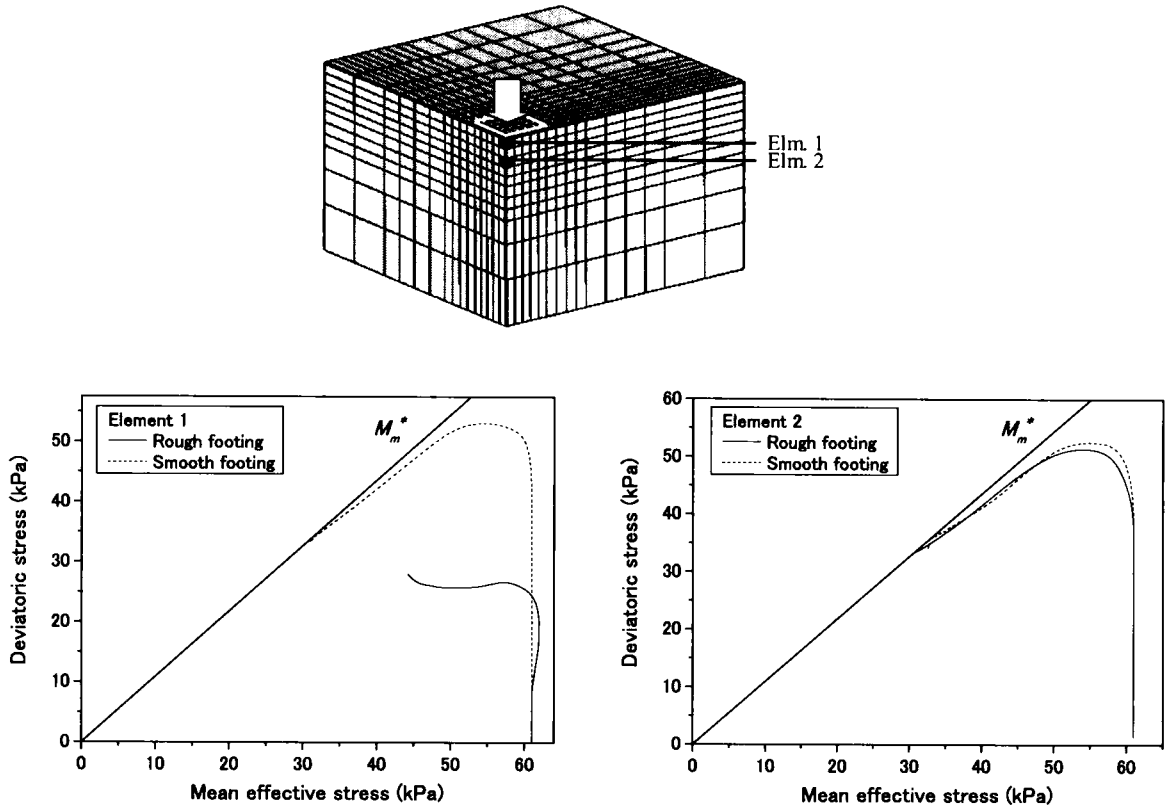

Figure 5.42 Stress paths of the soil under the center of the square footing

5.4 Summary

Finite element analyses using an elasto-viscoplastic constitutive model, considering the structural changes, are performed to investigate the effects of structural degradation and strain localization on the bearing behavior of a surface strip footing and a square footing on a saturated clay stratum. It is found that the soil structure and strength degradation lead to the strain localization during the loading of the footings on the structured soil. No strain localization can be observed in the case of soil with low-structure. This strain localization zone acts as a "slip line" and affects the bearing behavior of the strip footing.

By comparing the bearing capacity obtained from the method used here and that from the plasticity solution, it can be seen that the numerical analysis by the method used here predicts lower values for the bearing capacity factors for the footings on highly structured soil. Furthermore, it is found that the structural changes and the soil strength degradation have an influences on the bearing behavior of the foundations. It is important, therefore, to include the effects of microstructural changes in the bearing capacity analyses. The analysis also shows that different friction conditions at the footing surface yield different failure patterns.

As for the case of the footings on soil with strength which increases with depth, the friction conditions at the footing surface affect the shape and the depth of the failure mechanism, and consequently, result in different bearing capacities. Similar to the homogeneous soil case, soil strength degradation and strain localization due to the collapse of the soil structure affect the bearing behavior of the footings. For the low-structured soil case, the increasing rate of the load in the case of low-structured soil is considerably high since shear strength is increases with depth.

Numerical analyses of the square rough footing and the smooth footing problems are conducted under three-dimensional conditions. It is found that the loading of the rough square footing on a clay ground results in a the deformation pattern that agrees with the "local shear failure". The deformation zone of the predicted soil is shallower than that of the strip footing case, while the amount of load obtained is higher. The slip line is again simulated here for the highly structured soil case and this slip line affects the bearing behavior of the square footing in the same way as it affects the strip footing case.

As for the smooth footing case, when the footing is loaded on the low-structured soil, the deformation mechanism of the soil is not affected much by the footing frictional conditions. Consequently, the load obtained from the smooth footing case does not differ significantly from that of the rough footing case. On the other hand, the friction from the footing prominently affects the deformation mechanism of the highly structured soil under the smooth footing. Furthermore, when the footing is smooth, the soil at the footing surface is sheared and its strength is degraded. As a results, the load of the smooth footing on the highly structured soil is considerably lower than that of the rough footing. This again emphasizes the importance of considering the microstructure changes and strain localization in the analyses of shallow foundations on clay grounds.

Chapter 6

Adaptive Finite Element Refinement for the Elasto-viscoplastic Model

6.1 Introduction

For large deformations in a large strain analysis, it is well known that the two main approaches are the Eulerian and the Lagrangian formulations. Large deformation problems in solid mechanics have traditionally been solved numerically by the finite element method using the Lagrangian method. In many cases, however, after moderate deformation occurs, the mesh-updating process will cause the FE meshes to become highly distorted or even entangled. Particularly in the analysis of geotechnical problems, in which strain localization occurs, the strain of the soil in the localization zone is considerably larger than that in typical problems. This may affects the accuracy of the FE analysis.

To overcome this problem, an adaptive FE refinement has been introduced to the large strain FE analysis using an elasto-viscoplastic model considering the microstructural changes presented in Chapter 2. The aim of the study in this chapter is to examine the performance of the mesh refinement applied to the analysis method by taking into account the improvements in the accuracy of the analysis and the computation time.

h-refinement, in which the same class of elements continues to be used but the size of the elements is changed to provide maximum efficiency in achieving the desired solution, is adopted in the present study. The error estimator is based on the method proposed by Zienkiewicz and Zhu (1992) and is reviewed in Appendix A. An automatic quadrilateral mesh generation method proposed by Zhu et al. (1991) is introduced in Appendix B. In the following sections, prediction method of the required element size and a simple linear planar interpolation technique for stress and material properties is explained.

The application of the method is validated by simulating the shearing of a clay specimen under plane strain conditions with displacement control. The simulations have been performed with and without the remeshing technique. The results are then presented and the mesh refinement performance is explored and discussed.

6.2 Prediction of the Required Element Size

The error estimator reviewed in Appendix A allows us to determine the global and the local (elemental) energy norms of the error. If the error predicted is less than the permissible error prescribed, a mesh refinement is not required. In order to confirm this condition, the norm percentage error η must be determined, namely,

$$\eta = \frac{\|e\|_2}{\|u\|_2} \times 100\% \tag{6.1}$$

where $\|u\|_2$ is the total L_2 norm error and can be calculated as shown in the next equation:

$$\|u\|_2 = \left(\int_\Omega u \cdot u d\Omega\right)^{1/2} \tag{6.2}$$

where Ω represents the domain of the problem. If the norm percentage error for the overall domain is larger than the prescribed value, a mesh refinement must be performed. At this stage, it is required that the error in any element k should be

$$\|e\|_{2k} < \bar{\eta}\left(\frac{\|u\|^2}{m}\right)^{1/2} \equiv \bar{e}_m \tag{6.3}$$

in which $\bar{\eta}$ is the permissible error determined by the analyst and m is the total element number.

Any element that does not satisfy the condition in Equation (6.3) must be refined. To predict the element size, the following assumption is made:

$$\|e\|_{2k} \propto h_k^p \tag{6.4}$$

where h_k indicates the current element size and $p = 2$ is the polynomial order of the approximation. To satisfy the requirement in Equation (6.3), the size of the new refined element size should be smaller than that calculated from the following equation:

$$h_{new} = \xi_k^{-1/p} h_k \tag{6.5}$$

in which

$$\xi_k = \frac{\|e\|_{2k}}{\bar{e}_m} \tag{6.6}$$

In this study, the effective stress (σ'_{ij}) and the viscoplastic strain (ε^{vp}_{ij}) are chosen for used in the calculation of the error. This choice is done in order to take into account for the errors from the elastic part and the plastic parts. The norm percentage error used to predict the required element size in the new mesh is the average value of the errors calculated from the effective stress and the viscoplastic strain. By the new required element size calculated, the new refined mesh can be generated by using the mesh generation method (Zhu et al. 1991) reviewed in Appendix B.

6.3 Planar Interpolation

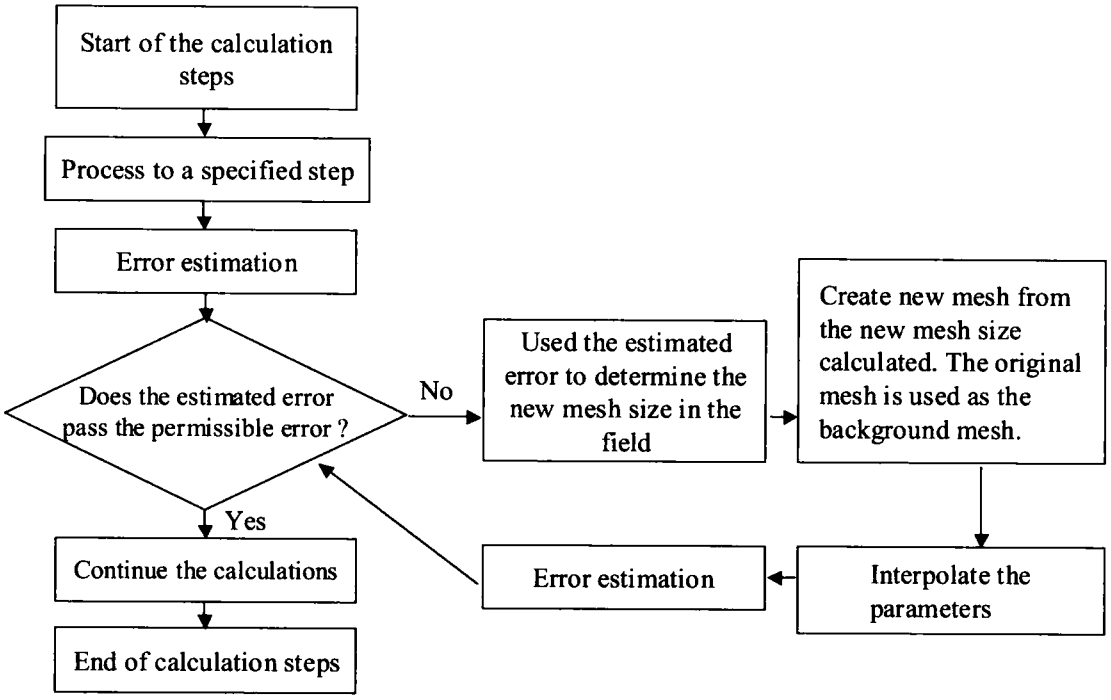

Figure 6.1 Flowchart of the developed adaptive finite element program

After the new mesh is generated from the method reviewed in the Appendix B, the stress levels and the material properties at the integration points of the generated mesh must be determined from the values of the old mesh. At this point, the SPR technique is used again. The procedure is explained as

- Update the old mesh. This forms the reference field for the interpolation.
- Find the element of the reference field in which the new integration point of the destination field (new mesh) lies in.

- Interpolate the parameter values at the new integration point (destination field). The parameters are interpolated using the SPR technique to find the value at the concerned coordinates in the reference mesh.

A flowchart of the developed program is shown in Figure 6.1.

6.4 Numerical Simulation

Table 6.1 Soil parameters

Coefficient of permeability k_0 (m/s)	0.8×10^{-9}
Elastic shear modulus G_0 (kPa)	13075
Compression index λ	0.508
Swelling index κ	0.0261
Initial void ratio e_0	1.70
Coefficient of earth pressure K_0	1.0
Compression yield stress σ'_{mbi} (kPa)	100.0
Stress ratio at maximum compression M^*_m	1.09
Viscoplastic parameter m'	18.5
Viscoplastic parameter C_0 (1/s)	1.3×10^{-13}
Structural parameter σ'_{maf} (kPa)	51.4
Structural parameter β	0,15

A numerical analysis has been carried out in order to validate the application of the mesh refinement with the analysis method currently used. A simulation of the shearing of a clay specimen was performed under plane strain conditions by the displacement control with and without remeshing.

Figure 6.2 shows the model for the soil and the associated boundary conditions. The size of the models is 0.1×0.1 m. The rate of the upper boundary nodal displacement adopted in this analysis is 0.00002 m/min. In the analysis, the time increment for each step of the calculation is set to be 30 sec with an upper boundary node displacement increment of 0.00001 m for each step of the calculation. The material parameters used in the analysis are listed in Table 6.1 with the coefficient of permeability and the K_0 values.

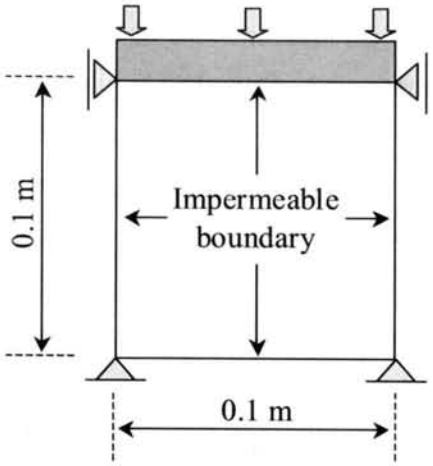

Figure 6.2 Model of the soil used in the analysis

6.5 Results and Discussion

Two cases of the analyses, in which the structural parameters are β=0 and β=15, are carried out to study the performance of the method applied to strain localization considering the degradation of the soil strength. The soil parameters are presented in Table 6.1. The permissible error used in the calculations is 10%. In the followings, the analysis case using the structural parameter $\beta = 0$ will be refereed to as Case 1, while Case 2 represents the analysis using the structural parameter $\beta = 15$.

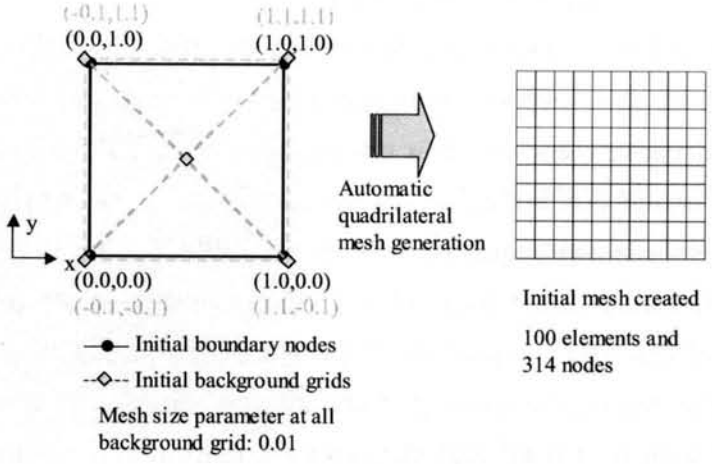

Figure 6.3 Initial boundary nodes and initial background nodes for the generation of the initial mesh and the generated initial mesh for Case 1

Let us start with Case 1 in which the the structural parameter β=0 is used. The initial boundary nodes and the initial background nodes for the generation of the initial mesh are shown in Figure 6.3. The generated initial mesh is also shown in the same figure. It is seen that by setting the mesh size parameter h_k at 0.01m for all background nodes, a

uniform rectangular mesh with an element size of 0.01×0.01 m can be obtained.

The first remeshing is performed after the displacement of the upper boundary has reached 0.0005 m (50 calculation steps). The contour of the parameters that are used in the error estimation is shown in Figure 6.4. Parameter ξ_k is calculated from Equation (6.6), and the obtained contour is also shown in the same figure. A large value for the error estimation is observed at the corner of the mesh and along the area where the soil is significantly sheared. The overall percentage error estimated at this stage is 9.09% as shown in the figure. This is lower than the permissible limit, which was set to be 10% and the analysis can therefore be continued without any mesh refinement.

The analysis is then continued by checking the error every 50 calculation steps (0.0005 m of upper boundary displacement increments). The overall percentage errors obtained at the upper boundary displacement of 0.0010 m, 0.0015 m, and 0.0020 m is 8.38%, 8.79%, and 9.52%, respectively. Since the estimated errors all pass the permissible limit, the analysis is performed without remeshing. The overall percentage error calculated with an upper boundary displacement of 0.0025 m (250 steps of calculation) is 10.47%. This value is larger than the error limit and the mesh needs to be refined. The distribution of the parameters that are used in the error estimation at this stage is shown in Figure 6.5 along with the contour of the calculated ξ_k. Note that, remeshing is needed in the area in which ξ_k is larger than 1.0. The new mesh size is calculated from the estimated error and the new mesh is then generated as shown in Figure 6.6. The new mesh is composed of 391 elements with 1270 nodes. It is seen that the size of the elements located near the corners of the mesh become smaller, and, consequently, the errors in these areas vanish in the new mesh. The material parameters are then interpolated from the original mesh to the new mesh and the error estimation is carried out again to examine the quality of the generated mesh. The overall error is estimated from the new mesh is 3.96%, and therefore, it passes the prescribed limit. Interpolated accumulated viscoplastic shear strain $\gamma^p \equiv \int \sqrt{de_{ij}^{vp} de_{ij}^{vp}}$, the mean effective stress, and the pore water pressure of the generated mesh are shown in Figure 6.7. From this figure, the quality of the interpolation technique can be validated.

The analysis is then continued and the error estimation is performed at every 0.0005 m increment of the upper boundary displacement. The error estimated at step 300 is 10.17% and the mesh is refined again. The new mesh contains 1211 elements with 3744 nodes. The estimated error falls to 7.04% and passes the permissible error. The analysis is then continued to step 800, while the estimated error stays below the permissible value.

Additional analyses for the same problem using 5×5 (25 elements) and 20×20 (400 elements) meshes have been conducted in order to compare the results with the adaptive

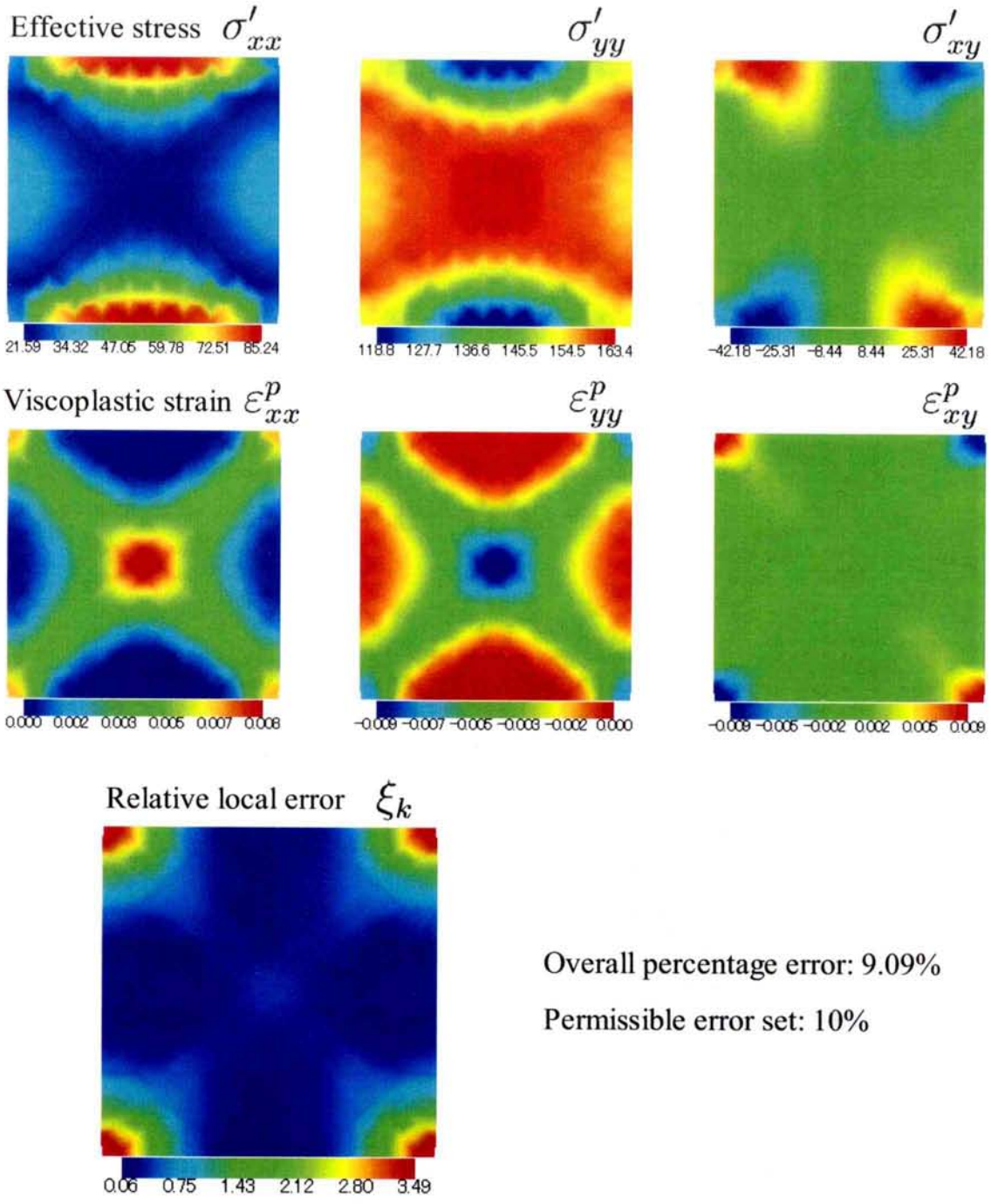

Figure 6.4 Distributions of the parameters used in the error estimation and the corresponding error estimated at 0.0005 m of the upper boundary incremental displacement for Case 1

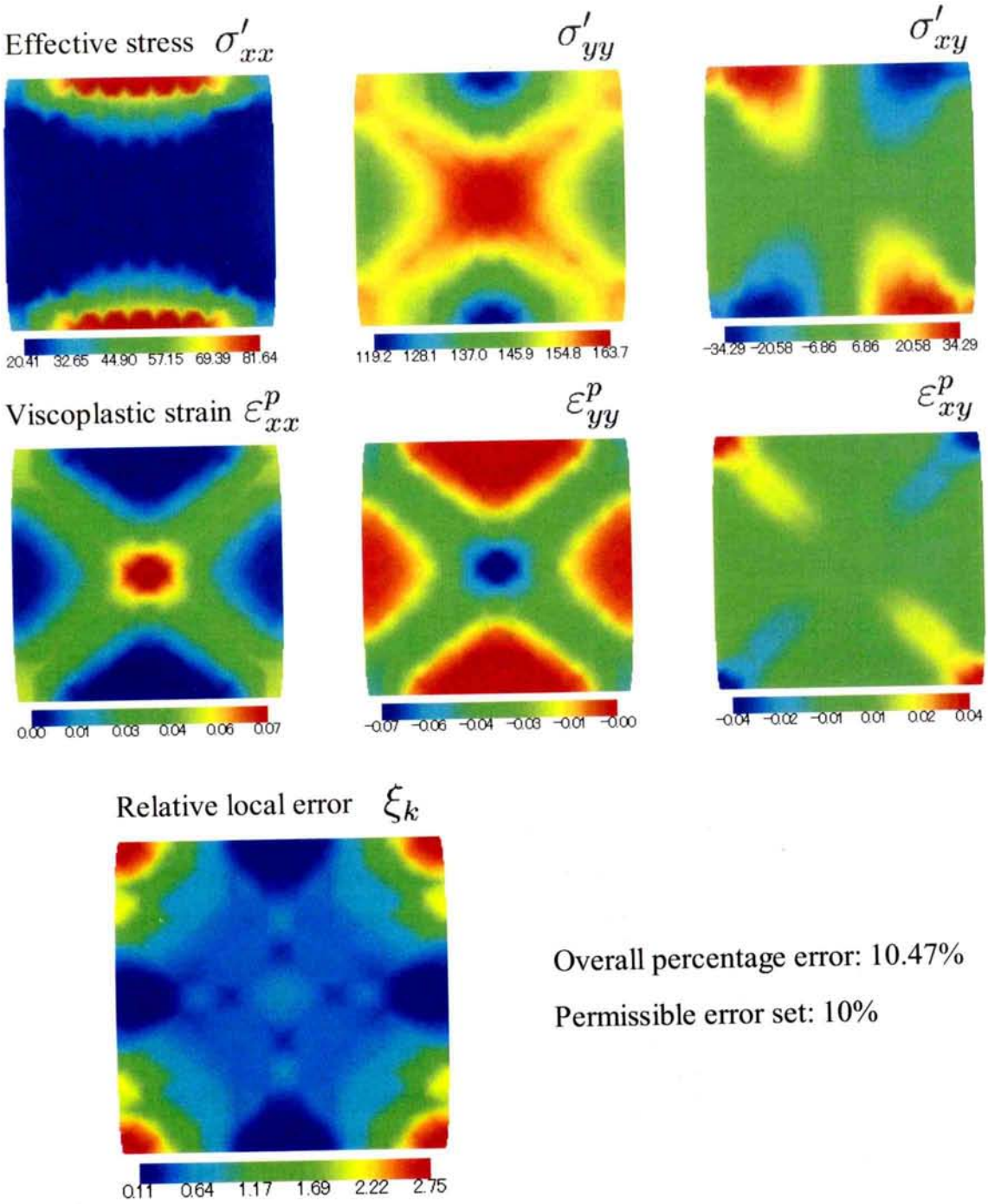

Figure 6.5 Distributions of the parameters used in the error estimation and the corresponding error estimated at 0.0025 m of the upper boundary incremental displacement for Case 1

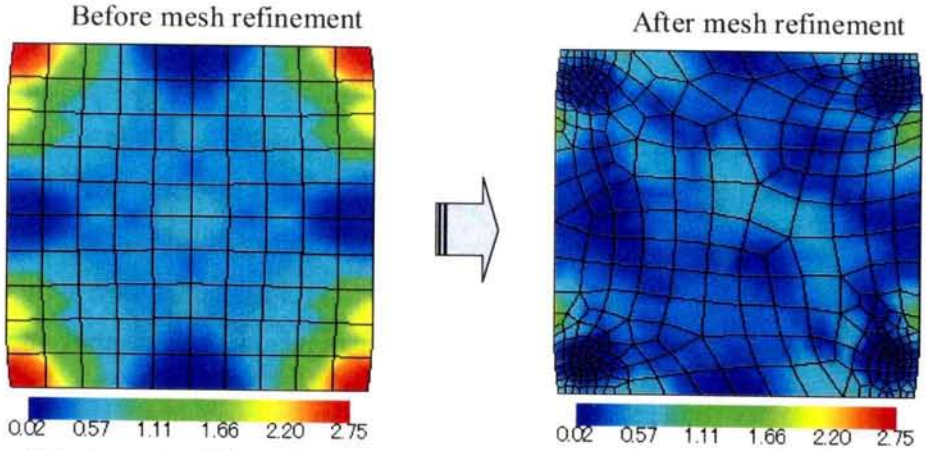

100 elements, 341 nodes

Relative error: 10.47%

Permissible error set: 10%

391 elements, 1270 nodes

Relative error: 3.96%

Permissible error set: 10%

Figure 6.6 Distributions of the relative local error before and after the mesh refinement for Case 1

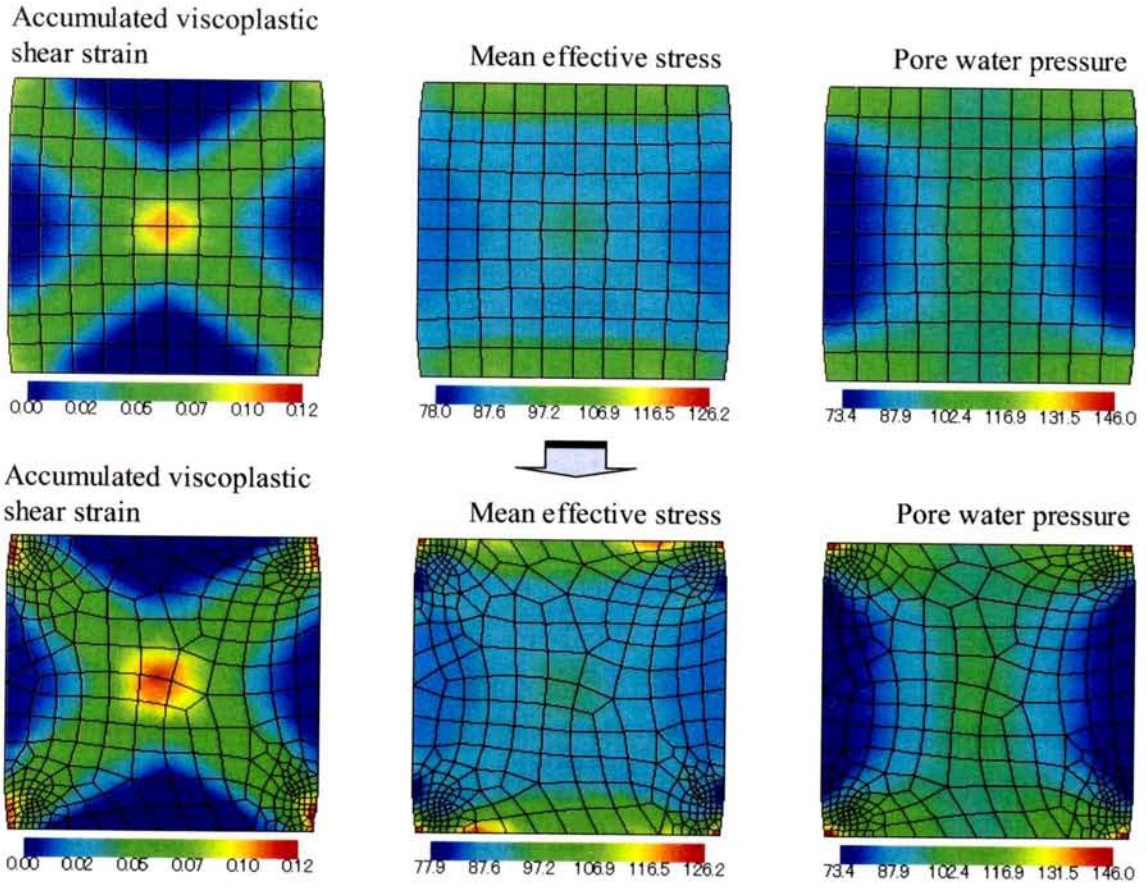

Figure 6.7 Distributions of the accumulated viscoplastic shear strain, the mean effective stress, and the pore water pressure in the original mesh and in the refined mesh for Case 1

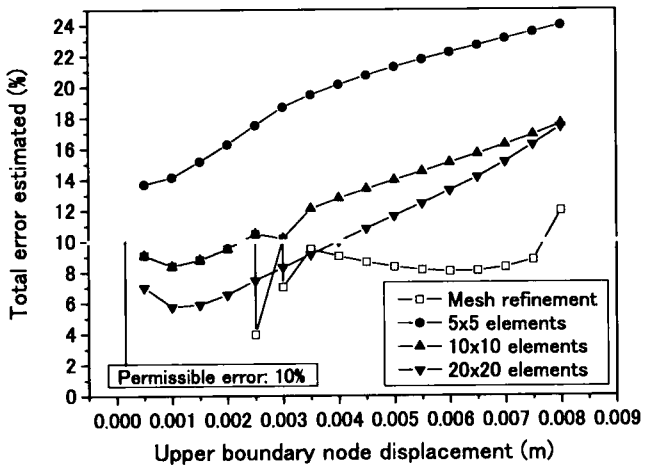

Figure 6.8 Relation between the estimated error and the displacement of the upper boundary in Case 1

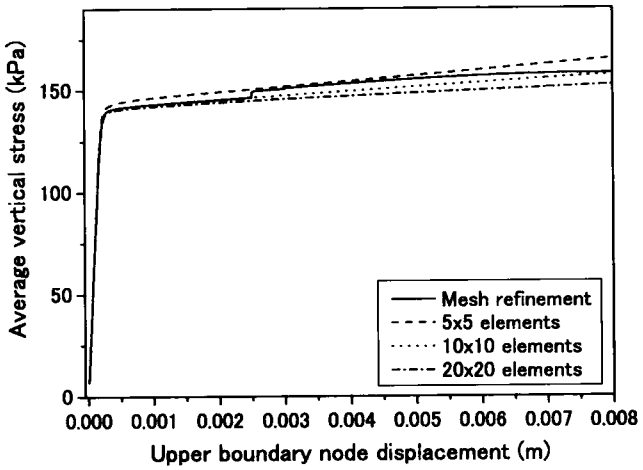

Figure 6.9 Relation between the average vertical stress and the displacement of the upper boundary for Case 1

refinement. The 5×5 (25 elements) mesh can be considered as an rough mesh, while the 10×10 (100 elements) mesh is considered to be a typical mesh, and the 20×20 (400 elements) mesh represents a fine mesh. Figure 6.8 shows the development of the estimated total error (%) with the displacement of the upper boundary. It is seen that the mesh which is composed of the higher number of elements yields a smaller estimated error from the analysis of the same problem. In the analyses for which mesh refinement is not conducted, the error grows larger with the displacement of the upper boundary, namely, the shear of the soil specimen. On the other hand, when the mesh refinement is performed, the estimated error remains below the permissible error limit. This indicates that the adopted method can refine and produce very well a new mesh with lower errors

for the analysis performed.

Figure 6.9 illustrates the relation between the average vertical stress and the displacement of the upper boundary for all cases. It is apparent that a relatively large fluctuation is produced after the first refinement. However, the average vertical stress converges to the results from the 10×10 (100 elements) mesh and the 20×20 (400 elements) mesh at a high displacement of the upper boundary.

Figures 6.10 and 6.11 show the distributions of the accumulated viscoplastic shear strain and the mean effective stress when the upper boundary displacement has reached 0.0075m for all meshes. A clear difference can be seen between the results of the refined mesh and the results of the 5×5 (25 elements) and the 10×10 (100 elements) mesh cases which yield larger errors. This again indicates that the refinement procedure improves the accuracy of the analysis from the initial typical mesh. However, the 20×20 (400 elements) mesh case provides rather similar results to those from the refined mesh case. Therefore, the mesh refinement did not yield much better results from the analysis using the fine mesh from the start of the calculation, despite the difference in the errors estimated.

Let us now consider the results of Case 2. In this case, the structural parameter β=15 is used. From the analysis. It is seen from the analysis that the degradation of the soil strength, due to the microstructural changes, gives the strain localization. Similar to Case 1, the initial mesh generated is composed of 100 uniform elements. Next, the first error estimation is performed after 50 calculation steps. The error estimated at this stage is appeared to be 10.02%, and thus, the mesh refinement is required. Figure 6.12 shows the distributions of the parameters that are used in the error estimation at this stage. The contour of the calculated ξ_k calculated is also illustrated in this figure. In this case, the larger viscoplastic strain and the strain localization are calculated as results of the structural changes. Consequently, a higher error than that in Case 1 is estimated and it is distributed along the shear band. The newly generated mesh created has 287 elements with 946 nodes. The error estimated from the new mesh is 3.00% as can be seen in Figure 6.13. This value falls within the permissible error limit (10%). Figure 6.14 shows the distribution of the relative local error before and after the mesh refinement when the upper boundary displacement has reached 0.002m. The contour shown in the figure gives us a clearer view of how the estimated error is concentrated in an x-shape shear band in the center of the mesh. Therefore, the size of the new elements generated within this area is small, and the error estimated in the new mesh becomes smoother and the total error calculated passes the prescribed error limit. This indicates that the refinement procedure

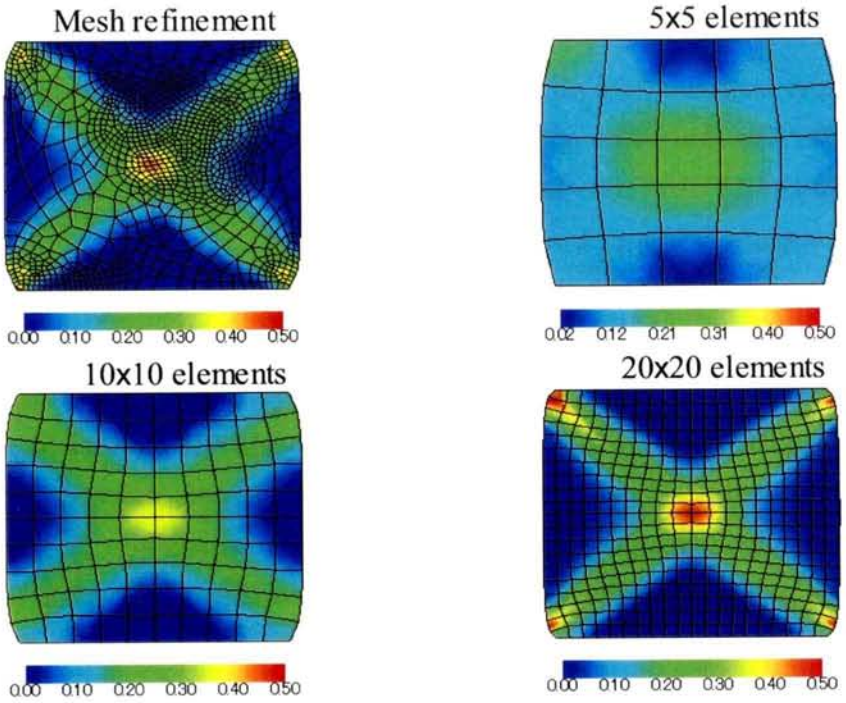

Figure 6.10 Distributions of the accumulated viscoplastic shear strain when the upper boundary displacement is 0.0075 m for Case 1

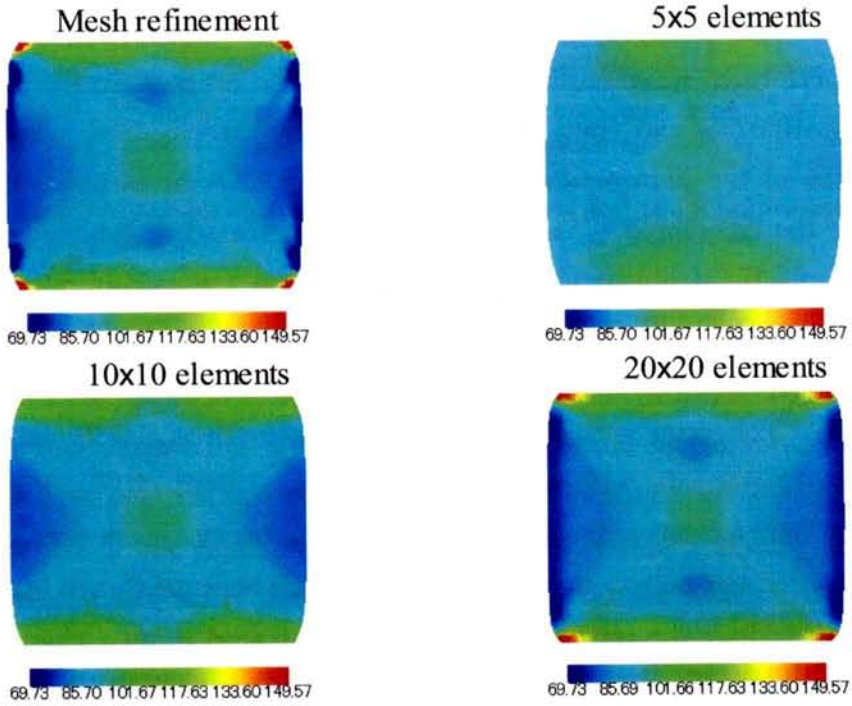

Figure 6.11 Distributions of the mean effective stress when the upper boundary displacement is 0.0075 m for Case 1

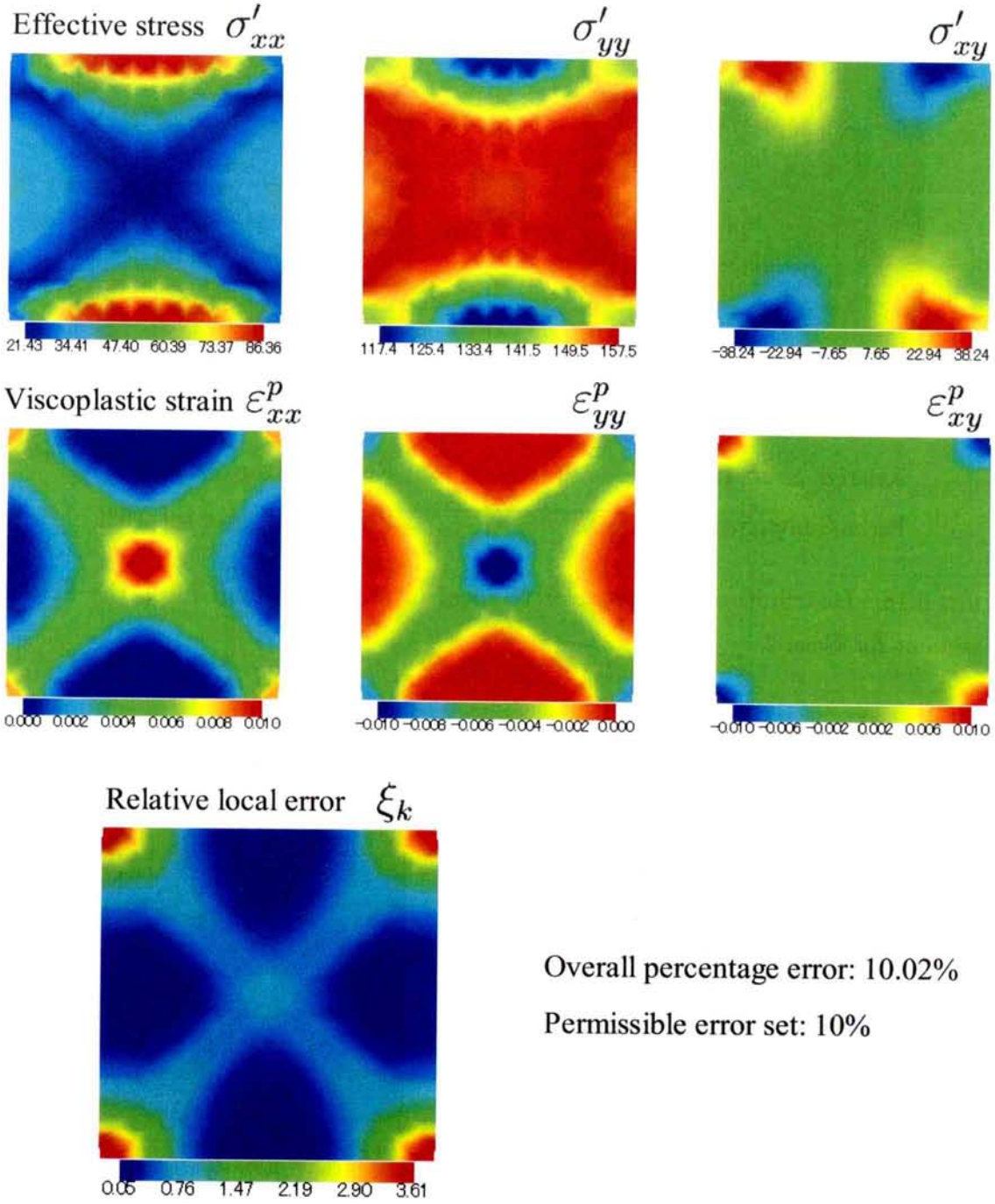

Figure 6.12 Distributions of the parameters used in the error estimation and the corresponding error estimated at 0.0005 m of the upper boundary incremental displacement for Case 2

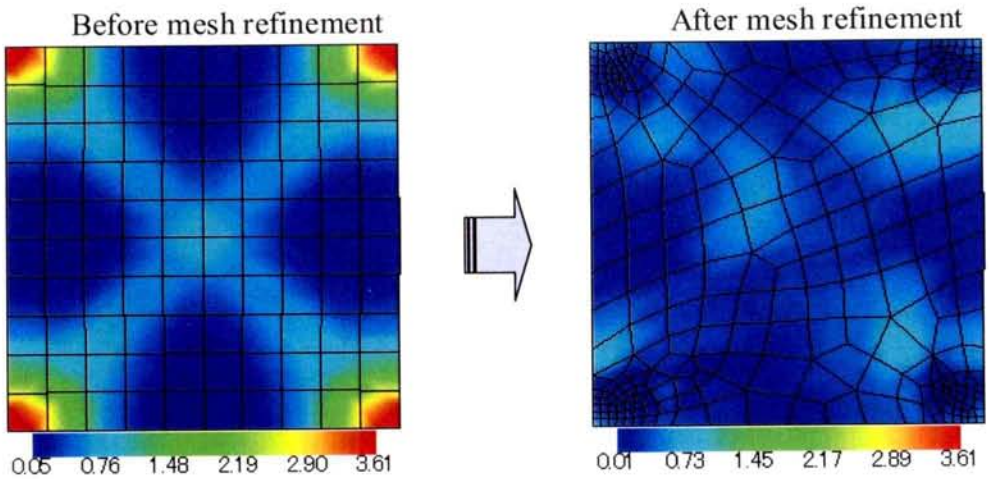

Figure 6.13 Distributions of the relative local errors before and after the first mesh refinement for Case 2

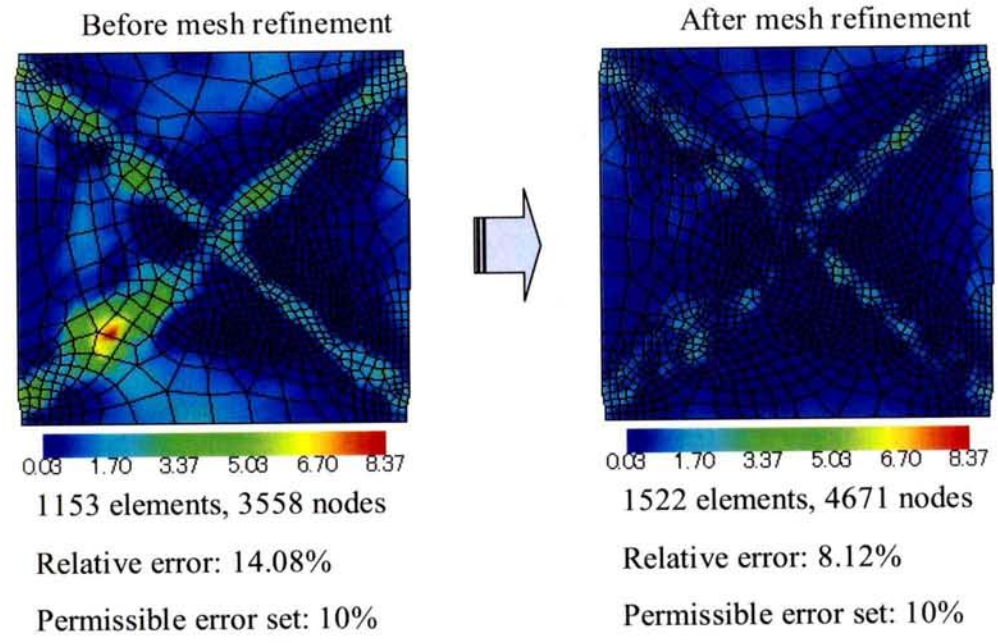

Figure 6.14 Distributions of the relative local errors before and after the mesh refinement when the upper boundary displacement has reached 0.002 m for Case 2

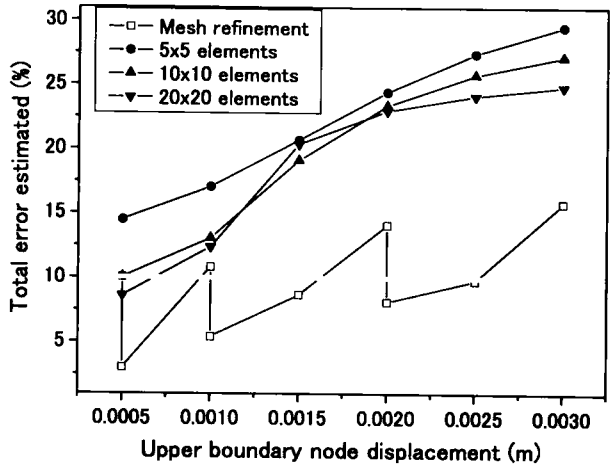

Figure 6.15 Relation between the estimated error and the displacement of the upper boundary for Case 2

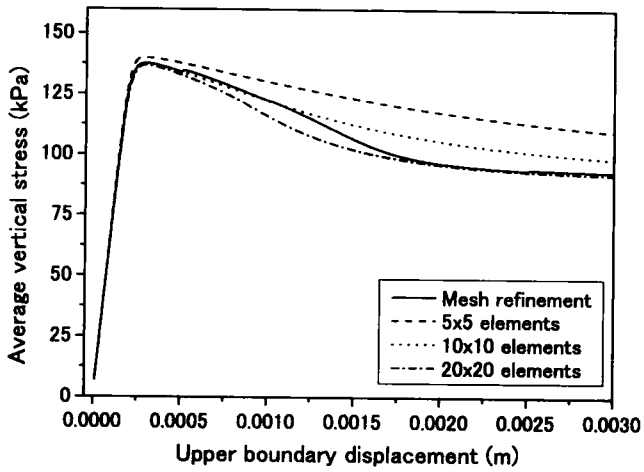

Figure 6.16 Relation between the average vertical stress and the displacement of the upper boundary for Case 2

used can deal with the errors in the strain localization area and can provide the optimum mesh. The analysis is then continued until the upper boundary displacement reaches 0.003 m. Figure 6.15 shows the development of the estimated total error (%) with the displacement of the upper boundary. The results demonstrated in this figure confirm for us that without the mesh refinement, the error estimated from this case is considerably higher than that for Case 1. The development of the average vertical stress with the displacement of the upper boundary is shown in Figure 6.16. In this case, the fluctuation produced from the refinement is very small. As the refinement is conducted and the error is reduced, the calculated average vertical stress converges to the results obtained from the 20×20 (400 elements) mesh case.

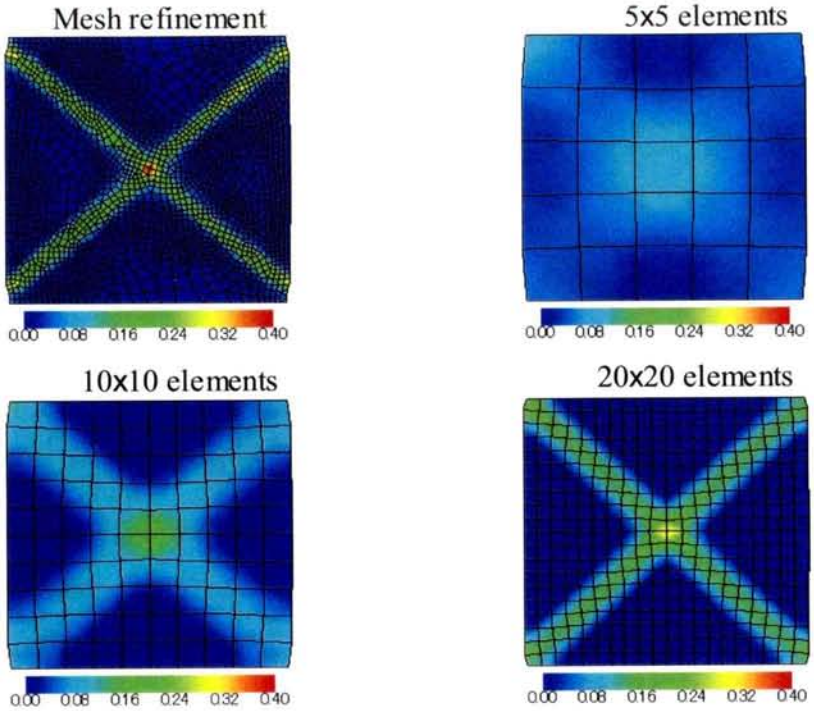

Figure 6.17 Distributions of the accumulated viscoplasctic shear strain when the upper boundary displacement is 0.0025 m for Case 2

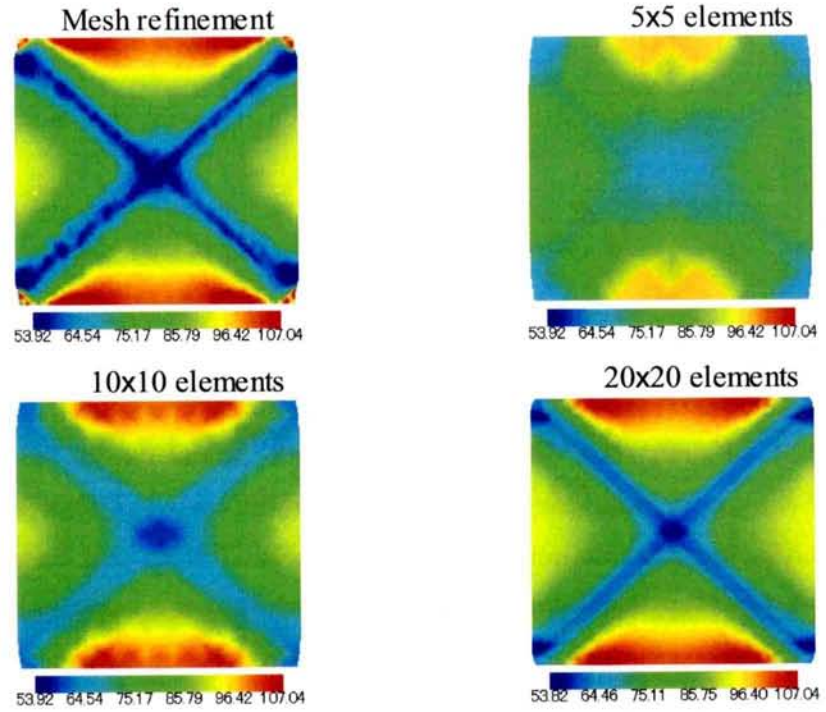

Figure 6.18 Distributions of the mean effective stress when the upper boundary displacement is 0.0025 m for Case 2

Distributions of the accumulated viscoplastic shear strain and the mean effective stress when the upper boundary displacement has reached 0.0025m are shown in Figures 6.17 and 6.18. Once again, the results of the 5×5 (25 elements) and the 10×10 (100 elements) mesh cases are quite different from those of the refined mesh case and the 20×20 (400 elements) mesh case. Now let us compare the results due to the mesh refinement and the 20×20 (400 elements) mesh case. It can be seen that the accumulated viscoplastic shear strain in the mesh refinement case is higher than that for the case of 400 elements case. As for the mean effective stress, no clear difference can be seen from the value outside the shear band area. On the other hand, the mean effective stress in the shear band area decreases more from the negative dilatancy in the mesh refinement case. This indicates that the adaptive refinement does increase the accuracy of the calculation in the case when strain localization occurs.

6.6 Summary

An adaptive refinement method has been introduced into the finite element analysis using an elasto-viscoplastic model considering the microstructural changes. The method works well to reduce the errors in the regenerated mesh. When the strain localization does not occur, however, a small difference is seen in the analysis results obtained from the mesh refinement case and the fine mesh case despite the higher error estimated from the fine mesh case. Therefore, the mesh refinement did not give much better results than that of the analysis using the fine mesh from the start of the calculation.

When strain localization does occur, the refinement reduces the estimated error as well. Moreover, the refined mesh yields better results from the analysis of the soil in the shear band zone than the fine mesh case.

Zienkiewicz and Zhu (1992) have performed several numerical analyses on elastic problems and compared the obtained mesh refinement results to the analytical solutions. They point out that with the recovered superconvergent solutions, the pointwise errors of the FE solution can be accurately estimated, while the control of such local errors is not as simple as the procedure for ensuring a specified overall energy norm error. The paper ended by concluding that the mesh refinement based on an error estimator using the SPR, leads to a good and effective analysis. It has been found in the FE analyses used in this study, however, that the refinement method is not an economic option for improving the quality of the analysis, especially if we consider the computation time in the evaluation of this method, since only a small improvement and a little higher accuracy are obtained

by increasing a large number of elements and degrees of freedom. Therefore, the author recommends that adaptive refinement be used in the trials to find an optimum initial mesh, instead of using the adaptive refinement in the analysis, and that the obtained mesh be used for the entire analysis.

Chapter 7

Conclusions and Future Work

7.1 Concluding Remarks

In the present dissertation, an elasto-viscoplastic constitutive model for clay and an elasto-plastic constitutive model for sand were used with a finite element formulation for the analysis of a water-saturated soil based on the finite deformation theory in order to study and to simulate the soil-foundation interaction problems of the foundation structures in the grounds composed of soft clay and sand that are subjected to large deformations and strain localization. The implementation of the mesh refinement process was also introduced into the analysis method used in this study. The following conclusions were obtained from the present study.

In **Chapter 2**, an elasto-viscoplastic constitutive model for normally consolidated clay with a second material function Φ_2 proposed by Adachi, Oka, and Mimura (1987), and an elasto-viscoplastic constitutive model for clayey soils considering structural changes, proposed by Kimoto (2002), were firstly introduced. In this study, the models were used to reproduce the important behaviors of a clay ground including the rate-dependent behavior, dilatancy, and the degradation of strength from the microstructural changes. An elasto-plastic model, based on the nonlinear kinematic hardening rule for sandy soils (Oka et al.(1999)), was then presented to simulate the ground composed of both clay and sandy materials. Finally, a finite element formulation for the analysis of water-saturated soil, based on the finite deformation theory, was described.

In **Chapter 3**, the study was divided into two parts. In the first part, numerical simulations under plane strain conditions were carried out to study the effects of vari-

ous parameters on the lateral earth pressure brought about by movements of a vertical backface retaining wall which supports horizontal backfill. The problem was separated into active and passive earth pressure cases. From the results of the study, the following summary and conclusions were drawn.

It was found that the friction between the wall and the soil affected the active and the passive earth pressure in a similar way, namely, a larger friction between the wall and the soil resulted in a larger decrease and/or increase in pressure on the wall from the initial values. The shear band behind the wall appeared in a straight line with an angle of around 45° to the horizontal plane in the case of a smooth wall. The friction between the wall and the soil caused the shear band to bend slightly at the lower edge of the wall. The negative dilatancy of normally consolidated clay affected changes in the pore water pressure and the volumetric strain of the soil behind the wall. A comparison showed that the friction more strongly influenced the amount of earth pressure in the case of the active earth pressure than in the case of the passive earth pressure.

The wall movement patterns were found to have a great influence on the deformations of the soil behind the wall and on the development of the earth pressure. The rotation of the wall around its top edge resulted in a shear zone shaped like a "hook". The pressure of the soil around the deeper parts of the wall developed first, followed by the pressure near the ground surface. On the other hand, the pressure of the soil near the ground surface will developed before the pressure of the soil in deeper positions in the case of the wall rotation around its bottom edge. In this case, the soil tended to deform in a "zone" rather than in the shear bands. The growth rate of the earth pressure on the wall in the translation movement pattern case was the fastest, followed by that associated with the rotation around the top edge case, and then the rotation around the bottom edge case, respectively.

In the second part, the problem of the soil-structure interaction of the braced excavation performed through a thick soft clay deposit was studied. The effects of the initial stress ratio and the struts layouts on the performance of the excavation were examined. Numerical simulations under idealized (symmetric) plane strain excavation geometry were undertaken in this part. The following conclusions were obtained from the analyses results.

When an excavation was performed through a thick soft clay deposit, the sheet pile wall tended to deflect with the position of the maximum lateral deflection located under the excavation level. The large displacements of the toe of the wall with the large amount

of heaving were obtained from the simulation. This indicated the low-base stability of the excavation system. It was found that the lateral deflections of the wall continued to grow largely with time even after the completion of the excavation. This was found to be due to both the consolidation process and the viscoplastic flow of the soil masses.

A comparison showed the agreement of the wall and the ground deformation patterns between the numerical results and the data from the case study, and thus, indicated that this study can quantitatively well reproduce the results of the case study well. From the analysis results, it is recommended that the ground improvement only on the excavation side is effective enough to reduce the ground deformation and wall displacement in the problem.

In **Chapter 4**, a case study of an embankment constructed near the shore of the Aji River in the bay area of Osaka Prefecture was studied. The parameters used in the constitutive models for the underlying thick alluvial clay layer in the construction field were carefully investigated with laboratory tests. The large and the long-term deformations of the ground and the displacement of the supporting structures caused by the construction were measured after the construction of the embankment near the bulkhead piles that were not embedded into a firm stratum. Numerical analyses were performed to study this problem. From the results, the following conclusions were obtained.

Large deformations of the underlying soil, due to the embankment load, is extended to deep parts of the clay layer. This ground deformation led to the lateral displacement of the nearby bulkhead piles since the piles were embedded in a soft stratum. A good agreement between the simulation results and the field measurement values was obtained, and this shows the efficiency of the calculation method adopted to reproduce the behavior of a soil ground subjected to large deformations. The significance of the rate sensitivity, the structural changes and the strength degradation of the clay to the results of the analyses was also confirmed.

It is important to point out that in this case study, the bulkhead piles were found to move horizontally as a whole. It was necessary, therefore, that the piles be installed into the underlying firm stratum to increase the stability of the supporting system. The results of the analyses showed that this countermeasure was able to prevent the ground flow at deep levels and resulted not only in a lower lateral displacement of the piles, but also in the smaller settlements of the ground.

In **Chapter 5**, a series of numerical analyses of footings on a clay deposit was car-

ried out to study the effects of microstructural changes and strength degradation on the bearing behavior of a shallow foundation. It was found that the soil structure and the strength degradation led to the strain localization during the loading of the footings on the structured soil. On the other hand, no strain localization was observed in the case of soil with low-structure. This structural change in the soil was found to affect the bearing behavior of the strip footing. A comparison indicated that the bearing capacity obtained from the method was lower than that of the plasticity solution, which was caused by the strength degradation of clay for the footings on highly structured soil. Therefore, we can conclude that it is important to include the effects of microstructural changes in the bearing capacity analyses. The analysis also showed that different friction conditions at the footing surface led to different failure patterns.

For the case of footings on soil with strength which increased with depth, this increase in soil strength was found to make the friction conditions at the footing surface to affect the shape and the depth of the failure mechanism, and consequently, resulting in different bearing capacities. Similar to the homogeneous soil case, soil strength degradation and strain localization due to the collapse of the soil structure affected the bearing behavior of the footings.

In **Chapter 6**, an adaptive refinement method was introduced into the large strain finite element analysis using an elasto-viscoplastic model considering microstructural changes. We have found that the method developed here can reduce the errors estimated in the regenerated mesh. However, the analysis results were not improved much when the strain localization did not occur. On the other hand, when strain localization did occur due to the degradation of the soil strength, the refined mesh improved the results of the analysis of the soil in the shear band area. Upon considering the computation time required for this adaptive refinement analysis, however, it was found that the method is not economical. Hence, the author recommends that the adaptive refinement be used in trials to find the optimum initial mesh for the analysis.

The numerical analysis with the finite element method, using the elasto-viscoplastic models in this study, has clarified some mechanisms of the soil-foundation interaction in a soft clay ground. In particular, the simulation results have given us a better understanding of the effects of the rate-sensitivity of clay, the strength degradation and the strain localization on the behavior of the ground and the corresponding supporting systems. Through the comparisons between the obtained results and the field measurements, the

performance of the numerical method adopted in the present study has been quantitatively validated. Hence, the method has been proved capable of providing an effective tool for researching soil-foundation interaction problems in soft clay grounds.

7.2 Recommendation for Future Work

Topics for future study are suggested based on the findings of this work. Subjects that deserved future investigation are listed below.

In this study, the simulation of the bracing sheet pile wall in thick soft clay deposit has been done. It was found that this bracing system cannot effectively limit the deformation of ground below the excavation level. It is necessary, therefore, to investigate the efficiency of other excavation methods in the thick soft clay deposit. For example, by using the retaining wall instead of the sheet pile wall, or by adopting the underwater excavation method.

In the adaptive mesh refinement procedure, we have confirmed that fluctuation of the analysis results might occur by the imperfection of the planar interpolation of the parameters. To overcome this problem, mesh enrichment method may be used instead of the complete mesh refinement.

References

[1] Adachi, T. and Oka, F. (1982), Constitutive equations for normally consolidated clay based on elasto-viscoplasticity, *Soils and Foundations*, **22**, 4, pp. 57-70.

[2] Adachi, T. and Okano, M. (1974), A constitutive equation for normally consolidated clay, *Soils and Foundations*, **14**, 4, pp. 55-73.

[3] Adachi, T., Oka, F. and Mimura, M. (1987), An elasto-viscoplastic theory for clay failure, *Proc. 8th Asian Regional Conf. on SMFE*, Kyoto, 1, JSSMFE, pp. 5-8.

[4] Adachi, T., Oka, F. and Mimura, M. (1987), Mathematical structure of an elasto-viscoplastic model for clay, *Soil and Foundations*, **27**, 3, pp. 31-42.

[5] Ahadi, A. (2004), Modelling of Granular Materials, Doctoral dissertation, Lund University.

[6] Biot, M.A. (1963), Mechanics of deformation and acoustic propagation in porous media, *Journal of Applied Physics*, **33**, pp. 1482-1498.

[7] Brown, P.T., Booker, J.R. (1985), Finite element analysis of excavation, *Computers and Geotechnics*, **1**, pp. 207-220.

[8] Davis, E. H., and Booker, J.R. (1973), The effects of increasing strength with depth on the bearing capacity of clays, *Géotechnique*, **18**, 1, pp. 67-91.

[9] Desai, C.S., Zaman, M.M., Lightner, J.G. and Siriwardane, H.J. (1984), Thin-layer element for interfaces and joints, *International Journal for Numerical and Analytical Methods in Geomechanics*, **8**, pp. 19-43.

[10] Griffiths, D.V. (1982), Computation of bearing capacity factors using finite elements, *Géotechnique*, **32**, pp. 195-202.

[11] Hansen, J.B. (1970), A revised and extended formula for bearing capacity, *Danish Geotechnical Institute*, Copenhagen, Bulletin No. 28, pp. 21.

[12] Hill, R. (1950), The mathematical theory of plasticity, Clarendon Press, Oxford.

[13] Higo, Y., Oka, F., Jiang, M. and Fujita, Y. (2005), Effects of transport of pore water and material heterogeneity on strain localization of fluid-saturated gradient-dependent viscoplastic geomaterial, *International Journal for Numerical and Analytical Methods in Geomechanics*, **29**, pp. 495-523.

[14] Hu, Y. and Randolph, M.F. (1998), A practical numerical approach for large deformation problems in soil, *International Journal for Numerical and Analytical Methods in Geomechanics*, **22**, pp. 327-350.

[15] Kimoto, S. (2002), Constitutive models for geomaterials considering structural changes and anisotropy, Doctoral thesis, Kyoto University.

[16] Kimoto, S. and Oka, F. (2003), An elasto-viscoplastic model for clay considering destructuralization and prediction of compaction bands, *Proc. Int. Workshop on Prediction and Simulation Methods in Geomechanics*, TC34 of ISSMGE, Athens, Greece, Oka, F., Vardoulakis, I., Murakami, A., and Kodaka, T. eds., pp. 65-68.

[17] Kimoto, S., Oka, F. and Higo, Y. (2004), Strain localization analysis of elasto-viscoplastic soil considering structural degradation, *Computer Methods in Applied Mechanics & Engineering*, **193**, pp. 2845-2866.

[18] Lambe, T.W. and Whitman, R.V. (1979), *Soil Mechanics, SI Version*, John Wiley & Sons, pp. 162-194.

[19] Leroueil, S., Hight, D.W. (2003), Behaviour and properties of natural soils and soft rocks, *Characterisation and Engineering Properties of Natural Soils*, Tan et al. (eds.) , pp. 29-253.

[20] Materials for the technical committee on the reinforcement method for the bank revetment of Aji River (2005), Office of Nishi-Osaka Chisui, Osaka Prefecture.

[21] Manoharan, N. and Dasgupta, S.P. (1995), Bearing capacity of surface footings by finite elements, *Computers & Structures*, **54**, 4, pp. 563-586.

[22] Merifield, R.S, Sloan, S.W. and Yu, H.S. (1999), Rigorous plasticity solutions for the bearing capacity of two-layered clays, *Géotechnique*, **49**, 4, pp. 471-490.

[23] Mesri, G., Shahien, M. and Feng, T.W. (1995), Compressibility parameters during primary consolidation, *Proceeding of International Symposium on Compression and Consolidation of Clayey Soils - IS-Hiroshima's 95*, Hiroshima, **2**, pp. 1021-1037.

[24] Meyerhof, G.G. (1950), A general theory of bearing capacity, Building research station note no. C143, Watford, England.

[25] Nakase, A.(1981), Bearing capacity of rectangular footings on clays of strength increasing linearly with depth, *Soils and Foundations*, **21**, 4, pp. 101-108.

[26] Oka, F. (1979), Constitutive theory for solid-fluid mixture and its application to stress wave propagation through cohesive soil, *Proc. of JSCE*, **272**, pp. 117-130.

[27] Oka, F. (1981), Prediction of time-dependent behaviour of clay, *Proc. 10th Int. Conf. on Soil Mech. and Foundation Engrg.*, 15-19 June, Stockholm, Balkema, **1**, pp. 215-218.

[28] Oka, F. (1992), A cyclic elasto-viscoplastic constitutive model for clay based on the non-linear hardening rule, *Proc. of the 4^{th} Int. Symp. on Numerical Models in Geomechanics*, Swansea, Pande, G.N. and Pietruszczak, S. eds., Balkema, pp. 105-114.

[29] Oka, F., Yashima, A., Tateishi, A., Taguchi, Y., Yamashita, S. (1999), A cyclic elasto-plastic constitutive model for sand considering a plane-strain dependence of the shear modulus, *Géotechnique*, **49**, 5, pp. 661-680.

[30] Oka, F., Higo, Y. and Kimoto, S. (2002), Effect of dilatancy on the strain localization of water-saturated elasto-viscoplastic soil, *International Journal of Solids and Structures*, **39**, pp. 3625-3647.

[31] Peirce, D., Shih, C. F. and Needleman, A. (1984), A tangent modulus method for rate dependent solids, *Computers & Structures*, **18**, 5, pp. 845-887.

[32] Peraire, J., Vahdati, M., Morgan, K. and Zienkiewicz, O. C. (1987), Adaptive remeshing for compressible flow computations, *Journal of Computational Physics*, **73**, pp. 449-466.

[33] Perzyna, P. (1963), The constitutive equation for work hardening and rate sensitive plastic materials, *Proc. of Vibrational Problems*, Warsaw, **4**, 3, pp. 281-290.

[34] Prandtl, L. (1920), Uber die harte plastischer korper. Nachrichen vonder Koniglichen Gesellschaft der Wissenschaften,. Gottingen, Math. Phys., Klasse, pp. 74-85.

[35] Roscoe, K. H., Schofield, A. N. and Thurairajah, A. (1963), Yielding of clays in state wetter than critical, *Géotechnique*, **13**, 3, pp. 221-240.

[36] Sekiguchi, H. and Ohta, H. (1977), Induced anisotropy and time dependency in clays, *Proc. Speciality Session 9*, 9th ICSMFE, Tokyo, pp. 229-238.

[37] Sekiguchi, K. and Oka, F. (1997), Ground deformation during a braced excavation in a thick soft clay deposit, *Journal of Structural Engineering*, **43A**, pp. 1403-1410.

[38] Sharma, K.G. and Desai, C.S. (1992), Analysis and implementation of thin-layer element for interfaces and joints, *Journal of Engineering Mechanics*, ASCE, **118**, 12, pp. 2442-2462.

[39] Siddiquee, M. S. A., Tatsuoka, F., Tanaka, T., Tani, K., Yoshida, K. and Morimoto, T. (2001), Model tests and FEM simulation of some factors affecting the bearing capacity of a footing on sand, *Soils and Foundations*, **41**, 2, pp. 53-76.

[40] Skempton, A.W. (1951), The bearing capacity of clays, Proc. British Building Research Congress, Division 1, Part 3, pp. 180-189.

[41] Sloan, S.W. and Randolph, M.F. (1982), Numerical prediction of collapse loads using finite element methods, *International Journal for Numerical and Analytical Methods in Geomechanics*, **6**, pp. 47-76.

[42] Sloan, S.W. (1988), Lower bound limit analysis using finite elements and linear programming, *International Journal for Numerical and Analytical Methods in Geomechanics*, **12**, pp. 61-77.

[43] Sloan, S.W. and Kleeman, P.W. (1995), Upper bound limit analysis using discontinuous velocity fields, *Computational Methods in Applied Mechanics and Engineering*, **127**, pp. 293-314.

[44] Tanaka, H., Adachi, T. and Toyoda, T. (1989), A case study on a braced excavation in soft soils, *Report of the Port and Harbour Research Institute*, **28**, 4, pp. 25-54.

[45] Takenaka, J. (1962), Sampling of clay and reliability, *Mechanics and Testing Method of Geologic Materials*, Edited by Kansai Branch of Japan Society of Testing Materials, pp. 1-22 (in Japanese).

[46] Terzaghi, K. (1943), Theoretical soil mechanics, Wiley, New York.

[47] Tetsuka, A. and Tsuchida E. (2003), Adaptive finite element method, Computational mechanics lecture series 2, Maruzen, Tokyo. (in Japanese)

[48] Tsuchida, T. (1990), Study on determination of undrained strength of clayey ground by means of triaxial tests, *Technical Note of the Port and Harbour Research Institute*, **688**, pp. 1-198.

[49] Ukritchon, B., Whittle, A.J. and Sloan S.W. (1998), Undrained limit analysis for combined loading of strip footings on clays, *Journal of Geotechnical and Geoenvironmental Engineering*, **124**, 3, pp. 265-274.

[50] Uto, K. (1967), Sounding of ground, Foundations of Structures, Edited by Kansai Branch of Japan Society of Testing Materials (in Japanese).

[51] Yashima, A., Tsukamoto, Y. and Zhang, F. (2002), Theory and practice in designing earth-retaining structures, *Tsuchi-to-Kiso*, JGS, **50**, 8, pp. 24-26 (in Japanese).

[52] Zdravkovic, L., Potts, D.M. and Jackson, C. (2003), Numerical study of the effect of preloading on undrained bearing capacity, *International Journal of Geomechanics ASCE*, **3**, 1, pp. 1-10.

[53] Zhu, J. Z., Zienkiewicz, O. C., Hinton, E., and WU, J. (1991), A new approach to the development of automatic quadrilateral mesh generation, *International Journal for Numerical Methods in Engineering*, **32**, pp. 849-866.

[54] Zienkiewicz, O. C. and Zhu, J. Z. (1992), The superconvergent patch recovery and a posteriori error estimates. Part 1: The recovery technique, *International Journal for Numerical Methods in Engineering*, **33**, pp. 1331-1364.

[55] Zienkiewicz, O. C. and Zhu, J. Z. (1992), The superconvergent patch recovery and a posteriori error estimates. Part 2: Error estimates and adaptivity, *International Journal for Numerical Methods in Engineering*, **33**, pp. 1365-1382.

[56] Zienkiewicz, O. C. and Taylor, R.L. (2000), The finite element method 5th edition volume 1: The basis. Butterworth-Heinemann.

Appendix A

Error Estimating Method

In this section, the Zienkiewicz-Zhu error estimator proposed by Zienkiewicz and Zhu (1992) is reviewed. This method is adopted to determine the FE discretization errors in the domain. Firstly, let us start by defining the error.

A finite element discretization error is defined as

$$e = u - u_h \tag{A.1}$$

where u is the exact solutions and u_h is an approximation obtained from the finite element method. The global L_2-norm and the corresponding element-wise norm of such an error are as shown in the following equation:

$$\|e\|_2 = \left(\int_\Omega e \cdot e d\Omega\right)^{1/2} \tag{A.2}$$

$$\|e\|_{2,e} = \left(\int_{\Omega e} e \cdot e d\Omega\right)^{1/2} \tag{A.3}$$

It is obvious that an exact solution for u is impossible to obtain in the practical computations. Instead of using an exact solution, therefore, the well-known SPR technique (Superconvergent Patch Recovery), developed by Zienkiewicz and Zhu (1992), is adopted to provides a more accurate estimated value at the integration points. The error from this method is calculated by replacing the exact value u in the Equation A.1 with the SPR approximation value as

$$e \approx e^* = u^* - u_h \tag{A.4}$$

where u^* is the superconvergent recovery value.

The superconvergent patch recovery value is based on the local discrete least squares smoothing and the local continuous least squares smoothing procedures. It is then assumed that the nodal recovery values u^* (such as stress or other gradients) comprises

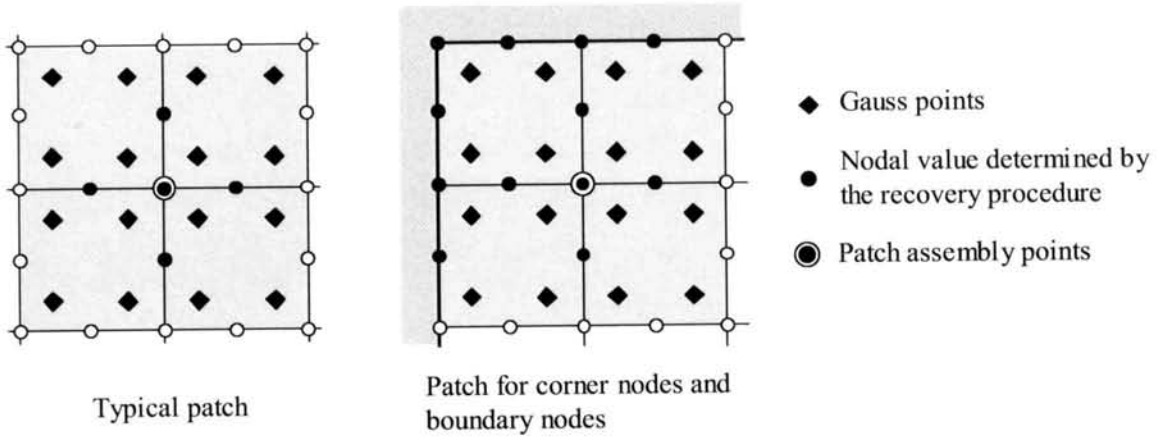

Figure A.1 Typical patch and patch for corner and boundary nodes for the SPR technique

a polynomial expansion of the same complete order p in the shape function $\mathbf{N}$ which is valid over a patch of elements surrounding a particular assembly of nodes under concern. Superconvergent recovery value u^*, which is the polynomial expansion of the complete order p, will be referred to as u_p^* from now on. The component of u_p^* is calculated from the polynomial expansion as

$$u_p^* = \mathbf{Pa} \tag{A.5}$$

in which

$$\mathbf{a} = [a_1, a_2, ..., a_9] \tag{A.6}$$

and for the eight-node quadrilateral element used in this study, $\mathbf{P}$ is obtained as follows:

$$\mathbf{P} = \left[1, x, y, x^2, xy, y^2, x^2y, xy^2\right] \tag{A.7}$$

This "patch" is a group of elements containing the vertex node under consideration. The number of sampling points in the patch must be greater than the number of parameters in the polynomial. Figure A.1 illustrates a typical patch and a patch including the corner and boundary nodes.

Next, the unknown parameter $\mathbf{a}$ must be determined. It was found that the best way to do this is to find its least squares fit to the set of superconvergent sampling points (the Gauss points) existing in the patch. To obtain this, we minimize

$$\begin{aligned} F(a) &= \sum_{i=1}^{n} \left\{u_h(x_i, y_i) - u_p^*(x_i, y_i)\right\}^2 \\ &= \sum_{i=1}^{n} \left\{u_h(x_i, y_i) - \mathbf{P}(x_i, y_i)\mathbf{a}\right\}^2 \end{aligned} \tag{A.8}$$

in which (x_i, y_i) are the coordinates of a group of sampling points, n is the total number of the sampling points, and k is the number of the sampling points for each element. Finally, we obtain

$$\mathbf{a} = \mathbf{A}^{-1}\mathbf{b} \tag{A.9}$$

where

$$\mathbf{A} = \sum_{i=1}^{n} \mathbf{P}^T(x_i, y_i)\mathbf{P}(x_i, y_i) \tag{A.10}$$

and

$$\mathbf{b} = \sum_{i=1}^{n} \mathbf{P}^T(x_i, y_i)u_h(x_i, y_i) \tag{A.11}$$

As parameter $\mathbf{a}$ is determined, we can now calculate $\mathbf{P}$ by simply substituting the appropriate x and y coordinates into Equation (A.7). Consequently, the nodal recovery value u_p^* can be obtained from Equation (A.5) and the estimated error can be obtained from Equations (A.2) and (A.3).

Appendix B

Mesh Generation Method

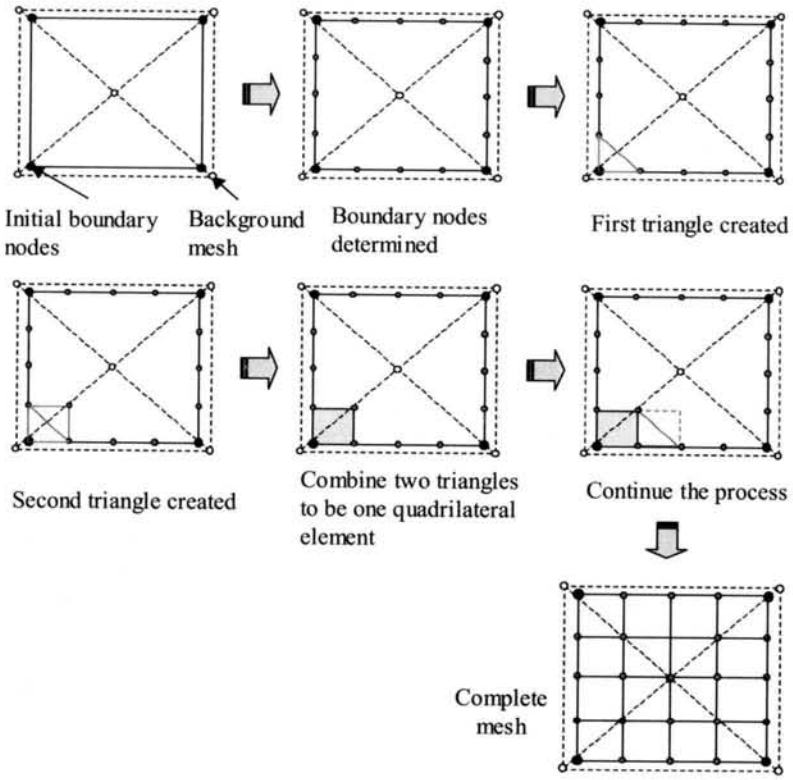

Figure B.1 Mesh generation procedure

In the refinement process, a fully automatic mesh generation algorithm, in which the local element size can be specified, is necessary. In this study, the automatic mesh generation method for the quadrilateral element proposed by Zhu et al. (1991) is adopted. In this method, the user must determine the initial boundary nodes, the background grid, and the element size parameter for each background grid. Then, the triangular elements will be created from the boundary nodes. The size of the elements created is determined by the element size parameters interpolating from the background grid. Two triangular

elements will then be combined into one quadrilateral element and the sides of this element will be used further as the boundary. This process will be continued until the domain is filled with the created elements and the generation is considered to be complete. The mesh generation procedure is illustrated in Figure B.1.